

FINAL PROJECT REPORT:  
NASA LANGLEY RESEARCH CENTER GRANT NCC-1-395  
A STUDY OF WAKE DEVELOPMENT AND STRUCTURE  
IN CONSTANT PRESURE GRADIENTS\*

Prof. Flint O. Thomas  
Prof. R. C. Nelson  
Dr. Xiaofeng Liu

\*based on the Ph.D. dissertation  
of Xiaofeng Li

FINAL PROJECT REPORT:

NASA GRANT NCC-1-395

A STUDY OF WAKE DEVELOPMENT AND STRUCTURE  
IN CONSTANT PRESSURE GRADIENTS

Abstract

Motivated by the application to high-lift aerodynamics for commercial transport aircraft, a systematic investigation into the response of symmetric / asymmetric planar turbulent wake development to constant adverse, zero and favorable pressure gradients has been conducted. The experiments are performed at a Reynolds number of 2.4 million based on the chord of the wake generator. A unique feature of this wake study is that the pressure gradients imposed on the wake flow field are held constant. The experimental measurements involve both conventional LDV and hot wire flow field surveys of mean and turbulent quantities including the turbulent kinetic energy budget. In addition, similarity analysis and numerical simulation have also been conducted for this wake study. A focus of the research has been to isolate the effects of both pressure gradient and initial wake asymmetry on the wake development. Experimental results reveal that the pressure gradient has a tremendous influence on the wake development, despite the relatively modest pressure gradients imposed. For a given pressure gradient, the development of an initially asymmetric wake is different from the initially symmetric wake. An explicit similarity solution for the shape parameters of the symmetric wake is obtained and agrees with the experimental results. The turbulent kinetic energy budget measurements of the symmetric wake demonstrate that except for the convection term, the imposed pressure gradient does not change the fundamental flow physics of turbulent kinetic energy transport. Based on the turbulent kinetic energy budget measurements, an approach to correct the bias error associated with the notoriously difficult dissipation estimate is proposed and validated through the comparison of the experimental estimate with a direct numerical simulation result.



## CONTENTS

LIST OF FIGURES . . . . .	vii
LIST OF SYMBOLS . . . . .	xiii
ACKNOWLEDGEMENTS . . . . .	xviii
CHAPTER 1: INTRODUCTION . . . . .	1
1.1 Background and Motivation . . . . .	1
1.2 Wake Flow in High-lift System . . . . .	4
1.3 Literature Review on Wake Development in Pressure Gradients . . . . .	7
1.3.1 Symmetric Wake . . . . .	7
1.3.2 Asymmetric Wake . . . . .	11
1.4 Uniqueness of the Current Wake Study . . . . .	14
1.5 Research Objectives . . . . .	15
CHAPTER 2: EXPERIMENTAL FACILITY AND MEASUREMENT AP- PARATUS . . . . .	17
2.1 Wind Tunnel and Model Geometry . . . . .	17
2.1.1 Wind Tunnel . . . . .	17
2.1.2 Splitter Plate as a Symmetric Wake Generator . . . . .	19
2.1.3 Splitter Plate as an Asymmetric Wake Generator . . . . .	21
2.2 Pressure Distribution in the Diffuser Test Section . . . . .	21
2.3 Basic Flow Parameters . . . . .	23
2.4 Flow Field Diagnostics . . . . .	26
2.4.1 LDV . . . . .	26
2.4.2 Hot-wire Anemometry . . . . .	28
2.5 Flow Field Validation . . . . .	30
CHAPTER 3: SYMMETRIC WAKE FLOW DEVELOPMENT AND STRUC- TURE IN PRESSURE GRADIENTS . . . . .	36
3.1 Symmetric Wake Flow Nomenclature . . . . .	36
3.2 The Initial Symmetric Wake for Different Pressure Gradients . . . . .	37
3.3 Validation of the Two-Dimensionality of the Flow Field . . . . .	37
3.4 Mean Wake Flow Profile in Zero Pressure Gradient . . . . .	40
3.5 Effect of Pressure Gradient on Mean Flow . . . . .	44
3.5.1 Mean Flow Profile . . . . .	44

3.5.2	Streamwise Evolution of the Wake Half-Width and Maximum Velocity Defect . . . . .	44
3.5.3	Wake Mean Flow Similarity in Pressure Gradients . . . . .	48
3.6	Effect of Pressure Gradient on Turbulence Quantities . . . . .	50
3.6.1	Comparison of Turbulence Intensity at the Same Streamwise Location . . . . .	50
3.6.2	Contour Plots of Turbulence Kinetic Energy . . . . .	52
3.6.3	Streamwise Evolution of Maximum Turbulence Intensity . . . . .	55
3.6.4	Effect of Pressure Gradient on Similarity of Turbulence Quantities . . . . .	58
3.7	Similarity analysis and Solution . . . . .	65
3.7.1	Similarity Analysis . . . . .	65
3.7.2	Universal Similarity Solution for Symmetric Turbulent Wake Mean Flow in Pressure Gradients . . . . .	75
3.7.3	Comparison of Analytical and Experimental Results on Wake Growth . . . . .	77
3.7.4	Discussion . . . . .	83
3.8	Numerical Simulation of the Symmetric Wake Flow . . . . .	88
3.8.1	Numerical Modelling . . . . .	89
3.8.2	Comparison of Numerical and Experimental Results . . . . .	89

CHAPTER 4: ASYMMETRIC WAKE FLOW DEVELOPMENT AND STRUCTURE IN PRESSURE GRADIENTS . . . . .	94
4.1 Asymmetric Wake Flow Nomenclature . . . . .	94
4.2 The Initial Asymmetric Wake . . . . .	95
4.3 Validation of the 2-Dimensionality of the Flow Field . . . . .	96
4.4 Effect of Wake Asymmetry on Wake Development and Structure . . . . .	97
4.4.1 Wake Mean Velocity Profiles . . . . .	98
4.4.2 Wake Width . . . . .	100
4.4.3 Maximum Velocity Defect . . . . .	102
4.4.4 Evolution of Degree of Asymmetry . . . . .	103
4.4.5 Lateral Drift of the Asymmetric Wake Profile . . . . .	105
4.4.6 Maximum Turbulence Intensity . . . . .	106
4.4.7 Discussion . . . . .	108
4.5 Comparison of Numerical and Experimental Results . . . . .	109

CHAPTER 5: TURBULENT KINETIC ENERGY BUDGET MEASUREMENT FOR THE SYMMETRIC WAKE . . . . .	116
5.1 Motivation and Objectives for the Turbulent Kinetic Energy Budget Measurement . . . . .	116
5.2 Transport Equation of the Turbulent Kinetic Energy . . . . .	117
5.3 Approaches for the Measurement of the Turbulent Kinetic Energy Budget . . . . .	121
5.3.1 Convection Terms . . . . .	122
5.3.2 Pressure Diffusion Terms . . . . .	122
5.3.3 Turbulence Diffusion Terms . . . . .	122
5.3.4 Production Terms . . . . .	123
5.3.5 Viscous Diffusion Terms . . . . .	123

5.3.6	Dissipation Terms . . . . .	123
5.4	TKE Budget Measurement Scheme . . . . .	127
5.5	Turbulent Kinetic Energy Budget in Zero Pressure Gradient . . . . .	130
5.5.1	Convection Term . . . . .	130
5.5.2	Production Term . . . . .	131
5.5.3	Turbulence Diffusion Term . . . . .	132
5.5.4	Dissipation Terms . . . . .	133
5.5.5	Turbulent Kinetic Energy Budget . . . . .	143
5.6	Turbulent Kinetic Energy Budget in Adverse Pressure Gradient . . . . .	147
5.6.1	Convection Term . . . . .	147
5.6.2	Production Term . . . . .	151
5.6.3	Turbulence Diffusion Term . . . . .	151
5.6.4	Dissipation Term . . . . .	151
5.6.5	Turbulent Kinetic Energy Budget . . . . .	155
5.7	Turbulent Kinetic Energy Budget in Favorable Pressure Gradient . . . . .	157
5.7.1	Convection Term . . . . .	157
5.7.2	Production Term . . . . .	157
5.7.3	Turbulence Diffusion Term . . . . .	158
5.7.4	Dissipation Terms . . . . .	160
5.7.5	Turbulent Kinetic Energy Budget . . . . .	162
5.8	Comparison of the Turbulent Kinetic Energy Budget in ZPG with the DNS Result . . . . .	164
5.9	Effect of the Pressure Gradient on Planar Wake TKE Budget . . . . .	165
5.10	An Approach to Correct the Bias Error of the Dissipation Estimate . . . . .	172
5.10.1	Sources of Bias Error Associated with the Dissipation Estimate . . . . .	172
5.10.2	Self-similar Behavior of Time Mean Square Derivative Profiles . . . . .	173
5.10.3	Property of Pressure Diffusion Term . . . . .	175
5.10.4	The Shooting Method Approach to Correct the Bias Error of the Dissipation Estimate . . . . .	175
CHAPTER 6: CONCLUSIONS AND RECOMMENDATIONS . . . . .		177
6.1	Conclusions . . . . .	177
6.1.1	Flow Field Validation . . . . .	178
6.1.2	Effects of Pressure Gradient on Wake Flow Development and Structure . . . . .	178
6.1.3	Results of the Similarity Analysis . . . . .	180
6.1.4	Effects of Wake Asymmetry on Wake Development and Struc- ture . . . . .	180
6.1.5	Numerical Simulation . . . . .	181
6.1.6	Turbulence Kinetic Energy Budget Measurement for Symmet- ric Wake . . . . .	182
6.2	Recommendations . . . . .	183
6.2.1	The Twin Airfoil Configuration Wake Experiment . . . . .	183
6.2.2	Investigation of the Effects of Pressure Gradient and Wake Asymmetry on the Large Scale Structure of Wake Flow . . . . .	185
BIBLIOGRAPHY . . . . .		187

APPENDIX A: DETERMINATION OF THE OPTIMAL SPACING BETWEEN MEASUREMENT STATIONS FOR THE TKE BUDGET MEASUREMENTS . . . . . 195

A.1 Lagrangian Interpolation and Central Difference Scheme . . . . . 195

A.2 Uncertainty of the Streamwise Derivative . . . . . 196

A.3 The Optimal Spacing between Measurement Stations . . . . . 199

A.4 Location of Measurement Stations . . . . . 199

## LIST OF FIGURES

1.1	A Boeing 737-100 Airplane Equipped with High-Lift System during the Take-off Process (Photograph Courtesy of NASA Langley Research Center). . . . .	2
1.2	A Conventional Theoretical $C_p$ Plot of a Four-Element Airfoil (The right-hand scale is the canonical form, referred to peak velocity at the nose of the flap. From Smith, 1975). . . . .	5
1.3	Highly Asymmetric Slat Wake Profile (from Thomas, Nelson and Liu, 1998). . . . .	6
2.1	Schematic of the Notre Dame Subsonic Wind Tunnel and Wake Test Section . . . . .	18
2.2	Schematic of the Test Section . . . . .	18
2.3	Symmetric Wake Splitter Plate Geometry . . . . .	19
2.4	Asymmetric Wake Splitter Plate Geometry . . . . .	20
2.5	Experimentally Measured Pressure Distribution for Zero, Adverse and favorable Pressure Gradient Cases . . . . .	24
2.6	Comparison of the Measured and Calculated External Flow Velocities for the Adverse Pressure Gradient Case . . . . .	25
2.7	Fiber Optic LDV Measurement System . . . . .	27
2.8	Typical Spectrum of the u-component for Symmetric Wake at APG . . . . .	29
2.9	Twin X-wire Probe Configuration for Dissipation Measurement . . . . .	30
2.10	Streamwise Pressure Distribution on the Symmetric Wake Splitter Plate . . . . .	31
2.11	Spanwise Pressure Distribution on the Symmetric Wake Splitter Plate . . . . .	32
2.12	Boundary Layer Profile at 50% Chord on the Symmetric Wake Splitter Plate . . . . .	33
2.13	Comparison of LDV and X-wire $U_{rms}$ and $V_{rms}$ Measurement Results at $x/c = 75\%$ on the Splitter Plate with the Klebanoff Data (Klebanoff: $Re_\delta = 7.8 \times 10^4$ ; Notre Dame Wake Study : $Re_\delta = 5.0 \times 10^4$ ) . . . . .	34

2.14	Comparison of LDV and X-wire $\overline{u'v'}$ Measurement Results at $x/c = 75\%$ on the Splitter Plate with the Klebanoff Data (Klebanoff: $Re_\delta = 7.8 \times 10^4$ ; Notre Dame Wake Study : $Re_\delta = 5.0 \times 10^4$ ) . . . . .	35
3.1	Wake Structure Nomenclature. . . . .	37
3.2	Comparison of Initial Wake Mean Velocity Profiles at $x/\theta_0 = 18$ . . . . .	38
3.3	Comparison of Initial Wake $U_{rms}$ Profiles at $x/\theta_0 = 18$ . . . . .	39
3.4	Spanwise Velocity Distribution at $x/\theta = 2.6$ Downstream of the Symmetric Wake Splitter Plate Trailing Edge. (a) Spanwise Velocity Distribution; (b) Location of Measurement in the Initial Wake. . . . .	40
3.5	The Similarity of Wake Profiles in Zero Pressure Gradient. . . . .	41
3.6	Streamwise Variation of Wake Half-width in Zero Pressure Gradient. . . . .	42
3.7	Streamwise Variation of Maximum Velocity Defect in Zero Pressure Gradient. . . . .	43
3.8	Comparison of Mean Velocity for Different Pressure Gradient Cases at $x/\theta_0 = 106$ . . . . .	45
3.9	Comparison of Streamwise Evolution of Wake Half-width for Different Pressure Gradient Cases. . . . .	46
3.10	Comparison of Streamwise Evolution of Maximum Velocity Defect for Different Pressure Gradient Cases. . . . .	47
3.11	Influence of Pressure Gradient on Wake Half-width and Maximum Velocity Defect. . . . .	49
3.12	Similarity Wake Profiles in Pressure Gradients. . . . .	51
3.13	Comparison of Turbulence Intensity Profiles for Different Pressure Gradient Cases at $x/\theta_0 = 106$ . . . . .	53
3.14	Comparison of Reynolds Stress Profiles for Different Pressure Gradient Cases at $x/\theta_0 = 106$ . . . . .	54
3.15	Comparison of Turbulence Kinetic Energy in Different Pressure Gradients. . . . .	56
3.16	Comparison of Streamwise Evolution of Maximum Turbulence Intensity in Different Pressure Gradients. . . . .	57
3.17	Comparison of Turbulence Intensity Profiles in Different Streamwise Locations for the ZPG case. . . . .	59
3.18	Comparison of Reynolds Stress Profiles in Different Streamwise Locations for the ZPG case. . . . .	60

3.19	Comparison of Turbulence Intensity Profiles at Different Streamwise Locations for the APG case. . . . .	61
3.20	Comparison of Reynolds Stress Profiles at Different Streamwise Locations for the APG case. . . . .	62
3.21	Comparison of Turbulence Intensity Profiles at Different Streamwise Locations for the FPG case. . . . .	63
3.22	Comparison of Reynolds Stress Profiles at Different Streamwise Locations for the FPG case. . . . .	64
3.23	Comparison of Streamwise Evolution of Turbulence Quantities in Similarity Scaling for the APG, ZPG and FPG cases. (a) Streamwise component turbulence intensity $\sqrt{u'^2}$ ; (b) lateral component turbulence intensity $\sqrt{v'^2}$ ; (c) Reynolds stress $-\overline{u'v'}$ . . . . .	66
3.24	Comparison of Coefficients $A$ , $B$ , $C$ and $D$ in APG, ZPG and FPG. . . . .	72
3.25	Comparison of the Streamwise Variation of $M$ in APG, ZPG and FPG. . . . .	74
3.26	Comparison of the Measured and the Similarity Predicted Wake Half-width in APG, ZPG and FPG. . . . .	78
3.27	Comparison of the Measured and Similarity Predicted Maximum Velocity Defect in APG, ZPG and FPG. . . . .	79
3.28	Effect of Early Input Location on Similarity Prediction for Wake Half-width. . . . .	80
3.29	Effect of Early Input Location on Similarity Prediction for Wake Maximum Velocity Defect. . . . .	81
3.30	Comparison of the Similarity Predicted and Wake Half-width with DNS Results. . . . .	83
3.31	Comparison of the Similarity Predicted Maximum Velocity Defect with DNS Results. . . . .	84
3.32	Comparison of the Numerical and Experimental Results on the Streamwise Evolution of the Wake Half-Width of the Symmetric Wake in APG, ZPG and FPG. . . . .	90
3.33	Comparison of the Numerical and Experimental Results on the Streamwise Evolution of the Maximum Velocity Defect of the Symmetric Wake in APG, ZPG and FPG. . . . .	91
3.34	Comparison of the Numerical and Experimental Mean Velocity Profiles for the Symmetric Wake in APG with the Spalart-Allmaras One-equation Model. . . . .	92

3.35	Comparison of the Numerical and Experimental Mean Velocity Profiles for the Symmetric Wake in APG with the Wilcox $k - \omega$ Two-equation Model. . . . .	93
4.1	Asymmetric Wake Structure Nomenclature. . . . .	95
4.2	Initial Asymmetric Wake Profile. . . . .	97
4.3	Comparison of Initial Symmetric and Asymmetric Wake Mean Velocity Profiles. . . . .	98
4.4	2-D Verification of the Asymmetric Wake at $x = 19 \text{ mm}$ . . . . .	99
4.5	Streamwise Evolution of the Symmetric Wake Mean Velocity Profile in ZPG. . . . .	100
4.6	Streamwise Evolution of the Asymmetric Wake Mean Velocity Profile in ZPG. . . . .	101
4.7	Streamwise Evolution of the Wake Width for the Symmetric and Asymmetric Wakes in Adverse, Aero and Favorable Pressure Gradients. . . . .	102
4.8	Streamwise Evolution of the Maximum Velocity Defect for the Symmetric and Asymmetric Wakes in Adverse, Zero and Favorable Pressure Gradients. . . . .	103
4.9	Streamwise Evolution of the Wake Half-Width in the Lower and Upper Shear Layer of the Asymmetric Wake in APG, ZPG and FPG. . . . .	104
4.10	Lateral Drift of the Center of the Asymmetric Wake. . . . .	106
4.11	Lateral Drift of the Entire Asymmetric Wake Represented by the Streamwise Evolution of the Three Characteristic Locations in the Wake. . . . .	107
4.12	Streamwise Evolution of the Maximum Turbulence Intensity for the Symmetric and Asymmetric Wakes in Adverse, Zero and Favorable Pressure Gradients. . . . .	108
4.13	Comparison of the Numerical and Experimental Mean Velocity Profiles for the Asymmetric Wake in FPG at $x = 140 \text{ cm}$ . . . . .	111
4.14	Comparison of the Numerical and Experimental Mean Velocity Profiles for the Asymmetric Wake in ZPG at $x = 140 \text{ cm}$ . . . . .	112
4.15	Comparison of the Numerical and Experimental Mean Velocity Profiles for the Asymmetric Wake in APG at $x = 140 \text{ cm}$ . . . . .	113
4.16	Comparison of the Numerical and Experimental Results on the Streamwise Evolution of the Wake Width and Maximum Velocity Defect of the Asymmetric Wake in FPG. . . . .	113

4.17	Comparison of the Numerical and Experimental Results on the Streamwise Evolution of the Wake Width and Maximum Velocity Defect of the Asymmetric Wake in ZPG. . . . .	114
4.18	Comparison of the Numerical and Experimental Results on the Streamwise Evolution of the Wake Width and Maximum Velocity Defect of the Asymmetric Wake in APG. . . . .	114
4.19	Comparison of the Numerical and Experimental Results on the Asymmetric Wake Mean Velocity Profile at Two Different Streamwise stations Before and After the Adjustment of the Wilcox (1998) $k - \omega$ Model. . . . .	115
5.1	Schematic of Measuring Nodal Points. . . . .	128
5.2	Convection Term of Symmetric Wake in ZPG at $x/\theta_0 = 141$ . . . . .	131
5.3	Production Term of Symmetric Wake in ZPG at $x/\theta_0 = 141$ . . . . .	132
5.4	Turbulence Diffusion Term of Symmetric Wake in ZPG at $x/\theta_0 = 141$ . . . . .	133
5.5	Comparison of $\overline{\left(\frac{\partial u'_1}{\partial x_1}\right)^2}$ Measured by X-wire and Parallel Probes in ZPG at $x/\theta_0 = 141$ . . . . .	134
5.6	Comparison of Dissipation Estimate with Different Approaches for ZPG at $x/\theta_0 = 141$ . . . . .	136
5.7	Comparison of $\overline{\left(\frac{\partial u'_1}{\partial x_3}\right)^2}$ Measured by Twin X-wire and Parallel Probes in ZPG at $x/\theta_0 = 141$ . . . . .	138
5.8	The Seven Measured Time Mean Square Derivatives in ZPG at $x/\theta_0 = 141$ . . . . .	140
5.9	Turbulent Kinetic Energy Budget of Symmetric Wake in ZPG at $x/\theta_0 = 141$ . . . . .	143
5.10	Relationship of Convection term and the Turbulent Kinetic Energy Flux. . . . .	146
5.11	Streamwise Development of Turbulent Kinetic Energy of Symmetric Wake in ZPG. . . . .	148
5.12	Convection Term of Symmetric Wake in APG at $x/\theta_0 = 141$ . . . . .	149
5.13	Comparison of V component Mean Profiles for the Symmetric Wake ZPG, APG and FPG Cases at $x/\theta_0 = 141$ . . . . .	150
5.14	Production Term of Symmetric Wake in APG at $x/\theta_0 = 141$ . . . . .	152
5.15	Diffusion Term of Symmetric Wake in APG at $x/\theta_0 = 141$ . . . . .	153

5.16	Comparison of Dissipation Estimate with Different Approaches for APG at $x/\theta_0 = 141$ . . . . .	154
5.17	Turbulent Kinetic Energy Budget of Symmetric Wake in APG at $x/\theta_0 = 141$ . . . . .	155
5.18	Streamwise Development of Turbulent Kinetic Energy of Symmetric Wake in APG. . . . .	156
5.19	Convection Term of Symmetric Wake in FPG at $x/\theta_0 = 141$ . . . . .	158
5.20	Production Term of Symmetric Wake in FPG at $x/\theta_0 = 141$ . . . . .	159
5.21	Diffusion Term of Symmetric Wake in FPG at $x/\theta_0 = 141$ . . . . .	160
5.22	Comparison of Dissipation Estimate with Different Approaches for FPG at $x/\theta_0 = 141$ . . . . .	161
5.23	Turbulent Kinetic Energy Budget of Symmetric Wake in FPG at $x/\theta_0 = 141$ . . . . .	162
5.24	Streamwise Development of Turbulent Kinetic Energy of Symmetric Wake in FPG. . . . .	163
5.25	Comparison of Dissipation Profiles of Symmetric Wake in ZPG with DNS (Moser, Rogers & Ewing, 1998) Result. . . . .	166
5.26	Comparison of Production Profiles of Symmetric Wake in ZPG with DNS (Moser, Rogers & Ewing, 1998) Result. . . . .	167
5.27	Comparison of Convection Profiles of Symmetric Wake in ZPG with DNS (Moser, Rogers & Ewing, 1998) Result. . . . .	168
5.28	Comparison of Turbulence Diffusion Profiles of Symmetric Wake in ZPG with DNS (Moser, Rogers & Ewing, 1998) Result. . . . .	169
5.29	Comparison of Pressure Diffusion Profiles of Symmetric Wake in ZPG with DNS (Moser, Rogers & Ewing, 1998) Result. . . . .	170
5.30	Comparison of TKE Budget Profiles of Symmetric Wake in ZPG, APG and FPG. . . . .	171
5.31	Self-similar Behavior of the Measured Mean Square Derivatives for ZPG at $x/\theta_0 = 141$ . . . . .	174
6.1	Schematic of the Twin Airfoil Configuration Wake Experiment. . . . .	184
A.1	Lagrangian Interpolation . . . . .	197
A.2	Uncertainty Analysis of $dk/dx$ for ZPG at $x = 101.6$ cm, $y = 0.0$ cm. . . . .	200
A.3	Uncertainty Analysis of $dU/dx$ for ZPG at $x = 101.6$ cm, $y = 0.0$ cm. . . . .	201



## LIST OF SYMBOLS

### *Roman Symbols*

$C_L$	lift coefficient
$C_{Lmax}$	maximum lift coefficient
$C_p$	pressure coefficient
$f$	frequency
$i$	streamwise measurement station
$k$	turbulent kinetic energy per unit mass
$k$	wave number, $k = 2\pi f/U$
$k_s$	coefficient for semi-isotropy assumption
$L/D$	lift to drag ratio
$p$	pressure
$Re$	Reynolds number
$r$	scaling factor for dissipation bias error correction
$t$	time
$U$	streamwise mean velocity component
$V$	lateral mean velocity component
$W$	spanwise mean velocity component
$U_{rms}$	root mean square of $u$ -component fluctuating velocity, $U_{rms} = \sqrt{u'^2}$
$V_{rms}$	root mean square of $v$ -component fluctuating velocity, $V_{rms} = \sqrt{v'^2}$

$W_{rms}$	root mean square of $w$ -component fluctuating velocity, $W_{rms} = \sqrt{w'^2}$
$u'$	streamwise fluctuating velocity component
$v'$	lateral fluctuating velocity component
$w'$	spanwise fluctuating velocity component
$X, Y, Z$	Cartesian coordinates for splitter plate boundary layer flow
$x, y, z$	Cartesian coordinates for wake flow
$x_p$	streamwise location where pressure gradient is imposed
$y_0$	lateral location of the center of wake
$y_1$	lateral location of 50% of $U_d$ in the lower shear layer of the wake
$y_2$	lateral location of 50% of $U_d$ in the upper shear layer of the wake

### *Greek Symbols*

$\delta$	wake half-width of the symmetric wake
$\delta_w$	wake width
$\delta_1$	wake half-width of the lower shear layer of the asymmetric wake
$\delta_2$	wake half-width of the upper shear layer of the asymmetric wake
$\delta^*$	displacement thickness
$\epsilon$	dissipation rate of turbulent kinetic energy
$\lambda$	wavelength

$\mu$	molecular viscosity
$\mu_t$	eddy viscosity
$\nu$	kinematic viscosity= $\mu/\rho$
$\theta$	momentum thickness
$\theta_0$	initial wake momentum thickness
$\theta_1$	momentum thickness of the lower shear layer of the asymmetric wake
$\theta_2$	momentum thickness of the upper shear layer of the asymmetric wake
$\eta$	non-dimensional $y$ coordinate
$\rho$	fluid density
$\tau$	shear stress
$\omega$	time-mean square vorticity fluctuation

*Superscripts*

'	fluctuation component
---	time-averaged quantity

## *Subscripts*

$e$	external velocity
$i$	tensor index, position of imposed pressure gradient
$j$	tensor index
$k$	tensor index
$p$	pressure
$0$	stagnation condition
$1$	tensor index, in $x$ direction
$2$	tensor index, in $y$ direction
$3$	tensor index, in $z$ direction
$\infty$	incoming free stream condition

## ACKNOWLEDGEMENTS

First, I would like to express my sincerest thanks to my advisors, Prof. Flint O. Thomas and Prof. Robert C. Nelson for their constant support, guidance, encouragement and inspiration throughout my research work. I would also like to express my thanks to Profs. Patrick F. Dunn, Mihir Sen, Albin A. Szewczyk, Joseph M. Powers, Mohamed Gad-el-Hak, Samuel Paolucci, Hafiz Atassi, David T. Leighton and Hsueh-Chia Chang for their inspirational courses in fluid dynamics and mathematics.

Also I am much obliged to the HSSERT and the departmental staff Mike Swadener, Joel Preston, Marilyn Walker and Nancy Davis for their invaluable assistance they rendered. The excellent day care program offered by the Notre Dame Early Childhood Development Center is also highly appreciated. The friendship and warmth of our Notre Dame family, together with the peaceful serenity of our beautiful Notre Dame campus, provides me an ideal environment for the exploration of the wonders in the turbulence world.

Finally, I am very grateful to Dr. Michael M. Rogers of NASA Ames Research Center for providing me with DNS data for comparison, to Dr. Christopher L. Rumsey, Mr. John R. Carlson and Mr. William L. Sellers III of NASA Langley Research Center for their technical collaboration and encouragement, and to Prof. William K. George of Chalmers University of Technology for his suggestion on the axisymmetric turbulence consideration during the APS DFD 2000 meeting. The financial support from NASA Ames and and NASA Langley Research Centers during my Ph.D. study at Notre Dame is also gratefully acknowledged.



## CHAPTER 1

### INTRODUCTION

#### 1.1 Background and Motivation

A high-lift system is a system of aerodynamic devices that is specifically designed and placed on the wing of a transport aircraft to improve the aerodynamic performance of the wing during the landing and take-off process. Typically, a high-lift system includes a leading edge slat and one or several trailing edge flap(s), as indicated in Figure 1.1. During the landing approach, while keeping the plane in the air, the pilot of an aircraft usually wants to set the approaching speed of the aircraft as slow as possible so that no high demand is placed on the length of the landing field and, more importantly, the landing safety can be more assured in this way. This requires that the maximum lift coefficient  $C_{Lmax}$  to be as large as possible. However, during the take-off process, the pilot usually wants the aircraft to climb to the cruise altitude as quickly as possible without burning too much fuel in the climbing process. This requires that the lift to drag ratio of the wing  $L/D$  to be as high as possible. All these wing aerodynamic performance requirements for aircraft landing and take-off can be fulfilled by the deployment of the high-lift system. That is why the high-lift systems are widely used in commercial transport aircraft in today's aviation world. A good high-lift design usually means tremendous economic benefits to the air transport carriers. For example, according to the trade study results reported by Mack and McMasters (1992), for a modest sized 150 passenger twin turbofan powered transport aircraft intended for domestic airline service, a

5% increase in take-off lift to drag ratio could result in either a 15% increase in payload from a given airport, or an 11% increase in range for the specified payload. Similarly, a 5% increase in maximum lift coefficient during landing approach could result in up to a 20% increase in payload for a given approach speed, or a 3 *knots* reduction in approach speed with the specified payload.

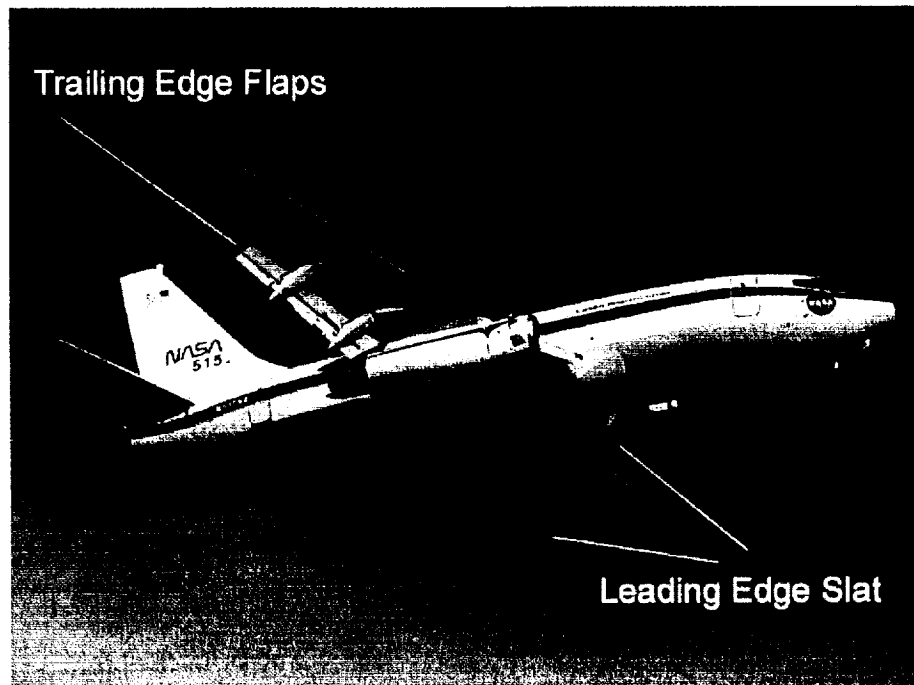


Figure 1.1. A Boeing 737-100 Airplane Equipped with High-Lift System during the Take-off Process (Photograph Courtesy of NASA Langley Research Center).

However, although the high-lift systems are widely used in today's commercial airline fleet, there are still prominent problems associated with the design and maintenance of high-lift systems. First, the high-lift system represents a large lead-time item in the design of new aircraft due to its inherent complexity and consequent emphasis on empiricism in its design. Second, high-lift systems are also high maintenance cost items on existing fleet. These problems will result in extra expenses on

the procurement and operating costs of an aircraft and eventually, high expenses on airline tickets. As aerospace engineers, we want to solve these problems. By solving these problems, the high costs associated the high-lift system design and maintenance will be reduced and eventually, everybody will benefit from this improvement. In fact, one key area in which there is an as yet unrealized potential for cost reductions is in the design of high-lift systems. To expeditiously accomplish the design of the high-lift system and to achieve improved aerodynamic performance with simpler high-lift configurations that involve fewer elements and reduced maintenance costs, reliable Computational Fluid Dynamics (CFD) design tools are required.

A prerequisite to achieving a reliable CFD design tool for high-lift system design is to clarify the flow physics issues associated with the high-lift system. Unfortunately, these flow physics issues remain largely unresolved. This stems from the fact that the flow over a multi-element airfoil is exceedingly complex and includes numerous viscous dominated effects. These effects are usually strongly coupled and the coupling can often obscure the “cause” and “effect” observations that are so essential in scientific experimentation.

Although the flow field over a multi-element airfoil is exceedingly complex, people can still find a reasonable approach to analyze it. Several years ago, Thomas *et al.* (1997) proposed the “high-lift building block flow” concept for the systematic exploration of the flow physics issues about the high-lift system. The basic idea of this concept is that the flow field over any multi-element airfoil may be broken down into certain generic component flows that are termed “high-lift building block flows” which include: (1) laminar separation bubbles, (2) large scale cove flow separation, (3) boundary-layer / wake interactions, i.e., the so-called confluent boundary layer, (4) boundary layer development under influence of both arbitrary streamwise pressure gradient and surface curvature, (5) multiple wake interactions,

(6) wake development in strong pressure gradients and with streamline curvature, (7) three-dimensional boundary layer transition, and (8) relaminarization of turbulent boundary layers.

Thomas *et al.* (1997) argued that the most useful approach to advance the state-of-the-art in high-lift aerodynamics is to perform benchmark fluid dynamics experiments involving individual high-lift building block flows, and understanding high-lift building block flows individually is a prerequisite to understanding their integrated behavior in a high-lift system.

Within the framework of the high-lift building block flow concept, several research projects focused on flow physics issues related to individual building block flows are actively conducted at the Hestert Center for Aerospace Research at the University of Notre Dame. In particular, the research topic, a study of wake development and structure in pressure gradients, is part of this systematic research effort in the high-lift aerodynamics research area. The research project presented in this dissertation will address key flow field physics issues surrounding one particularly important high-lift building block flow: that of wake development in arbitrary pressure gradients.

## 1.2 Wake Flow in High-lift System

In a high-lift system, each upstream element produces a wake that interacts aerodynamically with its downstream partners. For example, a slat develops its own boundary layer, which separates from its trailing edge, forming a wake of low-energy air that flows alongside the main airfoil and on downstream. Basically, there are two major features associated with the wake flow generated by the upstream element in a high-lift system. First, the wake flow in a high-lift system inevitably occurs in a strong pressure gradient environment, and dominantly, strong adverse pressure gradient, as shown in Figure 1.2 (from Smith, 1975). Second, the wake flow in a

high-lift system is usually highly asymmetric. Figure 1.3 shows a wake profile generated by a leading edge slat in a multi-element airfoil (Thomas, Nelson and Liu, 1998). From this figure we can see how asymmetric a wake profile is in a high-lift system.

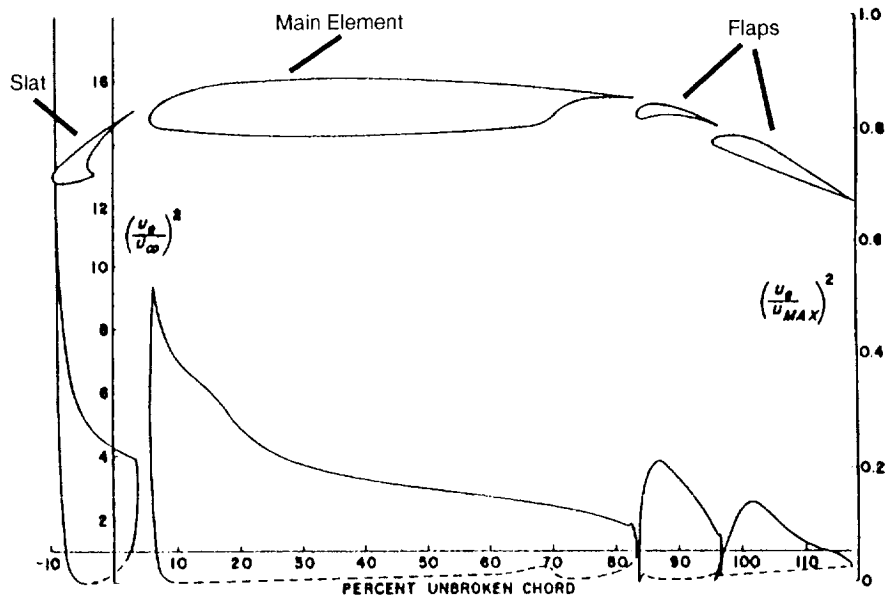


Figure 1.2. A Conventional Theoretical  $C_p$  Plot of a Four-Element Airfoil (The right-hand scale is the canonical form, referred to peak velocity at the nose of the flap. From Smith, 1975).

This kind of wake flow is very important in a high-lift system because its behavior is directly related to the aerodynamic performance of a high-lift system. As an example of the role that the wake development plays in the performance of the high-lift system, the growth rate of the slat wake will determine, in part, the location of onset of confluence with the main element boundary layer. Even in cases where there is no strong confluence on the main element, the slat wake will have the effect of moderating the surface pressure peak on the trailing flap(s). Flap pressure peak moderation helps maintain flow attachment and improves  $C_{Lmax}$ . The degree of flap

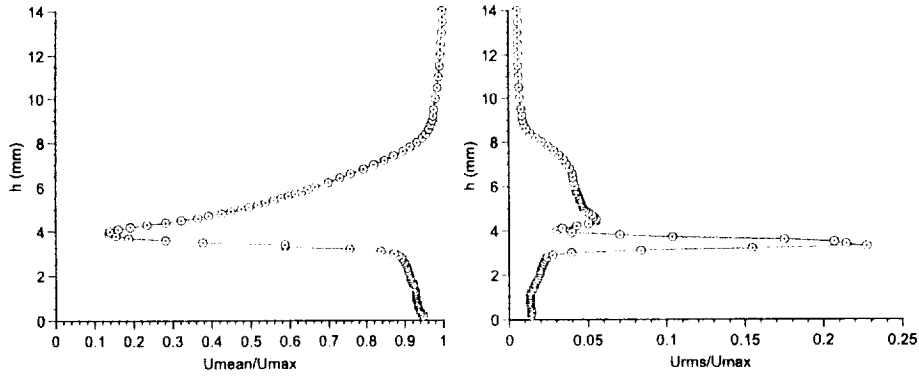


Figure 1.3. Highly Asymmetric Slat Wake Profile (from Thomas, Nelson and Liu, 1998).

surface pressure peak moderation is related directly to the wake width. In general, the thicker the wake, the more the flap pressure peak is moderated. This is due to an associated streamline displacement effect (See Garner, Meredith and Stoner, 1991).

Another example of the profound influence of wake widening on high-lift performance is apparent from the experimental study of Lin, Robinson and McGhee (1992). They explored the effect that sub-boundary layer scale vortex generators placed on the trailing flap surface had on flap flow attachment. The vortex generators augmented lift at low to moderate angles of attack. However, their results showed no benefit at high angles since flow attachment is maintained even without the use of vortex generators. This is due to the fact that at the highest angles of attack prior to stall, the main element wake thickens appreciably and has the effect of suppressing the trailing flap surface pressure peak. As a consequence the flap boundary layer flow remains attached. At low to moderate angles of attack the wake is comparatively thin and is less effective at moderating the flap surface pressure peak. This shows the somewhat surprising and non-intuitive behavior that can be encountered in high-lift systems as a consequence of the viscous flows involved.

In addition to issues related directly to wake widening, Smith (1975) notes that off surface flow reversal can occur if the wake encounters a sufficiently strong adverse pressure gradient. This has been termed by some as “wake bursting”. Indeed, the existence of the off surface flow reversal of the wake generated by an upstream element of a multi-element airfoil was successfully detected visually by Petrov (1978). Some measurements from the NASA Langley Low Turbulence Pressure Tunnel (e.g., Chin et al, 1993) show wake profiles over the trailing edge flap of a Douglas three element airfoil that appear very close to exhibiting off surface reversal.

This wake study is designed to simulate a particular kind of the high-lift building block flow, that is, the slat wake flow in a simplified yet more focused laboratory environment. More specifically, this wake research project is designed to investigate the symmetric/asymmetric planar wake flow development and structure subjected to a constant zero (ZPG), favorable (FPG) and adverse (APG) pressure gradient environment. It is expected that through a systematic experimental/numerical/analytical investigation into the symmetric/asymmetric wake development in pressure gradients, we can obtain a better understanding of the flow physics issues relevant to high-lift aerodynamics.

### 1.3 Literature Review on Wake Development in Pressure Gradients

#### 1.3.1 Symmetric Wake

The wake flow has been studied extensively in the 20th century. Past work has used a variety of experimental, analytical and computational techniques to examine the wake under various kinds of conditions. The literature on zero pressure gradient two-dimensional wake includes those by Townsend (1956), Reynolds (1962), Keffer (1965), Gerrard (1966), Chevray *et al.* (1969), Mattingly *et al.* (1972), Cebeci, *et al.* (1979), MacLennan *et al.* (1982), Fabris (1983), Wygnanski *et al.* (1986), Lasheras *et al.* (1986, 1988), Antonia *et al.* (1987), Patel *et al.* (1987), Meiburg *et al.* (1988),

Gharib *et al.* (1989), Cimbala *et al.* (1990), Corke *et al.* (1992), Marasli *et al.* (1992), Hayakawa *et al.* (1992), Maekawa *et al.* (1992) and Kopp *et al.* (1995).

Compared with the often-studied case of the symmetric wake in zero pressure gradient, there have been relatively fewer investigations involving wake development in non-zero pressure gradients. However, we should recognize that some preliminary efforts have been made in the past decades to investigate the problem of the wake development in arbitrary pressure gradients.

The investigation conducted by Hill, Schaub and Senoo (1963) on mean velocity development of the wake in a diffuser took place years before the high-lift application of wake was recognized. In their experiment, the wake of a rectangular bar passed through a two-dimensional diffuser with suction slots was studied with a 3-hole pressure probe. They demonstrated experimentally that for wake development in a diffuser, if the pressure gradient is large enough, the wake might grow rather than decay, so that a zone of stagnant or reversed flow develops. They performed an analytical study employing a simple “eddy viscosity” model on the basis of the experiment and obtained a calculation formula for mean flow parameters of the wake. They also argued that similarity of wake profiles seems to be an adequate assumption even with quite strong adverse pressure gradients. However, this assertion contradicts the result obtained by Gartshore (1967). Following Townsend (1956) and Patel and Newman (1961), Gartshore (1967) showed from the analysis of the thin shear layer momentum equation that the two-dimensional turbulent wake can be self-preserving only when it is subjected to appropriately tailored adverse pressure gradients. He also attempted to experimentally obtain this self-preserving wake by adjusting the pressure gradient downstream of a square rod until approximately constant ratio of maximum velocity defect to local external velocity was obtained.

Another relevant research work is the experiments and theoretical research conducted by Narasimha and Prabhu (1971) and Prabhu and Narasimha (1971) on plane turbulent wakes undergoing transition from an initial equilibrium state to a different final one as a result of a nearly impulsive pressure gradient perturbation. It should be pointed out that the pressure gradients in their experiment were imposed locally rather than globally on the flow field. One of the major conclusions of their study is that the approach to a new equilibrium state is exponential, with a relaxation length of the order of 103 momentum thickness.

In addition to wake research which involved only the wake in a pressure gradient environment, Zhou and Squire (1985) investigated the interaction of a wake with a turbulent boundary layer in zero and adverse pressure gradients downstream of airfoils of various shapes. To produce an adverse pressure gradient, a gauze resistance was added in their wind tunnel and a porous roof for boundary layer suction was implemented. The mean and fluctuating velocities were measured with an X-wire probe. They found that the level of turbulence in the wake has the strongest influence on the wake / boundary layer interaction.

Recently, Hoffenberg, Sullivan and Schneider (1995), Tummers, Passchier and Henkes (1997), and Hoffenberg and Sullivan (1998) carried out investigations on wake development in pressure gradients, respectively. In the experiment by Hoffenberg *et al.* (1995), the wake of a flat plate was subjected to an adverse pressure gradient in a two dimensional diffuser. Slot blowing was used to prevent the boundary layer on the diffuser wall from separation. Pitot probe surveys, laser Doppler velocimetry (LDV) measurements and flow visualization were used to investigate the physics of the decelerated wake. From their experiment, they concluded that as the magnitude of the imposed pressure gradient was increased, the wake became thicker and the turbulence level also increased. According to their experiment, wake

thickness more than tripled when the imposed adverse pressure gradient changed from zero to the point of reversal onset. They also documented strong wake reversal at a very strong adverse pressure gradient by means of flow visualization.

On the basis of their previous experiments, Hoffenberg *et al.* (1998) modified their test facility with suction slots opened at the inlet of the diffuser section. In addition to the experimental investigation of the wake development in the adverse pressure gradient, they also conducted numerical simulations. Their preliminary Computational Fluid Dynamics (CFD) simulation was performed with a NASA code, INS-2D. The extensive numerical simulations were performed with FLUENT, a commercial, finite-volume, Navier-Stokes solver. They examined and compared the capability of different turbulence models in predicting the experimental results and found the calculations under-predicted wake growth and failed to demonstrate wake reversal.

Tummers, Passchier and Henkes (1997) investigated the wake of a flat plate subjected to an adverse pressure gradient, which resulted in local flow reversal. Mean flow and turbulence quantities up to triple-velocity correlation were measured by using a three-component LDV system. Some of the terms in the turbulence kinetic energy equation were determined from the LDV measurement results. They also conducted numerical simulation of the wake development by solving the Reynolds-averaged Navier-Stokes equations and compared the numerical and experimental results. The comparison shows that both a  $k - \epsilon$  model and a differential stress model correctly predicted the spreading rate of the wake, but the mean velocity and the kinetic energy on the wake centerline were poorly predicted.

Most recently, Driver and Mateer (2000) conducted a fundamental investigation into the adverse pressure gradient effect on the wake reversal (the so-called “off-body” separation) in a pressurized wind tunnel. The wake is generated by a flat

splitter plate with a chord length of 419 *mm*. The Reynolds number of their experiment based on plate length is 10 million. Surface jet blowing with a 2% of the total tunnel mass flow rate was used to prevent separation on diffuser walls. Several cases of adverse pressure gradient producing flows ranging from no reversed flow to massively reversed flow were investigated by use of a two-component laser-Doppler velocimeter to measure the mean and fluctuating velocities. The adverse pressure gradient is imposed by means of changing the divergence angle of the diffuser test section. They found that the separated wake flow fields and the nearly separated wake flows in the diffuser test section produce almost identical pressure distributions, independent of the size or the existence of the separation bubble. Once the flow is near separation, the displacement effects of the wake grow proportionally to increases in the diffuser test section divergence. The cross-stream gradient of the Reynolds shear stress is not significantly altered by the presence of separation, although the magnitude of the turbulent Reynolds stress increases with the increasing size of the reverse flow region. In addition, they also performed numerical simulations for the experimental cases using the NASA INS2D code. Turbulence models used in the computation include the Spalart-Allmaras one-equation model and Menter's SST ( $k - \omega$ ) model. They found both models failed to capture the wake flow reversals and the associated wake displacement effects seen in the experiment. In their experiment, they also investigated the effects of streamline curvature and "overhang" on the wake reversal.

### 1.3.2 Asymmetric Wake

Compared with the symmetric wake in pressure gradient, there have been fewer studies of the asymmetric wake in the pressure gradients. The only known effort specifically on the investigation of asymmetric wake development in adverse pressure gradient is the experiment by Roos (1997). In Roos' experiment, an airfoil-

simulation plate was used to generate the type of asymmetric wake that is often seen in a high-lift system. A pair of airfoils placed on the top and bottom of the test section were used to generate a strong adverse pressure gradient. Three techniques were used to generate the asymmetric wake. First, the nose of the flat plate wake generator is drooped at an angle. Second, an adverse pressure gradient was imposed on the boundary layer on the splitter plate to thicken the boundary layer. Finally, suction slot is opened on the plate to control the thickness of the boundary layer. Roos' experiment demonstrated the significance of turbulent wake asymmetry on the development of wake turbulence. One shortcoming of Roos' experiment is that apparent unsteadiness existed in the initial asymmetric wake by examining the experimental wake profile.

Hah and Lakshminarayana (1982) investigated asymmetric wake generated by a symmetric airfoil (NACA 0012) placed at an angle of attack in a  $1.5\text{ m} \times 1.5\text{ m} \times 2\text{ m}$  wind tunnel. No pressure gradient was imposed on the flow field for wake development. An X-wire was used for the flow field survey. Their experiments indicated that the asymmetric wake becomes nearly symmetric after one chord downstream of the trailing edge of the airfoil. The streamwise velocity defect in the asymmetric wake decays more slowly compared to that of a symmetric wake. The streamline curvature due to the airfoil loading has a substantial effect on both the velocity profile and the turbulence structure. Their numerical simulation of the same wake indicated that the turbulence closure models need some modification to account for the asymmetric characteristics of the wake.

Several previous research efforts about the wake development focused specifically on the effect of both curvature and pressure gradient on two-dimensional wake (Savill (1983); Nakayama (1987), Ramjee and Neelakandan (1989) and John and Schobeiri (1996)). One of the byproducts provided by these studies is some information on

asymmetric wake development. Savill (1983) investigated a cylinder wake that is turned abruptly by  $90^\circ$  by means of a back plate so that it is both highly curved and influenced by a streamwise pressure gradient. The data for mean velocity and turbulent stress indicated a strong influence of curvature for the wake. The turbulent stress fields are complex owing to the coexistence of the stabilized (outer-half) and destabilized (inner-half) regions across the wake and the interaction between them. Nakayama (1987) carried out a study of the effect of mild pressure gradient and mild streamline curvature on a small deficit wake. The mild pressure gradient and mild streamline curvature environment was achieved by an airfoil-like thin plate placed at small angles in the external flow. Despite the governing mild pressure gradient and curvature, the measured data indicates a strong sensitivity of turbulence quantities (especially the Reynolds shear stress) to the curvature and pressure gradient. Ramjee and Neelakandan (1989) examined the wake of a rectangular cylinder in a longitudinally curved duct. They compared mean velocity and Reynolds stress results to those for the rectangular cylinder in a straight duct. They found that the mean velocity profile of the wake was not symmetric about the centerline of the curved duct. They also found that the unstable side contribution to half-width was greater than that in a straight duct and that the stable side contribution to half-width was less than that in a straight duct. They also found the wake defect was greater in the curved duct than in the straight duct. John and Schobeiri (1996) investigated experimentally the two-dimensional wake behind a stationary circular cylinder in a curved channel at positive (adverse) pressure gradient. An X-hot-film probe was used to carry out the flow field survey. Their results showed strong asymmetry in velocity and Reynolds stress components. However, they found the mean velocity defect profiles in similarity coordinates are almost symmetric and follow the same Gaussian function for straight wake data. They also made comparison of

the wake development in a curved channel at positive and zero streamwise pressure gradients and found the decay rate of velocity defect is slower and the growth of the wake width is faster for a positive (adverse) streamwise pressure gradient.

#### 1.4 Uniqueness of the Current Wake Study

Among the existing literature on wake development in flows with pressure gradients, the research efforts by Hoffenberg *et al.* (1995, 1998), Tummers *et al.* (1997), Roos (1997) and Driver *et al.* (2000) resemble to some extent the present Ph.D. dissertation research. However, the pressure gradients imposed for these aforementioned studies were all x-dependent, making it difficult to distinguish the effects of the pressure gradient and the distance of streamwise evolution on the wake growth. In addition, none of these studies incorporated the investigation of the influence of the favorable pressure gradient on wake development and structure. These untouched aspects of the wake research will be tackled in this wake study. In particular, compared to all the previous wake research, the present wake study has the following uniqueness:

- The imposed pressure gradient is maintained constant throughout the flow field investigated, allowing the effect of the pressure gradient to be isolated from the complication with other effects such as the streamwise evolution;
- The present wake study incorporates a systematic experimental investigation that investigates not only the adverse pressure gradient effects, but also zero and favorable pressure gradient effects on wake development;
- The symmetric wake and the asymmetric wake in pressure gradients will be investigated respectively so that the effect of wake initial asymmetry can be distinguished from the pressure gradient effect;

- The present turbulence kinetic energy budget measurement for the symmetric wake at different constant pressure gradients is also unique.

### 1.5 Research Objectives

This wake study will focus on near wake behavior due to its relevance for high lift applications. The focus of the proposed study will be to examine the response of both symmetric and asymmetric wake development and structure to these well-defined pressure fields. In each case, however, the wake initial conditions are maintained to be identical upstream of the imposition of the pressure field. The objective of the proposed wake study will be to answer the following questions:

- What is the structure and growth rate of wakes under constant pressure gradient conditions? How is wake widening related to  $dP/dx$ ?
- What role does initial wake asymmetry play in wake growth? Do symmetric and asymmetric wakes develop differently in a given pressure gradient condition? If so, how and why?
- How are individual terms in the wake turbulent kinetic energy budget influenced by the imposed pressure gradient? Such detailed information regarding the effect on the turbulent flow structure is essential for the development of improved turbulence models.

To address fundamental questions regarding wake development as outlined above, the wake study involves a systematic experimental investigation which is performed in a step by step manner. In phase I, the development and structure of an initially symmetric wake in constant pressure gradient environments will be investigated. In phase II, the influence of the wake asymmetry on the wake development and structure in constant pressure gradient environments will be addressed. In phase III, as

a natural consequence of the work performed during phases I and II, the turbulent kinetic energy budget measurement at selected stations for symmetric wake cases at different pressure gradients will be performed. In addition to the experimental investigation efforts, similarity analysis and numerical simulation have also been conducted for this wake study. A focus of the research has been to isolate the effects of both pressure gradient and initial wake asymmetry on the wake development. The experimental setup, procedures, approaches and results, together with the results of the similarity analysis and the numerical simulations for this wake study, will be presented and discussed in the following chapters of this dissertation.

## CHAPTER 2

### EXPERIMENTAL FACILITY AND MEASUREMENT APPARATUS

#### 2.1 Wind Tunnel and Model Geometry

##### 2.1.1 Wind Tunnel

The experiments were performed in an in-draft subsonic wind tunnel facility located at the Hestert Center for Aerospace Research at the University of Notre Dame. The schematic of the wind tunnel is shown in Figure 2.1. Ambient laboratory air is drawn into a contraction inlet with  $2.743\text{ m}$  by  $2.743\text{ m}$  effective area by an eight-bladed fan connected to an  $18.6\text{ kW}$  AC induction motor. The contraction ratio of the tunnel inlet is  $20.25 : 1$  with 12 anti-turbulence screens, which leads to a uniform test section inlet velocity profile with low turbulence intensity level (less than  $0.1\%$  with signal high-pass filtered at  $3\text{ Hz}$  and less than  $0.06\%$  with signal high-pass filtered at  $10\text{ Hz}$ ).

The wind tunnel consists of two consecutive test sections, the inlet test section and the diffuser test section, both of which were specifically constructed for the wake development experiment, as shown in Figure 2.2. The inlet test section is  $1.829\text{ m}$  in length,  $0.610\text{ m}$  in width and  $0.356\text{ m}$  in height. The length and width of the diffuser test section are the same as those of the inlet test section while both the top and bottom walls of the diffuser test section were adjustable in order to create a pressure gradient environment. The top and bottom walls of the diffuser test section were made of sheet metal, and their contour can be adjusted by means of seven groups of turnbuckles. In this manner, the contour can be optimized to produce a desired

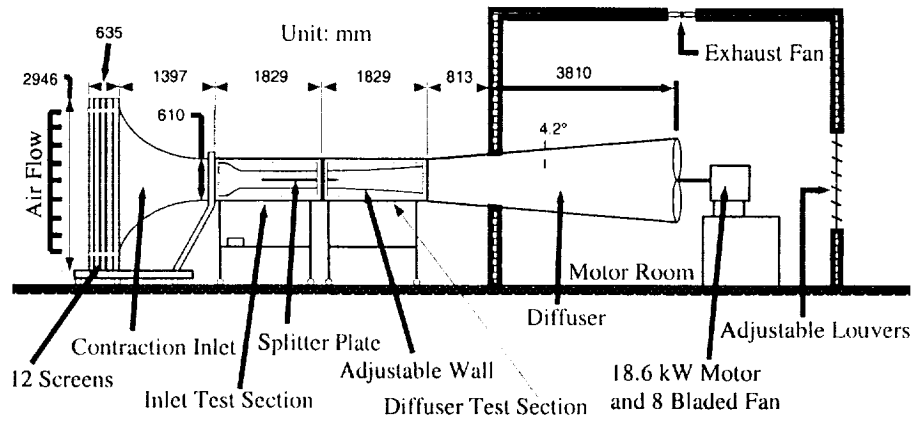


Figure 2.1. Schematic of the Notre Dame Subsonic Wind Tunnel and Wake Test Section

constant pressure gradient environment. The relative error of the imposed constant pressure gradient is no more than 1.7% to the 95% confidence level for the worst case. To facilitate flow visualization and LDV measurement, both the inlet and the diffuser test sections have a sidewall made of glass. A schematic of the test sections is given in Figure 2.2.

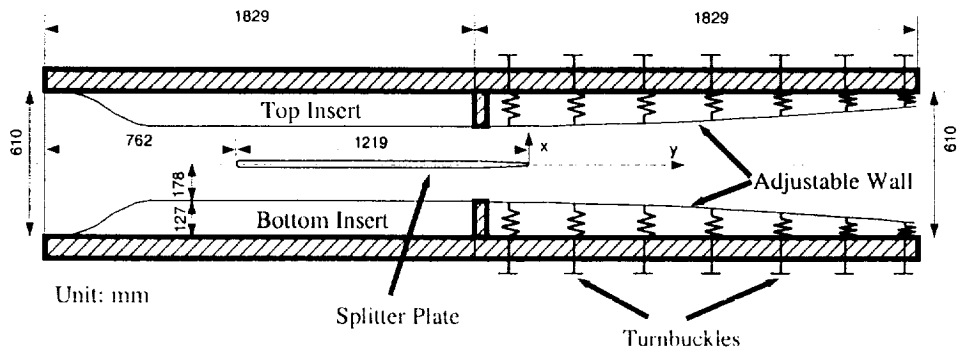


Figure 2.2. Schematic of the Test Section

### 2.1.2 Splitter Plate as a Symmetric Wake Generator

The symmetric wake generating body is a two-dimensional splitter plate with round nose and tapered trailing edge, as illustrated in Figure 2.3. The chord length of the flat plate is 1.219 m. The last 0.203 m of the plate consists of a 2.2° linear symmetric taper down to a trailing edge of 1.6 mm thickness. The plate has multiple surface pressure taps and their associated internal tubing. The model is sidewall mounted with end plates used to minimize the influence of tunnel sidewall boundary layers. The boundary layer on the plate was artificially tripped by distributed roughness over the nose.

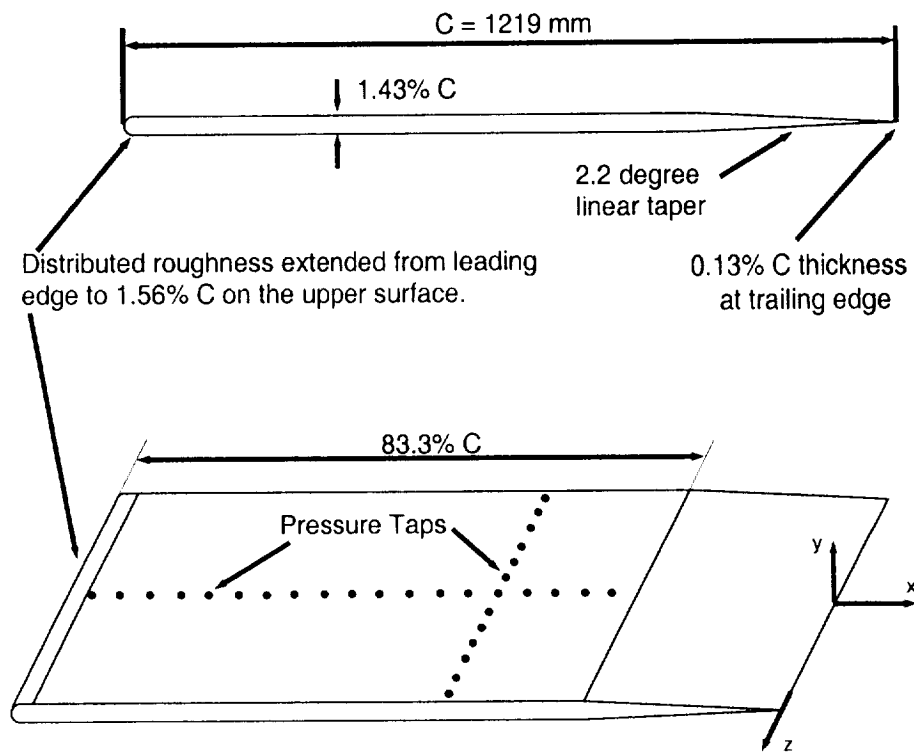


Figure 2.3. Symmetric Wake Splitter Plate Geometry

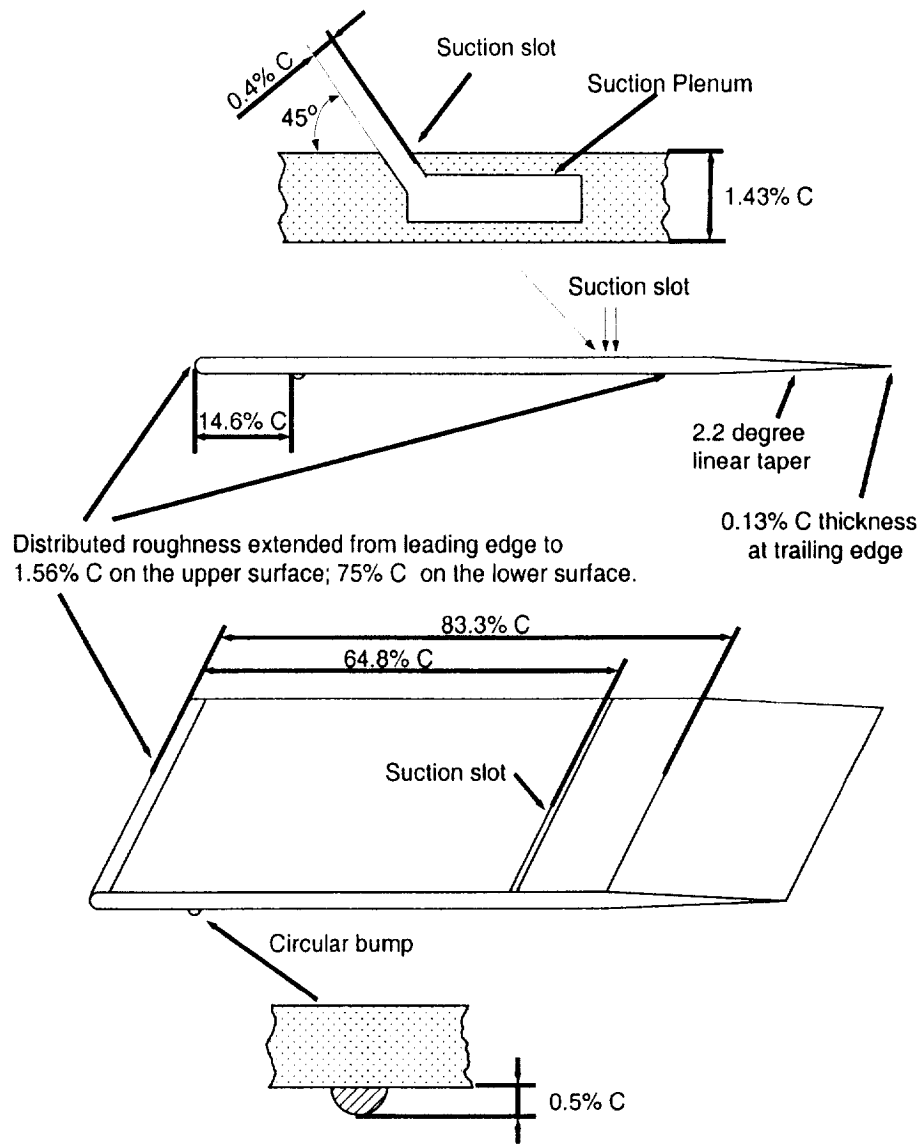


Figure 2.4. Asymmetric Wake Splitter Plate Geometry

### 2.1.3 Splitter Plate as an Asymmetric Wake Generator

For the generation and control of the initially asymmetric wake, three flow control techniques are applied, as shown in Figure 2.4. First, a suction slot is placed on the top surface of the plate at the 65% chord position. The suction slot is connected to an internal plenum that, in turn, is connected via suitable external plumbing to a large rotary vacuum pump. Care was taken to insure that the suction flow rate was spanwise uniform. Using suction, the top plate turbulent boundary layer thickness is reduced. Second, a small, spanwise uniform, semi-circular bump placed at the 14.6% chord position on the lower side of the plate thickens the boundary layer on that side. Finally, to eliminate the unsteady effects on the boundary layer flow separation introduced by the semi-circular bump, distributed roughness was placed on the lower surface of the plate from the leading edge all the way down to 75% chord position. The combination of these techniques gives rise to an initially asymmetric wake profile similar to that encountered in actual high-lift systems. The degree of asymmetry, represented by the ratio of the momentum thickness of the lower shear layer to that of the upper shear layer of the wake, is 2.5. As was the case in the symmetric wake study, the asymmetric wake profile is spanwise uniform. For details of the asymmetric wake, see Chapter 5.

## 2.2 Pressure Distribution in the Diffuser Test Section

For both symmetric and asymmetric wake cases, the pressure gradient is imposed on the wake by means of fully adjustable top and bottom wall contours of a diffuser test section. The flexible wall is iteratively adjusted by means of seven groups of turnbuckles, as shown in Figure 2.2, until the desired constant streamwise pressure gradient  $dC_p/dx$  is attained. The pressure coefficient  $C_p$  is defined as:

$$C_p = \frac{p - p_\infty}{p_0 - p_\infty} \quad (2.1)$$

where  $p$  is the static pressure measured at a given wall pressure tap,  $p_0$  and  $p_\infty$  are total and static pressures measured by a Pitot-static tube which is placed 10 *cm* upstream of the leading edge of the splitter plate.

Four sets of experiments were conducted for the investigation of wake development: 1) zero pressure gradient (base flow, abbreviated as ZPG,  $dC_p/dx = 0.000 \pm 0.004/m$ ); 2) moderate adverse pressure gradient (abbreviated as APG,  $dC_p/dx = 0.338 \pm 0.002/m$ ); 3) moderate favorable pressure gradient (abbreviated as FPG,  $dC_p/dx = -0.60 \pm 0.01/m$ ); and 4) severe favorable pressure gradient ( $dC_p/dx = -2.18 \pm 0.03/m$ ). The measured streamwise pressure distributions corresponding to these different experimental sets are shown in Figure 2.5. These pressure distributions are measured by taps located on the sidewall of the diffuser test section at the same lateral (i.e.  $y$ ) location as the centerline of the wake. LDV-based  $U_e(x)$  measurements were found to be consistent with the measured wall pressure variation, confirming the suitability of the pressure tap placement. This is shown in Figure 2.6 along with the external velocity calculated from the measured pressure distribution via Bernoulli equation (i.e., the inviscid 1-D theory). The difference between the two curves shown in Figure 2.6 is due to the wall boundary effect which is not accounted in the calculation by using the Bernoulli equation.

Note that in Figure 2.5, a zero pressure gradient zone is deliberately left at the beginning portion of the flow field to ensure that the wake initial condition is identical in each case. Maintenance of the same wake initial condition in each experiment and the use of a constant pressure gradient creates a very “clean” experiment

and facilitate meaningful comparison with Computational Fluid Dynamics (CFD) predictions.

Figure 2.5 also shows stronger favorable and adverse pressure gradients for which the Turbulence Kinetic Energy (TKE) budget measurement were not performed. The larger adverse pressure gradient case was run but found to give rise to intermittent unsteady flow separation near the aft portion of the diffuser wall. Wake measurements for this case will not be presented in this dissertation. This case may be regarded as an effective upper limit on the magnitude of the constant adverse pressure gradient that can be produced by the diffuser without incurring intermittent unsteady flow separation effects.

### 2.3 Basic Flow Parameters

The experiments were run at a Reynolds number  $Re$  of  $2.4 \times 10^6$  (based on the chord length of splitter plate and a free stream velocity of  $30.0 \pm 0.2$  m/s) for all ZPG, APG and FPG cases. For the severe favorable pressure gradient case, the Reynolds number  $Re$  is  $2.0 \times 10^6$  (corresponding to a free stream velocity of  $24.0$  m/s).

As a basis for comparison, it may be noted that a Boeing 737-100 operating at a wing chord Reynolds number of  $15.7 \times 10^6$  during landing approach will have a slat Reynolds number of about  $1.8 \times 10^6$ .

For the ZPG, APG and FPG cases, which have the same tunnel speed of  $30$  m/s, the initial wake momentum thickness  $\theta_0 = 7.2$  mm. The Reynolds number  $Re_\theta$  based on the initial wake momentum thickness  $\theta_0$  is  $1.5 \times 10^4$ .

For the severe favorable pressure gradient case, since the tunnel speed was changed to  $24.0$  m/s, the initial wake momentum thickness  $\theta_0$  was correspondingly increased to  $8.1$  mm. The Reynolds number  $Re_\theta$  based on the initial wake momentum thickness  $\theta_0$  is  $1.3 \times 10^4$  for the severe favorable pressure gradient case.

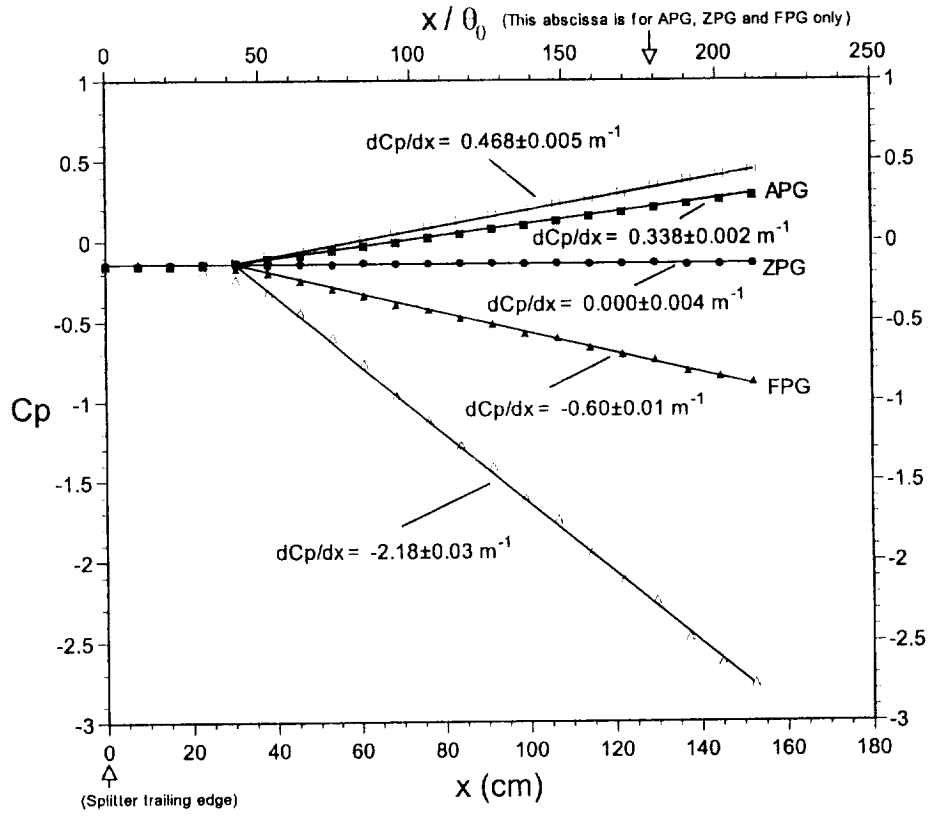


Figure 2.5. Experimentally Measured Pressure Distribution for Zero, Adverse and favorable Pressure Gradient Cases

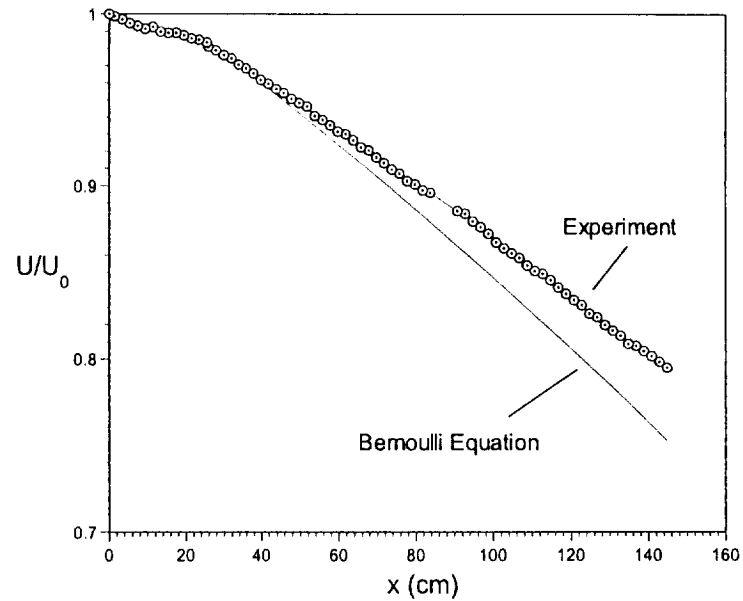


Figure 2.6. Comparison of the Measured and Calculated External Flow Velocities for the Adverse Pressure Gradient Case

This study focuses on near wake behavior due to its relevance to high-lift applications. From Figure 2.5, it can be seen that the useful length of the test section for the investigation of the wake development spans 152 *cm* downstream of the trailing edge of the splitter plate. This streamwise range corresponds to  $0 < x/\theta_0 < 212$  for the symmetric wake development. As a comparison, the range of the slat wake development in a high-lift system is on the order of  $x/\theta_0 = 370$ , based on the experimental data obtained for a confluent boundary layer study by Thomas, Nelson and Liu (2000). The flow field survey was made at the center span location for a variety of streamwise locations within the aforementioned range of the diffuser test section.

## 2.4 Flow Field Diagnostics

The conventional flow field survey for both symmetric and the asymmetric wake subjected to pressure gradients was conducted by using both LDV and hot-wire anemometry. For the turbulence kinetic energy budget measurement, unlike the flow field survey, only the constant temperature hot wire anemometry (CTA) is used since CTA is the only capable tool to date that can be used to fulfill the stringent spatial and temporal requirements for a successful TKE budget measurement, especially for the dissipation and diffusion measurement.

### 2.4.1 LDV

The detailed development and flow structure of the symmetric and asymmetric wake subjected to pressure gradients was investigated non-intrusively with an Aerometrics three-component fiber optic Laser Doppler Velocimeter system. The fiber optic LDV system was operated in two-component back-scatter mode in order to measure the streamwise velocity component,  $u$  and the cross-stream velocity component,  $v$ . The 514.5  $nm$  and 488  $nm$  laser wavelengths were used to measure the  $u$  and  $v$  components of velocity, respectively. Frequency shifting was used in order to unambiguously resolve flow direction. The measurements were made in the coincidence mode and results for both mean flow and turbulence intensities presented in this dissertation represent ensemble averages over at least 10,000 valid coincident burst events.

The transceiver of the LDV system was mounted to a computer controlled traverse table, as illustrated in Figure 2.7. The accuracy of the movement of the traverse table in horizontal and vertical direction was 0.4  $\mu m$ . The width and height of the measurement probe volume of the LDV system was 234.4  $\mu m$  and 234.0  $\mu m$ , respectively. Wind tunnel seeding was performed at the tunnel inlet

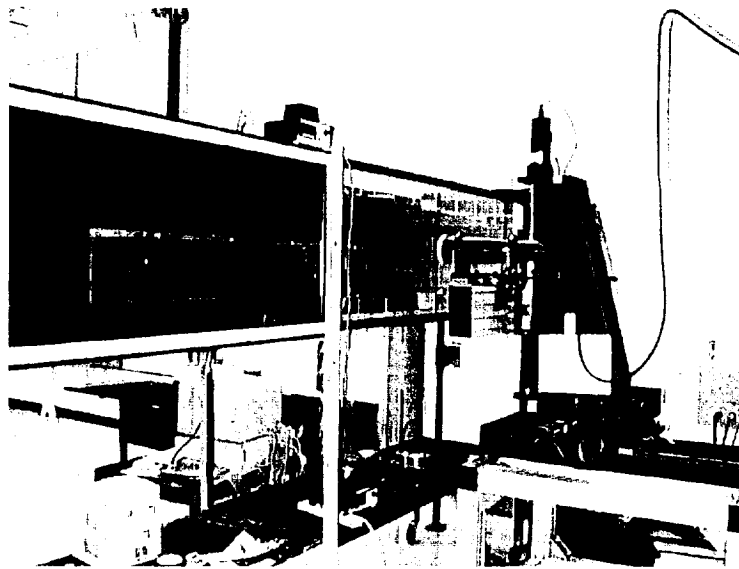


Figure 2.7. Fiber Optic LDV Measurement System

with an Aerometrics Particle Generator Model APG-100 using a 1:2 mixture of propylene glycol and distilled water. Polystyrene micro-spheres were also tried as LDV seeding particles. However it was found that the polystyrene micro-spheres resulted in a distorted boundary layer profile due to the electrostatic attraction of the polystyrene micro-spheres toward the plexiglass plate. All LDV data presented in this dissertation (unless specifically noted), are based on the measurement using propylene glycol spray the seeding particles.

LDV is a reliable and convenient flow diagnostic tool for mean flow velocity and turbulence statistics measurement. Unfortunately, it is not an efficient tool for the Reynolds stress measurement. For the Aerometrics LDV system used for this wake study, to obtain a reliable LDV Reynolds stress measurement that is equivalent to the X-wire measurement result, the LDV must be operated at a gate scale setting of 0.005, which requires at least 200,000 sampling attempts so as to have 10,000 coincident burst events for a converged Reynolds stress measurement. The total

sampling time at this stringent gate scale setting is typically 5 to 10 minutes for one spatial measurement point in the flow field, which is in many circumstances impractical. Therefore for the Reynolds stress data, we resort to the X-wire measurement. All Reynolds stress data measurement presented in this dissertation are based on X-wire rather than LDV measurement results.

#### 2.4.2 Hot-wire Anemometry

A multi-channel TSI IFA 100 anemometer together with X-wire probes (Auspex type AHWX-100) was used for the whole flow field survey. In addition to the X-wire probes, a dual parallel sensor probe (Auspex type AHWG-100) was also used for the fluctuating derivative measurements required for the dissipation estimate. The wires of the above probes are made of tungsten with a nominal diameter of  $5 \mu m$ . The distance between the tips of the X-wire prongs is about  $1.2 mm$ . The spacing between the dual sensors of the parallel probe is  $0.3 mm$ . The length of the parallel probe sensor is around  $0.9 mm$ . As a comparison, the Kolmogorov microscale  $L_K (L_k = (\nu^3/\epsilon)^{1/4})$  of the wake flow studied here is approximately  $0.1 mm$ . For the TKE budget measurement, the anemometer output is low-pass filtered at  $20 kHz$  and anti-alias digitally sampled at  $40 kHz$ . The  $20 kHz$  Nyquist frequency is chosen to correspond approximately to the highest resolvable frequency of the hot-wire probes (roughly  $\sim 30 kHz$  at a free stream velocity of  $30 m/s$ ). The total record length at each measurement point is  $13.1 s$ . The  $40 kHz$  sampling frequency is located in the  $k^{-7}$  law zone in the frequency spectrum for the wake flow, as shown in Figure 2.8, suggesting the dissipation which takes place beyond the inertial subrange is captured by the hot wire sampling frequency setting.

Since requirement for the mean flow and Reynolds stress measurement is not as strict as the dissipation measurement, the anemometer output low-pass filtering was loosened to  $5 kHz$  and correspondingly, the sampling frequency was lowered

to 10 kHz. From Figure 2.8 it can be seen that the 5 kHz Nyquist frequency is located at the end of  $k^{-5/3}$  law zone, indicating that this frequency still covers most turbulence kinetic energy. As a matter of fact, the turbulence intensity sampled at 10 kHz consists of 99% of that sampled at the 40 kHz, which suggests that the second moment is not as sensitive to the sampling frequency as those time mean square derivatives in the dissipation term.

To fulfill the dissipation measurement requirement based on the locally axisymmetric homogeneous turbulence assumption, a twin X-wire probe configuration was used for the fluctuation velocity derivative measurement, as shown in Figure 2.9. In fact, this twin X-wire configuration is primarily designed for the mean-square derivative  $\overline{(\frac{\partial v'}{\partial z})^2}$  measurement, which cannot be measured by using a single X-wire probe. The spacing between the centers of the two X-wire probes is approximately 1.3 mm, which is determined from the digital image of the twin X-wire configuration.

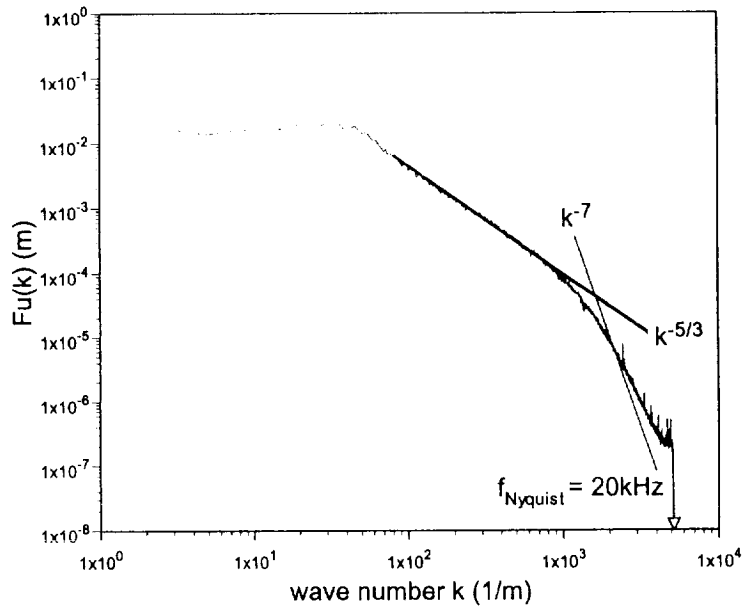


Figure 2.8. Typical Spectrum of the u-component for Symmetric Wake at APG

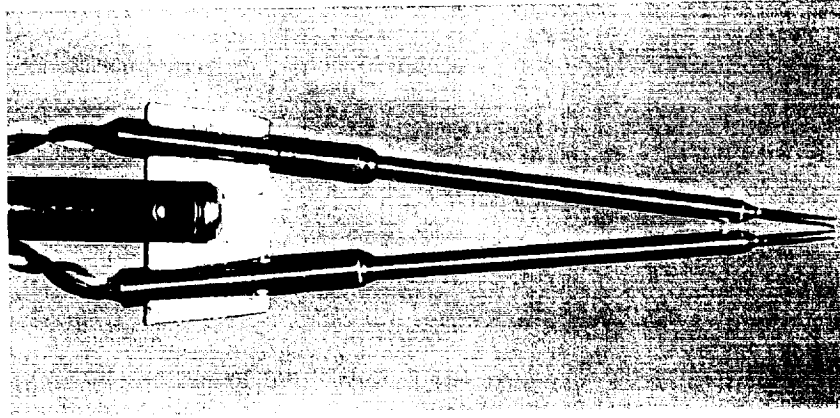


Figure 2.9. Twin X-wire Probe Configuration for Dissipation Measurement

## 2.5 Flow Field Validation

Before the detailed wake investigation was conducted, surface pressure distributions and boundary layer profiles on the symmetric wake splitter plate were first documented. Figure 2.10 and Figure 2.11 present streamwise and spanwise surface pressure distributions on the splitter plate, respectively. Figure 2.10 shows that after  $X = 20 \text{ cm}$ , the splitter plate boundary layer develops under a slightly favorable pressure gradient condition. This is a result of the boundary layer growth on both the plate surface and the tunnel walls. Figure 2.11 shows the spanwise pressure distribution at a fixed streamwise location. The spanwise pressure is very nearly uniform, varying within the range of  $\pm 4\%$  of the mean to the 95% confidence level. This suggests the flow is approximately two-dimensional in the mean. Boundary layer surveys at different spanwise locations on the splitter plate also confirmed the mean flow two-dimensionality of the splitter plate flow field.

Figure 2.12 presents the boundary layer mean velocity profile obtained at the 50% chord location of the symmetric wake splitter plate by using LDV with propylene glycol spray as seeding particles. From Figure 2.12 it can be seen that the splitter

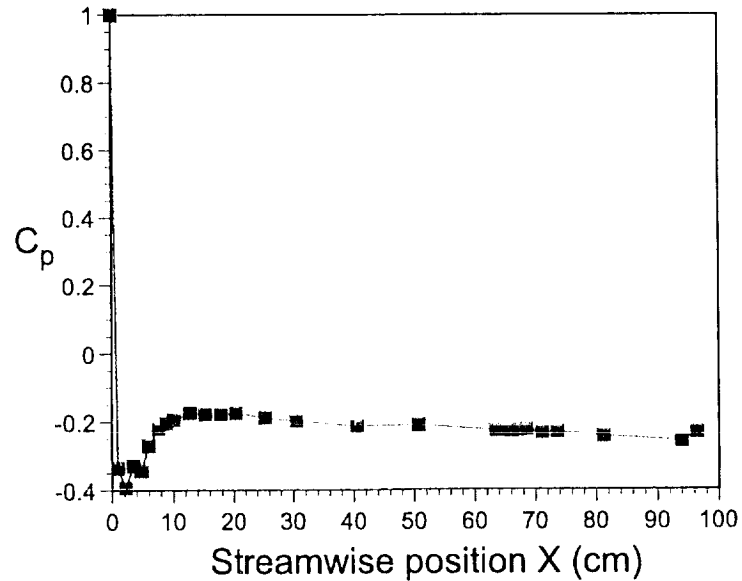


Figure 2.10. Streamwise Pressure Distribution on the Symmetric Wake Splitter Plate

plate boundary layer exhibits the classic log law-of-the-wall behavior. Similar mean flow behavior of the splitter plate boundary layer is observed up to the 99.9% chord location.

The  $u$ -component and  $v$ -component boundary layer turbulence intensity profiles at the 75% chord location of the symmetric wake splitter plate measured by X-wire and LDV (both propylene glycol spray and polystyrene micro-spheres as seeding particles) are compared with the flat plate turbulent boundary layer data obtained by Klebanoff (1954), as shown in Figure 2.13. Both X-wire and LDV measured  $U_{rms}$  and  $V_{rms}$  profiles agree with the classic Klebanoff results very well.<sup>1</sup> Similarly, the Reynolds stress  $\overline{u'v'}$  profile measured by X-wire and LDV also agree with the Klebanoff result, as illustrated in Figure 2.14.

<sup>1</sup>It was found in our experiment that the polystyrene micro-spheres as LDV seeding particles resulted in a deceiving thinner boundary layer profile due to the electrostatic effect, although the non-dimensional  $U_{rms}$  and  $V_{rms}$  profiles agreed with the Klebanoff data. The LDV with propylene glycol spray as seeding particles did not have this problem.

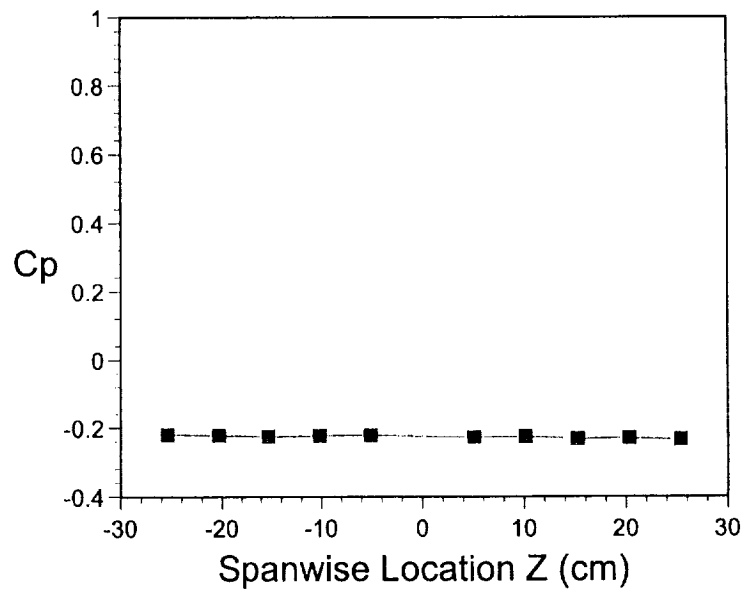


Figure 2.11. Spanwise Pressure Distribution on the Symmetric Wake Splitter Plate

The two-dimensionality of the symmetric wake flow field will be discussed in Section 3.2.

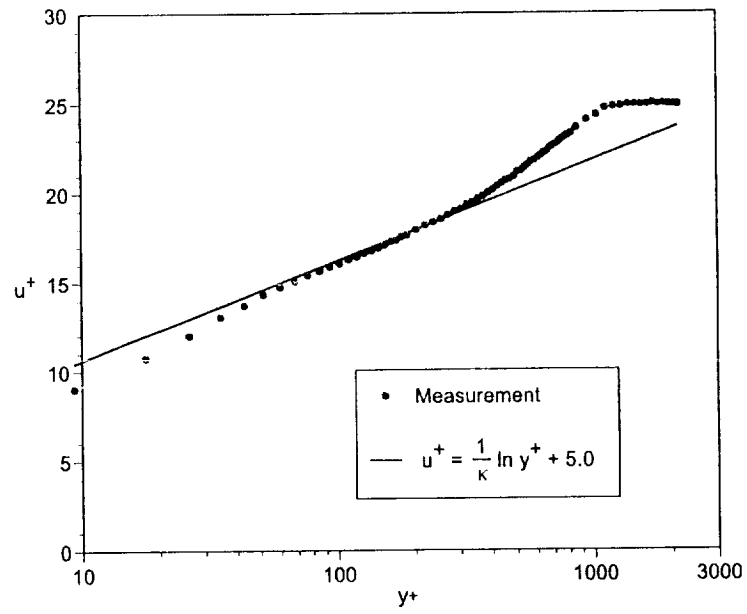


Figure 2.12. Boundary Layer Profile at 50% Chord on the Symmetric Wake Splitter Plate

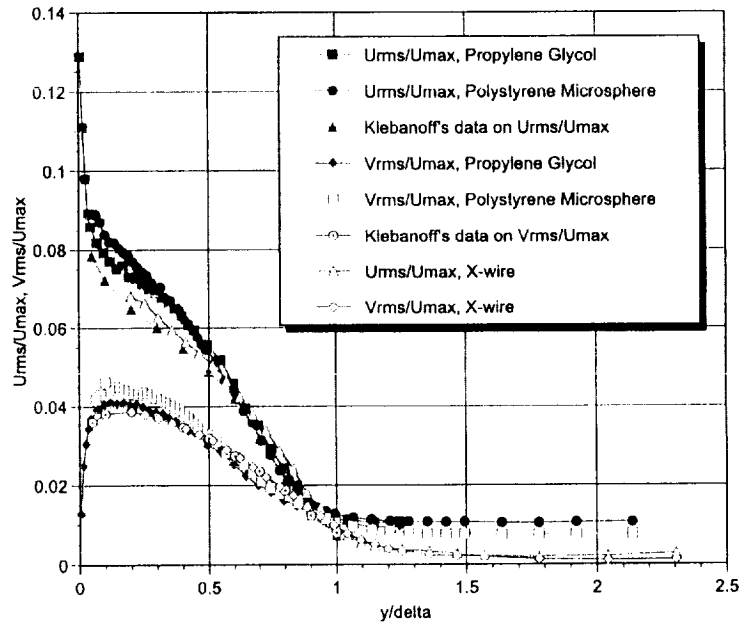


Figure 2.13. Comparison of LDV and X-wire  $U_{rms}$  and  $V_{rms}$  Measurement Results at  $x/c = 75\%$  on the Splitter Plate with the Klebanoff Data (Klebanoff:  $Re_\delta = 7.8 \times 10^4$ ; Notre Dame Wake Study :  $Re_\delta = 5.0 \times 10^4$ )

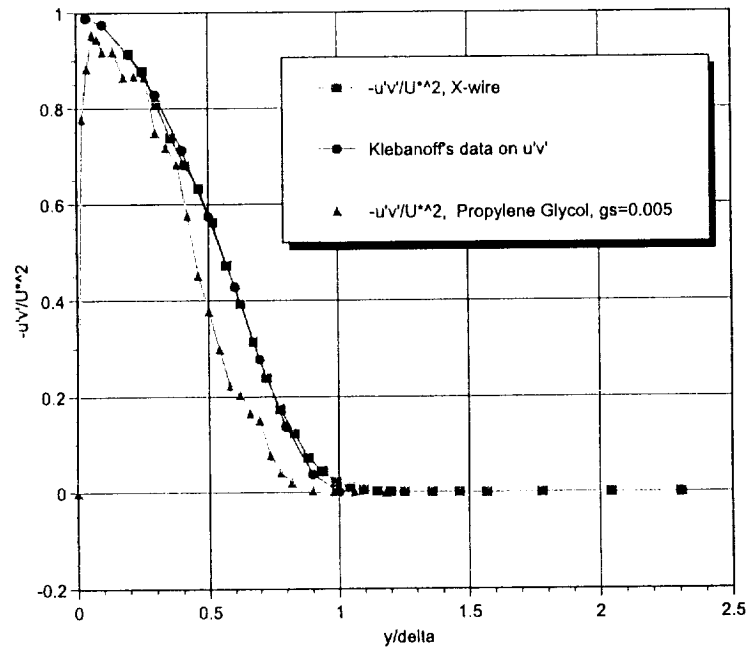


Figure 2.14. Comparison of LDV and X-wire  $\overline{u'v'}$  Measurement Results at  $x/c = 75\%$  on the Splitter Plate with the Klebanoff Data (Klebanoff:  $Re_\delta = 7.8 \times 10^4$ ; Notre Dame Wake Study :  $Re_\delta = 5.0 \times 10^4$ )

## CHAPTER 3

### SYMMETRIC WAKE FLOW DEVELOPMENT AND STRUCTURE IN PRESSURE GRADIENTS

In this chapter, experimental results for the mean and turbulence quantities of the wake flow that develops when subjected to imposed pressure gradients will be presented. The four constant pressure gradient cases will be abbreviated as APG, ZPG, FPG and FPG2, respectively, representing the constant adverse, zero, moderately favorable and severely favorable pressure gradient cases. The similarity of the wake flow in different pressure gradients will be discussed, and the experimental evidence for similarity will be presented.

#### 3.1 Symmetric Wake Flow Nomenclature

Figure 3.1 presents key nomenclature that will be used in characterizing the mean flow development of the wake. In the discussion to follow,  $u_d(x, y)$  will be used to denote the local wake velocity defect while  $U_d(x)$  will denote the maximum local velocity defect in the wake, as illustrated in Figure 3.1. The wake half-width, corresponding to the lateral distance from the centerline of the wake to the 50% maximum velocity defect location, is denoted as  $\delta(x)$ . The origin of the  $x - y$  coordinates of the flow field in the diffuser test section is located at the trailing edge of the splitter plate.

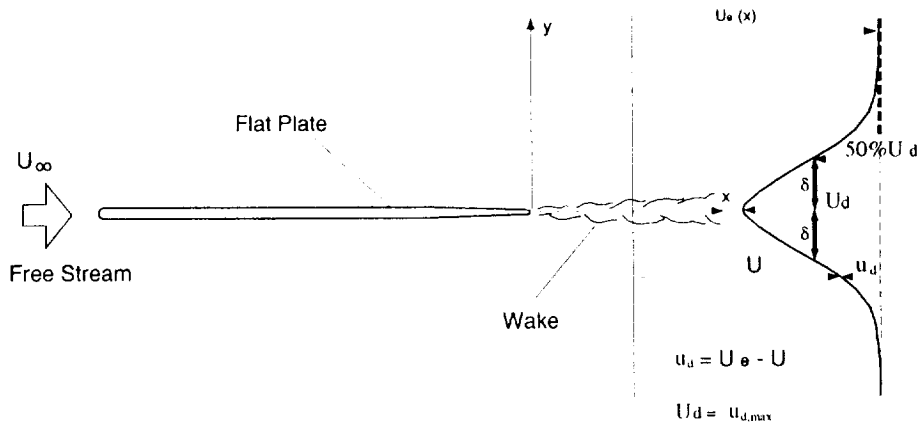


Figure 3.1. Wake Structure Nomenclature.

### 3.2 The Initial Symmetric Wake for Different Pressure Gradients

Due to the existence of the common zero-pressure gradient zone at the beginning portion of the wake flow field, the initial wake profiles are virtually identical for each experimental case, as shown in Figure 3.2. In addition, the turbulence intensities of the initial wake are also very nearly the same, as shown in Figure 3.3. The slight asymmetry of the turbulence intensity profiles might be traced back to the imperfect symmetry of the entire splitter plate setup due to manufacturing and installation defects.

### 3.3 Validation of the Two-Dimensionality of the Flow Field

Before conducting the detailed LDV flow field surveys for the different pressure gradient cases, the quality of the flow field in the diffuser test section was also carefully examined and documented. Examination of the results of these measurements verified the two-dimensionality of the flow field. As an example, Figure 3.4 shows the spanwise distribution of the streamwise velocity component  $\bar{U}$  at two different locations within the initial wake. It should be pointed out that the slight spanwise

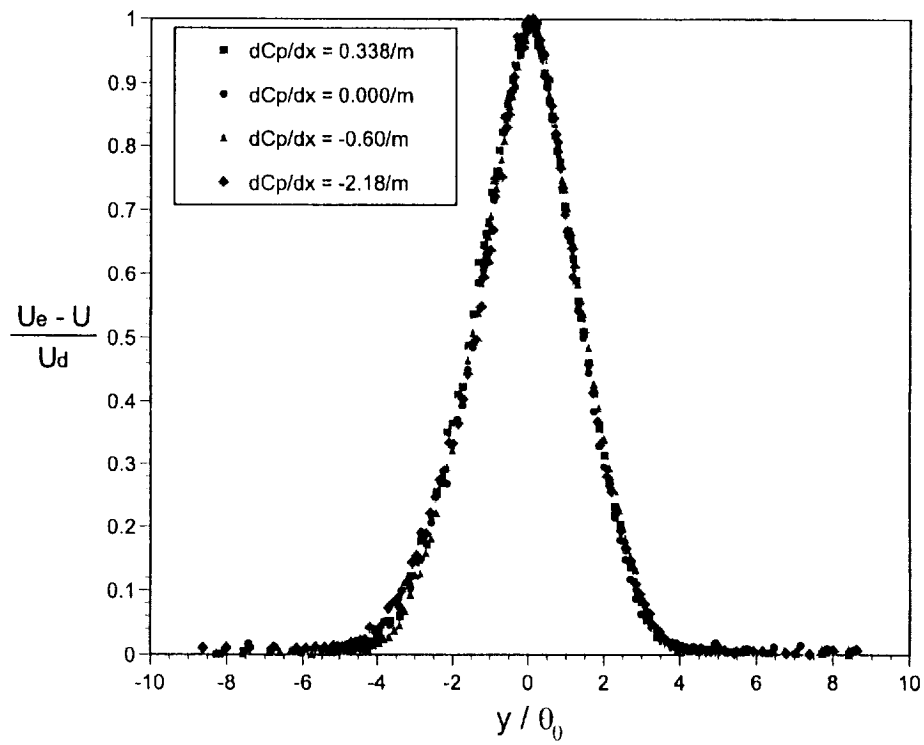


Figure 3.2. Comparison of Initial Wake Mean Velocity Profiles at  $x/\theta_0 = 18$

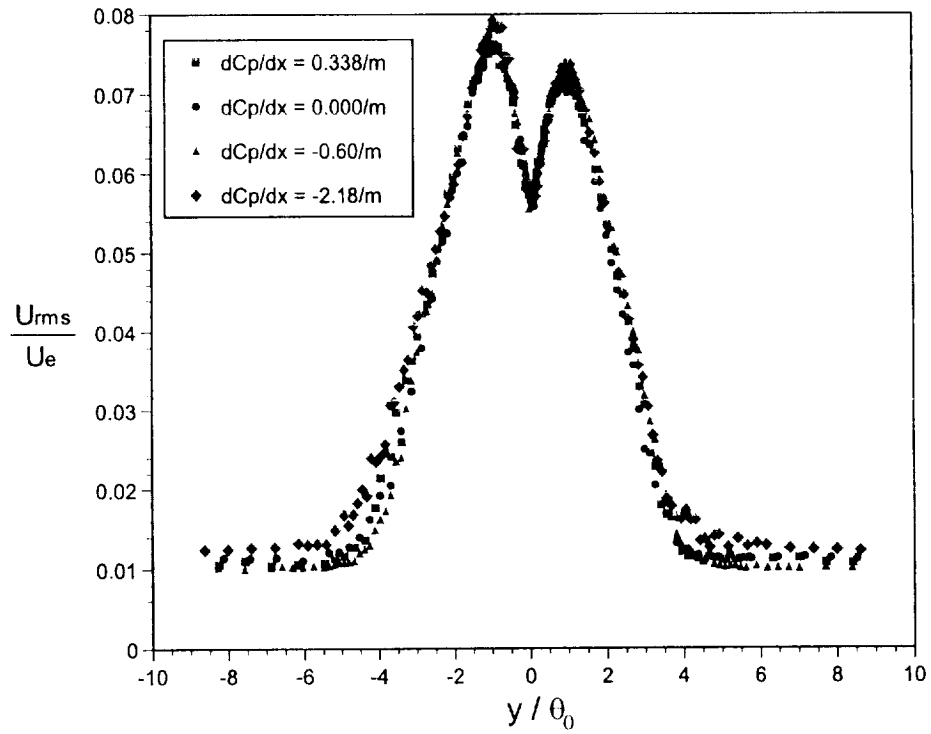


Figure 3.3. Comparison of Initial Wake  $U_{rms}$  Profiles at  $x/\theta_0 = 18$

variation of  $\bar{U}$  at the location of  $y = 5 \text{ mm}$  was traced to a slight misalignment of traverse system with the wind tunnel coordinates rather than an actual spanwise variation of the flow field itself. LDV measurement of the wake at different spanwise locations at measurement stations located farther downstream reveals that the mean flow two-dimensionality of the wake remains quite satisfactory in the diffuser test section up to the last measurement station at  $x = 145 \text{ cm}$ .

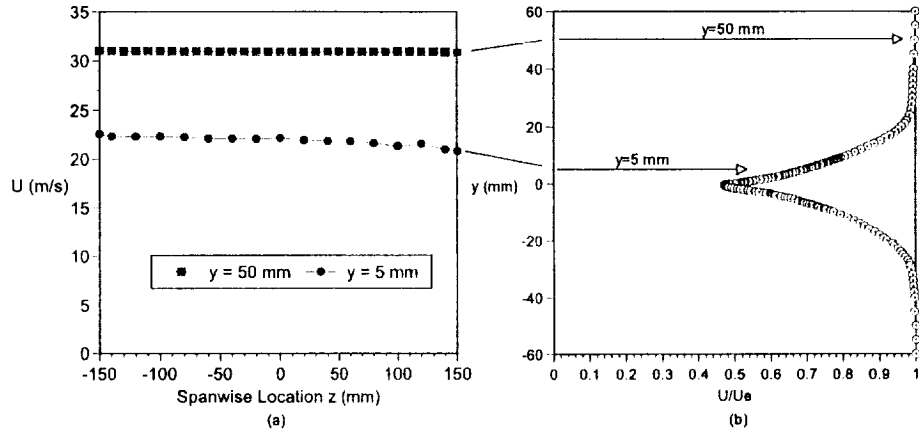


Figure 3.4. Spanwise Velocity Distribution at  $x/\theta = 2.6$  Downstream of the Symmetric Wake Splitter Plate Trailing Edge. (a) Spanwise Velocity Distribution; (b) Location of Measurement in the Initial Wake.

### 3.4 Mean Wake Flow Profile in Zero Pressure Gradient

The zero pressure gradient wake serves both as a convenient baseline for comparison with the nonzero pressure gradient wake development and as a means to further validate the flow field facility. This is because the zero pressure gradient wake is expected to exhibit well defined mean flow similarity scaling sufficiently far downstream of the splitter plate trailing edge. In particular, the wake half-width  $\delta(x)$  and the maximum velocity defect  $U_d(x)$  should vary as  $x^{1/2}$  and  $x^{-1/2}$ , respectively (Townsend, 1956 and Schlichting, 1979). Experimental results for the zero pressure

gradient case show the expected mean flow similarity scaling. Figure 3.5 presents mean velocity profiles at several streamwise locations. The local velocity defect is scaled by the maximum velocity defect  $U_d(x)$  while the lateral spatial coordinate is scaled with the wake half-width  $\delta(x)$ . Using this scaling, the mean velocity profiles collapse to exhibit the classic similarity behavior. The streamwise variation of the wake half-width  $\delta$  and the maximum velocity defect  $U_d$  for the zero pressure gradient case are plotted in Figure 3.6 and 3.7, respectively, which show that for  $x/\theta_0 > 40$ ,  $(\delta/\theta_0)^2$  and  $1/(U_d/U_e)^2$  are proportional to  $x/\theta_0$ , as required for mean velocity similarity.

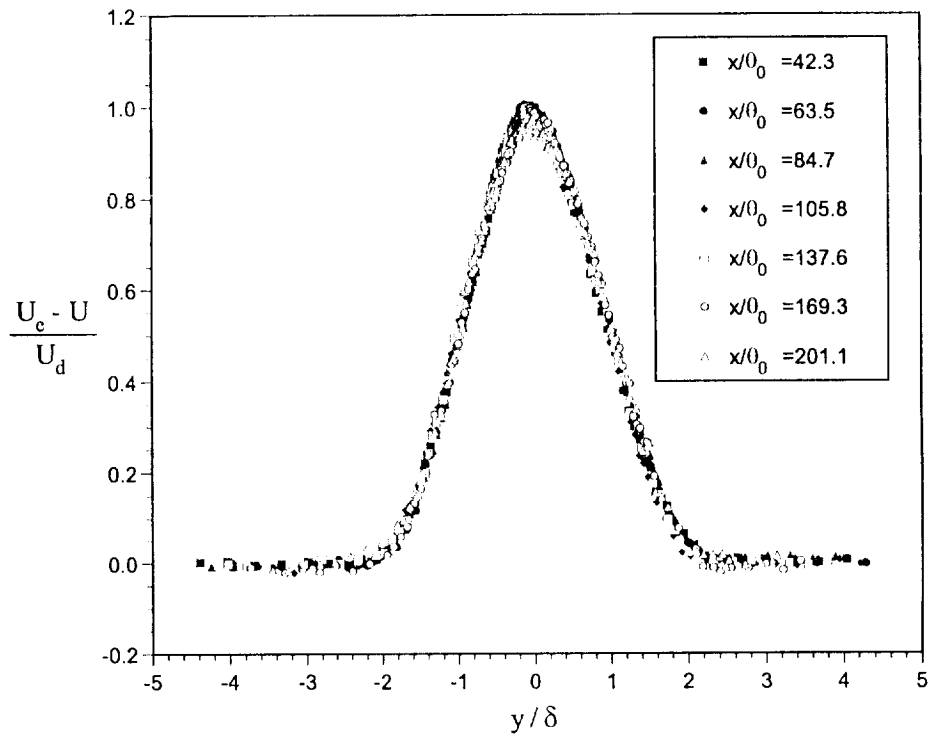


Figure 3.5. The Similarity of Wake Profiles in Zero Pressure Gradient.

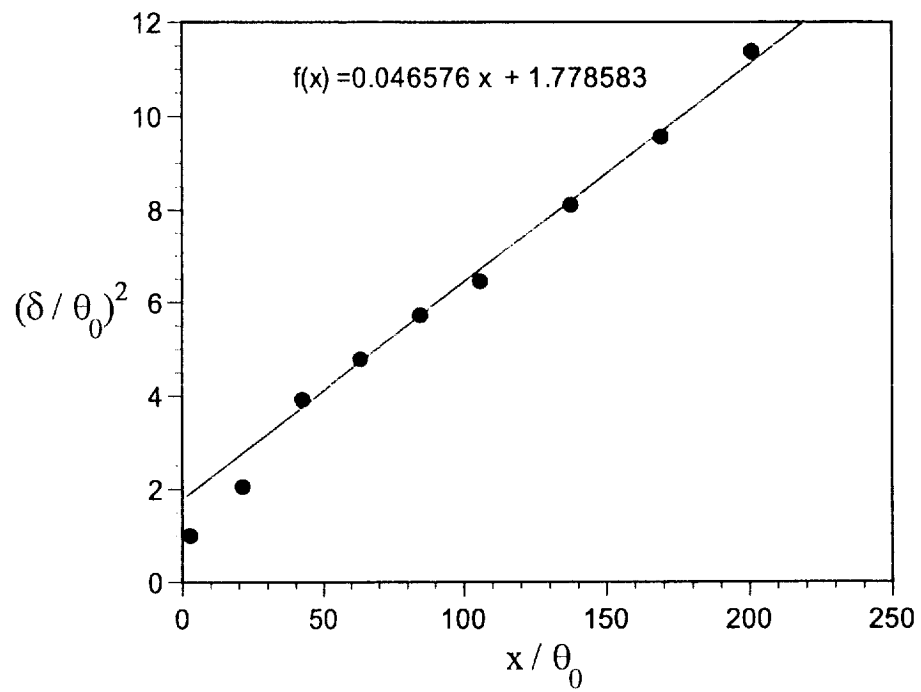


Figure 3.6. Streamwise Variation of Wake Half-width in Zero Pressure Gradient.

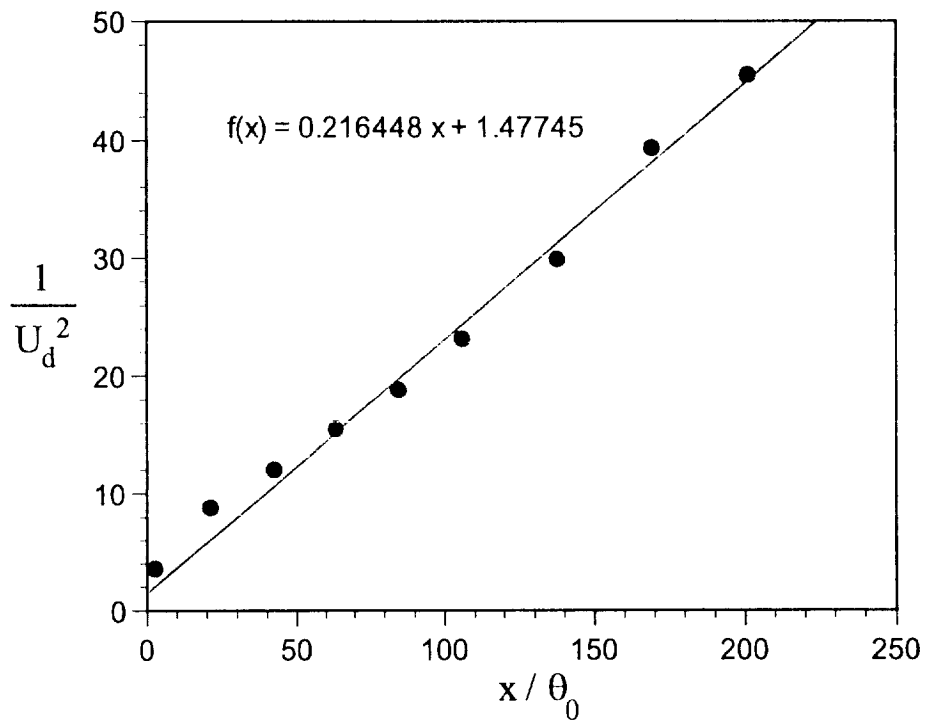


Figure 3.7. Streamwise Variation of Maximum Velocity Defect in Zero Pressure Gradient.

## 3.5 Effect of Pressure Gradient on Mean Flow

### 3.5.1 Mean Flow Profile

Examination of the experimental results shows that the influence of the pressure gradient on wake development and structure is very significant. As an example, Figure 3.8 presents a comparison of normalized streamwise mean velocity  $\bar{U}/U_c$  profiles for zero, moderate adverse, moderate favorable and severe favorable pressure gradient cases as obtained at the same non-dimensionalized streamwise location of  $x/\theta_0 = 106$ . It can be seen from Figure 3.8 that when the adverse pressure gradient is imposed, both of the wake width and the velocity defect are increased. In contrast, when the wake develops in a favorable pressure gradient, the wake width is reduced and the velocity defect decays faster in relation to corresponding zero pressure gradient values.

### 3.5.2 Streamwise Evolution of the Wake Half-Width and Maximum Velocity Defect

A summary of the effect of pressure gradient on the mean flow characteristics is presented in Figures 3.9 and 3.10. Figure 3.9 presents the streamwise variation in wake half-width  $\delta(x)$  for each case. Note that the effect of pressure gradients on the spreading is nearly immediate after the imposition of the pressure gradient. It can be seen from Figure 3.9 that at the last measurement station, the wake width for the adverse pressure gradient case is approximately 35% greater than that of the zero pressure gradient case. For the severely favorable pressure gradient case, the wake is nearly 40% thinner than that of the zero pressure gradient case.

Figure 3.10 presents the streamwise variation in maximum wake defect,  $U_a(x)$  for each case. Again the effect of the imposed pressure gradient on the mean flow is immediate after the imposition of the pressure gradient. From Figure 3.10, it can be seen that at the last measurement station, the maximum velocity defect for the adverse pressure gradient case is approximately 67% larger than that of

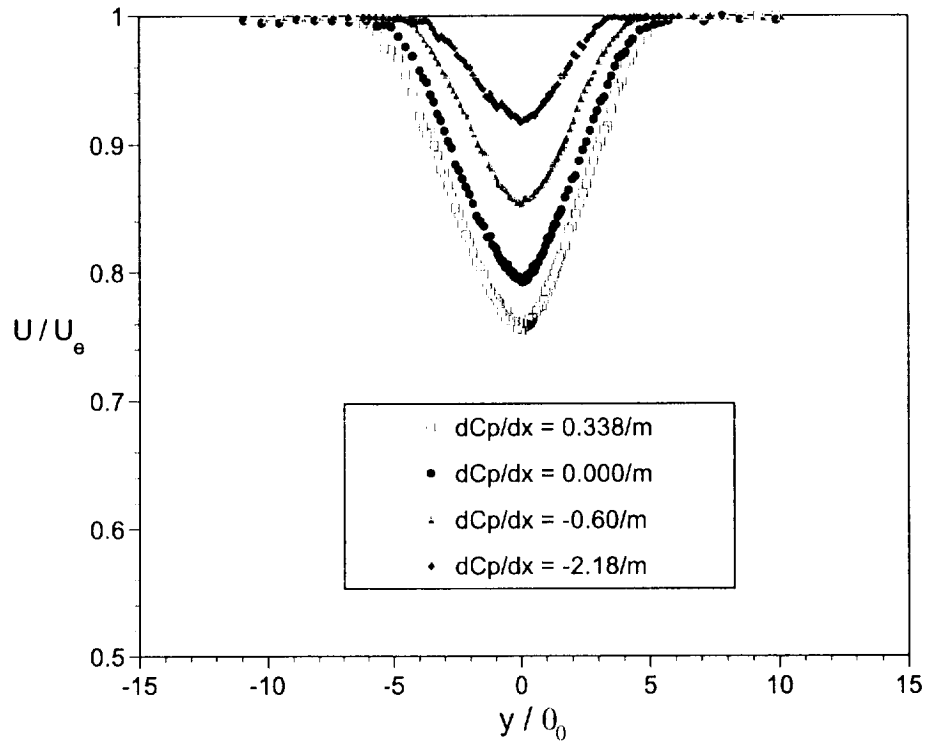


Figure 3.8. Comparison of Mean Velocity for Different Pressure Gradient Cases at  $x/\theta_0 = 106$ .

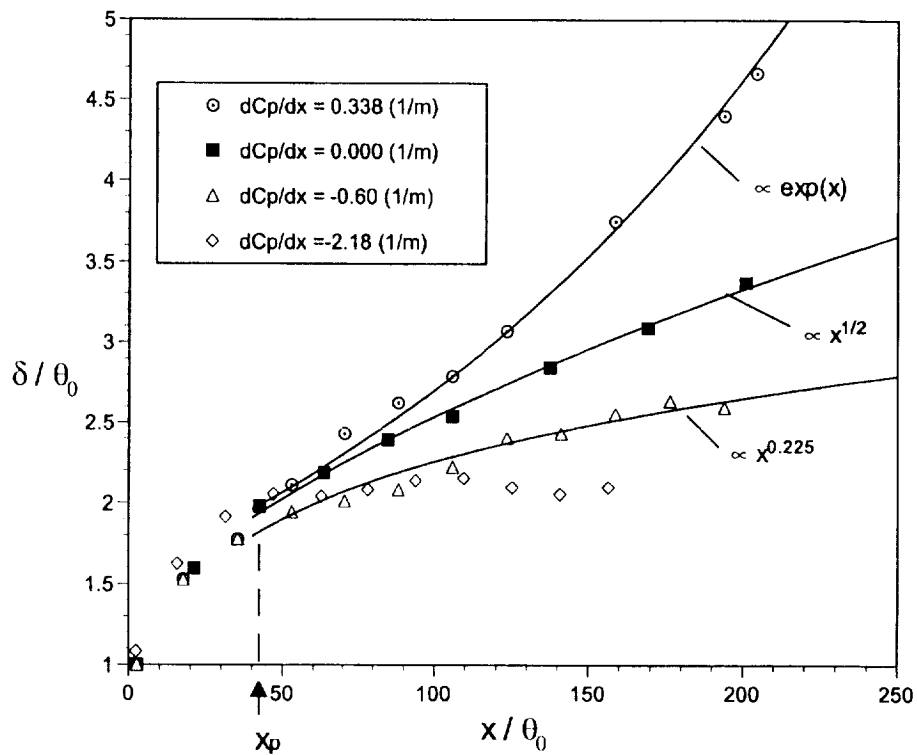


Figure 3.9. Comparison of Streamwise Evolution of Wake Half-width for Different Pressure Gradient Cases.

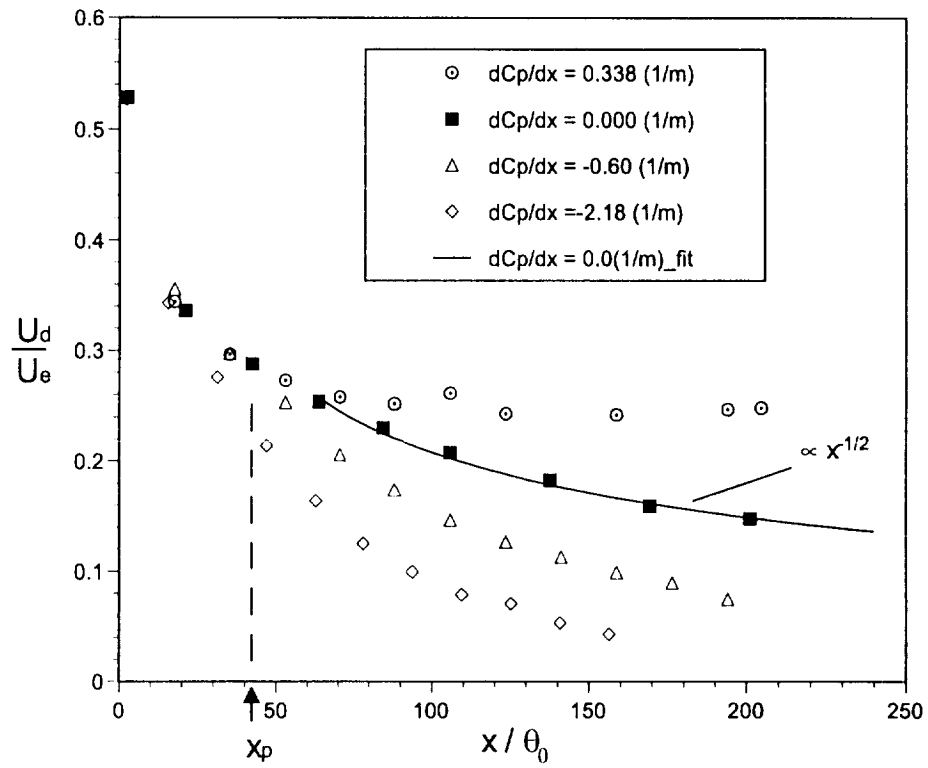


Figure 3.10. Comparison of Streamwise Evolution of Maximum Velocity Defect for Different Pressure Gradient Cases.

the zero pressure gradient case. For the severely favorable pressure gradient case, the maximum velocity defect is nearly 73% smaller than that of the zero pressure gradient case.

As shown by Hill *et al.* (1963), Smith (1975), Petrov (1978) and Hoffenberg *et al.* (1995), if the adverse pressure gradient is high enough or the imposition length of a relatively small adverse pressure gradient is long enough, stagnation or even reversal of the wake flow (the so-called “wake bursting”) will occur. Apparently, the adverse pressure gradient used in this study is neither sufficiently strong nor imposed long enough to result in the wake reversal. However, from Figure 3.10, it can be seen that at least the decay of the velocity defect is arrested at the imposed adverse pressure gradient.

To directly examine the influence of pressure gradient on the wake mean flow characteristics, Figure 3.11 presents the wake half-width  $\delta$  and maximum velocity defect  $U_d(x)$  vs. pressure gradient  $dC_p/dx$  at fixed non-dimensionalized streamwise locations, respectively. From this figure, it can be seen that both the wake half-width  $\delta$  and maximum velocity defect  $U_d(x)$  are very sensitive to the imposed pressure gradient with particularly strong effects being associated with adverse pressure gradient. In addition, the response of the wake is nonlinearly related to the imposed pressure gradient and is asymmetric about the zero pressure gradient condition. We can also infer from this figure that should we impose higher adverse pressure gradients than used in this study, we can expect much greater wake widening and maximum velocity defect.

### 3.5.3 Wake Mean Flow Similarity in Pressure Gradients

As shown previously in Figure 3.8, the influence of the pressure gradient on wake mean flow profile is significant. However, as presented in Figure 3.12, if non-dimensionalized by the local maximum velocity defect  $U_d$  and the wake half-width

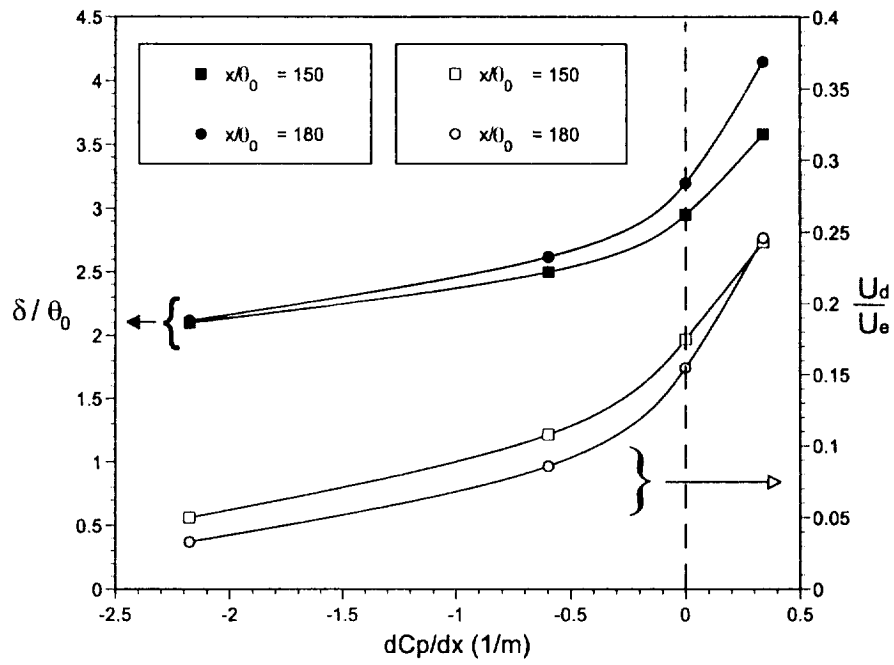


Figure 3.11. Influence of Pressure Gradient on Wake Half-width and Maximum Velocity Defect.

$\delta$ , the wake mean velocity profiles for APG, ZPG and FPG cases will collapse to a universal wake shape, suggesting the similarity behavior not only exists for the wake mean flow in zero pressure gradient, but also in the adverse and favorable pressure gradients investigated. In particular, although not presented in Figure 3.12, the wake mean profiles for APG, ZPG and FPG cases exhibit self-similar behavior as early as  $x/\theta_0 \approx 40$ , with the corresponding maximum velocity defect of  $U_d/U_e \approx 0.3$ . The dark curve in Figure 3.12 represents a curve-fit of the experimental data which is given by

$$f(\eta) = e^{-0.637\eta^2 - 0.056\eta^4} \quad (3.1)$$

where  $\eta = y/\delta$ .

This expression is exactly the same as that obtained by Wygnanski, Champagne and Marasli (1986) in an experimental investigation of wake development in zero pressure gradient by using various wake generators. As pointed out by Wygnanski *et al.* (1986), the other exponential function which is traditionally used to describe the wake mean velocity profile, i.e.,

$$f(\eta) = e^{-0.693\eta^2} \quad (3.2)$$

overestimates the mean velocity at the outer edge of the wake<sup>1</sup>.

## 3.6 Effect of Pressure Gradient on Turbulence Quantities

### 3.6.1 Comparison of Turbulence Intensity at the Same Streamwise Location

Similar to the effect on the mean flow field, the influence of the pressure gradient on wake turbulence quantities is also very significant. As an example, Figure 3.13 and

---

<sup>1</sup>In fact, as shown in Narasimha and Prabhu (1972), the traditional exponential function of the wake profile (3.2) can be solved from equation (3.15) with the assumptions of the eddy viscosity of  $\nu_0 = k_0 U_d \delta$  and  $A \equiv C = 2k_0 l n 2$ . For definition of  $A$  and  $C$ , see Section 3.7.

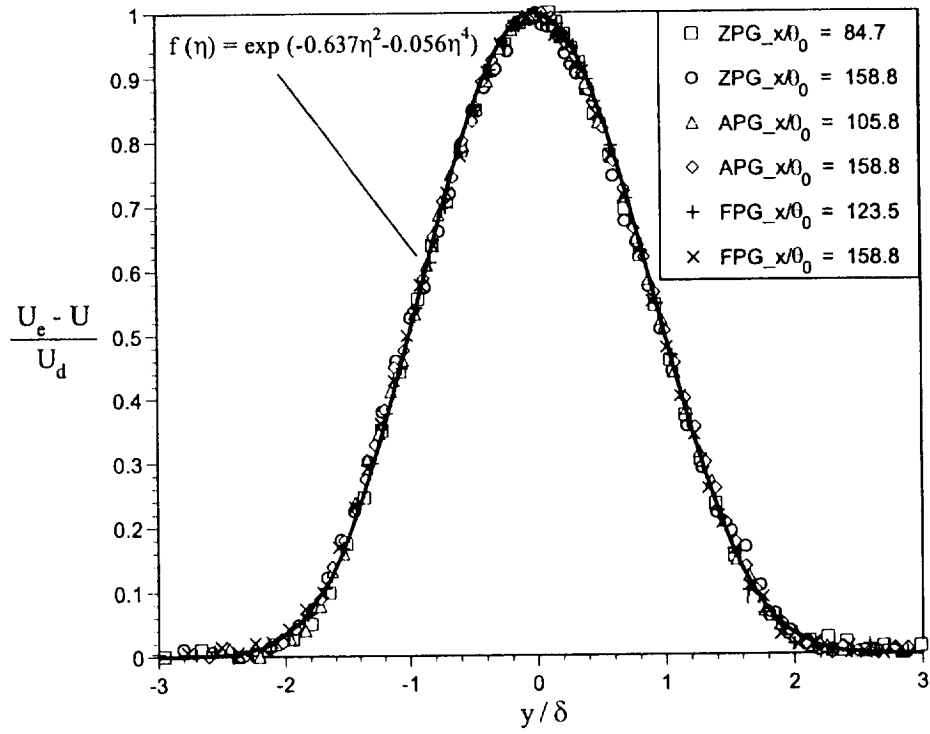


Figure 3.12. Similarity Wake Profiles in Pressure Gradients.

3.14 present comparisons of streamwise component turbulence intensity  $\sqrt{u'^2}/U_e$  and Reynolds stress  $-\overline{u'v'}/U_e^2$  profiles for zero, moderate adverse, moderate favorable and severe favorable pressure gradient cases as obtained at the same streamwise location of  $x/\theta_0 = 106$ . It can be seen from Figure 3.13 and 3.14 that when the adverse pressure gradient is imposed, the turbulence intensity and the Reynolds stress are both amplified. In contrast, when the wake develops in a favorable pressure gradient, the turbulence intensity and Reynolds stress both decrease in relation to the zero pressure gradient values. This behavior might find its explanation from the pressure gradient effect on the mean shear. From the results presented in Section 3.5, we learn that when the adverse pressure gradient is imposed to the wake flow field, the maximum velocity defect decay rate is reduced, in other words, when adverse pressure gradient is imposed, the magnitude of mean shear is preserved and it is larger than that for the zero and favorable pressure gradient cases. Since the Reynolds stress is directly proportional to the mean shear, we can expect that Reynolds stress with higher magnitude will be associated with the adverse pressure gradient case. Large mean shear and high Reynolds stress will lead to high turbulence production rate and eventually, lead to large turbulence intensity. That is why we see the adverse pressure gradient results in a amplified turbulence intensity and Reynolds stress.

### 3.6.2 Contour Plots of Turbulence Kinetic Energy

Complete profiles of  $\sqrt{u'^2}/U_e$ ,  $\sqrt{v'^2}/U_e$  and Reynolds stress  $-\overline{u'v'}/U_e^2$  for each pressure gradient condition have been documented. From the X-wire measurement, it is found that the spanwise velocity fluctuation root mean square  $\sqrt{w'^2}$  has the same profile shape as the streamwise velocity fluctuation root mean square  $\sqrt{u'^2}$  but with a different maximum magnitude. However, the maximum magnitude of  $\sqrt{w'^2}$  is approximately the same as that of the lateral velocity fluctuation root mean square

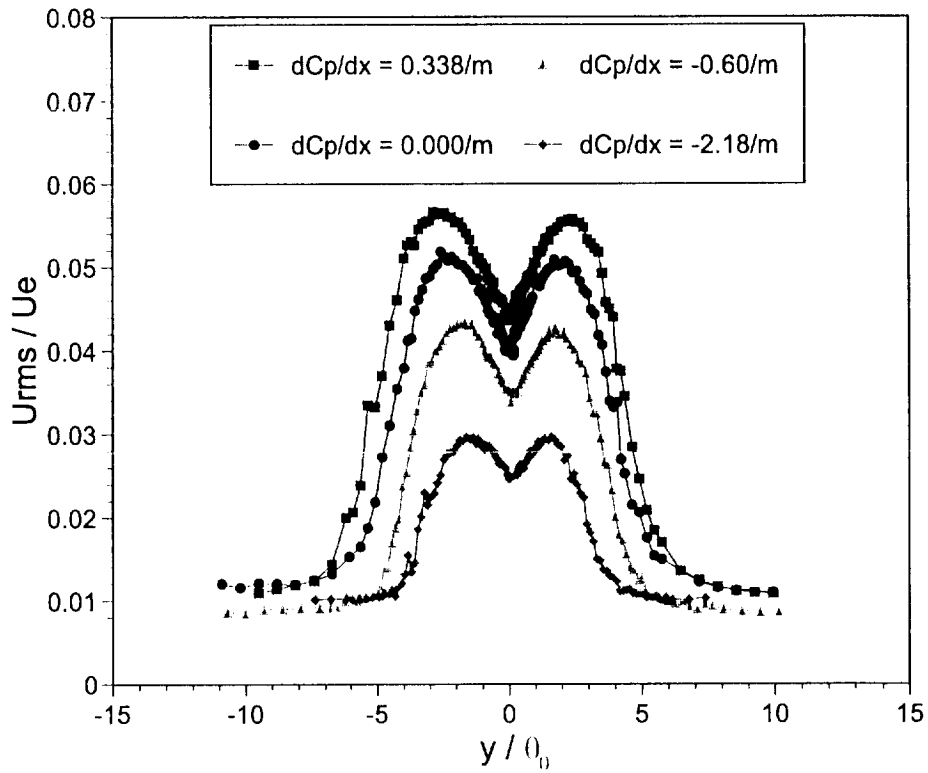


Figure 3.13. Comparison of Turbulence Intensity Profiles for Different Pressure Gradient Cases at  $x/\theta_0 = 106$ .

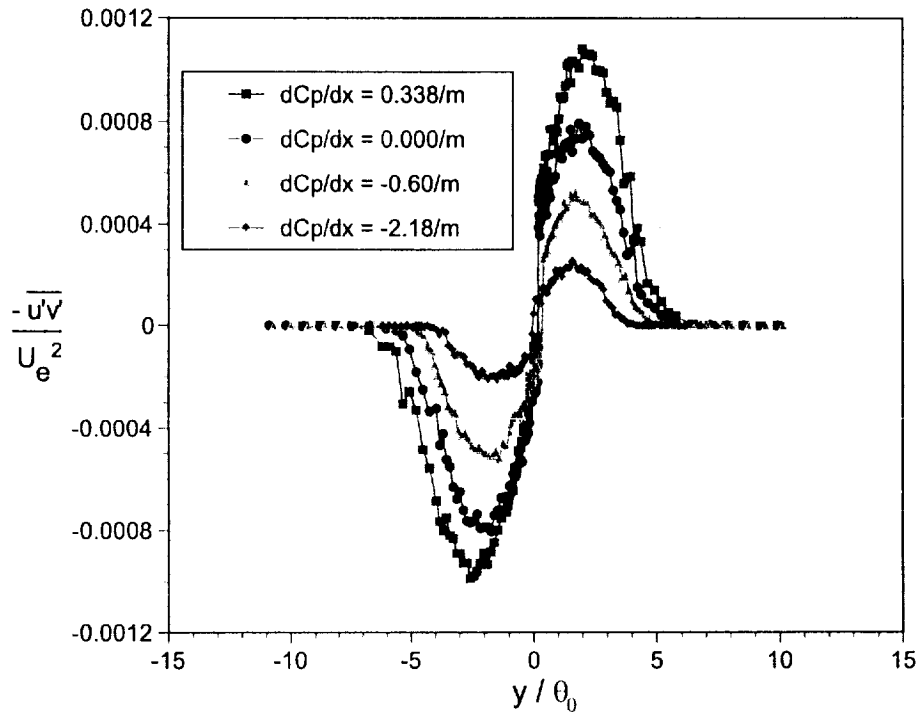


Figure 3.14. Comparison of Reynolds Stress Profiles for Different Pressure Gradient Cases at  $x/\theta_0 = 106$ .

$\sqrt{v'^2}$ . Based on this experimental observation,  $\sqrt{w'^2}$  can be expressed in terms of the measured lateral and streamwise velocity fluctuation root mean square quantities  $\sqrt{v'^2}$  and  $\sqrt{u'^2}$  as:

$$\sqrt{w'^2} = \sqrt{u'^2} \frac{\sqrt{v'^2}_{max}}{\sqrt{u'^2}_{max}} \quad (3.3)$$

The uncertainty of  $\sqrt{w'^2}$  based on this estimate is 9% at the peak value location and 3% at the center of the wake. With the measured  $\sqrt{u'^2}$  and  $\sqrt{v'^2}$  profiles, together with relation (3.3), one can obtain the turbulence kinetic energy  $k$  ( $k \equiv \frac{1}{2}(\overline{u'^2} + \overline{v'^2} + \overline{w'^2})$ ) for the wake flow. In order to examine the effect of the imposed pressure gradients on the streamwise evolution of the turbulence, we present the contour plots of the scaled turbulence kinetic energy in the wake flow for APG, ZPG and FPG cases in Figure 3.15. From these contour plots, it can be seen again vividly that the adverse pressure gradient results in a rapid growth in lateral dimension and sustains turbulent kinetic energy for the wake flow while on the contrary, the favorable pressure gradient helps to reduce the wake growth rate and the level of the relative turbulence kinetic energy.

### 3.6.3 Streamwise Evolution of Maximum Turbulence Intensity

To view the effect of the pressure gradient more clearly, Figure 3.16 presents the evolution of the local maximum turbulence intensity for each pressure gradient. As shown in this figure, the adverse pressure gradient tends to increase the turbulence intensity of the wake above its zero pressure gradient counterpart while the favorable pressure gradient tends to decrease it.

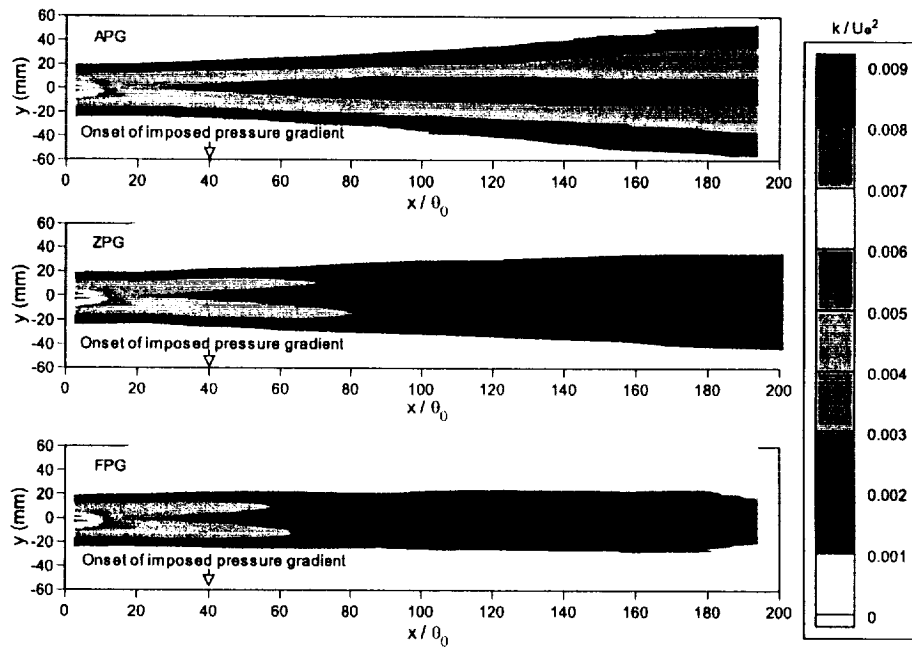


Figure 3.15. Comparison of Turbulence Kinetic Energy in Different Pressure Gradients.

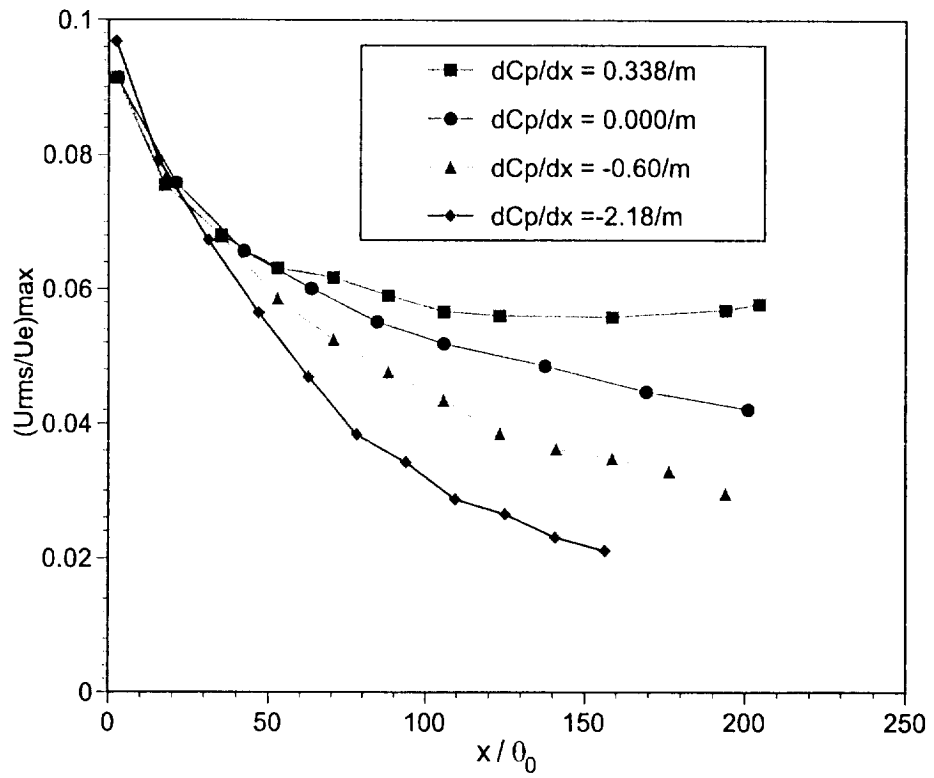


Figure 3.16. Comparison of Streamwise Evolution of Maximum Turbulence Intensity in Different Pressure Gradients.

### 3.6.4 Effect of Pressure Gradient on Similarity of Turbulence Quantities

#### 3.6.4.1 Zero Pressure Gradient

In the previous sections, it is shown that if the local velocity defect and the lateral spatial coordinate are scaled by the maximum velocity defect  $U_d$  and the wake half-width  $\delta$ , respectively, the mean velocity profiles collapse to exhibit the similarity behavior. However, if the same scaling is applied to the streamwise velocity component rms  $\sqrt{u'^2}$  and the Reynolds stress  $-\overline{u'v'}$  for the zero pressure gradient, the profiles do not exhibit similarity behavior until  $x/\theta_0 = 170$ , as shown in Figure 3.17 and Figure 3.18. This is expected since for this wake study the domain of investigation mostly resides in the near wake region. It is well known that the mean flow quantities generally exhibit similarity scaling prior to the second order moments.

#### 3.6.4.2 Adverse Pressure Gradient

Figure 3.19 and Figure 3.20 show the rms  $\sqrt{u'^2}$  and the Reynolds stress  $-\overline{u'v'}$  profiles scaled by the maximum velocity defect  $U_d$  and the wake half-width  $\delta$  for the adverse pressure gradient at different streamwise locations. Compared with the ZPG case, it can be seen that these quantities for the APG case exhibit the similarity behavior much more earlier upstream than the ZPG case, indicating that the adverse pressure gradient has a favorable effect for turbulence quantities of the wake to reach similarity.

#### 3.6.4.3 Favorable Pressure Gradient

Unlike the ZPG and APG cases, it seems that the similarity of the turbulence intensity and the Reynolds stress are both delayed further downstream, as shown in

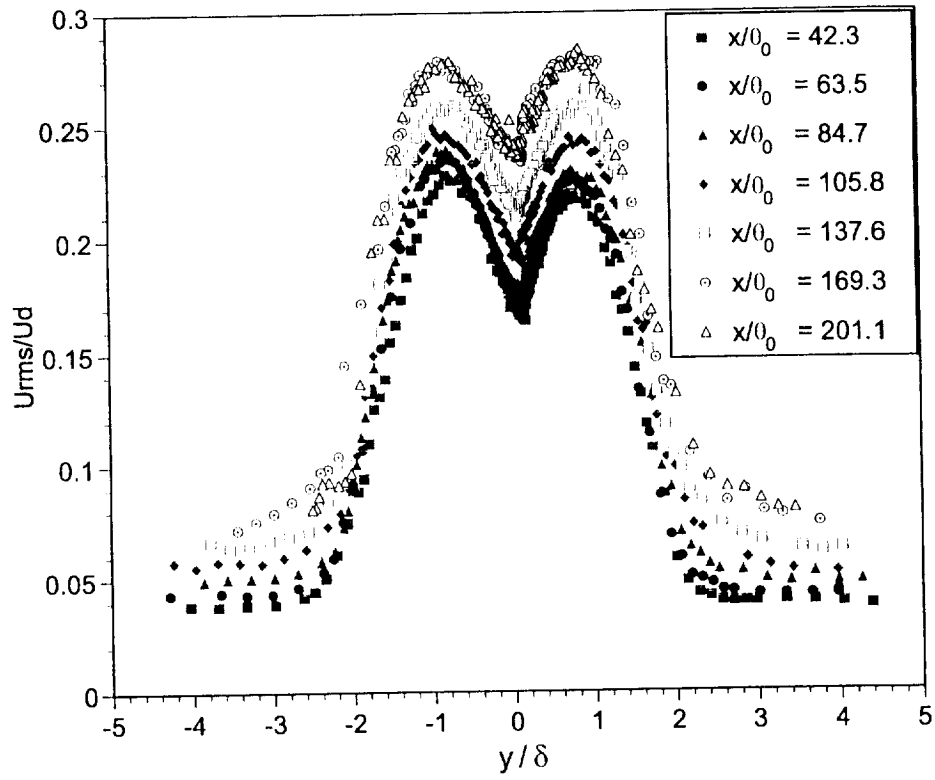


Figure 3.17. Comparison of Turbulence Intensity Profiles in Different Streamwise Locations for the ZPG case.

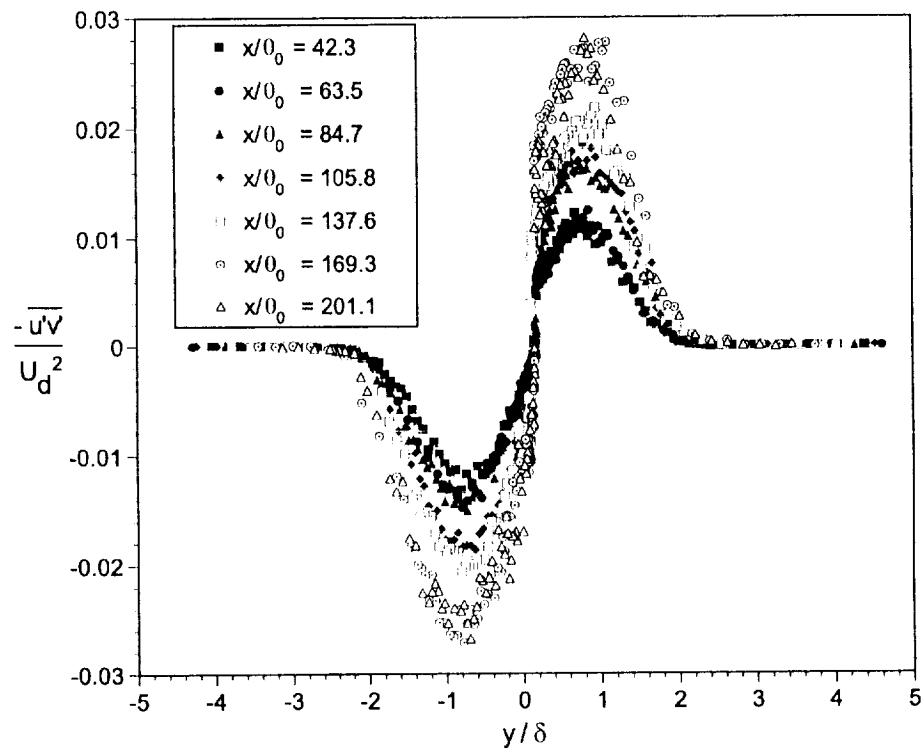


Figure 3.18. Comparison of Reynolds Stress Profiles in Different Streamwise Locations for the ZPG case.

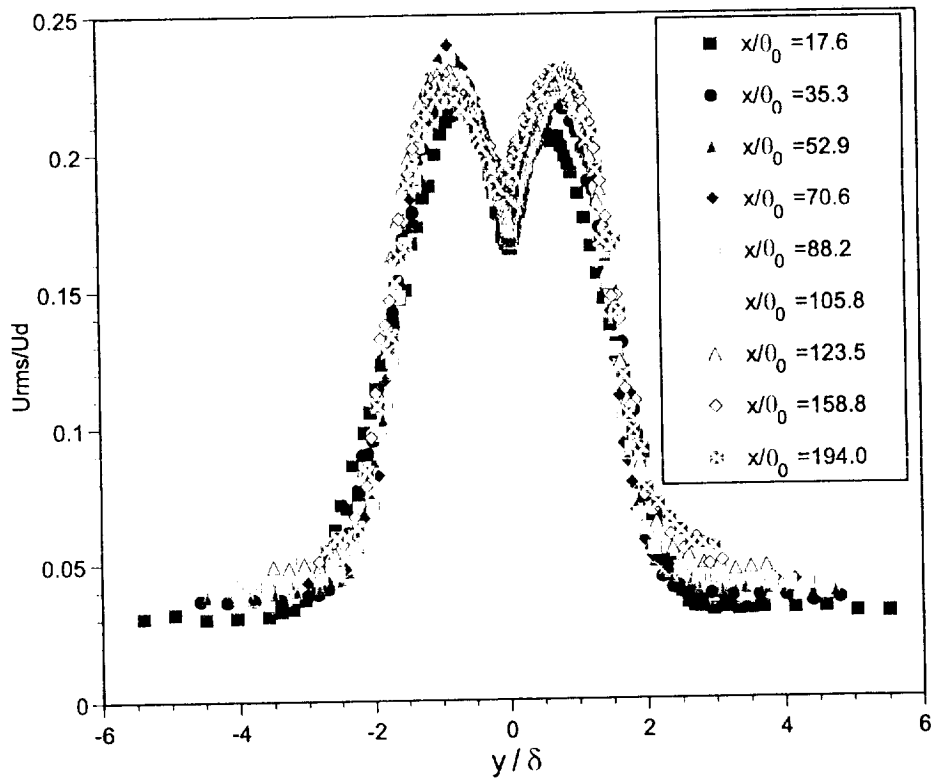


Figure 3.19. Comparison of Turbulence Intensity Profiles at Different Streamwise Locations for the APG case.

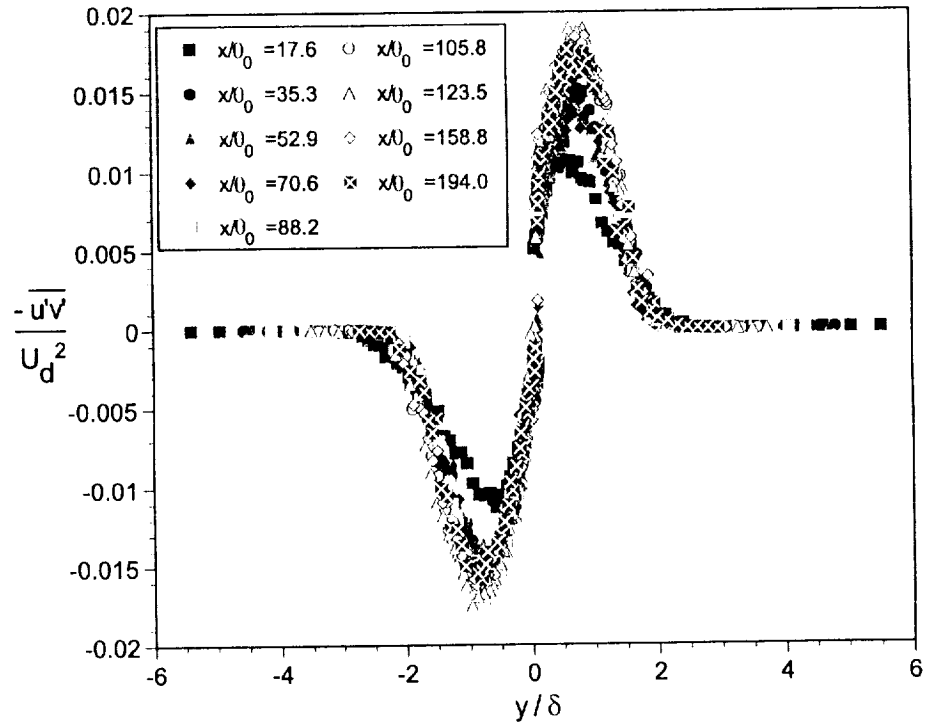


Figure 3.20. Comparison of Reynolds Stress Profiles at Different Streamwise Locations for the APG case.

Figure 3.21 and Figure 3.22, in which the rms  $\sqrt{u'^2}$  and the Reynolds stress  $-\overline{u'v'}$  profiles are scaled by the maximum velocity defect  $U_d$  and the wake half-width  $\delta$ .

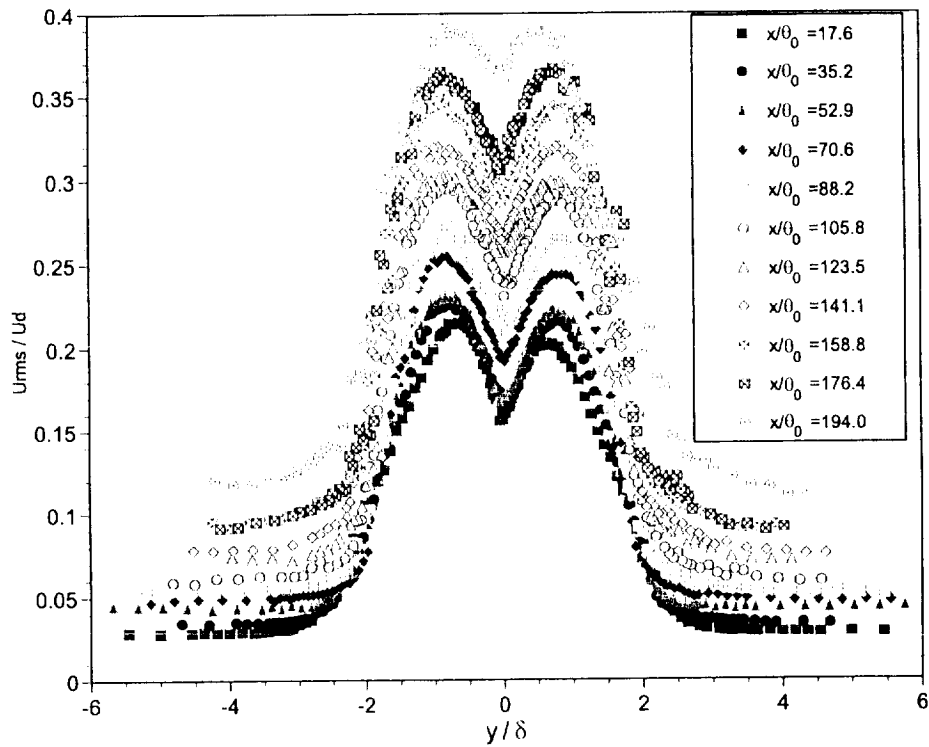


Figure 3.21. Comparison of Turbulence Intensity Profiles at Different Streamwise Locations for the FPG case.

#### 3.6.4.4 Summary Plot

To summarize the effect of pressure gradient on the similarity of turbulence quantities, Figure 3.23 (a) (b) and (c) present comparisons of the streamwise evolution of streamwise component turbulence intensity  $\sqrt{u'^2}$ , lateral component turbulence intensity  $\sqrt{v'^2}$  and Reynolds stress  $-\overline{u'v'}$  for APG, ZPG and FPG cases. In this figure, the turbulence quantities are all taken at the local maximum mean shear location (roughly at  $y/ = 0.8$ ) and are all scaled by the local maximum velocity defect

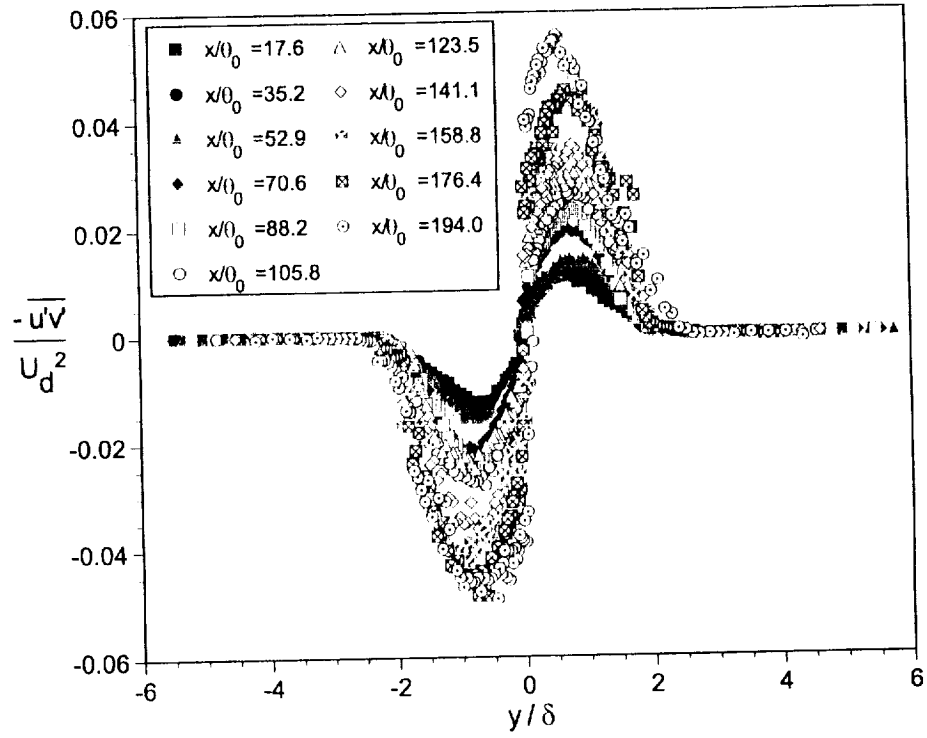


Figure 3.22. Comparison of Reynolds Stress Profiles at Different Streamwise Locations for the FPG case.

$U_d$ . This figure clearly shows that the adverse pressure gradient precipitates the wake development process to reach a similarity state for the turbulence quantities such as turbulence intensity and Reynolds stress while the favorable pressure gradient significantly postpones the process. For example, in the APG case, it seems that the streamwise component turbulence intensity  $\sqrt{u'^2}$  reaches similarity as early as at  $x/\theta_0 = 50$  and the Reynolds stress  $-\overline{u'v'}$  reaches similarity at  $x/\theta_0 = 90$ , as shown in Figure 3.23 (a) and (c). As a contrast, in the ZPG case, both the streamwise component turbulence intensity  $\sqrt{u'^2}$  and the Reynolds stress  $-\overline{u'v'}$  reach similarity as late as at  $x/\theta_0 = 170$ . For the FPG case, there is no evidence of similarity within the streamwise range of investigation. Similar trend can be found in Figure 3.23 (b). This indicate that the decay of the magnitude of the turbulence quantities is at much slower pace than the decay of the mean velocity defect for the favorable pressure gradients.

### 3.7 Similarity analysis and Solution

#### 3.7.1 Similarity Analysis

Many investigators, such as Hill *et al.* (1963), Gartshore (1967), Narasimha and Prabhu (1972), Townsend (1976) and Rogers (2001), have explored the similarity issues regarding the wake flow. Their analyses were either applicable or directly oriented to the wake development in pressure gradients. In the following analysis, we will start from the momentum equation in the form that was used by Gartshore (1967) and then derive an important result about the wake similarity subjected to pressure gradients which was also obtained by Narasimha and Prabhu (1972). Then from that result, we will finally derive the explicit expressions for wake half-width and maximum velocity defect for wake flow subjected to pressure gradients.

The governing equations for the planar incompressible turbulent wake flow can be written as

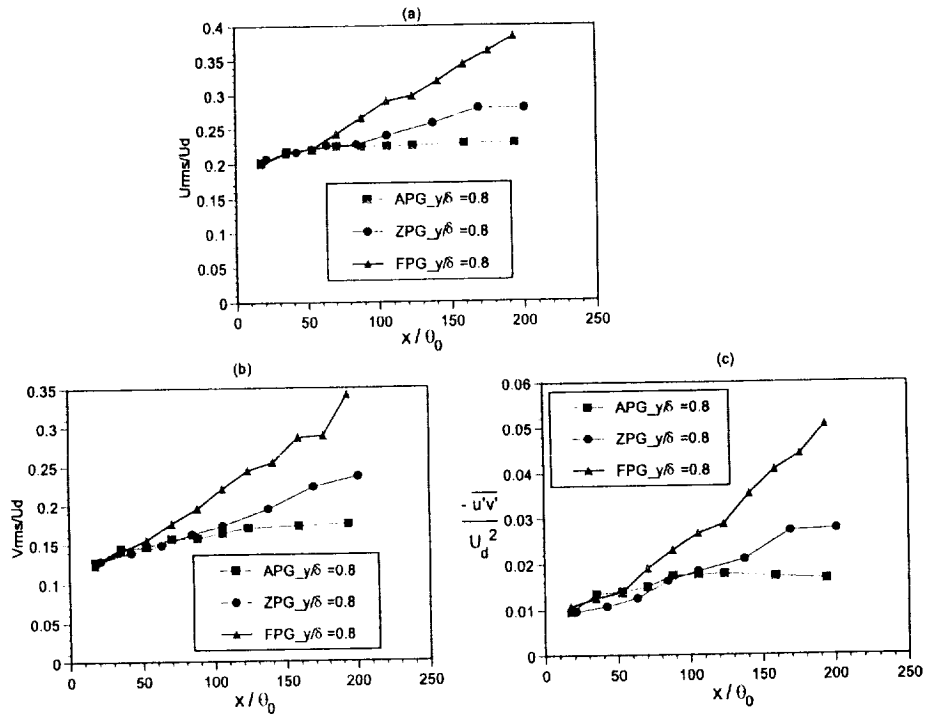


Figure 3.23. Comparison of Streamwise Evolution of Turbulence Quantities in Similarity Scaling for the APG, ZPG and FPG cases. (a) Streamwise component turbulence intensity  $\sqrt{u'^2}$ ; (b) lateral component turbulence intensity  $\sqrt{v'^2}$ ; (c) Reynolds stress  $-\overline{u'v'}$ .

$$\frac{\partial u}{\partial x} + \frac{\partial v}{\partial y} = 0 \quad (3.4)$$

$$u \frac{\partial u}{\partial x} + v \frac{\partial u}{\partial y} + \frac{\partial \overline{u'v'}}{\partial y} + \frac{\partial(\overline{u'^2} - \overline{v'^2})}{\partial x} = U_e \frac{dU_e}{dx} + \nu \frac{\partial^2 u}{\partial y^2} \quad (3.5)$$

For free shear flow, the viscous term in the momentum equation is negligible because it is much smaller compared with other terms (This assertion is verified based on measured data). In addition, for high Reynolds number flow with low turbulence intensity,  $(\overline{u'^2} - \overline{v'^2})$  is a very small quantity compared to  $U_e^2$ . As a consequence, the streamwise gradient of the quantity  $(\overline{u'^2} - \overline{v'^2})$  is much smaller than the streamwise gradient of  $U_e^2$ , if the two streamwise derivatives have the same reference length scale  $L$  (The meaning of  $L$  will be discussed later). Hence, compared to the term  $U_e \frac{dU_e}{dx}$ , the term  $\frac{\partial(\overline{u'^2} - \overline{v'^2})}{\partial x}$  can also be neglected from the momentum equation. Therefore, the momentum equation can be simplified as

$$u \frac{\partial u}{\partial x} + v \frac{\partial u}{\partial y} + \frac{\partial \overline{u'v'}}{\partial y} = U_e \frac{dU_e}{dx} \quad (3.6)$$

Now we seek the similarity solution of the form

$$\begin{cases} u = U_e - U_d f(\eta) \\ \overline{u'v'} = U_d^2 g(\eta) \\ \eta = y/\delta(x) \end{cases} \quad (3.7)$$

where  $U_d = U_d(x)$  is the maximum velocity defect and  $\delta = \delta(x)$  is the wake half-width, as shown in Figure 3.1.

With the continuity equation (3.4) and the notation (3.7) the momentum equation (3.6) can be written as

$$\begin{aligned}
& -\left[\frac{\delta}{U_d^2} \frac{d(U_e U_d)}{dx}\right] f + \left[\frac{\delta}{U_d} \frac{dU_d}{dx}\right] f^2 + \left[\frac{1}{U_d} \frac{d(U_e \delta)}{dx}\right] \eta f' \\
& - \left[\frac{1}{U_d} \frac{d(U_d \delta)}{dx}\right] f' \int_0^\eta f d\eta + g' = 0
\end{aligned} \tag{3.8}$$

Denote

$$A = -\left[\frac{\delta}{U_d^2} \frac{d(U_e U_d)}{dx}\right]$$

$$B = \left[\frac{\delta}{U_d} \frac{dU_d}{dx}\right]$$

$$C = \left[\frac{1}{U_d} \frac{d(U_e \delta)}{dx}\right]$$

$$D = -\left[\frac{1}{U_d} \frac{d(U_d \delta)}{dx}\right]$$

Then Equation (3.8) can be written as

$$Af + Bf^2 + C\eta f' + Df' \int_0^\eta f d\eta + g' = 0 \tag{3.9}$$

Since the coefficient of the term  $g'$  is a constant, for similarity solution, it is required that the coefficients of the other terms in Equation (3.9), namely,  $A$ ,  $B$ ,  $C$  and  $D$ , must be independent of  $x$ , or more specifically, must be constants.

To solve this equation, we consider the so-called shallow wake case, for which  $U_d \ll U_e$ . Now we compare the order of magnitude of the coefficients  $A$ ,  $B$ ,  $C$  and  $D$ .

$$\frac{B}{A} = -\frac{\frac{\delta}{U_d} \frac{dU_d}{dx}}{\frac{\delta}{U_d^2} \frac{d(U_e U_d)}{dx}} = -\frac{\frac{d(\frac{1}{2}U_d^2)}{dx}}{\frac{d(U_e U_d)}{dx}} \sim O\left(\frac{U_d}{U_e}\right) = O(\epsilon)$$

$$\frac{D}{C} = -\frac{\frac{1}{U_d} \frac{d(U_d \delta)}{dx}}{\frac{1}{U_d} \frac{d(U_e \delta)}{dx}} \sim O\left(\frac{U_d}{U_e}\right) = O(\epsilon)$$

$$\frac{C}{A} = -\frac{\frac{1}{U_d} \frac{d(U_e \delta)}{dx}}{\frac{\delta}{U_d^2} \frac{d(U_e U_d)}{dx}} = -\frac{U_d \frac{d(\delta U_e)}{dx}}{\delta \frac{d(U_e U_d)}{dx}} \sim O(1)$$

The above comparison of the relative magnitude of the coefficients of Equation (3.9) suggests that, as long as  $U_d \ll U_e$ ,

$$B \ll A \tag{3.10}$$

$$D \ll C \tag{3.11}$$

$$A \sim C \tag{3.12}$$

In fact, for high Reynolds number thin shear layer type of wake flow, we have

$$B = \frac{\delta}{U_d} \frac{dU_d}{dx} \sim O\left(\frac{\delta}{L}\right) \sim O\left(\frac{u'}{U}\right) \ll 1 \tag{3.13}$$

$$D = -\frac{1}{U_d} \frac{d(U_d \delta)}{dx} \sim O\left(\frac{\delta}{L}\right) \sim O\left(\frac{u'}{U}\right) \ll 1 \tag{3.14}$$

where  $L$  is the longitudinal reference length scale of the wake,  $u'$  is the streamwise fluctuating velocity and  $U$  is the mean velocity.<sup>2</sup>

---

<sup>2</sup>The relationship of  $O\left(\frac{\delta}{L}\right) \sim O\left(\frac{u'}{U}\right)$  may find its analogous example in boundary layer flow as described by Tennekes and Lumley (1972, p16). The mean flow of the wake is largely dependent

Therefore, for thin shear layer type of shallow wake flow, the two coefficients  $B$  and  $D$  in Equation (3.9) are far less than all the other coefficients and their associated terms can then be neglected. To the first order approximation, the equation (3.9) can be simplified as

$$Af + C\eta f' + g' = 0 \quad (3.15)$$

i.e.,

$$-\left[\frac{\delta}{U_d^2} \frac{d(U_c U_d)}{dx}\right] f + \left[\frac{1}{U_d} \frac{d(U_c \delta)}{dx}\right] \eta f' + g' = 0 \quad (3.16)$$

Further, integration of equation (3.9) with the consideration of the fact that  $\int_{-\infty}^{+\infty} \eta f' d\eta = -\int_{-\infty}^{+\infty} f d\eta$  and  $\int_{-\infty}^{+\infty} g' d\eta = 0$  yields <sup>3</sup>

$$-\left[\frac{\delta}{U_d^2} \frac{d(U_c U_d)}{dx}\right] \int_{-\infty}^{+\infty} f d\eta - \left[\frac{1}{U_d} \frac{d(U_c \delta)}{dx}\right] \int_{-\infty}^{+\infty} f d\eta = 0 \quad (3.17)$$

i.e.,

$$A \int_{-\infty}^{+\infty} f d\eta - C \int_{-\infty}^{+\infty} f d\eta = 0 \quad (3.18)$$

Since  $\int_{-\infty}^{+\infty} f d\eta \neq 0$ , we have

---

on the behavior of large scale motion.  $u'$  and  $\delta$  can be regarded as the characteristic velocity and length scales associated with the largest eddies in the wake flow. Thus the physical meaning of the longitudinal reference length scale  $L$  may be understood as the convective distance of the largest eddies at a convective speed of  $U$  during a period of rollover time  $\delta/u'$ . Therefore we have  $O\left(\frac{\delta}{L}\right) \sim O\left(\frac{u'}{U}\right)$ . Since we consider low turbulence intensity wake flow, the relationship  $O\left(\frac{u'}{U}\right) \ll 1$  is also valid.

<sup>3</sup>Integration by part, we have  $\int_{-\infty}^{+\infty} \eta f' d\eta = \eta f_{-\infty}^{+\infty} - \int_{-\infty}^{+\infty} f d\eta$ . However,  $f(\eta)$  decays faster than  $1/\eta$  at large  $\eta$ , thus  $\eta f_{-\infty}^{+\infty} = 0$  and  $\int_{-\infty}^{+\infty} \eta f' d\eta = -\int_{-\infty}^{+\infty} f d\eta$ . For symmetric wake,  $g'$  is an odd function and therefore,  $\int_{-\infty}^{+\infty} g' d\eta = 0$ .

$$A = C \quad (3.19)$$

which is consistent with the analysis of the order of magnitude for  $A$  and  $C$ .

In fact, the neglect of the two terms associated with  $B$  and  $D$  of Equation (3.9) and the equivalence of the two coefficients  $A$  and  $C$  can be justified from the experimental evidence as shown in Figure 3.24, in which the relative magnitude of the four coefficients of  $A$ ,  $B$ ,  $C$  and  $D$  for APG, ZPG and FPG cases are shown. It can be seen from Figure 3.24 that indeed the relationships (3.10)  $\sim$  (3.14) are approximately valid within the streamwise range of the investigation for the pressure gradient cases investigated.

The above analysis indicates that, to the first order approximation of Equation (3.9), we only need to require that

$$A = C = K \quad (3.20)$$

where  $K$  is a constant, to guarantee the similarity solution. In other words, the maximum velocity defect  $U_d$  and the wake half-width  $\delta$  must satisfy the following two equations so that the the similarity solution of the wake flow in the sense of the first order approximation exists.

$$-\left[ \frac{\delta}{U_d^2} \frac{d(U_c U_d)}{dx} \right] = K \quad (3.21)$$

$$\left[ \frac{1}{U_d} \frac{d(U_e \delta)}{dx} \right] = K \quad (3.22)$$

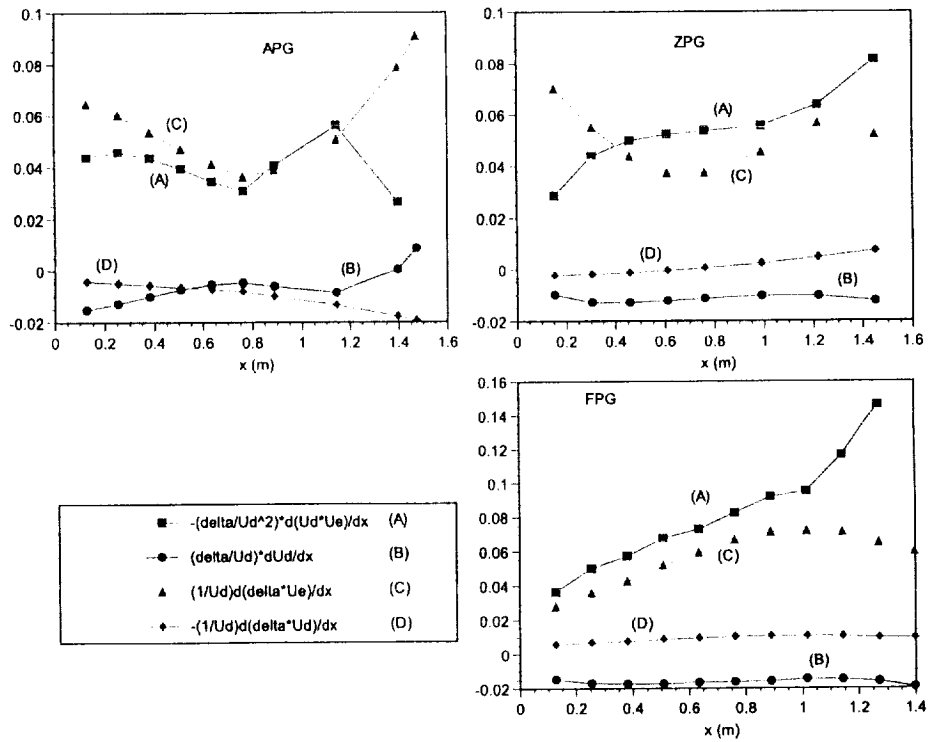


Figure 3.24. Comparison of Coefficients  $A$ ,  $B$ ,  $C$  and  $D$  in APG, ZPG and FPG.

To solve the above two equations, we need to utilize the the full integration result of equation (3.17). After some manipulations, equation (3.19) can be rewritten as

$$\frac{1}{U_d \delta} \frac{d(U_d \delta)}{dx} = -\frac{2}{U_e} \frac{dU_e}{dx} \quad (3.23)$$

Integration of equation (3.23) with respect to  $x$  yields

$$U_e^2 U_d \delta = M \equiv \text{constant} \quad (3.24)$$

To verify if  $M$  is constant for the wake flow that we investigated, we plot the  $M$  values for the APG, ZPG and FPG cases at various streamwise locations in Figure 3.25. It can be seen that, within a 20% uncertainty level, this quantity can be roughly regarded as a constant for all APG, ZPG and FPG cases, with a value of  $M$  varying roughly between  $100 \sim 150 \text{ m}^4/\text{s}^3$ . In fact, since  $U_d \delta$  can be roughly regarded as the volume flow rate deficit of the wake and  $U_e^2$  can be regarded as the kinetic energy of the mean flow per unit volume, the product  $M = U_e^2 U_d \delta$  can then be regarded as the mean flow kinetic energy deficit of the wake. Thus the physical meaning of Equation (3.24) is that the mean flow kinetic energy deficit of the wake flow in pressure gradients is approximately a constant if the wake velocity defect is small.

Integration of equation (3.21) with respect to  $x$  and utilizing the fact that  $M = U_e^2 U_d \delta \equiv \text{constant}$  yields

$$\frac{1}{(U_e U_d)^2} = \frac{2KT}{M} + C_1 \quad (3.25)$$

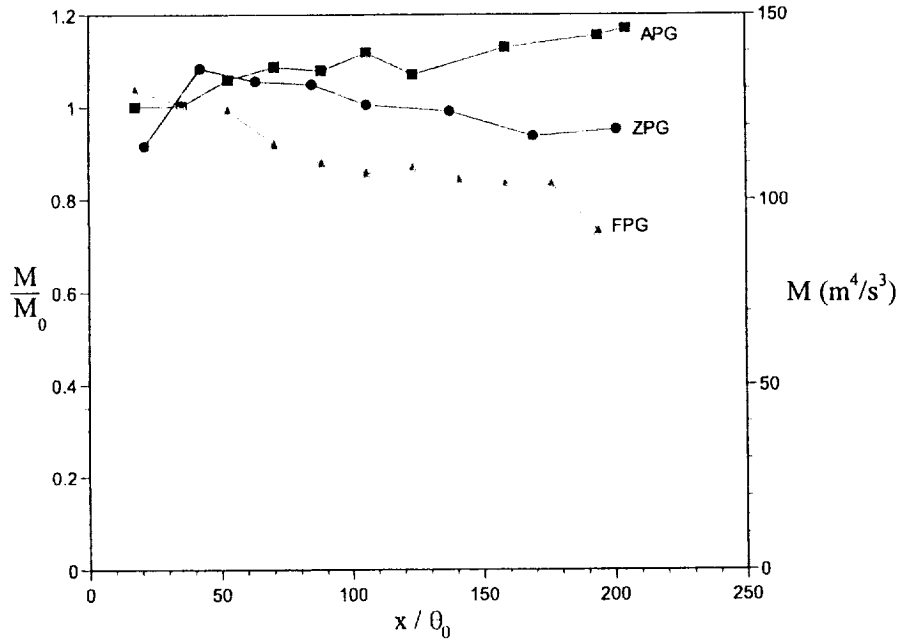


Figure 3.25. Comparison of the Streamwise Variation of  $M$  in APG, ZPG and FPG.

where  $T(x) \equiv \int_0^x \frac{dx}{U_e(x)}$  is the so-called “time-of-flight variable” and  $C_1$  is an integration constant.

Similarly, integration of equation (3.21) with respect to  $x$  yields

$$\frac{(U_e \delta)^2}{M^2} = \frac{2KT}{M} + C_2 \quad (3.26)$$

where  $C_2$  is also an integration constant. Later on, it will be shown that

$$C_1 = C_2 \quad (3.27)$$

so that equations (3.25) and (3.26) can be combined and expressed as

$$\frac{(U_e \delta)^2}{M^2} = \frac{1}{(U_e U_d)^2} = \frac{2KT}{M} + C_1 \quad (3.28)$$

which was also derived by Narasimha and Prabhu (1972).

### 3.7.2 Universal Similarity Solution for Symmetric Turbulent Wake Mean Flow in Pressure Gradients

From equation (3.28), we can solve the explicit expressions for the maximum velocity defect  $U_d(x)$  and the wake half-width  $\delta(x)$  as follows in terms of  $K, M$  and  $T(x)$ , provided  $K$  and  $M$  are both constants for the wake.

$$U_d(x) = \frac{M}{U_e \sqrt{2KMT + C_1 M^2}} \quad (3.29)$$

$$\delta(x) = \frac{\sqrt{2KMT + C_1 M^2}}{U_e} \quad (3.30)$$

where  $T(x) \equiv \int_0^x \frac{dx}{U_e(x)}$ .

Suppose at  $x = x_0$ , the external velocity  $U_e(x_0)$ , the maximum velocity defect  $U_d(x_0)$  and the wake half-width  $\delta(x_0)$  are all known and can be denoted as  $U_{e0}$ ,  $U_{d0}$  and  $\delta_0$  respectively. The time of flight  $T(x)$  at  $x = x_0$  can be denoted as  $T_0$ . Since, from (3.24),  $M = U_e^2 U_d \delta \equiv \text{constant}$ , we can then take

$$M = U_{e0}^2 U_{d0} \delta_0 \quad (3.31)$$

Then from equations (3.25) and (3.26), one can immediately show that

$$C_1 = \frac{1}{(U_{c0}U_{d0})^2} - \frac{2KT_0}{U_{c0}^2 U_{d0} \delta_0} = C_2 \quad (3.32)$$

Substitution of (3.31) and (3.32) into (3.29) and (3.30), respectively, and noticing that

$$T - T_0 \equiv \int_0^x \frac{dx}{U_e(x)} - \int_0^{x_0} \frac{dx}{U_e(x)} = \int_{x_0}^x \frac{dx}{U_e(x)}$$

we can obtain

$$\frac{U_d(x)}{U_{d0}} = \frac{1}{\frac{U_c}{U_{c0}} \sqrt{1 + 2K \frac{U_{d0}}{\delta_0} \int_{x_0}^x \frac{dx}{U_e(x)}}} \quad (3.33)$$

$$\frac{\delta(x)}{\delta_0} = \frac{\sqrt{1 + 2K \frac{U_{d0}}{\delta_0} \int_{x_0}^x \frac{dx}{U_e(x)}}}{\frac{U_c}{U_{c0}}} \quad (3.34)$$

with constant  $K$  experimentally determined as  $K \approx 0.04 \sim 0.06$ . In non-dimensional form, relations (3.33) and (3.34) can be expressed as

$$U_d^* = \frac{1}{U_e^* \sqrt{1 + 2K \Delta T^*}} \quad (3.35)$$

$$\delta^* = \frac{\sqrt{1 + 2K \Delta T^*}}{U_c^*} \quad (3.36)$$

where

$$U_d^* = \frac{U_d}{U_{d0}}$$

$$\delta^* = \frac{\delta}{\delta_0}$$

$$U_e^* = \frac{U_e}{U_{e0}}$$

$$\Delta T^* = \frac{U_{d0}}{\delta_0} \int_{x_0}^x \frac{dx}{U_e(x)}$$

### 3.7.3 Comparison of Analytical and Experimental Results on Wake Growth

Relations (3.33) and (3.34) clearly indicate that both global wake parameters  $U_d(x)$  and  $\delta(x)$  are only functions of external velocity  $U_e(x)$ , or, equivalently, functions of the imposed streamwise pressure gradient  $dP(x)/dx$ . Once the initial wake parameters  $U_{d0}$  and  $\delta_0$  together with the downstream external velocity  $U_e(x)$  are all known, both global wake parameters  $U_d(x)$  and  $\delta(x)$  can then be predicted by using relations (3.33) and (3.34).

To verify the capability of relations (3.33) and (3.34) in predicting the growth of the wake mean flow, comparisons of the streamwise variation of the wake half-width  $\delta$  and the maximum velocity defect  $U_d$  as predicted from relations (3.33) and (3.34) with the experimental measurement results are presented in Figure 3.26 and 3.27, respectively. The initial input position is taken at the location where the imposed pressure gradient commences ( $x/\theta_0 \approx 42$ ). It is known from the experiments that at this location the wake mean profile has already exhibited similarity behavior. As mentioned earlier, the parameter  $K$  is an experimentally determined constant with a value varying from  $0.04 \sim 0.06$ . For predictions shown in Figures 3.26 and 3.27, the constant  $K$  is taken as  $K = 0.045$ . The agreement is observed to be quite good which validates the suitability of the similarity results (3.33) and (3.34) in computing the global evolution of the wake in pressure gradients.

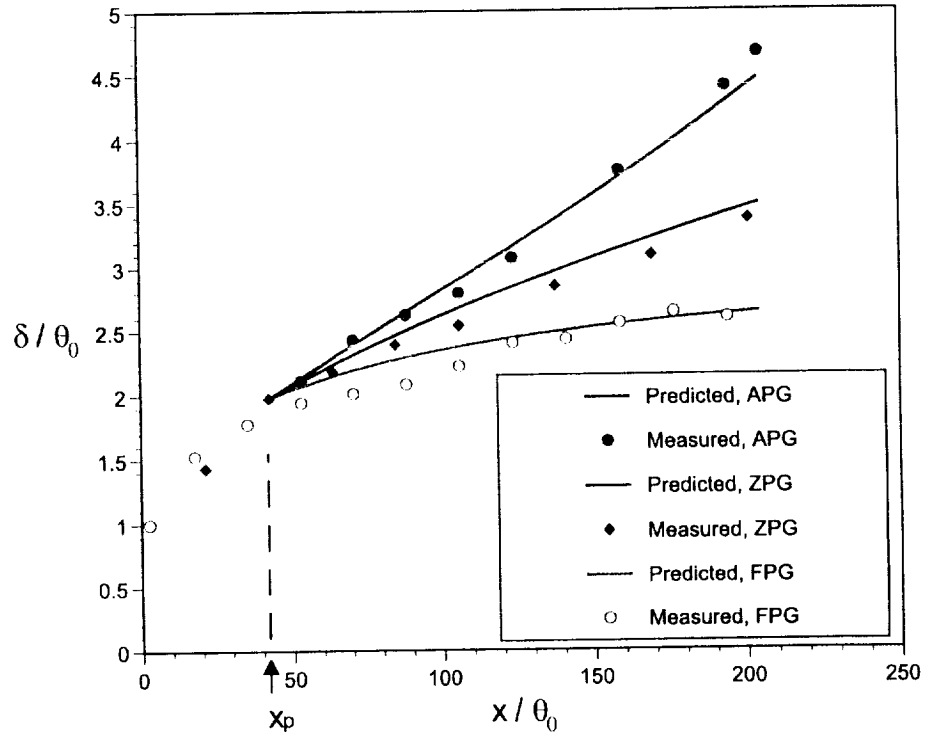


Figure 3.26. Comparison of the Measured and the Similarity Predicted Wake Half-width in APG, ZPG and FPG.

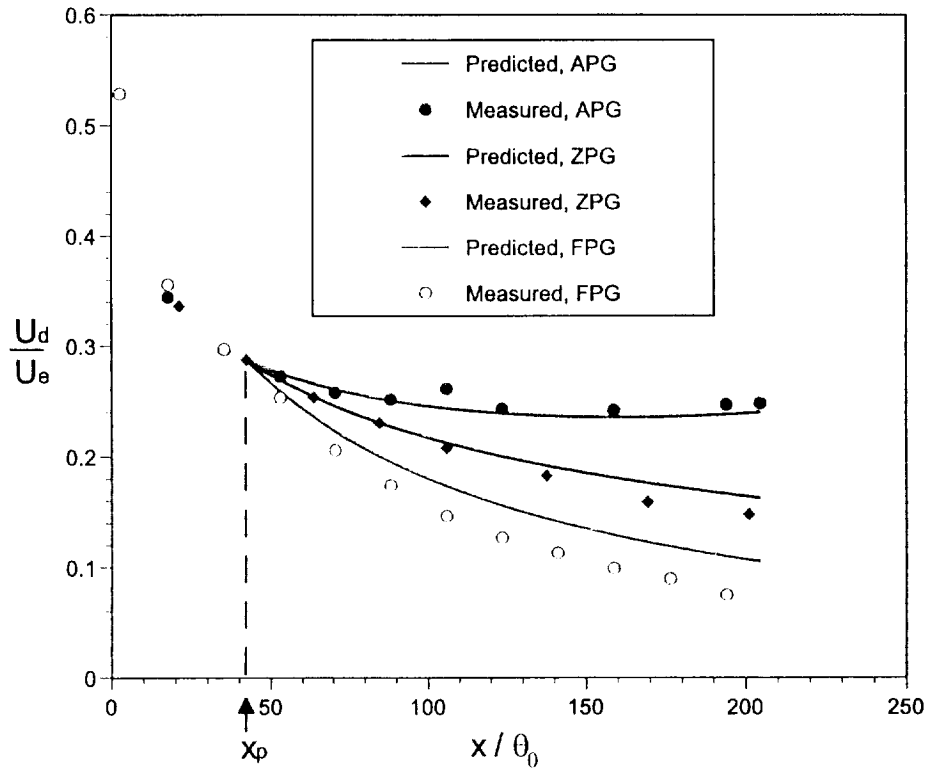


Figure 3.27. Comparison of the Measured and Similarity Predicted Maximum Velocity Defect in APG, ZPG and FPG.

Although the derivation of relations (3.33) and (3.34) is based on the shallow wake assumption, the two relations are also applicable to locations where the velocity defect is not small. In Figures 3.28 and 3.29, where the comparisons of the prediction and the experimental data on  $\delta$  and  $U_d$  are shown again, respectively, the initial input position for the prediction is taken at  $x/\theta_0 \approx 3$  where the wake mean profile is definitely not self-similar. However, as shown in Figures 3.28 and 3.29, the prediction agree amazingly well with the tendency of the pressure gradient effect on the wake growth, although disparities between the prediction and the experiments exist for  $\delta$  in APG, ZPG and FPG and  $U_d$  in FPG. Again the constant  $K$  is taken as 0.045 for this prediction.

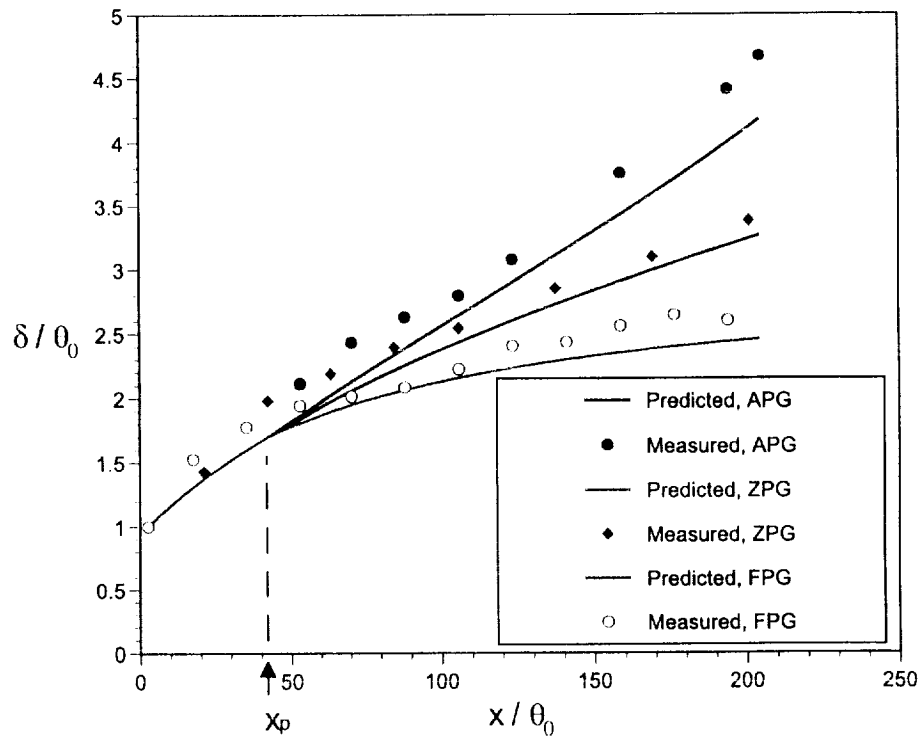


Figure 3.28. Effect of Early Input Location on Similarity Prediction for Wake Half-width.

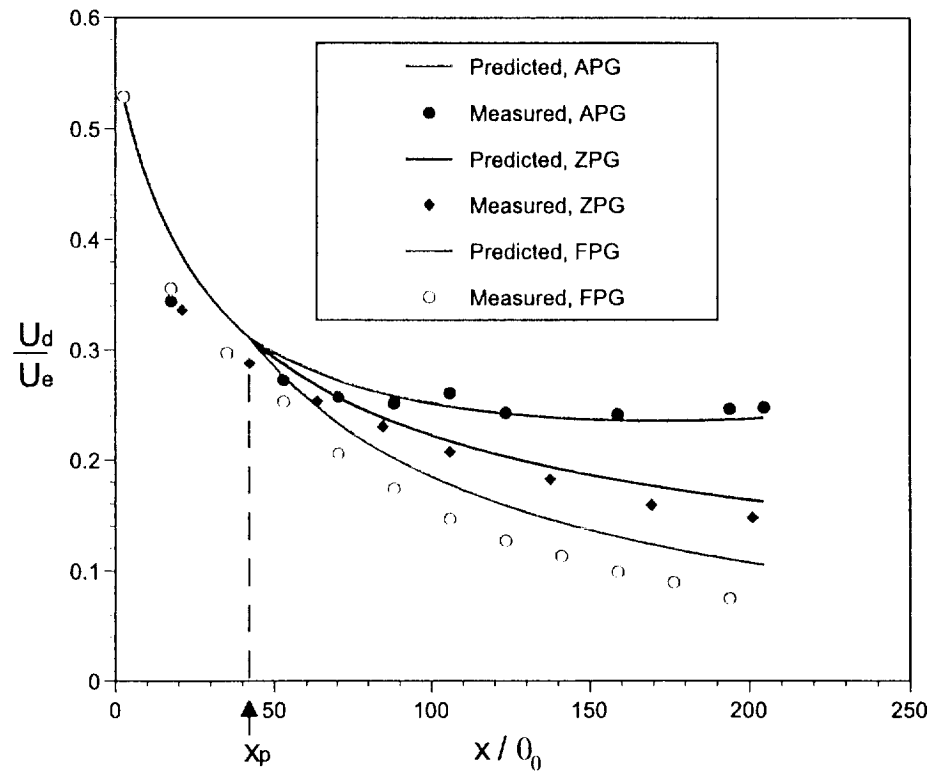


Figure 3.29. Effect of Early Input Location on Similarity Prediction for Wake Maximum Velocity Defect.

To investigate the suitability of the application of relations (3.33) and (3.34) to much stronger pressure gradients, predictions based on (3.33) and (3.34) are compared with Cases C and D of the DNS (Direct Numerical Simulation) results of a temporally evolving, strained planar turbulent wake undertaken by Rogers (2001), as shown in Figures 3.30 and 3.31. To facilitate the comparison, relations (3.33) and (3.34) are transformed to the temporal evolving form in accordance with the the DNS predictions. The global wake parameters in the temporal domain take the form

$$\frac{U_d(\tau)}{U_d(\tau_0)} = \frac{1}{e^{\bar{a}(\tau-\tau_0)} \sqrt{1 + 4K(\tau - \tau_0)}} \quad (3.37)$$

$$\frac{\delta(\tau)}{\delta(\tau_0)} = \frac{\sqrt{1 + 4K(\tau - \tau_0)}}{e^{\bar{a}(\tau-\tau_0)}} \quad (3.38)$$

where

$$\bar{a} = \frac{2\delta_0}{U_{d0}} \frac{dU_c}{dx}$$

$$\tau = \frac{U_{d0}}{2\delta_0} \int_0^x \frac{dx}{U_c(x)}$$

As the previous predictions, the constant  $K$  is again taken as 0.045 for the comparison with Rogers DNS data. The non-dimensional constant streamwise strain  $\bar{a}$  applied to Cases C (equivalent to adverse pressure gradient) and D (equivalent to favorable pressure gradient) are  $\bar{a} = -0.271$  and  $\bar{a} = +0.271$ , respectively. As a basis for comparison, the non-dimensional strain  $\bar{a}$  is only approximately  $-0.01$  and  $+0.1$ , respectively, for the APG and FPG cases in this wake study at the beginning location of the imposed pressure field. Figures 3.30 and 3.31 present the comparison of predicted evolution of  $\delta$  and  $U_d$  with the DNS results in the log-linear plot

format as appeared in Rogers paper. Except for the the positive strain (favorable pressure gradient) case, the agreement between the similarity prediction and the DNS results for the negative strain (adverse pressure gradient) is fairly impressive.

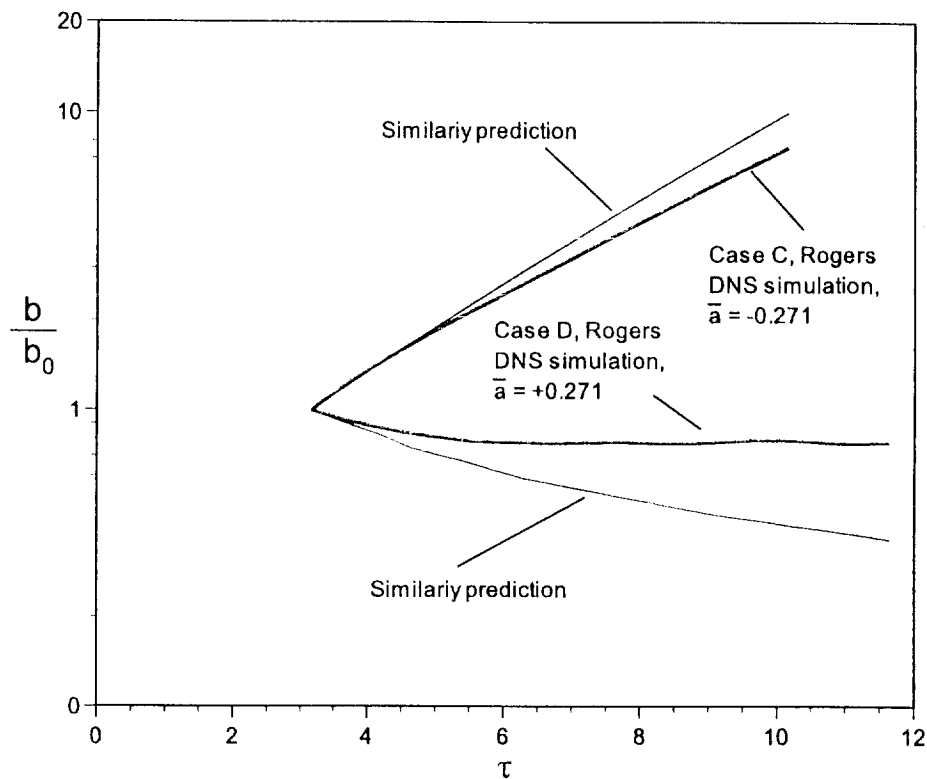


Figure 3.30. Comparison of the Similarity Predicted and Wake Half-width with DNS Results.

### 3.7.4 Discussion

The comparisons presented in the above section clearly show that with the shallow wake assumption, relations (3.33) and (3.34) provide us an easy-to-use yet powerful engineering tool for the prediction of the wake growth subjected to arbitrary pressure gradient environment. With the prediction formula (3.33) and (3.34) as well as the universal shape function (3.1), the entire mean flow field of planar wake in arbitrary

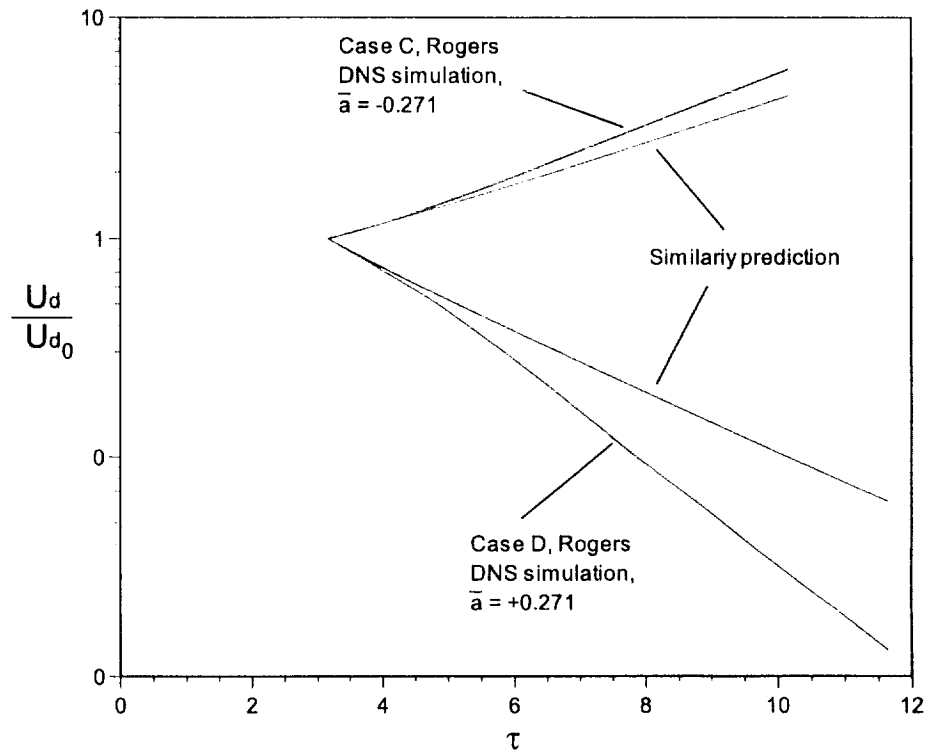


Figure 3.31. Comparison of the Similarity Predicted Maximum Velocity Defect with DNS Results.

pressure gradients can then be determined approximately without invoking any turbulence modelling.

As pointed out earlier, the prediction formula (3.33) and (3.34) indicate that both global wake shape parameters  $U_d(x)$  and  $\delta(x)$  are only functions of external velocity  $U_e(x)$ , or, equivalently, functions of the imposed streamwise pressure gradient  $dP(x)/dx$ . Actually, for predictions of  $U_d(x)$  and  $\delta(x)$  based on formula (3.33) and (3.34) for engineering applications, the external free stream velocity distribution  $U_e(x)$  or, equivalently, the pressure distribution, might not necessarily to be known in advance. For example, for the prediction of turbulent wake flow in a duct, as an engineering approach, a shooting method based on iteration process may be invoked to finally locate the prediction of the external free stream velocity distribution  $U_e(x)$ , wake shape parameters  $U_d(x)$  and  $\delta(x)$  and the information about the wall boundary layer growth by utilizing the prediction formula listed above together with the appropriate boundary layer theories regarding boundary layer growth in pressure gradients.

It should be pointed out that as matter of fact, for the special case of far wake flow in a zero pressure gradient environment, where  $U_e = \text{constant}$  and  $x/\delta_0 \gg 1$ , relations (3.33) and (3.34) will be reduced to the well-recognized classic results for the wake similarity at zero pressure gradient as

$$U_d \sim x^{-\frac{1}{2}} \quad (3.39)$$

and

$$\delta \sim x^{\frac{1}{2}} \quad (3.40)$$

indicating relations (3.33) and (3.34) are consistent with the classic results.

In addition, formula (3.33) and (3.34) also clearly shows that the wake shape parameters  $\delta$  and  $U_d$  depend on its initial condition, which confirms the assertion

of George (1989) and agrees with the experimental observation of Wygnanski *et al.* (1986). However, this dependence of wake shape parameters does not mean that the wake shape function  $f(\eta)$  also depends on its initial condition. As demonstrated by Wygnanski *et al.* (1986) through their experimental research of turbulence wake flow, the normalized mean velocity shape profile of a turbulent wake is independent of the initial conditions or the nature of the wake generator.

It is also interesting to note that the analytical result of Rogers (2001),  $U_d(t)\delta(t) = U_{d0}\delta_0 e^{(a_{22}-a_{11})t}$ , is only a natural consequence of the relations (3.37) and (3.38). More accurately, the analytical result of Rogers (2001) is only an equivalent expression of the relation  $M = U_c^2 U_d \delta$  in the temporal domain.

According to equation (3.24), for shallow wake flow, to the first order accuracy, the product  $U_c^2 U_d \delta$  should be a constant. Obviously, to maintain the constancy of the product,  $U_d$  and  $\delta$  must adjust themselves accordingly when the free stream velocity  $U_c$  changes. Different pressure gradient imposed to the wake flow field will result in different free stream velocity distribution and therefore the response of the wake behavior will also be different. For example, as shown in Figures 3.9, the adverse pressure gradient will significantly enhance the spreading rate of the wake flow while the favorable pressure gradient will decrease it. Although the imposed adverse pressure gradient is relatively small, the effect on the wake widening is still quite significant.

Although the comparisons made in the previous section show that the application of formula (3.33) and (3.34) can be extended to regions where the maximum velocity defect is not relatively small, for reliable applications of formula (3.33) and (3.34), it should keep in mind that the key assumption for this linearized similarity analysis is the shallow wake assumption, i.e., the maximum velocity defect is far less than the external velocity,  $U_d \ll U_c$ . But how small the maximum velocity defect  $U_d$

compared to the external velocity  $U_e$  is enough to guarantee similarity behavior of the wake mean flow profile? To answer this question, we may resort to the examination of the experimental data. As mentioned earlier in Section 3.5.3, the wake mean profiles for APG, ZPG and FPG cases exhibit similarity behavior as early as  $x/\theta_0 \approx 40$ , with the corresponding maximum velocity defect of  $U_d/U_e \approx 0.3$ . Based on this information, it seems that the shallow wake assumption is roughly valid for  $U_d/U_e \approx 0.3$ . In other words, as long as the maximum velocity defect is less than 30% of the external velocity, the wake mean flow is likely to exhibit a similarity behavior, regardless of what pressure gradient is imposed to the flow field. However, it seems that the shallow wake flow assumption might not be the sufficient condition to guarantee the similarity behavior of turbulent wake mean flow, as discussed later.

As discussed in Section 3.6 for the turbulence characteristics of the symmetric wake development, the Reynolds stress profiles exhibit similarity behavior further downstream than the mean flow profiles. The question why we can see a similar mean velocity profile while the Reynolds stress terms still not reaching the similarity state may find the answer from the fact that the coefficient of the Reynolds stress term  $g'(\eta)$  in the linearized momentum equation (3.15) is far greater than the coefficients of other terms ( $A = C = 0.04 \sim 0.06 \ll 1$ ). As a result, the order of magnitude of the normalized velocity defect function  $f(\eta)$  should be far greater than the Reynolds stress similarity profile function in order to maintain the balance of equation (3.15). Therefore, the normalized velocity defect function  $f(\eta)$  is relatively insensitive to the perturbation of the Reynolds stress from its similarity profile. That is why we can still observe an approximate similar wake mean profile before the Reynolds stress term reaches its similarity state.

Further investigation of the relationship between the similarity of mean velocity profile and the similarity of the Reynolds stress profile might shed light on the

limitation of usage of the above mean wake profile similarity analysis results. As discussed in Section 3.6, the adverse pressure gradient tends to precipitate the process of the Reynolds stress profile to reach similarity state while the favorable pressure gradient tends to prevent the similarity of Reynolds stress from happening. Shown in Figure 3.23 (c), the maximum Reynolds stress scaled by the maximum velocity defect maintain a value no more than 0.03 throughout the entire flow field of investigation for both APG and ZPG cases. However, the maximum Reynolds stress scaled by the maximum velocity defect is kept increasing throughout the entire flow field investigated for the FPG case. At the end of the flow field of investigation, the scaled maximum Reynolds stress is increased to the magnitude of roughly 0.05. This indicate that the decay of the magnitude of the Reynolds stress is at much slower pace than the decay of the mean velocity defect for the favorable pressure gradients. This unique feature of the increasing magnitude of scaled Reynolds stress for favorable pressure gradient results in difficulty in maintaining the balance of the linearized momentum equation (3.15) and as a consequence, the prediction based on formula (3.33) and (3.34) is unable to faithfully depict the wake growth subjected to severe favorable pressure gradients, as shown in Figures 3.30 and 3.31.

### 3.8 Numerical Simulation of the Symmetric Wake Flow

Numerical simulation of the symmetric wake flow subjected to pressure gradients same as the the experimental cases was conducted independently at NASA Langley Research Center (Carlson, Duquesne, Runsey and Gatski, 2001, and Duquesne *et al.*, 1999) and the University of Notre Dame (Brooks, 1999 and Liu *et al.*, 1999b). Based on the code developed by Brooks (1999), the author also conducted the numerical simulation of the symmetric wake in pressure gradients. The numerical modelling and results will be presented briefly in the following sections.

### 3.8.1 Numerical Modelling

The numerical simulation is based on the thin shear layer type of Reynolds Averaged Navier-Stokes equation

$$\frac{\partial u}{\partial x} + \frac{\partial v}{\partial y} = 0$$

$$u \frac{\partial u}{\partial x} + v \frac{\partial u}{\partial y} = U_e \frac{dU_e}{dx} - \frac{\partial \overline{u'v'}}{\partial y} + \nu \frac{\partial^2 u}{\partial y^2}$$

with the eddy-viscosity concept

$$\overline{u'v'} = \nu_\tau \frac{\partial u}{\partial y}$$

The turbulence models utilized in this numerical simulation include the Cebeci-Smith algebraic model, the Spalart-Allmaras one-equation model and the Wilcox (1998)  $k-\omega$  two-equation model. For the last two turbulence models, the momentum equation is decoupled from the turbulence model transport equations by using velocity values at the nearest upstream nodal points. The numerical marching scheme is fully implicit, second order accurate in both  $x$  and  $y$  directions for the mean momentum equation, first order accurate in both  $x$  and  $y$  directions for the Spalart-Allmaras model and second order accurate in both  $x$  and  $y$  directions for the Wilcox (1998)  $k-\omega$  model. For details of the implementation of the numerical scheme, see Brooks (1999).

### 3.8.2 Comparison of Numerical and Experimental Results

Numerical simulation was conducted for the symmetric wake flow subjected to adverse, zero and favorable pressure gradients using all three aforementioned turbulence models. Figures 3.32 and Figures 3.33 present comparisons of the numerical

and experimental results on the streamwise evolution of the wake half-width and the maximum velocity defect of the symmetric wake flow in APG, ZPG and FPG. From these two figures, it can be seen that both of the Spalart-Allmaras and the Wilcox (1998)  $k-\omega$  models predict the wake growth rate and the maximum velocity defect decay quite satisfactorily compared with the experimental data. However, the Cebeci-Smith algebraic model fails in faithfully predicting the characteristics of the symmetric wake development and the simulation results based on this model will not be presented here.

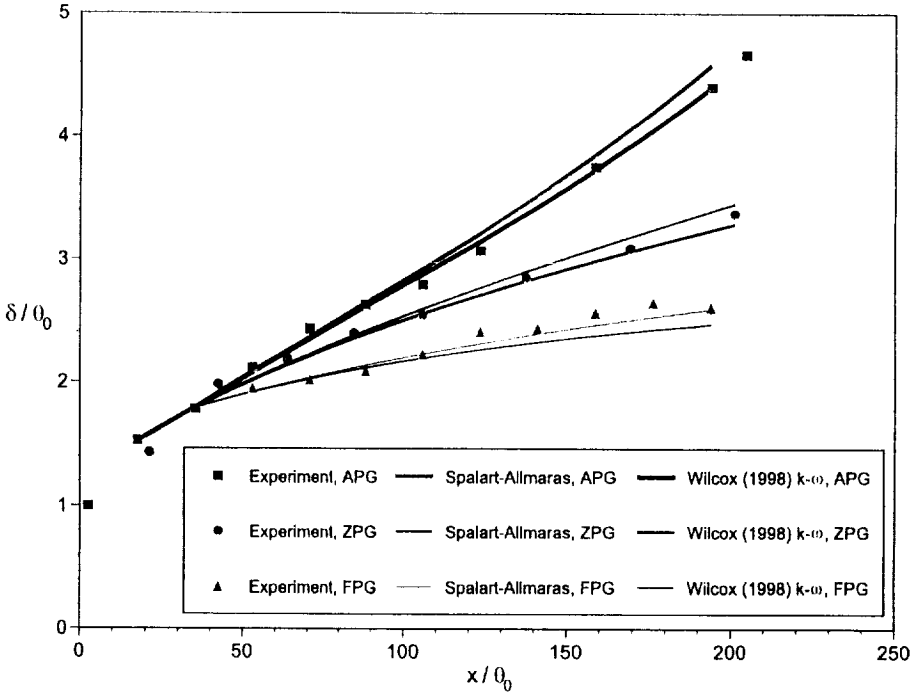


Figure 3.32. Comparison of the Numerical and Experimental Results on the Streamwise Evolution of the Wake Half-Width of the Symmetric Wake in APG, ZPG and FPG.

Close examination of the performance of the Spalart-Allmaras model reveals that the Spalart-Allmaras model faithfully predicts the symmetric wake mean velocity profile

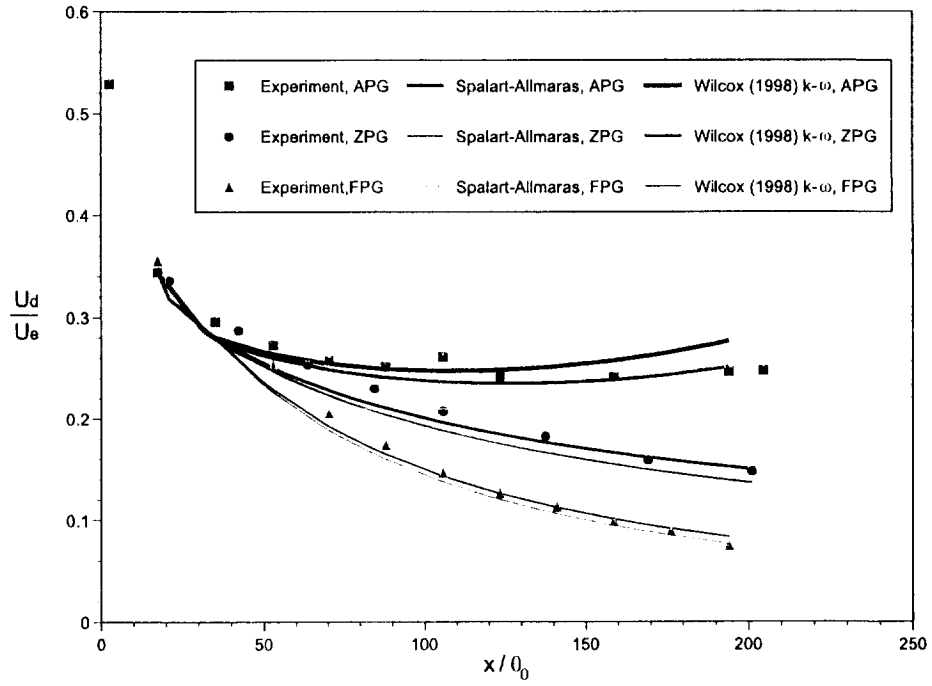


Figure 3.33. Comparison of the Numerical and Experimental Results on the Stream-wise Evolution of the Maximum Velocity Defect of the Symmetric Wake in APG, ZPG and FPG.

for all APG, ZPG and FPG cases, as shown in Figures 3.34, in which numerical wake mean velocity profile based on the Spalart-Allmaras model is compared with the experimental data at different streamwise measurement stations for the APG case. The Wilcox (1998)  $k - \omega$  model also has a good performance for both of the ZPG and FPG cases of the symmetric wake flow. However, Wilcox (1998)  $k - \omega$  over-estimates the maximum velocity defect at downstream locations in the flow field, as shown in Figures 3.35.

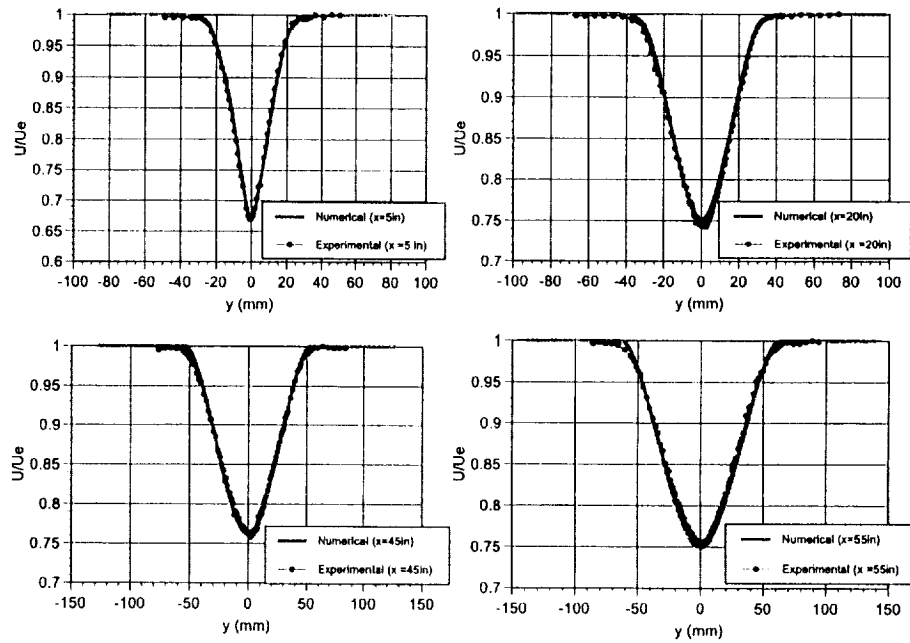


Figure 3.34. Comparison of the Numerical and Experimental Mean Velocity Profiles for the Symmetric Wake in APG with the Spalart-Allmaras One-equation Model.

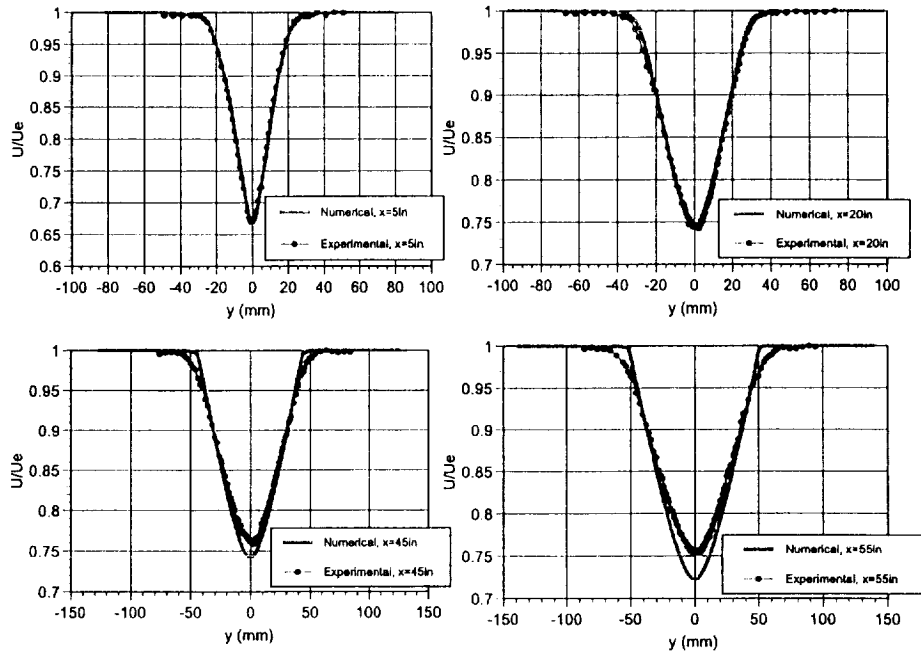


Figure 3.35. Comparison of the Numerical and Experimental Mean Velocity Profiles for the Symmetric Wake in APG with the Wilcox  $k - \omega$  Two-equation Model.

## CHAPTER 4

### ASYMMETRIC WAKE FLOW DEVELOPMENT AND STRUCTURE IN PRESSURE GRADIENTS

#### 4.1 Asymmetric Wake Flow Nomenclature

Before presenting the results for the asymmetric wake, it is necessary to clarify the nomenclature used to characterize the mean flow development of the asymmetric wake. Like the symmetric wake case,  $u_d(x, y)$  will be used to denote the local wake velocity defect while  $U_d(x)$  will denote the maximum local velocity defect in the asymmetric wake, as illustrated in Figure 4.1. However, unlike the symmetric wake case, it is necessary to identify specifically the wake half-widths corresponding to the upper and lower shear layers in order to characterize the the asymmetry of the wake. The wake half-width corresponding to the lateral distance from the center of the wake to the 50% maximum velocity defect location in the lower shear layer (the thick side of the wake) is denoted as  $\delta_1$ . The wake half-width corresponding to the lateral distance from the center of the wake to the 50% maximum velocity defect location in the upper shear layer (the thin side of the wake) is denoted as  $\delta_2$ , as shown in Figure 4.1. Similarly, the momentum thickness of the lower shear layer (thick side of the wake) is denoted as  $\theta_1$  while that of the upper shear layer (thin side of the wake) is denoted as  $\theta_2$ . The degree of asymmetry of the wake is represented by the ratio of the momentum thickness of the lower shear layer to that of the upper shear layer of the wake,  $\theta_1/\theta_2$ . The total wake width is denoted by  $\delta_w$ ,

where, for the asymmetric wake,  $\delta_w = \delta_1 + \delta_2$ ; for the symmetric wake,  $\delta_w = 2\delta$ , where  $\delta$  is the wake half-width of the symmetric wake.

Like the symmetric wake case, the origin of the  $x - y$  coordinates of the flow field in the diffuser test section is located at the trailing edge of the splitter plate.

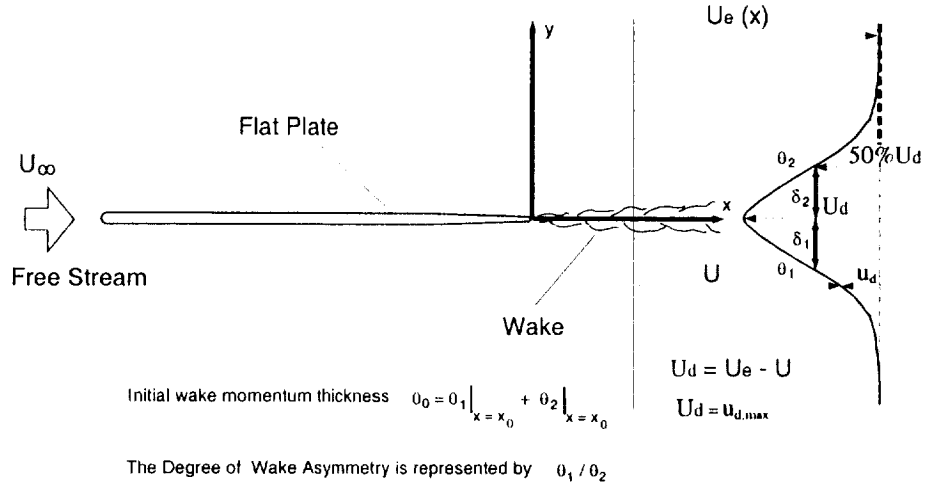


Figure 4.1. Asymmetric Wake Structure Nomenclature.

#### 4.2 The Initial Asymmetric Wake

Figure 4.2 presents the initial profiles of the  $u$ -component mean velocity  $U_{mean}$ , the root-mean-square of the  $u$ -component velocity fluctuation  $U_{rms}$ , the  $v$ -component mean velocity  $V_{mean}$ , the root-mean-square of the  $v$ -component velocity fluctuation  $V_{rms}$  and the Reynolds shear stress  $-\overline{u'v'}$  of the asymmetric wake, measured by an X-wire probe at  $x = 19 \text{ mm}$  from the trailing edge of the splitter plate. The momentum thicknesses of the lower and upper shear layers of the initial wake are  $\theta_1 = 7.13 \text{ mm}$  and  $\theta_2 = 2.88 \text{ mm}$ , respectively. The displacement thicknesses of the lower and upper shear layers of the initial wake are  $\delta_1^* = 9.32 \text{ mm}$  and  $\delta_2^* = 3.92 \text{ mm}$ , respectively. Thus, the degree of asymmetry, represented by the

ratio of the momentum thickness of the lower and upper shear layer of the wake,  $\theta_1/\theta_2$ , is 2.5. The initial wake momentum thickness of the asymmetric wake  $\theta_0$  is 10 mm ( $\theta_0 = \theta_1 + \theta_2$ ).

To compare the initial wake profile of the asymmetric wake with the symmetric one, we plot the initial wake mean velocity profiles of the symmetric and asymmetric wakes together in the same plot in Figure 4.3. From this figure, it can be seen that due to the implementation of suction on the upper surface of the asymmetric wake splitter plate, the upper shear layer of the asymmetric wake is thinned if compared to that of the symmetric wake. As a contrast, due to the application of the separation bump and distributed roughness on the lower surface of the asymmetric wake splitter plate, the lower shear layer of the asymmetric wake is significantly thickened if compared to its symmetric wake counterpart. In addition, from Figure ??, it can also be seen that there is not much scatter of data for all the mean velocity and RMS profiles, which means, unlike the experiment of Roos (1997), there is no noticeable unsteadiness associated with the initial asymmetric wake for this study. This indicates that the unsteadiness introduced by the separation bump, which is placed at the upstream location of the splitter plate lower surface as shown in Figure 2.4, is damped by the application of the distributed roughness.

#### 4.3 Validation of the 2-Dimensionality of the Flow Field

As mentioned before in Section 3.3 for the symmetric wake, the quality of the flow field for the asymmetric wake was also carefully examined and documented. Again, like the symmetric wake case, examination of the results of these measurements verified the two-dimensionality of the flow field of the asymmetric wake. For example, Figure 4.4 shows the comparison of the  $u$ -component velocity mean and RMS profiles of the asymmetric wake measured at different spanwise locations ( $z = -152$  mm,  $0$  mm and  $+152$  mm) at the same streamwise measurement station

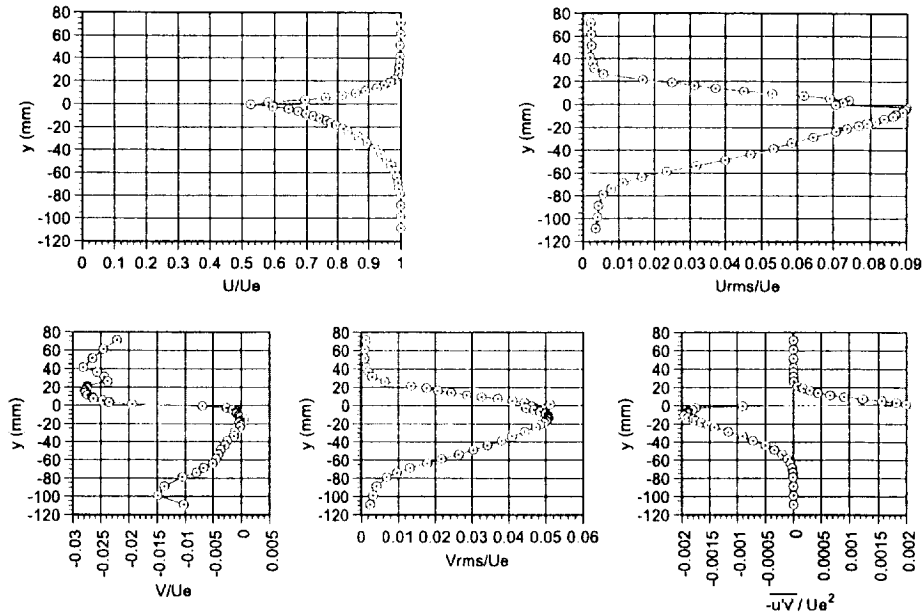


Figure 4.2. Initial Asymmetric Wake Profile.

( $x = 19 \text{ mm}$ ). Obviously, the profiles measured at different spanwise locations overlap each other, indicating satisfactory two-dimensionality of the asymmetric wake flow field. Like the symmetric wake case, LDV measurement of the wake at different spanwise locations at measurement stations located farther downstream reveals that the mean flow two-dimensionality of the wake remains quite satisfactory in the diffuser test section up to the last measurement station at  $x = 145 \text{ cm}$ .

#### 4.4 Effect of Wake Asymmetry on Wake Development and Structure

Like the symmetric wake case, the asymmetric wake flow field survey was conducted for the adverse (APG), zero (ZPG) and favorable (FPG) pressure gradient cases. The direct comparison of the symmetric wake and asymmetric wake experimental results in the same pressure gradient case will reveal the influence of the wake asymmetry on the wake development and structure. In the meanwhile, comparison

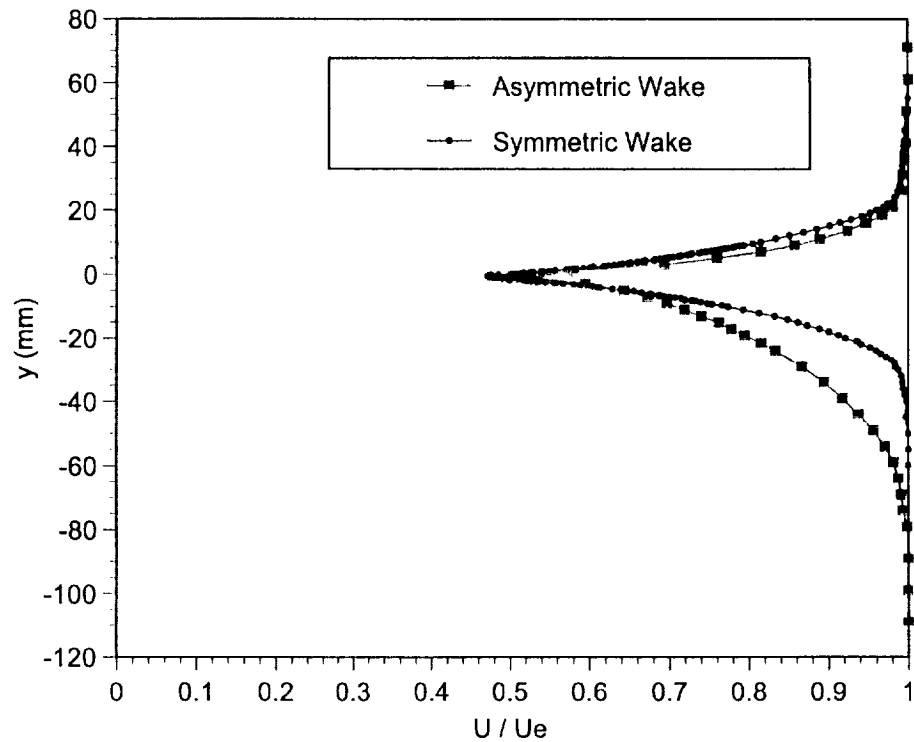


Figure 4.3. Comparison of Initial Symmetric and Asymmetric Wake Mean Velocity Profiles.

of the asymmetric experimental data in different pressure gradients can be used to verify the pressure gradient effect on the wake development and structure which was discussed in Chapter 3. In the following sections, the experimental results of the asymmetric wake flow subjected to pressure gradients will be presented and the effect of the wake asymmetry on wake development and structure will be addressed. In addition, the pressure gradient effect on the asymmetric wake flow will also be discussed.

#### 4.4.1 Wake Mean Velocity Profiles

To get a qualitative understanding of the effect of asymmetry on the wake flow, we first examine the comparison of the streamwise evolution of the mean velocity

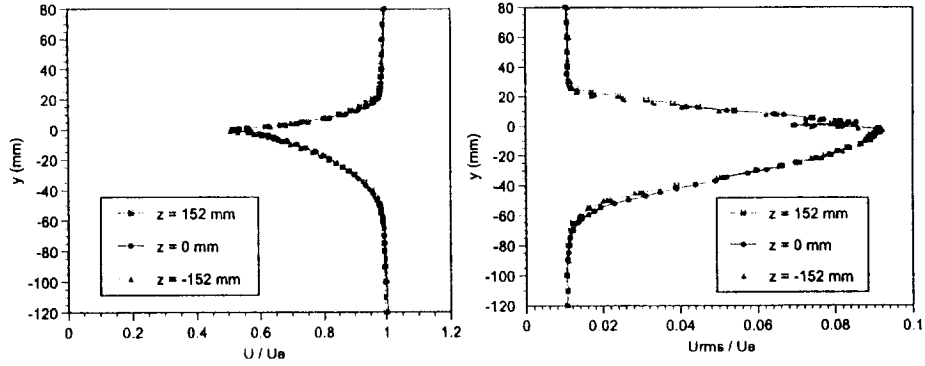


Figure 4.4. 2-D Verification of the Asymmetric Wake at  $x = 19 \text{ mm}$ .

profiles for the symmetric and asymmetric wakes in zero pressure gradient, as shown in Figure 4.5 and Figure 4.6. These two figures are drawn in the same scale so that direct comparison in terms of physical dimensions is appropriate. Figure 4.5 clearly shows that for the symmetric wake in zero pressure gradient, when the wake develops downstream, the wake width is kept increasing and the maximum velocity defect is decreasing. In the meanwhile, the wake mean velocity profile remains symmetric. However, as shown in Figure 4.6, for the asymmetric wake in zero pressure gradient, it seems that the wake widens faster than the symmetric wake case and the shape of the asymmetric wake gradually become more and more symmetric. Moreover, unlike the symmetric wake case, the center of the wake of the asymmetric wake shifts to its thicker side when it develops downstream. The same phenomenon can also be observed for the asymmetric wake flow in adverse and favorable pressure gradients, suggesting the wake asymmetry does have its own special effect on the wake development. To quantitatively describe the wake asymmetry effect, we will present the experimental results on streamwise evolutions of the wake width, maximum velocity defect, center of wake and turbulence intensity

of the asymmetric wake developing in adverse, zero and favorable pressure gradients in the sections to follow.

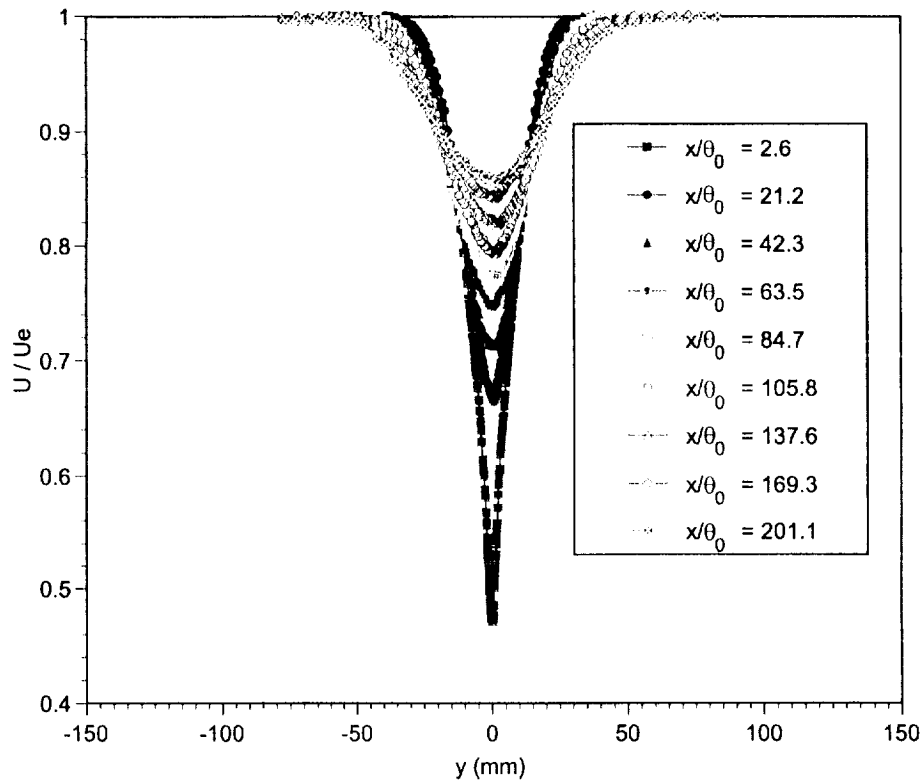


Figure 4.5. Streamwise Evolution of the Symmetric Wake Mean Velocity Profile in ZPG.

#### 4.4.2 Wake Width

The effect of wake asymmetry on the wake width can be seen obviously from Figure 4.7, in which the streamwise evolution of the wake width for the symmetric and asymmetric wakes in adverse, zero and favorable pressure gradients are shown. In this figure, both the wake width and the abscissa are scaled by the initial wake momentum thickness with the blank and the solid data points representing the symmetric and asymmetric wake results, respectively. This figure clearly shows that the

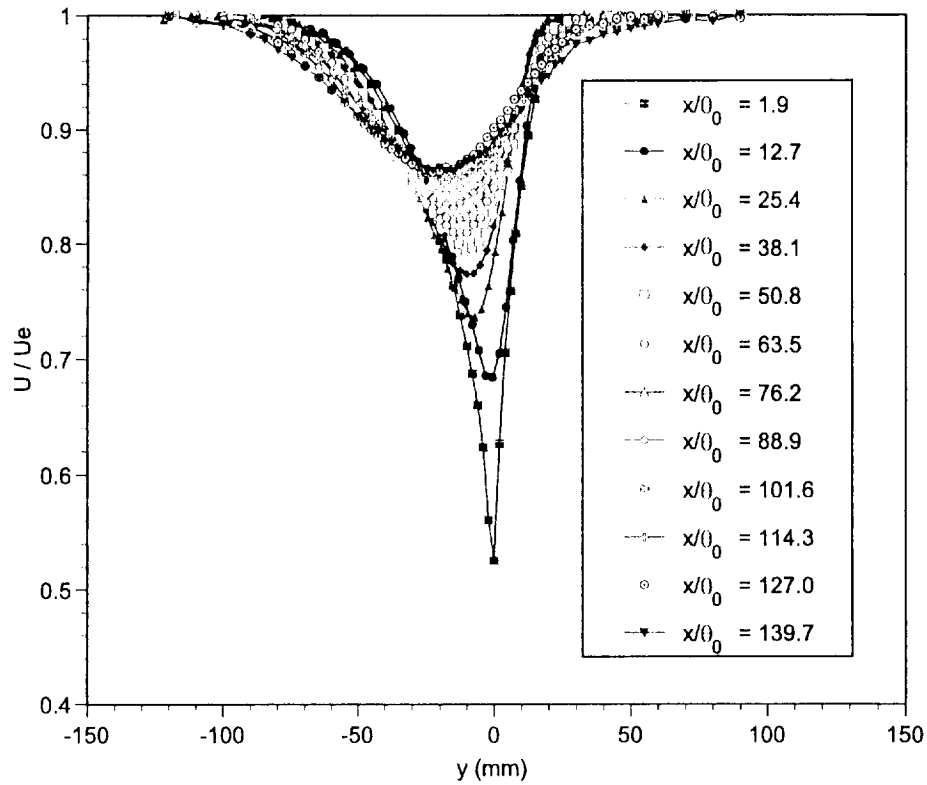


Figure 4.6. Streamwise Evolution of the Asymmetric Wake Mean Velocity Profile in ZPG.

scaled wake width is significantly increased and the wake widening rate is promoted in each pressure gradient case when the asymmetry is introduced to the wake. In addition, this figure also shows that the effect of the pressure gradient on the asymmetric wake width is the same as that on the symmetric wake, i.e., the change of pressure gradient from favorable to adverse will result in a significant increase in the wake widening rate, and the pressure gradient effect can be immediately seen after it is imposed to the flow field.

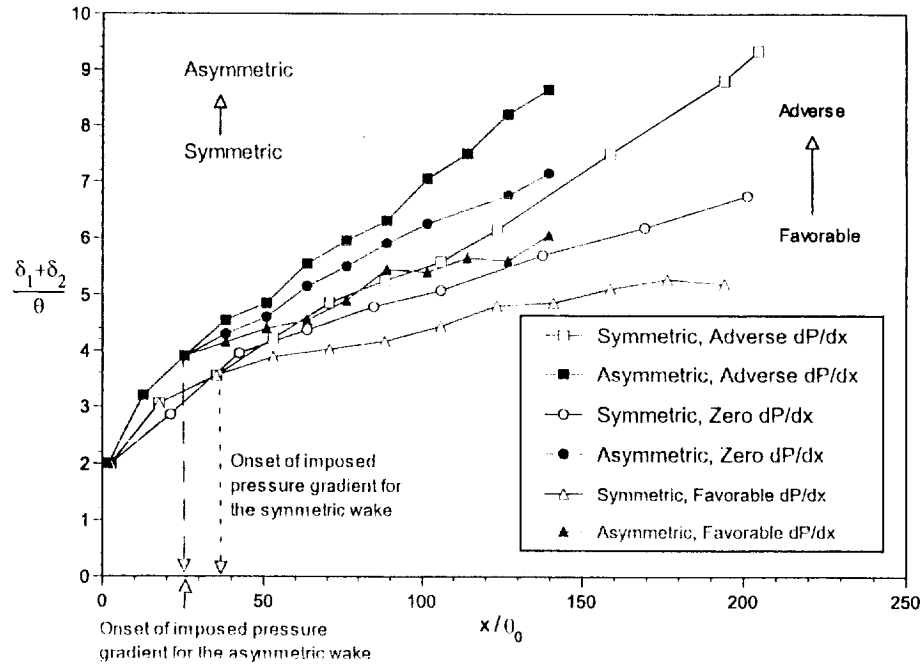


Figure 4.7. Streamwise Evolution of the Wake Width for the Symmetric and Asymmetric Wakes in Adverse, Aero and Favorable Pressure Gradients.

#### 4.4.3 Maximum Velocity Defect

The effect of wake asymmetry on the maximum velocity defect is shown clearly in Figure 4.8, which presents the streamwise evolution of the maximum velocity defect for the symmetric and asymmetric wakes in adverse, zero and favorable pressure gradients. Again in Figure 4.8, the blank data points represent the symmetric wake cases while the solid data points represent the asymmetric wake cases. The abscissa is scaled by the initial wake momentum thickness. From this figure, it can be seen that when the asymmetry is introduced to the wake, the decay of the maximum velocity defect is precipitated for each pressure gradient case. Also shown in this figure is the pressure gradient effect on the wake maximum velocity defect. It is apparent that the effect of the pressure gradient effect on the asymmetric wake flow

is the same as that on the symmetric wake flow, i.e., the change of pressure gradient from favorable to adverse will result in a significant reduction of the velocity defect decay rate, and once again, the pressure gradient effect is immediately visible after it is imposed to the flow field.

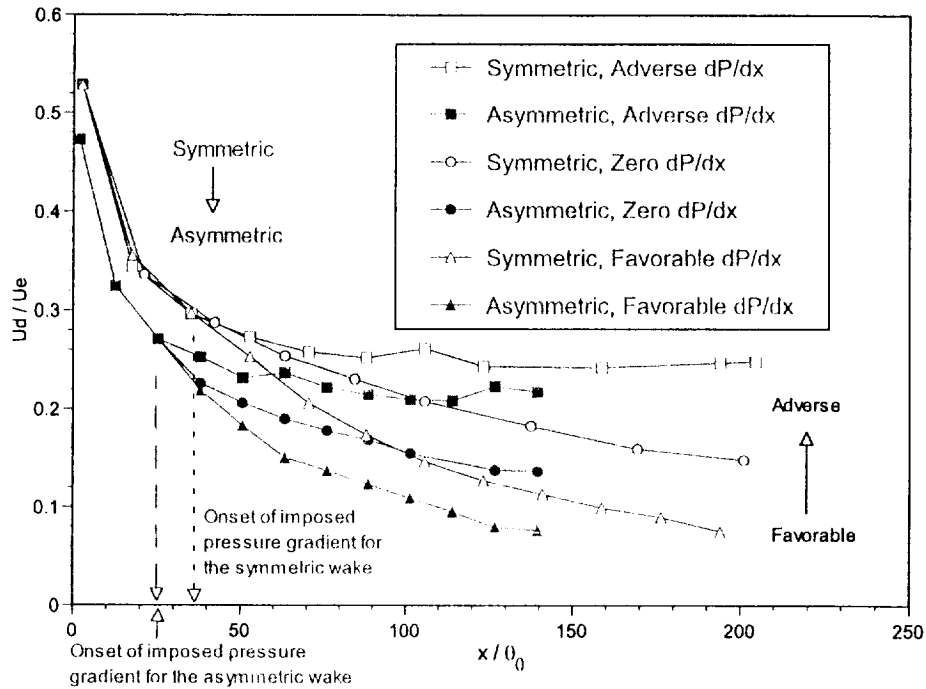


Figure 4.8. Streamwise Evolution of the Maximum Velocity Defect for the Symmetric and Asymmetric Wakes in Adverse, Zero and Favorable Pressure Gradients.

#### 4.4.4 Evolution of Degree of Asymmetry

For the asymmetric wake, the wake half-widths of the lower and upper shear layers  $\delta_1$  and  $\delta_2$  are different due to asymmetry. In addition to the ratio of the momentum thicknesses of the lower and upper shear layers,  $\theta_1/\theta_2$ , the relative magnitude of  $\delta_1$  and  $\delta_2$  can also be viewed as an indication of the degree of wake asymmetry. In this sense, the comparison of the streamwise evolution of  $\delta_1$  and  $\delta_2$  can be used to gauge the streamwise variation of the degree of wake asymmetry. Figure 4.9 shows

the streamwise evolution of  $\delta_1$  and  $\delta_2$  of the asymmetric wake for APG, ZPG and FPG cases. From this figure, it can be seen that the upper and lower shear layers of the asymmetric wake are growing at different rates, and the growing rate of the thin side (the upper layer) of the wake is faster than that of the thick side (the lower layer). As a result, the difference between  $\delta_1$  and  $\delta_2$  is getting smaller and smaller when the wake develops downstream for all pressure gradient cases. This implies that the degree of wake asymmetry is gradually reduced when the wake develops downstream and the shape of the wake becomes more and more symmetric with the development of the asymmetric wake in all pressure gradient cases investigated.

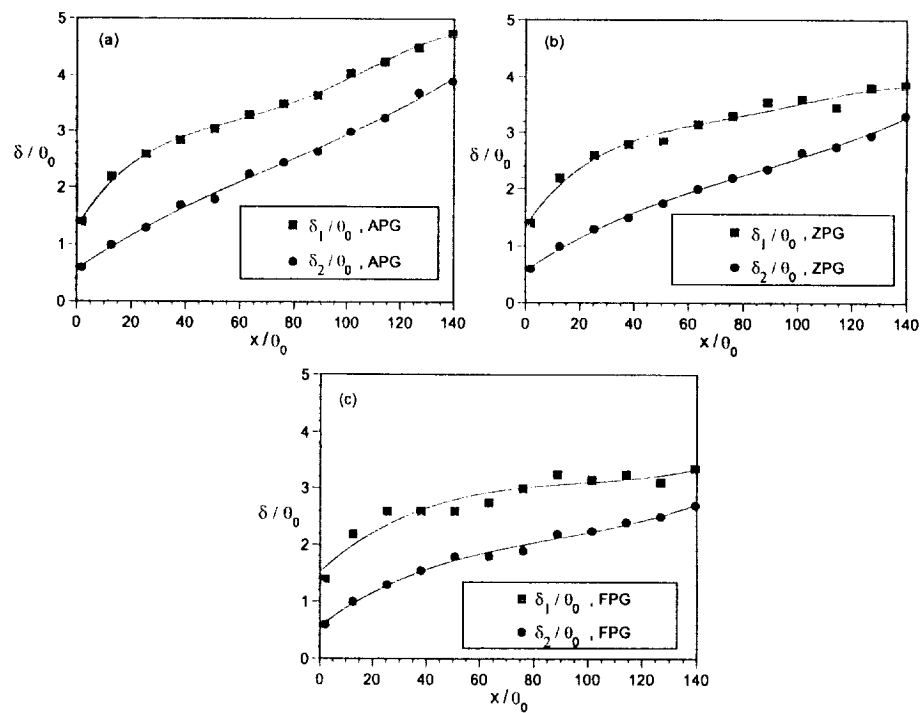


Figure 4.9. Streamwise Evolution of the Wake Half-Width in the Lower and Upper Shear Layer of the Asymmetric Wake in APG, ZPG and FPG.

#### 4.4.5 Lateral Drift of the Asymmetric Wake Profile

Another distinguishing feature of the asymmetric wake development is the lateral drift of the center of the wake to its thicker side, as mentioned earlier in Section 4.4.1. Figure 4.10 shows the lateral drift of the center of the asymmetric wake in adverse, zero and favorable pressure gradients. The ordinate of the plot is the physical  $y$  location of the center of the wake in the laboratory coordinate system. Shown also in this figure are the locations of the centers of the symmetric wake as a basis for a direct comparison. Again in this figure, solid data points represent the asymmetric wake cases and the blank data points represent the symmetric wake cases. Theoretically, for the symmetric wake, the location of the center of wake should be zero. In Figure 4.10, the deviation of the  $y$  location of the center of the symmetric wake can be viewed as an experimental error of the whole measurement system. With this observation, it can be seen that for all pressure gradient cases investigated, the lateral drift of the center of the asymmetric wake is far beyond the experimental error which means the drift is real and significant. As mentioned before, the drift of the center of the asymmetric wake is toward its thick side (the lower layer side).

Actually, not only the center of the wake, but also the whole asymmetric wake profile drifts to its thick side when the asymmetric wake develops downstream. To illustrate this global trend, Figure 4.11 shows the streamwise evolution of the physical lateral locations of the center of the wake (denoted as  $y_0$ ), the  $50\%U_d$  in the lower shear layer (denoted as  $y_1$ ) and the  $50\%U_d$  in the upper shear layer (denoted as  $y_2$ ) for the asymmetric wake in adverse, zero and favorable pressure gradients. The streamwise evolution of the three characteristic locations of the asymmetric wake roughly demonstrates the global movement of the asymmetric wake structure during the development of the asymmetric wake in pressure gradients. From Figure 4.11,

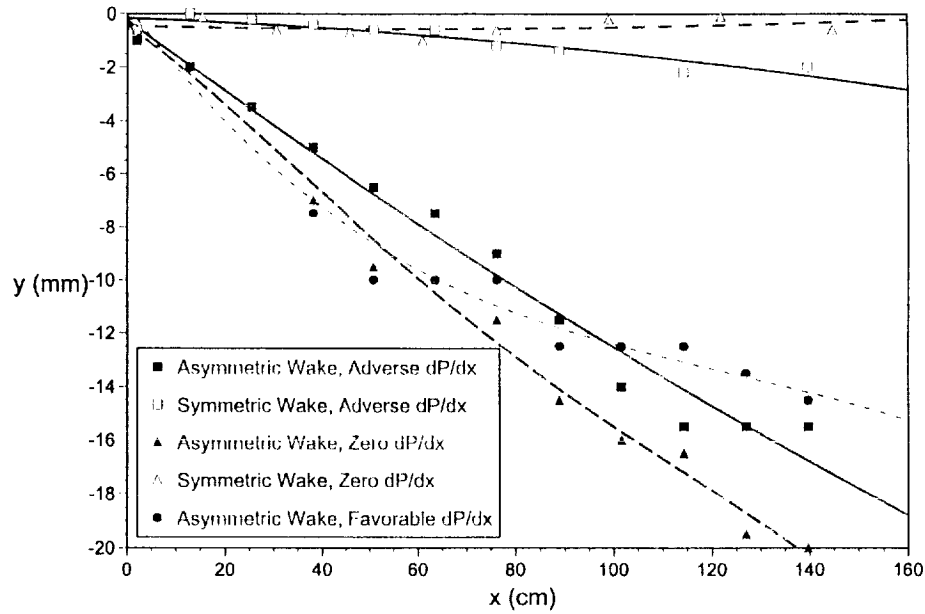


Figure 4.10. Lateral Drift of the Center of the Asymmetric Wake.

it can be seen that, for all pressure gradients investigated, the whole asymmetric wake profile is gradually turning to its thicker side. The lateral maneuver of the asymmetric wake is solely due to the movement of the structure with the wake itself rather than any external effect such as the tunnel wall contour. The tunnel wall contour for the asymmetric wake is set up to the symmetric positions with respect to the centerline of the the tunnel. Hence any asymmetric lateral movement of the asymmetric wake is solely due to the asymmetric wake itself.

#### 4.4.6 Maximum Turbulence Intensity

Wake asymmetry also has an effect on the turbulence field. For example, Figure 4.12 shows the streamwise evolution of the maximum turbulence intensity (located in the thicker layer side of the wake) of the asymmetric wake. To facilitate comparison, the streamwise evolution of the maximum turbulence intensity of the symmetric wake

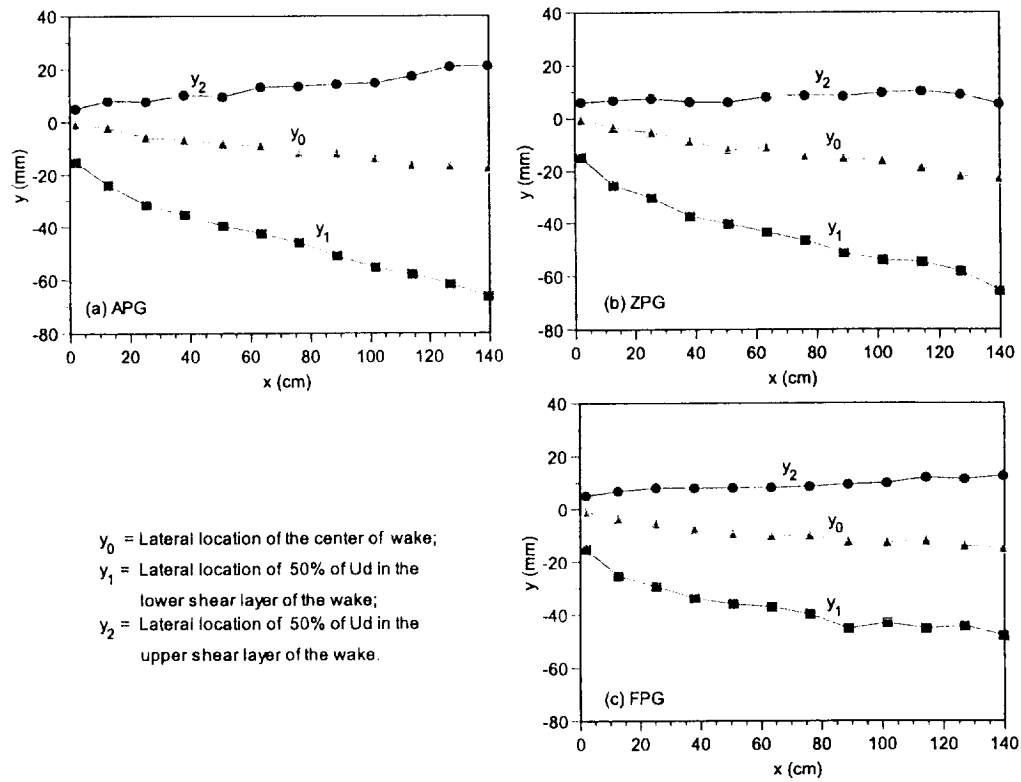


Figure 4.11. Lateral Drift of the Entire Asymmetric Wake Represented by the Streamwise Evolution of the Three Characteristic Locations in the Wake.

is also shown in this figure. The abscissa is scaled by the initial wake momentum thickness. Unlike the wake asymmetry effect on the mean flow characteristics, the wake asymmetry on the turbulence field seems much more complicated. It seems that, from Figure 4.12, the maximum turbulence intensity is augmented for the adverse pressure gradient case and reduced for the zero and favorable pressure gradient cases.

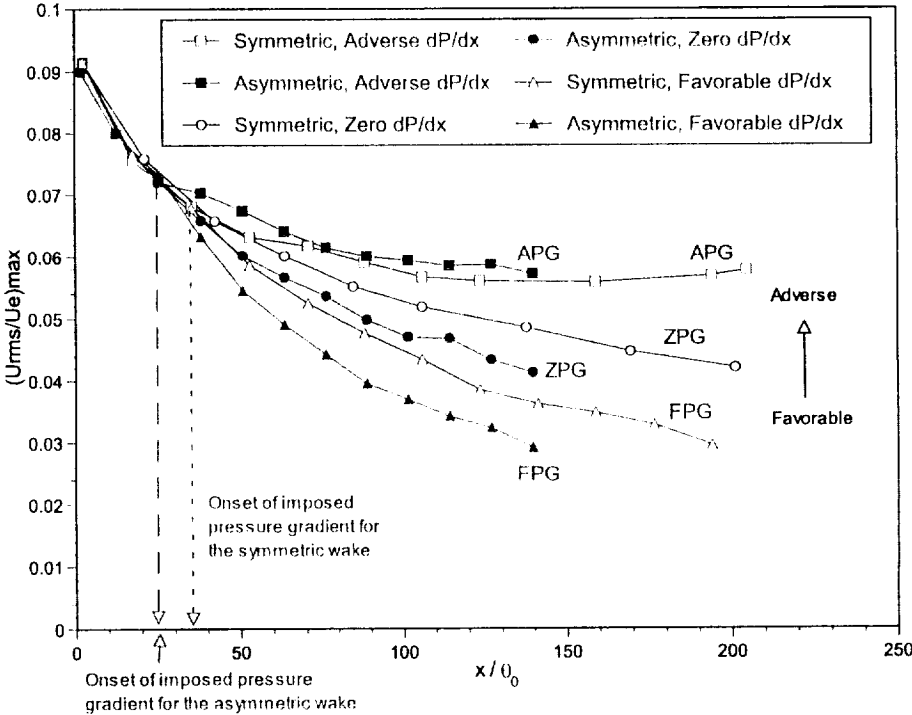


Figure 4.12. Streamwise Evolution of the Maximum Turbulence Intensity for the Symmetric and Asymmetric Wakes in Adverse, Zero and Favorable Pressure Gradients.

#### 4.4.7 Discussion

From the above results showing the effects of the wake asymmetry and pressure gradient on the wake flow, it seems that the effect of the wake asymmetry and the

effect of the pressure gradient are roughly independent with each other for the wake mean flow characteristics. This suggests that these two effects are probably based on two different type of mechanism affecting the mean flow field. The role that the wake asymmetry plays in the turbulence field is not as distinguishable as that in the mean flow field and still needs further investigation. The distinguished behavior of the effects of the wake asymmetry and the pressure gradient on the wake mean flow might find an explanation from the the thin shear layer type of the Reynolds Averaged Navier-Stokes (RANS) equation (Equation 3.5). The pressure gradient has its own term  $U_e \frac{dU_e}{dx}$  in the RANS equation. The wake asymmetry, representing the asymmetry of the mean shear in the upper and lower shear layers of the wake *per se*, is related to the Reynolds stress term  $\frac{\partial \overline{u'v'}}{\partial y}$ . The two terms are not coupled in the RANS equation (Equation 3.5) so that we can see distinguished behavior of the effects of the wake asymmetry and the pressure gradient on the wake mean flow development. However, for the turbulence field, the wake asymmetry and the pressure gradient are coupled in the production term (see Equation 5.6). This might be the reason why the effect of wake asymmetry on the turbulence field is not as distinguishable as that on the mean flow field.

#### 4.5 Comparison of Numerical and Experimental Results

Like the symmetric wake case, numerical simulation was also conducted for the asymmetric wake flow subjected to the same experimental adverse, zero and favorable pressure gradients using the Spalart-Allmaras one-equation and the Wilcox (1998)  $k - \omega$  two-equation models. Due to its poor performance for the symmetric wake flow simulation, the Cebeci-Smith algebraic model was not used for this asymmetric wake flow simulation. The numerical code developed by Brooks (1999) was modified to improve simulation results. For a brief introduction of the numerical modelling, see Section 3.8.1.

Unlike the symmetric wake flow simulation, both Spalart-Allmaras and Wilcox (1998)  $k - \omega$  models confront difficulties in the simulation of the asymmetric wake flow in the adverse pressure gradient. In fact, the Wilcox (1998)  $k - \omega$  model even fails in faithfully simulating the wake mean flow for all APG, ZPG and FPG cases. For example, Figures 4.13, 4.14 and 4.15 present the comparisons of the experimental and the numerical results on the wake mean velocity profile at the last measurement station ( $x = 140 \text{ cm}$ ) of the asymmetric wake flow in favorable, zero and adverse pressure gradients, respectively. These three plots clearly show that the Wilcox (1998)  $k - \omega$  model overestimates the asymmetric wake maximum velocity defect for all three pressure gradient cases. In addition, from these three figures it can also be seen that although the performance of the Spalart-Allmaras model is quite satisfactory for the favorable and zero pressure gradient cases, it overestimates the wake mean profile for the adverse pressure gradient case.

To investigate the performance of both Spalart-Allmaras and Wilcox (1998)  $k - \omega$  models in predicting the global characteristics of the asymmetric wake flow development, Figures 4.16, 4.17 and 4.18 present comparisons of the numerical and experimental results on the streamwise evolution of the wake width and the maximum velocity defect of the asymmetric wake flow in FPG, ZPG and APG, respectively. From these two figures, it can be seen that the Spalart-Allmaras model predicts the wake growth rate and the maximum velocity defect decay quite accurately for the FPG and ZPG cases. However, the Spalart-Allmaras model overestimates both wake width and the maximum velocity defect for the APG case at the downstream locations. As for the Wilcox (1998)  $k - \omega$  model, it overestimates the maximum velocity defect for both ZPG and APG cases and underestimate the wake width for the FPG and APG cases.

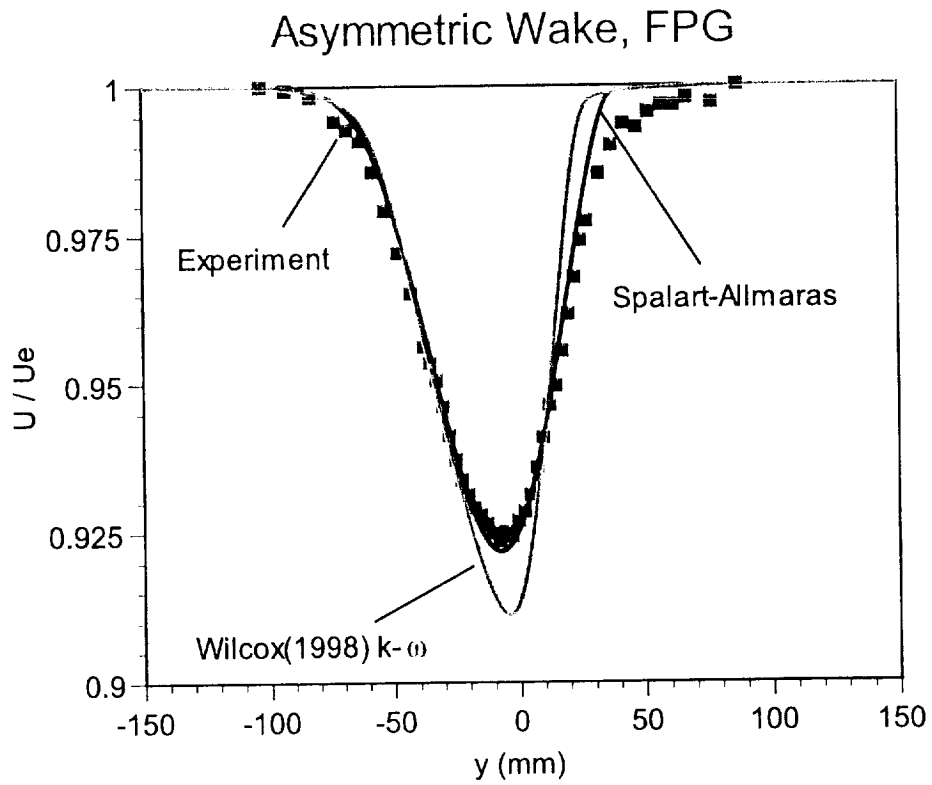


Figure 4.13. Comparison of the Numerical and Experimental Mean Velocity Profiles for the Asymmetric Wake in FPG at  $x = 140$  cm.

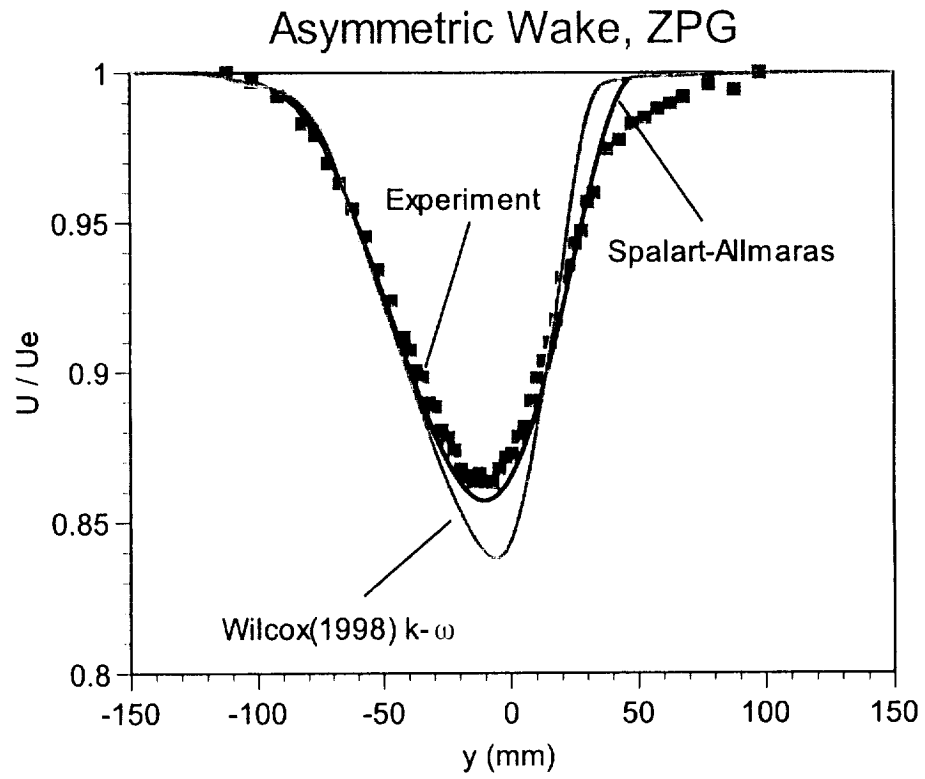


Figure 4.14. Comparison of the Numerical and Experimental Mean Velocity Profiles for the Asymmetric Wake in ZPG at  $x = 140$  cm.

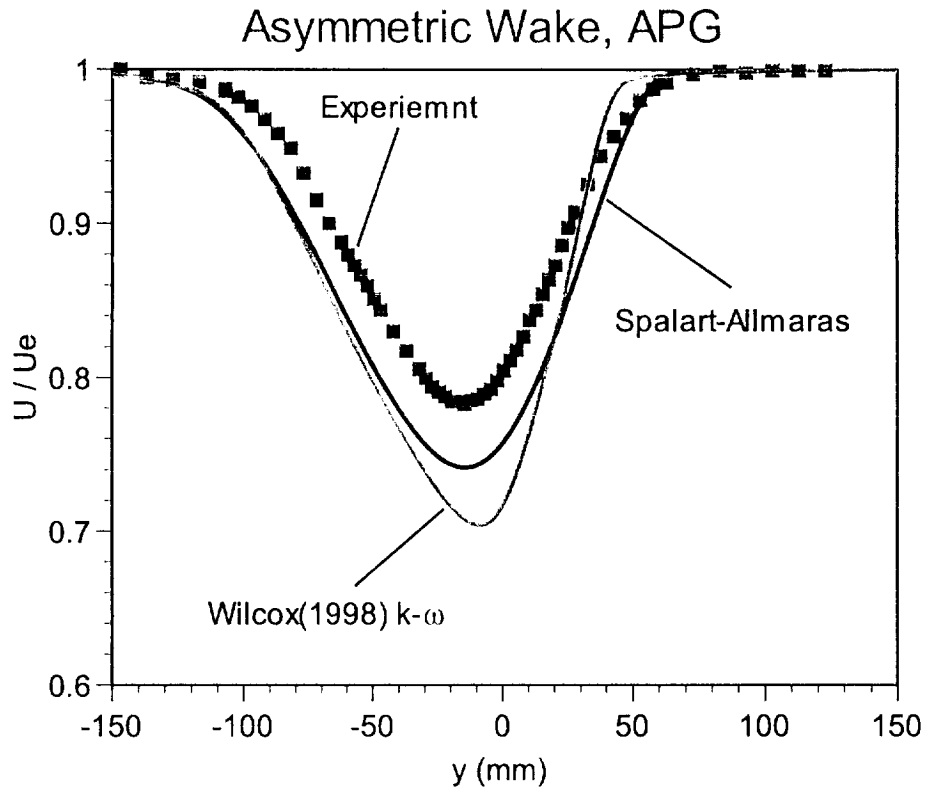


Figure 4.15. Comparison of the Numerical and Experimental Mean Velocity Profiles for the Asymmetric Wake in APG at  $x = 140 \text{ cm}$ .

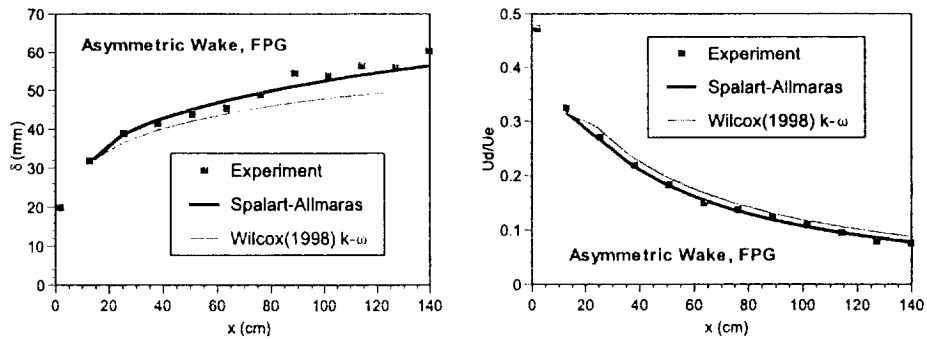


Figure 4.16. Comparison of the Numerical and Experimental Results on the Streamwise Evolution of the Wake Width and Maximum Velocity Defect of the Asymmetric Wake in FPG.

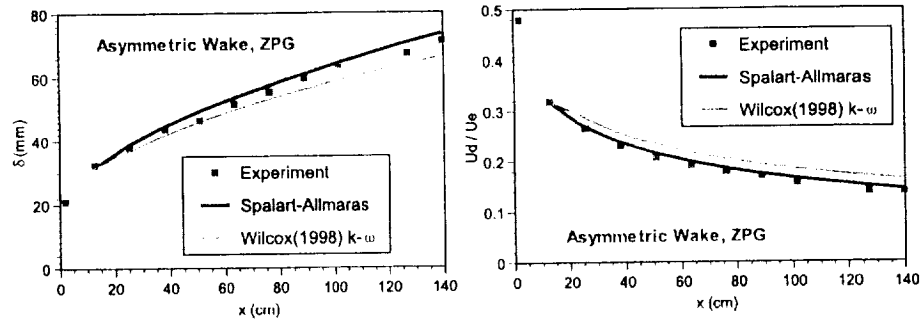


Figure 4.17. Comparison of the Numerical and Experimental Results on the Stream-wise Evolution of the Wake Width and Maximum Velocity Defect of the Asymmetric Wake in ZPG.

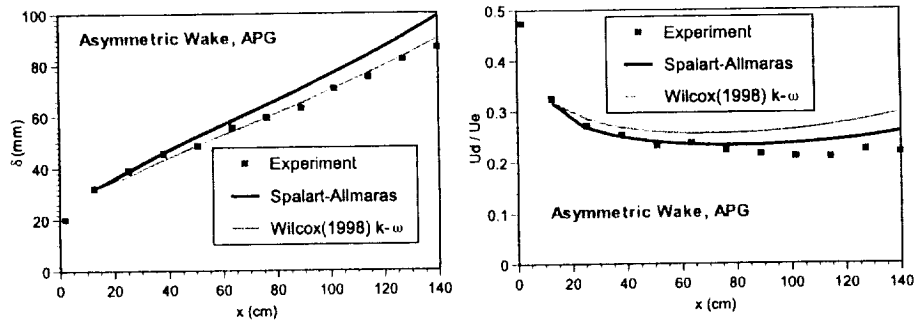


Figure 4.18. Comparison of the Numerical and Experimental Results on the Stream-wise Evolution of the Wake Width and Maximum Velocity Defect of the Asymmetric Wake in APG.

In fact, the performance of the Wilcox (1998)  $k - \omega$  model can be improved by adjusting the constants within the model. Figure 4.19 presents the comparison of the numerical and experimental results on the asymmetric wake mean velocity profile at two different streamwise stations before and after the adjustment of the the Wilcox (1998)  $k - \omega$  model. Obviously, the performance of the Wilcox (1998)  $k - \omega$  model can be significantly improved after the adjustment of the constants, as shown in Figure 4.19.

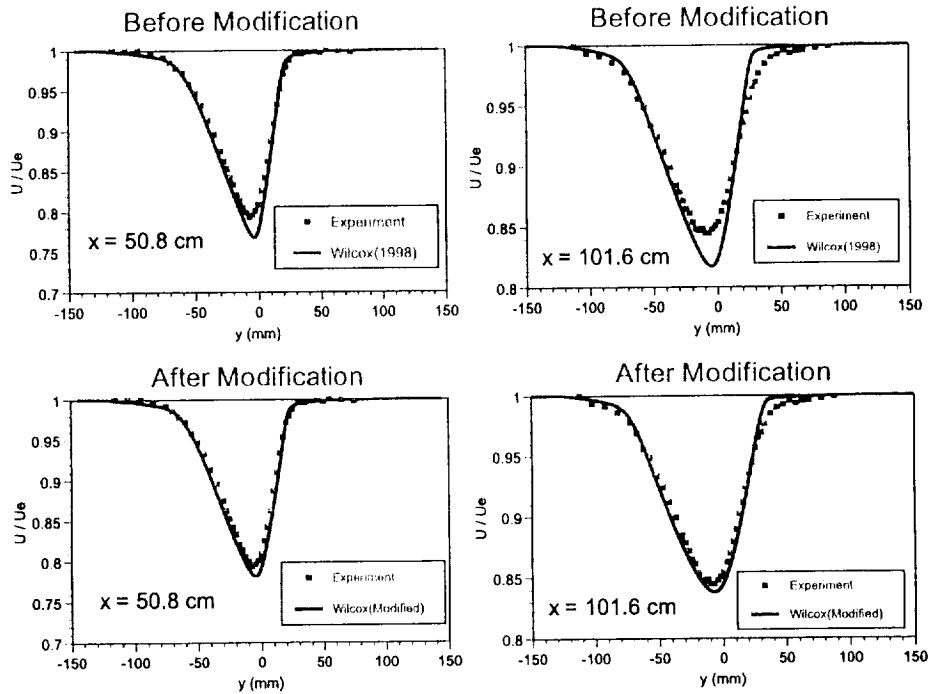


Figure 4.19. Comparison of the Numerical and Experimental Results on the Asymmetric Wake Mean Velocity Profile at Two Different Streamwise stations Before and After the Adjustment of the Wilcox (1998)  $k - \omega$  Model.

## CHAPTER 5

### TURBULENT KINETIC ENERGY BUDGET MEASUREMENT FOR THE SYMMETRIC WAKE

#### 5.1 Motivation and Objectives for the Turbulent Kinetic Energy Budget Measurement

By the conclusion of the conventional wake flow field survey, a detailed database documenting the development of both initially symmetric and asymmetric wakes in zero, constant favorable and adverse pressure gradients had been completed. The extensive experimental database clearly shows the strong effects of pressure gradient and wake asymmetry on the near wake development. Numerical simulations of this wake flow conducted at NASA Langley (Carlson *et al.*, 2001) and at Notre Dame (Brooks, 1999; Liu *et al.*, 1999b) show that the existing turbulent models can capture the global wake development behavior such as wake widening and maximum velocity defect decay rate within a reasonable level of agreement. However, the numerical simulation results also show that there is still room for the turbulence model to be improved.

As a natural consequence of the previous wake investigation, detailed examination of the turbulent kinetic energy budget for the wake flow can greatly facilitate understanding of the observed effects of pressure and wake asymmetry on the wake flow development. In addition, the measurement of the turbulent kinetic energy budget for the wake flow in pressure gradient will be of interest in the development

of more realistic turbulence models for turbulent flow. In brief, the TKE budget measurement of the wake study will fulfill the following research objectives:

- To understand the mechanism of the turbulence kinetic energy transport within the near wake flow;
- To investigate the influence of the pressure gradient on the turbulent kinetic energy transport and to provide an explanation for the observed effects of pressure gradient and wake asymmetry on the wake flow development;
- To provide experimental evidence for possible modification of turbulence model and/or the motivation for new approaches to numerically simulating the wake flow.

## 5.2 Transport Equation of the Turbulent Kinetic Energy

The TKE budget measurement scheme is motivated by previous attempts to characterize the turbulent kinetic energy budget in free shear flows, in particular, Wygnanski and Fiedler (1969), Gutmark and Wygnanski (1976), Panchapakesan and Lumley<sup>1</sup> (1993), George and Hussein (1991), Hussein, Capp and George (1994) and Heskestad (1965) in jet flows, Raffoul, Nejad and Gould (1995) and Browne, Antonia and Shah (1987) in bluff body wakes, Patel and Sarda (1990) in a ship wake, Faure and Robert (1969) in the wake of a self-propelled body, Wygnanski and Fiedler (1970) in a planar mixing layer, Zhou, Heine and Wygnanski (1996) in a plane wall jet in a round jet. Before introducing the TKE budget measurement scheme, it is necessary to first discuss the TKE transport equations in the following paragraphs.

From Hinze (1975, p.72, Equation 1-110), the turbulent kinetic energy equation can be written as

$$\begin{aligned}
\frac{D}{Dt} \left( \frac{\overline{q^2}}{2} \right) &= \underbrace{-\frac{\partial}{\partial x_i} \overline{u'_i \left( \frac{p'}{\rho} + \frac{q^2}{2} \right)}}_{\text{I}} - \underbrace{\overline{u'_i u'_j} \frac{\partial \overline{U}_j}{\partial x_i}}_{\text{II}} + \underbrace{\nu \frac{\partial}{\partial x_i} \overline{u'_j \left( \frac{\partial u'_i}{\partial x_j} + \frac{\partial u'_j}{\partial x_i} \right)}}_{\text{IV}} \\
&\quad - \underbrace{\nu \left( \frac{\partial u'_i}{\partial x_j} + \frac{u'_j}{\partial x_i} \right) \frac{\partial u'_j}{\partial x_i}}_{\text{V}} \tag{5.1}
\end{aligned}$$

where  $u'_i$  is the turbulent fluctuating velocity component,  $p'$  is the fluctuating pressure, and  $\frac{1}{2}\overline{q^2} \equiv \frac{1}{2}\overline{u'_i u'_i} = k$  is the turbulent kinetic energy per unit mass. Term I on the left hand side of Equation (5.1) represents the convection of turbulent kinetic energy along mean flow stream lines. Term II represents the transport of turbulent kinetic energy by both the turbulent velocity fluctuations themselves and by pressure fluctuations. Term III represents turbulent kinetic energy production by the Reynolds stress working against the mean strain rate. Term IV represents viscous diffusion of turbulence. Term V represents the viscous dissipation of turbulent kinetic energy into heat.

For incompressible, homogeneous turbulent flow, the turbulent kinetic energy equation takes the form (Hinze 1975, p.74, Equation 1-111),

$$\begin{aligned}
\frac{D}{Dt} \left( \frac{\overline{q^2}}{2} \right) &= \underbrace{-\frac{\partial}{\partial x_i} \overline{u'_i \left( \frac{p'}{\rho} + \frac{q^2}{2} \right)}}_{\text{I}} - \underbrace{\overline{u'_i u'_j} \frac{\partial \overline{U}_j}{\partial x_i}}_{\text{II}} + \underbrace{\frac{\nu}{2} \frac{\partial^2 \overline{q^2}}{\partial x_i \partial x_i}}_{\text{IV}} - \underbrace{\nu \frac{\partial u'_j}{\partial x_i} \frac{\partial u'_j}{\partial x_i}}_{\text{V}} \tag{5.2}
\end{aligned}$$

where Terms I, II and III are the same as those in Equation (5.1), whereas Terms IV and V take different forms of their counterparts in Equation (5.1). For free shear flows, unlike turbulent boundary layer flow near the wall, there is no spacial dramatic changes for the quantity  $\overline{q^2}$ . Hence, Term IV, the viscous diffusion term,

is usually negligible compared to other terms <sup>1</sup>. Therefore, the only accountable difference between Equations (5.1) and (5.2) for free shear flows is the last term, i.e., the dissipation term.

We will denote the streamwise, lateral and spanwise spatial coordinates as  $x_1$ ,  $x_2$  and  $x_3$ , respectively. Later on, the spatial coordinates  $x_1$ ,  $x_2$  and  $x_3$ , the velocity components  $U_1$ ,  $U_2$  and  $U_3$  and the fluctuating velocity components  $u'_1$ ,  $u'_2$  and  $u'_3$  will be represented by  $x$ ,  $y$ ,  $z$ ,  $U$ ,  $V$ ,  $W$ ,  $u$ ,  $v$  and  $w$  respectively for convenience.

Expansion of the dissipation term in equation (5.1) gives

$$\begin{aligned} \epsilon_{inhomo} = \nu & \left[ 2 \overline{\left( \frac{\partial u'_1}{\partial x_1} \right)^2} + \overline{\left( \frac{\partial u'_2}{\partial x_1} \right)^2} + \overline{\left( \frac{\partial u'_3}{\partial x_1} \right)^2} + \overline{\left( \frac{\partial u'_1}{\partial x_2} \right)^2} + 2 \overline{\left( \frac{\partial u'_2}{\partial x_2} \right)^2} + \overline{\left( \frac{\partial u'_3}{\partial x_2} \right)^2} \right. \\ & + \overline{\left( \frac{\partial u'_1}{\partial x_3} \right)^2} + \overline{\left( \frac{\partial u'_2}{\partial x_3} \right)^2} + 2 \overline{\left( \frac{\partial u'_3}{\partial x_3} \right)^2} + 2 \overline{\left( \frac{\partial u'_1}{\partial x_2} \right) \left( \frac{\partial u'_2}{\partial x_1} \right)} \\ & \left. + 2 \overline{\left( \frac{\partial u'_1}{\partial x_3} \right) \left( \frac{\partial u'_3}{\partial x_1} \right)} + 2 \overline{\left( \frac{\partial u'_2}{\partial x_3} \right) \left( \frac{\partial u'_3}{\partial x_2} \right)} \right] \end{aligned} \quad (5.3)$$

Similarly, expansion of the dissipation term in equation (2) gives

$$\begin{aligned} \epsilon_{homo} = \nu & \left[ \overline{\left( \frac{\partial u'_1}{\partial x_1} \right)^2} + \overline{\left( \frac{\partial u'_2}{\partial x_1} \right)^2} + \overline{\left( \frac{\partial u'_3}{\partial x_1} \right)^2} + \overline{\left( \frac{\partial u'_1}{\partial x_2} \right)^2} + \overline{\left( \frac{\partial u'_2}{\partial x_2} \right)^2} + \overline{\left( \frac{\partial u'_3}{\partial x_2} \right)^2} \right. \\ & \left. + \overline{\left( \frac{\partial u'_1}{\partial x_3} \right)^2} + \overline{\left( \frac{\partial u'_2}{\partial x_3} \right)^2} + \overline{\left( \frac{\partial u'_3}{\partial x_3} \right)^2} \right] \end{aligned} \quad (5.4)$$

---

<sup>1</sup>The neglect of the viscous diffusion term is verified from the flow field survey data. For example, based on the experimental data, a typical value of the second derivative of the turbulence kinetic energy  $\frac{\partial^2 k}{\partial x^2}$  for the wake flow investigated here is approximately on the order of  $1.0 \text{ s}^{-2}$ , which leads to a value of the viscous diffusion term on the order of  $1.0 \times 10^{-5} \text{ m}^2/\text{s}^3$ . In other words, this means that the magnitude of the viscous diffusion term is only about  $1.0 \times 10^{-7}$  times of the peak value of the dissipation term.

As we know, strictly speaking, the wake flow is not a homogeneous turbulence flow and therefore, Equation (5.3), the inhomogeneous expression for dissipation should be utilized for the the estimate of the dissipation in turbulent wake flow. However, to date, no one has been able to successfully measure the cross derivative correlation terms in the inhomogeneous form of the dissipation as listed in Equation (5.3), though there was an attempt by Browne, Antonia and Shah (1987). As all previous reported efforts for the direct measurement of the dissipation term, in our study, we will first make a concession and only consider Equation (5.2), the incompressible homogeneous turbulence kinetic energy equation. Later on, we will discuss how to correct the possible bias error due to the homogenous assumption (See Section 5.10 for details.).

With the aforementioned notations, Equation (5.2) can be expanded as,

$$\begin{aligned}
& \frac{\partial}{\partial t} \left( \frac{\overline{q^2}}{2} \right) + \overline{U_1} \frac{\partial}{\partial x_1} \left( \frac{\overline{q^2}}{2} \right) + \overline{U_2} \frac{\partial}{\partial x_2} \left( \frac{\overline{q^2}}{2} \right) + \overline{U_3} \frac{\partial}{\partial x_3} \left( \frac{\overline{q^2}}{2} \right) = \\
& - \frac{\partial}{\partial x_1} \overline{u'_1 \frac{p'}{\rho}} - \frac{\partial}{\partial x_2} \overline{u'_2 \frac{p'}{\rho}} - \frac{\partial}{\partial x_3} \overline{u'_3 \frac{p'}{\rho}} - \frac{\partial}{\partial x_1} \overline{\frac{1}{2} (u_1'^3 + u_1' u_2'^2 + u_1' u_3'^2)} \\
& - \frac{\partial}{\partial x_2} \overline{\frac{1}{2} (u_1'^2 u_2' + u_2'^3 + u_2' u_3'^2)} - \frac{\partial}{\partial x_3} \overline{\frac{1}{2} (u_1'^2 u_3' + u_2'^2 u_3' + u_3'^3)} \\
& - \overline{u_1'^2} \frac{\partial \overline{U_1}}{\partial x_1} - \overline{u_1' u_2'} \frac{\partial \overline{U_2}}{\partial x_1} - \overline{u_1' u_3'} \frac{\partial \overline{U_3}}{\partial x_1} - \overline{u_1' u_2'} \frac{\partial \overline{U_1}}{\partial x_2} \\
& - \overline{u_2'^2} \frac{\partial \overline{U_2}}{\partial x_2} - \overline{u_2' u_3'} \frac{\partial \overline{U_3}}{\partial x_2} - \overline{u_1' u_3'} \frac{\partial \overline{U_1}}{\partial x_3} - \overline{u_2' u_3'} \frac{\partial \overline{U_2}}{\partial x_3} - \overline{u_3'^2} \frac{\partial \overline{U_3}}{\partial x_3} \\
& + \frac{\nu}{2} \frac{\partial^2 \overline{q^2}}{\partial x_1^2} + \frac{\nu}{2} \frac{\partial^2 \overline{q^2}}{\partial x_2^2} + \frac{\nu}{2} \frac{\partial^2 \overline{q^2}}{\partial x_3^2} \\
& - \nu \left[ \left( \frac{\partial u_1'}{\partial x_1} \right)^2 + \left( \frac{\partial u_1'}{\partial x_2} \right)^2 + \left( \frac{\partial u_1'}{\partial x_3} \right)^2 + \left( \frac{\partial u_2'}{\partial x_1} \right)^2 \right]
\end{aligned}$$

$$+ \left[ \overline{\left(\frac{\partial u'_2}{\partial x_2}\right)^2} + \overline{\left(\frac{\partial u'_2}{\partial x_3}\right)^2} + \overline{\left(\frac{\partial u'_3}{\partial x_1}\right)^2} + \overline{\left(\frac{\partial u'_3}{\partial x_2}\right)^2} + \overline{\left(\frac{\partial u'_3}{\partial x_3}\right)^2} \right] \quad (5.5)$$

For steady, 2-D flow in the mean, we have  $\frac{\partial}{\partial t}(\bar{\quad}) = 0$ ,  $\bar{U}_3 = 0$  and  $\frac{\partial}{\partial x_3}(\bar{\quad}) = 0$ . Also we have, from the continuity equation,  $\frac{\partial \bar{U}_2}{\partial x_2} = -\frac{\partial \bar{U}_1}{\partial x_1}$ . Thus, the turbulent kinetic energy equation can be simplified as follows:

$$\begin{aligned} & \underbrace{\bar{U}_1 \frac{\partial}{\partial x_1} \left( \frac{\overline{q^2}}{2} \right)}_{\text{Convection}} + \underbrace{\bar{U}_2 \frac{\partial}{\partial x_2} \left( \frac{\overline{q^2}}{2} \right)}_{\text{Convection}} = \underbrace{-\frac{\partial}{\partial x_1} \overline{u'_1 p'}}_{\text{Pressure Diffusion}} - \underbrace{\frac{\partial}{\partial x_2} \overline{u'_2 p'}}_{\text{Pressure Diffusion}} \\ & - \underbrace{\frac{\partial}{\partial x_1} \frac{1}{2} \overline{(u_1^3 + u'_1 u_2^2 + u'_1 u_3^2)}}_{\text{Turbulence Diffusion}} - \underbrace{\frac{\partial}{\partial x_2} \frac{1}{2} \overline{(u_1^2 u_2 + u_2^3 + u'_2 u_3^2)}}_{\text{Turbulence Diffusion}} \\ & - \underbrace{\left( \overline{u_1^2} - \overline{u_2^2} \right) \frac{\partial \bar{U}_1}{\partial x_1}}_{\text{Production}} - \underbrace{\overline{u'_1 u'_2} \left( \frac{\partial \bar{U}_1}{\partial x_2} + \frac{\partial \bar{U}_2}{\partial x_1} \right)}_{\text{Production}} + \underbrace{\frac{\nu}{2} \frac{\partial^2 \overline{q^2}}{\partial x_1^2}}_{\text{Viscous Diffusion}} + \underbrace{\frac{\nu}{2} \frac{\partial^2 \overline{q^2}}{\partial x_2^2}}_{\text{Viscous Diffusion}} \\ & - \nu \left[ \overline{\left( \frac{\partial u'_1}{\partial x_1} \right)^2} + \overline{\left( \frac{\partial u'_1}{\partial x_2} \right)^2} + \overline{\left( \frac{\partial u'_1}{\partial x_3} \right)^2} + \overline{\left( \frac{\partial u'_2}{\partial x_1} \right)^2} \right. \\ & \left. + \overline{\left( \frac{\partial u'_2}{\partial x_2} \right)^2} + \overline{\left( \frac{\partial u'_2}{\partial x_3} \right)^2} + \overline{\left( \frac{\partial u'_3}{\partial x_1} \right)^2} + \overline{\left( \frac{\partial u'_3}{\partial x_2} \right)^2} + \overline{\left( \frac{\partial u'_3}{\partial x_3} \right)^2} \right] \quad (5.6) \\ & \text{Dissipation} \end{aligned}$$

A primary effort for this Ph.D. research is to successfully measure the individual terms in the above 2-D simplified incompressible homogeneous TKE transport equation.

### 5.3 Approaches for the Measurement of the Turbulent Kinetic Energy Budget

The procedure used for the experimental estimate of each term in turbulent kinetic energy balance will be outlined below.

### 5.3.1 Convection Terms

According to the literature, the convection terms are usually obtained from direct measurement. In this wake study, this term will be obtained by use of an X-wire probe. In particular, the streamwise spatial derivative  $\frac{\partial}{\partial x_1}(\overline{q^2})$  will be evaluated from the measurement of  $\overline{q^2}$  at three adjacent streamwise measurement stations. The lateral spatial derivative  $\frac{\partial}{\partial x_2}(\overline{q^2})$  will be obtained from lateral survey data.

### 5.3.2 Pressure Diffusion Terms

This term is not directly measurable. In the jet studies by Wygnanski and Fiedler (1969) and Gutmark and Wygnanski (1976), this term was inferred from the balance of the turbulent kinetic energy equation. In a more recent axisymmetric jet study by Panchapakesan and Lumley (1993), the pressure transport term was simply neglected. In a cylinder wake study by Browne, Antonia and Shah (1987), they demonstrated that the pressure transport term obtained by forcing a balance of the turbulent kinetic energy equation approximates to zero. In the measurement for a jet flow conducted by Hussein, Capp and George(1994), they ignored the term  $\overline{\left(\frac{u'p'}{\rho}\right)}$  and attempted to estimate  $\overline{\left(\frac{u_2'p'}{\rho}\right)}$  by integrating the difference of the so-called "transport dissipation" and the "homogeneous dissipation". In this study, this term will be inferred from the forced balance of the turbulent kinetic energy equation.

### 5.3.3 Turbulence Diffusion Terms

An X-wire probe can be used to obtain  $\overline{u_1'^3}$ ,  $\overline{u_1'u_2'^2}$ ,  $\overline{u_1'u_3'^2}$ ,  $\overline{u_1'^2u_2'}$  and  $\overline{u_1'^3}$  by direct measurement. The remaining term  $\overline{u_2'u_3'^2}$  can be obtained indirectly from additional X-wire measurements through application of a procedure developed by Townsend (1949) and described by Wygnanski and Fiedler (1969). Alternately, both Panchapakesan and Lumley (1993) and Hussein, Capp and George (1994) simply assumed

that  $\overline{u'_2 u'_3{}^2} \approx \overline{u'_3{}^3}$  for their jet flow measurements, and asserted that the error introduced by this assumption is less than 10%. In this study, we will also use the X-wire measurement to obtain the turbulence diffusion term with the assumption that  $\overline{u'_2 u'_3{}^2} \approx \overline{u'_3{}^3}$ .

#### 5.3.4 Production Terms

The shear and dilatational production terms have already been measured in the conventional flow field survey of the wake study for both symmetric and asymmetric wakes using an Aerometrics LDV system in two-component coincidence mode. These experiments show that, despite the streamwise pressure gradients imposed, the wake is shear dominated. That is,  $-(\overline{u_1'^2} - \overline{u_2'^2}) \frac{\partial \overline{U_1}}{\partial x_1} \ll -\overline{u_1' u_2'} \left( \frac{\partial \overline{U_1}}{\partial x_2} + \frac{\partial \overline{U_2}}{\partial x_1} \right)$  in each case. For this study, these terms will be measured again by using the X-wire probe in order to ensure repeatability.

#### 5.3.5 Viscous Diffusion Terms

All previously cited investigations of turbulent kinetic energy budget in free shear flows have ignored the viscous diffusion terms. Wygnanski and Fiedler (1969) and Gutmark and Wygnanski (1976) claim the neglect of these terms was based on the assertion of Laufer (1954) that these types of terms are comparatively small in the turbulent kinetic energy equation. Panchapakesan and Lumley (1993) explained that in free turbulent flows, away from walls, the viscous contribution to the transport terms are negligible in comparison with the turbulent contribution. In high Reynolds number free shear flows, like the wake studied here, the viscous diffusion is expected to be negligible.

#### 5.3.6 Dissipation Terms

The viscous dissipation terms could be handled in one of the following five ways, according to the literature.

1) Isotropic Turbulence Assumption: If it is assumed that viscous dissipation takes place at the smallest scales of motion which may be approximated as locally isotropic, then the viscous dissipation term simplifies to,

$$\epsilon = 15\nu \overline{\left(\frac{\partial u'_1}{\partial x_1}\right)^2} \quad (5.7)$$

The fluctuating spatial derivative can be obtained by invoking the Taylor's frozen field hypothesis

$$\frac{\partial}{\partial x} \approx -\frac{1}{\overline{U_1}} \frac{\partial}{\partial t} \quad (5.8)$$

This was the technique employed by Gutmark and Wygnanski (1976) for their jet flow measurement.

2) Locally Axisymmetric Homogeneous Turbulence Assumption: This is an approach proposed by George and Hussein (1991). They demonstrated that as long as the time averaged derivatives in the dissipation term (3) satisfy the following conditions for the so-called locally axisymmetric homogeneous turbulence,

$$\overline{\left(\frac{\partial u'_1}{\partial x_2}\right)^2} = \overline{\left(\frac{\partial u'_1}{\partial x_3}\right)^2} \quad (5.9)$$

$$\overline{\left(\frac{\partial u'_2}{\partial x_1}\right)^2} = \overline{\left(\frac{\partial u'_3}{\partial x_1}\right)^2} \quad (5.10)$$

$$\overline{\left(\frac{\partial u'_2}{\partial x_2}\right)^2} = \overline{\left(\frac{\partial u'_3}{\partial x_3}\right)^2} \quad (5.11)$$

$$\overline{\left(\frac{\partial u'_2}{\partial x_3}\right)^2} = \overline{\left(\frac{\partial u'_3}{\partial x_2}\right)^2} \quad (5.12)$$

$$\overline{\left(\frac{\partial u'_2}{\partial x_2}\right)^2} = \frac{1}{3} \overline{\left(\frac{\partial u'_1}{\partial x_1}\right)^2} + \frac{1}{3} \overline{\left(\frac{\partial u'_2}{\partial x_3}\right)^2} \quad (5.13)$$

$$\overline{\left(\frac{\partial u'_2}{\partial x_3}\right) \left(\frac{\partial u'_3}{\partial x_2}\right)} = \frac{1}{6} \overline{\left(\frac{\partial u'_1}{\partial x_1}\right)^2} - \frac{1}{3} \overline{\left(\frac{\partial u'_2}{\partial x_3}\right)^2} \quad (5.14)$$

$$\overline{\left(\frac{\partial u'_1}{\partial x_2}\right) \left(\frac{\partial u'_2}{\partial x_1}\right)} = \overline{\left(\frac{\partial u'_1}{\partial x_3}\right) \left(\frac{\partial u'_3}{\partial x_1}\right)} = -\frac{1}{2} \overline{\left(\frac{\partial u'_1}{\partial x_1}\right)^2} \quad (5.15)$$

then the dissipation term can be estimated from either

$$\epsilon = \nu \left[ \frac{5}{3} \overline{\left(\frac{\partial u'_1}{\partial x_1}\right)^2} + 2 \overline{\left(\frac{\partial u'_1}{\partial x_3}\right)^2} + 2 \overline{\left(\frac{\partial u'_2}{\partial x_1}\right)^2} + \frac{8}{3} \overline{\left(\frac{\partial u'_2}{\partial x_3}\right)^2} \right] \quad (5.16)$$

or

$$\epsilon = \nu \left[ -\overline{\left(\frac{\partial u'_1}{\partial x_1}\right)^2} + 2 \overline{\left(\frac{\partial u'_1}{\partial x_2}\right)^2} + 2 \overline{\left(\frac{\partial u'_2}{\partial x_1}\right)^2} + 8 \overline{\left(\frac{\partial u'_2}{\partial x_2}\right)^2} \right] \quad (5.17)$$

In Equation (5.16), the  $\overline{\left(\frac{\partial u'_1}{\partial x_1}\right)^2}$  and the  $\overline{\left(\frac{\partial u'_1}{\partial x_3}\right)^2}$  terms can be obtained from the parallel probe measurement while the  $\overline{\left(\frac{\partial u'_2}{\partial x_1}\right)^2}$  term can be obtained from an X-wire measurement. The estimate of the  $\overline{\left(\frac{\partial u'_2}{\partial x_3}\right)^2}$  term requires a twin X-wire probe configuration, which will be discussed in details in Section 3.4 and 4.2.4.2.

3) Semi-Isotropic Turbulence Assumption: This is an approach for the estimate of unmeasured or immeasurable fluctuating velocity derivatives in the homogeneous dissipation term based on measured fluctuating velocity derivatives. For example, the streamwise derivatives  $\overline{\left(\frac{\partial u'_1}{\partial x_1}\right)^2}$ ,  $\overline{\left(\frac{\partial u'_2}{\partial x_1}\right)^2}$  and  $\overline{\left(\frac{\partial u'_3}{\partial x_1}\right)^2}$  can be each estimated by invoking the Taylor's hypothesis as described above. The lateral and spanwise derivatives,  $\overline{\left(\frac{\partial u'_1}{\partial x_2}\right)^2}$  and  $\overline{\left(\frac{\partial u'_1}{\partial x_3}\right)^2}$  can be obtained by a closely spaced parallel hot-wire probes. The four remaining derivatives  $\overline{\left(\frac{\partial u'_2}{\partial x_2}\right)^2}$ ,  $\overline{\left(\frac{\partial u'_2}{\partial x_3}\right)^2}$ ,  $\overline{\left(\frac{\partial u'_3}{\partial x_2}\right)^2}$  and  $\overline{\left(\frac{\partial u'_3}{\partial x_3}\right)^2}$  in the dissipation term can be subsequently estimated by invoking a semi-isotropy assumption, as described in Wygnanski and Fiedler (1969) for their jet flow mea-

surement, which assumes the nine spatial derivatives in the dissipation term observe the following semi-isotropy relationship:

$$\begin{aligned}
k_s \overline{\left(\frac{\partial u'_1}{\partial x_1}\right)^2} &= \overline{\left(\frac{\partial u'_2}{\partial x_1}\right)^2} = \overline{\left(\frac{\partial u'_3}{\partial x_1}\right)^2} \\
\overline{\left(\frac{\partial u'_1}{\partial x_2}\right)^2} &= k_s \overline{\left(\frac{\partial u'_2}{\partial x_2}\right)^2} = \overline{\left(\frac{\partial u'_3}{\partial x_2}\right)^2} \\
\overline{\left(\frac{\partial u'_1}{\partial x_3}\right)^2} &= \overline{\left(\frac{\partial u'_2}{\partial x_3}\right)^2} = k_s \overline{\left(\frac{\partial u'_3}{\partial x_3}\right)^2}
\end{aligned} \tag{5.18}$$

where  $k_s$  is the semi-isotropy coefficient. In this study, the coefficient  $k_s$  will be determined from the streamwise mean square derivative measurements, which will be described in details in Section 4.

4) Direct Measurement of All Nine Terms: The most sophisticated method is to measure all nine terms that make up the total dissipation by use of two X-wires as described by Browne, Antonia and Shah (1987) for their cylinder wake study. Their study indicated that the local isotropy assumption is not valid for a cylinder wake in the self-preserving region with relatively low Reynolds number. Keep in mind that it is the local isotropy assumption that forms the basis of the first method mentioned above for evaluating the dissipation terms. It should be very interesting to verify the local isotropy assumption for the wake development in pressure gradients at high Reynolds number. In this study, we will not use this approach to measure the dissipation term, since the spatial resolution of the twin X-wire probe configuration is too large to get a reliable dissipation measurement.

5) Forced Balance of the TKE Equation: Finally, the easiest way to evaluate the dissipation terms might be forcing a balance of the turbulent kinetic energy equation,

provided that the pressure transport terms are negligible. This was the approach taken by Panchapakesan and Lumley (1993).

In the wake study here, the dissipation term will be estimated by using all of the above except the fourth approaches. The results will then be compared and reviewed in the context of the TKE balance.

#### 5.4 TKE Budget Measurement Scheme

To obtain the streamwise derivatives that are essential for the TKE budget estimate, we need to conduct lateral traverse at three consecutive streamwise measurement stations. The spatial derivatives can then be estimated as finite differences of the data taken at these streamwise separated nodal points. For example, suppose we want to estimate the TKE budget at station  $i$ , as shown in Figure 5.1, we need to conduct the lateral traverse not only at station  $i$ , but also at stations  $i + 1$  and  $i - 1$  as well. More specifically, to estimate the TKE budget at station  $i$ , we need a total of eight different traverses at stations  $i$ ,  $i - 1$  and  $i + 1$ , respectively. The quantities measured during each traverse are outlined below.

- Traverse I: At station  $i$ , conduct the lateral traverse of the twin X-wire configuration to get  $\overline{U_1}$ ,  $\overline{U_2}$ ,  $\overline{u_1'^2}$ ,  $\overline{u_2'^2}$ ,  $\overline{u_1'^3}$ ,  $\overline{u_1'u_2'^2}$ ,  $\overline{u_1'^2u_2'}$ ,  $\overline{\left(\frac{\partial u_1'}{\partial x_3}\right)^2}$ ,  $\overline{\left(\frac{\partial u_2'}{\partial x_3}\right)^2}$ ,  $\overline{\left(\frac{\partial u_1'}{\partial x_1}\right)^2}_A$ ,  $\overline{\left(\frac{\partial u_2'}{\partial x_1}\right)^2}_A$ ,  $\overline{\left(\frac{\partial u_1'}{\partial x_1}\right)^2}_B$  and  $\overline{\left(\frac{\partial u_2'}{\partial x_1}\right)^2}_B$ , where the subscription  $A$  and  $B$  denote the quantity obtained by X-wire A and B of the twin. The orientation of the twin X-wire at this traverse is equivalent to the one specified in Figure 1(d) of Browne, Antonia and Shah (1987).
- Traverse II: At station  $i$ , rotate the twin X-wire configuration and conduct the lateral traverse to get  $\overline{U_1}$ ,  $\overline{U_3}$ ,  $\overline{u_1'^2}$ ,  $\overline{u_3'^2}$ ,  $\overline{u_1'^3}$ ,  $\overline{u_1'u_3'^2}$ ,  $\overline{\left(\frac{\partial u_1'}{\partial x_2}\right)^2}$ ,  $\overline{\left(\frac{\partial u_3'}{\partial x_2}\right)^2}$ ,  $\overline{\left(\frac{\partial u_1'}{\partial x_1}\right)^2}_A$ ,  $\overline{\left(\frac{\partial u_3'}{\partial x_1}\right)^2}_A$ ,  $\overline{\left(\frac{\partial u_1'}{\partial x_1}\right)^2}_B$  and  $\overline{\left(\frac{\partial u_3'}{\partial x_1}\right)^2}_B$ , The orientation of the twin X-wire at this

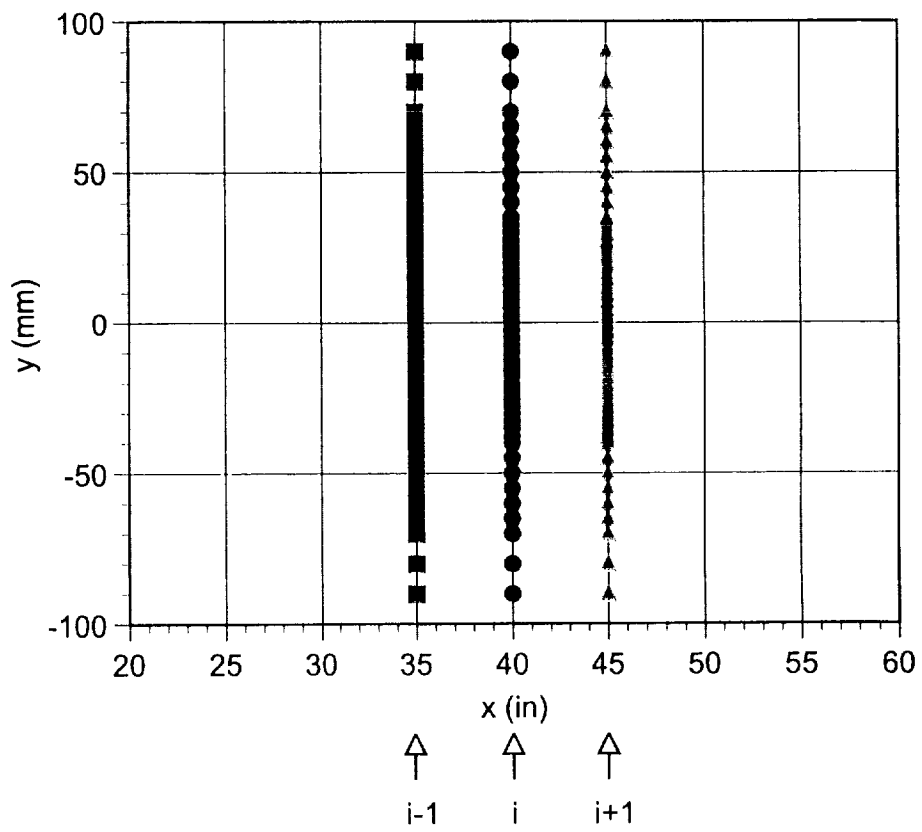


Figure 5.1. Schematic of Measuring Nodal Points.

traverse is equivalent to the one specified in Figure 1(b) of Browne, Antonia and Shah (1987).

- Traverse III: At station  $i$ , conduct the parallel probe lateral traverse to get  $\overline{\left(\frac{\partial u'_1}{\partial x_2}\right)^2}$ ,  $\overline{\left(\frac{\partial u'_1}{\partial x_1}\right)^2}_A$  and  $\overline{\left(\frac{\partial u'_1}{\partial x_1}\right)^2}_B$ .
- Traverse IV: At station  $i$ , rotate the parallel probe and conduct the lateral traverse to get  $\overline{\left(\frac{\partial u'_1}{\partial x_3}\right)^2}$ ,  $\overline{\left(\frac{\partial u'_1}{\partial x_1}\right)^2}_A$  and  $\overline{\left(\frac{\partial u'_1}{\partial x_1}\right)^2}_B$ .
- Traverse V: At station  $i + 1$  ( $\Delta x = 5in$ ), conduct the lateral traverse of the single X-wire to get  $\overline{U_1}$ ,  $\overline{U_2}$ ,  $\overline{u_1'^2}$ ,  $\overline{u_2'^2}$ ,  $\overline{u_1'^3}$ ,  $\overline{u_1' u_2'^2}$ ,  $\overline{u_1'^2 u_2'}$ .
- Traverse VI: At station  $i + 1$  ( $\Delta x = 5in$ ), rotate the single X-wire and conduct the lateral traverse to get  $\overline{U_1}$ ,  $\overline{U_3}$ ,  $\overline{u_1'^2}$ ,  $\overline{u_3'^2}$ ,  $\overline{u_1'^3}$ ,  $\overline{u_1' u_3'^2}$ .
- Traverse VII: At station  $i - 1$  ( $\Delta x = 5in$ ), conduct the lateral traverse of the single X-wire to get  $\overline{U_1}$ ,  $\overline{U_2}$ ,  $\overline{u_1'^2}$ ,  $\overline{u_2'^2}$ ,  $\overline{u_1'^3}$ ,  $\overline{u_1' u_2'^2}$ ,  $\overline{u_1'^2 u_2'}$ .
- Traverse VIII: At station  $i - 1$  ( $\Delta x = 5in$ ), rotate the single X-wire and conduct the lateral traverse to get  $\overline{U_1}$ ,  $\overline{U_3}$ ,  $\overline{u_1'^2}$ ,  $\overline{u_3'^2}$ ,  $\overline{u_1'^3}$ ,  $\overline{u_1' u_3'^2}$ .

The convection terms of the TKE budget can be estimated from the data taken at Traverses I and II. The turbulence diffusion terms from Traverses I, II, V, VI, VII and VIII. The production terms from the data taken at Traverses I, V and VII. The dissipation terms from Traverses I, II, III and IV. Appropriate piece-wise curve-fitting methods were used in order to obtain a smooth curve for the estimation of derivatives.

## 5.5 Turbulent Kinetic Energy Budget in Zero Pressure Gradient

To facilitate the interpretation of the TKE budget measurement result, we move the convection term  $\overline{U_1} \frac{\partial}{\partial x_1} \left( \frac{q^2}{2} \right) + \overline{U_2} \frac{\partial}{\partial x_2} \left( \frac{q^2}{2} \right)$  in Equation (5.6) to the right hand side of the equation so that the TKE conservation equation reads

$$\begin{aligned}
0 = & -\overline{U_1} \frac{\partial}{\partial x_1} \left( \frac{q^2}{2} \right) - \overline{U_2} \frac{\partial}{\partial x_2} \left( \frac{q^2}{2} \right) - \frac{\partial}{\partial x_1} \overline{u'_1 p'} - \frac{\partial}{\partial x_2} \overline{u'_2 p'} \\
& \text{Convection} \qquad \qquad \qquad \text{Pressure Diffusion} \\
& - \frac{\partial}{\partial x_1} \overline{\frac{1}{2} (u_1'^3 + u_1' u_2'^2 + u_1' u_3'^2)} - \frac{\partial}{\partial x_2} \overline{\frac{1}{2} (u_1'^2 u_2' + u_2'^3 + u_2' u_3'^2)} \\
& \text{Turbulence Diffusion} \\
& - \left( \overline{u_1'^2} - \overline{u_2'^2} \right) \frac{\partial \overline{U_1}}{\partial x_1} - \overline{u_1' u_2'} \left( \frac{\partial \overline{U_1}}{\partial x_2} + \frac{\partial \overline{U_2}}{\partial x_1} \right) + \frac{\nu}{2} \frac{\partial^2 \overline{q^2}}{\partial x_1^2} + \frac{\nu}{2} \frac{\partial^2 \overline{q^2}}{\partial x_2^2} \\
& \text{Production} \qquad \qquad \qquad \text{Viscous Diffusion} \\
& - \nu \left[ \overline{\left( \frac{\partial u_1'}{\partial x_1} \right)^2} + \overline{\left( \frac{\partial u_1'}{\partial x_2} \right)^2} + \overline{\left( \frac{\partial u_1'}{\partial x_3} \right)^2} + \overline{\left( \frac{\partial u_2'}{\partial x_1} \right)^2} \right. \\
& \left. + \overline{\left( \frac{\partial u_2'}{\partial x_2} \right)^2} + \overline{\left( \frac{\partial u_2'}{\partial x_3} \right)^2} + \overline{\left( \frac{\partial u_3'}{\partial x_1} \right)^2} + \overline{\left( \frac{\partial u_3'}{\partial x_2} \right)^2} + \overline{\left( \frac{\partial u_3'}{\partial x_3} \right)^2} \right] \tag{5.19} \\
& \text{Dissipation}
\end{aligned}$$

In the following discussions, the term convection will refer to the one in Equation (5.19).

### 5.5.1 Convection Term

The convection term  $-\overline{U_1} \frac{\partial}{\partial x_1} \left( \frac{q^2}{2} \right) - \overline{U_2} \frac{\partial}{\partial x_2} \left( \frac{q^2}{2} \right)$  consists of two parts, the streamwise convection  $-\overline{U_1} \frac{\partial}{\partial x_1} \left( \frac{q^2}{2} \right)$  and the lateral convection  $-\overline{U_2} \frac{\partial}{\partial x_2} \left( \frac{q^2}{2} \right)$ . These terms can be measured directly. The lateral distribution of these two terms for the symmetric

wake at ZPG at  $x/\theta_0 = 141$  is presented in Figure 5.2. In this figure the convection terms are non-dimensionalized by using the local wake half-width  $\delta$  as the reference length scale and the local maximum velocity defect  $U_d$  as the reference velocity scale. From this figure, it can be seen that for the symmetric wake in ZPG, the streamwise convection dominates in the total convection distribution.

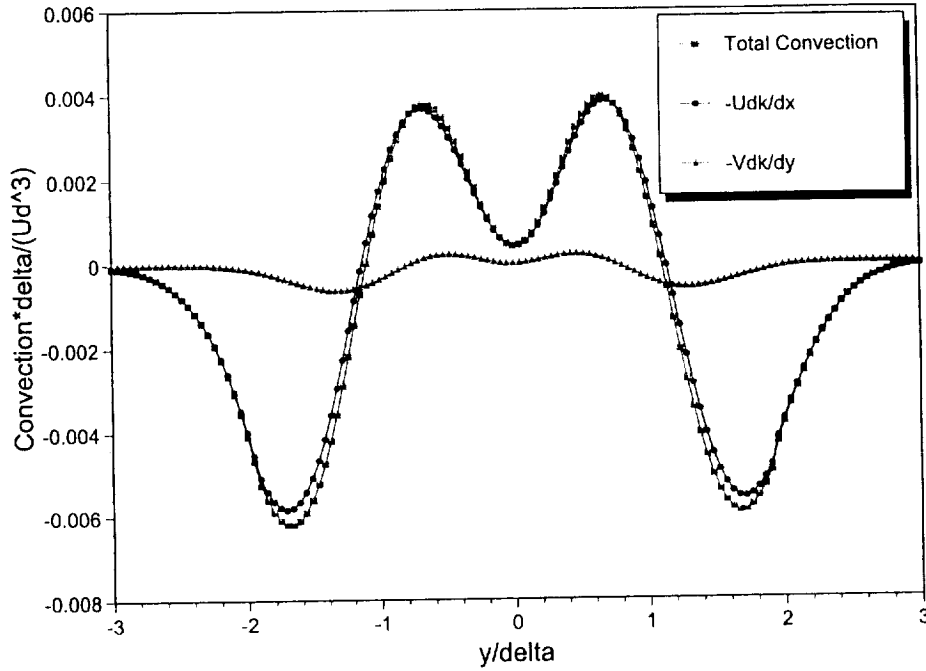


Figure 5.2. Convection Term of Symmetric Wake in ZPG at  $x/\theta_0 = 141$ .

### 5.5.2 Production Term

The turbulence production term  $-\left(\overline{u_1'^2} - \overline{u_2'^2}\right) \frac{\partial \overline{U_1}}{\partial x_1} - \overline{u_1' u_2'} \left(\frac{\partial \overline{U_1}}{\partial x_2} + \frac{\partial \overline{U_2}}{\partial x_1}\right)$  consists of two parts; the shear production term  $-\overline{u_1' u_2'} \left(\frac{\partial \overline{U_1}}{\partial x_2} + \frac{\partial \overline{U_2}}{\partial x_1}\right)$  and the dilatational production term  $-\left(\overline{u_1'^2} - \overline{u_2'^2}\right) \frac{\partial \overline{U_1}}{\partial x_1}$ . These terms are measured directly. Figure 5.3 compares these production terms for the symmetric wake at ZPG at  $x/\theta_0 = 141$ . This figure clearly shows that the wake flow at zero pressure gradient is shear dominated and the

dilatational production is approximately zero, just as expected. In fact, for the wake flow at zero pressure gradient,  $-\left(\overline{u_1'^2} - \overline{u_2'^2}\right) \frac{\partial \overline{U_1}}{\partial x_1} - \overline{u_1' u_2'} \left(\frac{\partial \overline{U_1}}{\partial x_2} + \frac{\partial \overline{U_2}}{\partial x_1}\right) \approx -\overline{u_1' u_2'} \frac{\partial \overline{U_1}}{\partial x_2}$  since  $\frac{\partial \overline{U_1}}{\partial x_1} \approx 0$  and  $\frac{\partial \overline{U_2}}{\partial x_1} \approx 0$ . The same result was obtained during the flow field survey of the symmetric wake by using LDV, as presented in the Liu *et al.*(1999a).

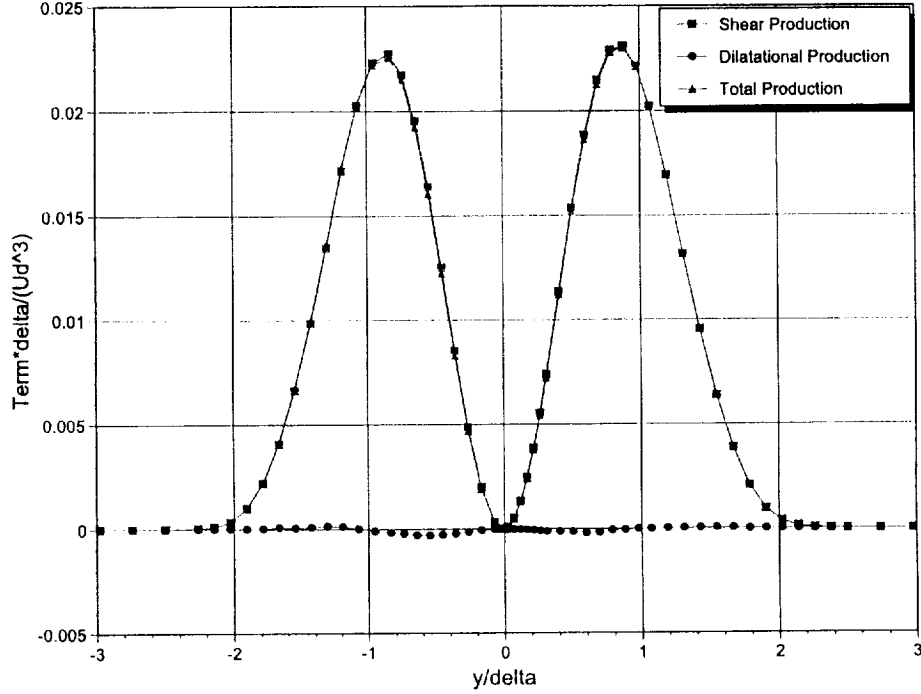


Figure 5.3. Production Term of Symmetric Wake in ZPG at  $x/\theta_0 = 141$ .

### 5.5.3 Turbulence Diffusion Term

The turbulent diffusion term  $-\frac{\partial}{\partial x_1} \frac{1}{2} \left( \overline{u_1^3 + u_1' u_2'^2 + u_1' u_3'^2} \right) - \frac{\partial}{\partial x_2} \frac{1}{2} \left( \overline{u_1'^2 u_2' + u_2'^3 + u_2' u_3'^2} \right)$  is composed of two parts, the streamwise turbulent diffusion  $-\frac{\partial}{\partial x_1} \frac{1}{2} \left( \overline{u_1^3 + u_1' u_2'^2 + u_1' u_3'^2} \right)$  and the lateral turbulent diffusion  $-\frac{\partial}{\partial x_2} \frac{1}{2} \left( \overline{u_1'^2 u_2' + u_2'^3 + u_2' u_3'^2} \right)$ . Figure 5.4 shows the profile of these diffusion terms for the symmetric wake at ZPG at  $x/\theta_0 = 141$ . It can be seen that obviously, for the wake at zero pressure gradient, the lateral turbulent diffusion is the dominant turbulent diffusion mechanism and the streamwise

turbulent diffusion is negligible. To verify the accuracy of the measurement of the diffusion term, the profile of the total turbulent diffusion term is integrated along the lateral direction across wake. The integration result is essentially zero, as one would expect, since lateral diffusion serves only to redistribute turbulent kinetic energy. This result can also be viewed as an indication of the accuracy of the diffusion term measurement.

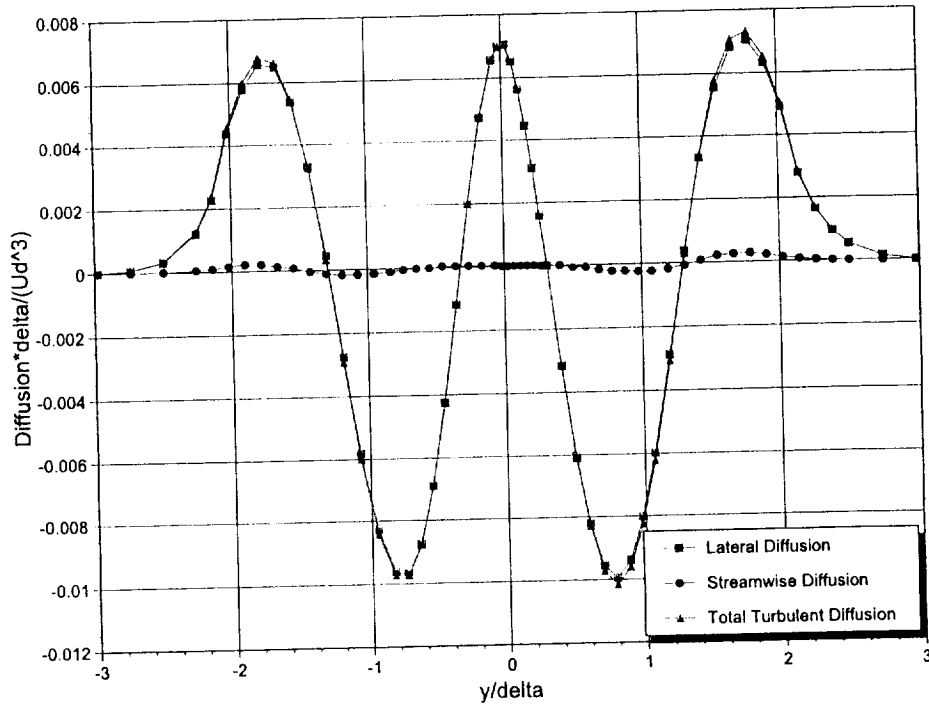


Figure 5.4. Turbulence Diffusion Term of Symmetric Wake in ZPG at  $x/\theta_0 = 141$ .

#### 5.5.4 Dissipation Terms

Following the TKE measurement scheme outlined in Section 5.4, we were able to obtain a comprehensive set of data which allow us to estimate the dissipation term in four different approaches, namely, (a), the isotropic turbulence assumption approach, (b), the locally axisymmetric turbulence assumption approach, (c), the

semi-isotropic assumption approach and (d) the forced TKE balance approach, as described in Section 5.3. The methodology of these approaches and the corresponding results will be presented in the following subsections, respectively.

#### 5.5.4.1 Dissipation Based on Isotropic Turbulence Assumption

The approach based on the isotropic turbulence assumption requires the estimate of the mean square derivative term  $\overline{\left(\frac{\partial u'_1}{\partial x_1}\right)^2}$ , which can be obtained from data series measured in Traverse I, II, III and IV by invoking the Taylor's frozen field hypothesis  $\frac{\partial}{\partial x} \approx -\frac{1}{U_1} \frac{\partial}{\partial t}$ . All results obtained in Traverses I to IV using X-wire and parallel probes for the quantity  $\overline{\left(\frac{\partial u'_1}{\partial x_1}\right)^2}$  at ZPG are shown in Figure 5.5.

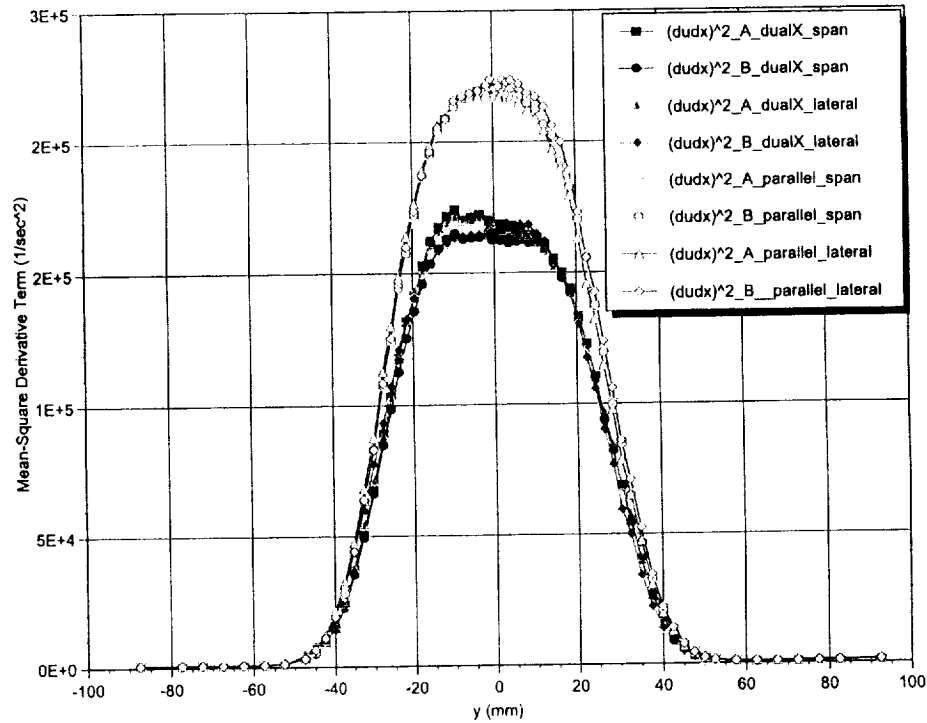


Figure 5.5. Comparison of  $\overline{\left(\frac{\partial u'_1}{\partial x_1}\right)^2}$  Measured by X-wire and Parallel Probes in ZPG at  $x/\theta_0 = 141$ .

From Figure 5.5, it can be seen that the parallel probe gives higher measurement values for the quantity  $\overline{\left(\frac{\partial u'_1}{\partial x_1}\right)^2}$  than the X-wire probe. This disparity can be attributed to the difference between the effective sensing length of the wires on the parallel and the X-wire probes. The length of the sensors on the parallel probe is only 0.9 mm while the distance between the tip of the X-wire prongs is about 1.2 mm. According to Wallace and Foss (1995), the sensing length of the probe is crucial for the measurement of the mean-square derivatives such as for the quantity  $\overline{\left(\frac{\partial u'_1}{\partial x_1}\right)^2}$ . Usually a longer wire gives rise to smaller magnitude of the mean-square derivative measurement due to spatial filtering, which is exactly the case in Figure 5.5. Thus the quantity  $\overline{\left(\frac{\partial u'_1}{\partial x_1}\right)^2}$  measured by using the parallel probe is likely to be closer to the true value of  $\overline{\left(\frac{\partial u'_1}{\partial x_1}\right)^2}$  compared to the X-wire measurement. This was one of the motivations for using the parallel probe results for the dissipation estimates. The dissipation estimate for the ZPG case based on the isotropic turbulence assumption is presented in Figure 5.6. This figure also presents dissipation estimates based on other approaches for direct comparison. The discussion of the comparison of the the dissipation estimate with different approaches can be found in Section 5.5.4.5.

#### 5.5.4.2 Dissipation Based on Locally Axisymmetric Turbulence Assumption

As described in Section 5.3, as long as the turbulence field satisfies the conditions set forth in Equations (5.9)-(5.15), the dissipation term can be estimated via the so-called locally axisymmetric turbulence assumption, which, as shown in Equation (5.16), requires the measurement of four mean-square derivatives  $\overline{\left(\frac{\partial u'_1}{\partial x_1}\right)^2}$ ,  $\overline{\left(\frac{\partial u'_1}{\partial x_3}\right)^2}$ ,  $\overline{\left(\frac{\partial u'_2}{\partial x_1}\right)^2}$  and  $\overline{\left(\frac{\partial u'_2}{\partial x_3}\right)^2}$ . The verification of the prerequisites for the application of the locally axisymmetric turbulence assumption will be discussed in Section 5.5.4.6. In

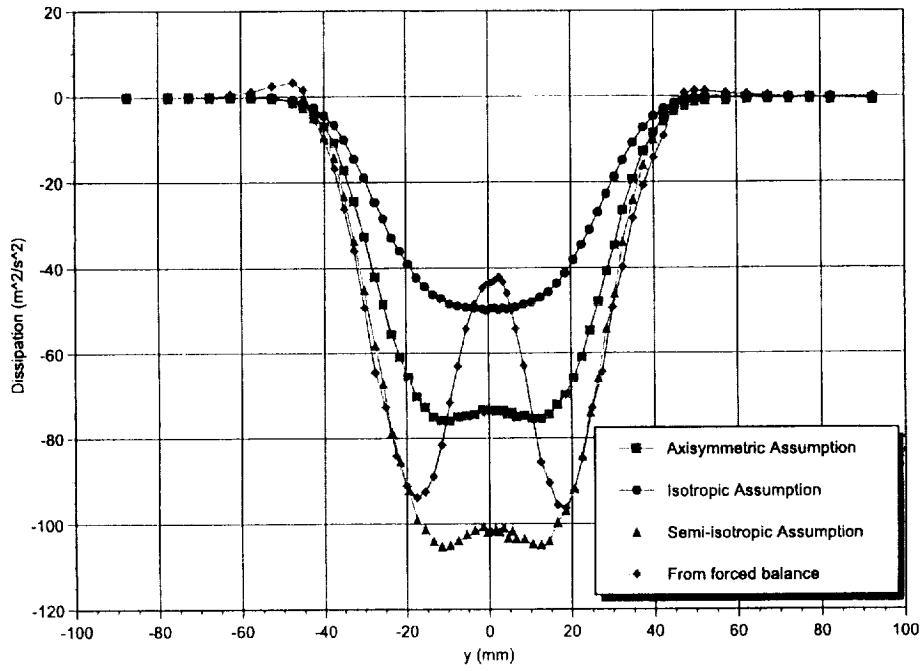


Figure 5.6. Comparison of Dissipation Estimate with Different Approaches for ZPG at  $x/\theta_0 = 141$ .

the following paragraphs, the methodology for the determination of the four mean-square derivatives will be discussed and the results will be presented.

First, the determination of the mean-square derivative  $\overline{\left(\frac{\partial u'_1}{\partial x_1}\right)^2}$  has been described in Section 5.5.4.1, and as in the isotropic assumption approach, this mean-square derivative is measured with the parallel probe.

Secondly, as described in Section 5.4, both Traverse I (twin X-wire configuration) and Traverse IV (parallel probe) can provide the mean-square derivative  $\overline{\left(\frac{\partial u'_1}{\partial x_3}\right)^2}$ . The comparison of the measured profile of the the mean-square derivative  $\overline{\left(\frac{\partial u'_1}{\partial x_3}\right)^2}$  by the twin X-wire configuration and the parallel probe is shown in Figure 5.7. Again, as was the case for  $\overline{\left(\frac{\partial u'_1}{\partial x_1}\right)^2}$  the measurement, the parallel probe yield a higher magnitude of the quantity. The much smaller magnitude of  $\overline{\left(\frac{\partial u'_1}{\partial x_3}\right)^2}$  measured by the twin X-wire configuration is primarily due to the poor spatial resolution of the twin X-wire configuration. Obviously, the mean-square derivative  $\overline{\left(\frac{\partial u'_1}{\partial x_3}\right)^2}$  measured by the parallel probe is closer to the true value and therefore is used for the dissipation estimate.

The mean-square derivative  $\overline{\left(\frac{\partial u'_2}{\partial x_1}\right)^2}$  can be obtained from an X-wire in Traverse I by invoking the Taylor's frozen field hypothesis. As is known from the discussion in Section 5.5.4.1, the quantity  $\overline{\left(\frac{\partial u'_1}{\partial x_1}\right)^2}$  obtained by the X-wire is smaller than its counterpart obtained by the parallel probe due to the relatively larger size of the X-wire probe. Similarly, it is reasonable to assume that the quantity  $\overline{\left(\frac{\partial u'_2}{\partial x_1}\right)^2}$  measured by the X-wire is also reduced in magnitude at the same rate as the quantity  $\overline{\left(\frac{\partial u'_1}{\partial x_1}\right)^2}$ , if compared with a parallel probe measurement. With this assumption, one can obtain a correction coefficient from Figure 5.5, which is nothing but the ratio between  $\overline{\left(\frac{\partial u'_1}{\partial x_1}\right)^2}_{parallelprobe}$  and  $\overline{\left(\frac{\partial u'_1}{\partial x_1}\right)^2}_{X-wire}$  and then apply this correction coefficient to  $\overline{\left(\frac{\partial u'_2}{\partial x_1}\right)^2}$  to improve the accuracy of the measurement. That is the method

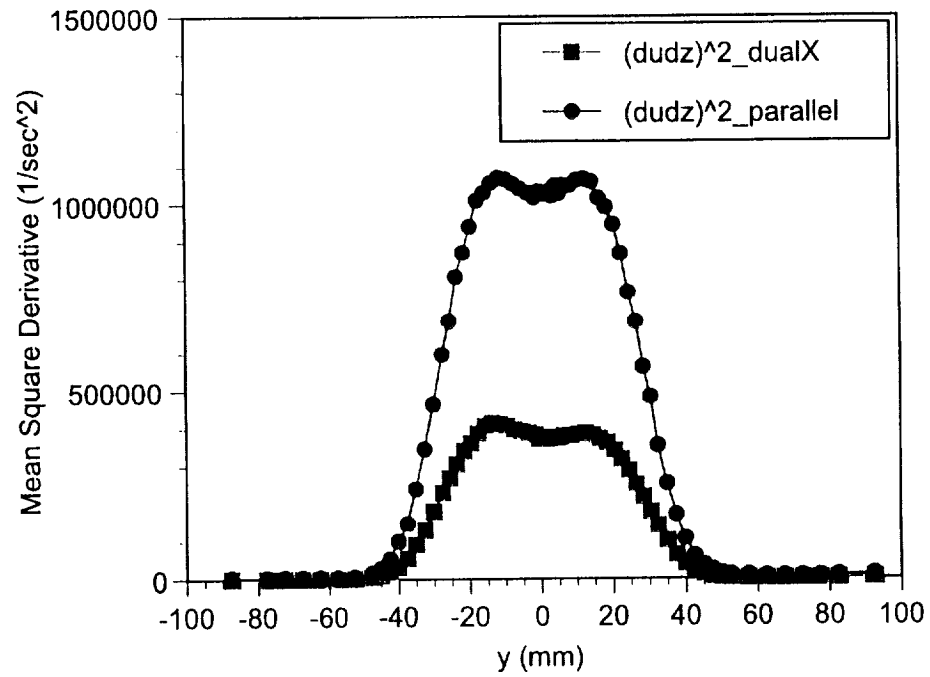


Figure 5.7. Comparison of  $\overline{\left(\frac{\partial u'_1}{\partial x_3}\right)^2}$  Measured by Twin X-wire and Parallel Probes in ZPG at  $x/\theta_0 = 141$ .

we used for the determination of the quantity  $\overline{\left(\frac{\partial u'_2}{\partial x_1}\right)^2}$ , which is involved in the final dissipation estimate.

The quantity  $\overline{\left(\frac{\partial u'_2}{\partial x_3}\right)^2}$  can only be obtained from the twin X-wire configuration measurement in Traverse I. In fact, as mentioned in Section 2.2.2, this twin X-wire configuration is primarily designed for the mean-square derivative  $\overline{\left(\frac{\partial u'_2}{\partial x_3}\right)^2}$  measurement. As was the case for the quantity  $\overline{\left(\frac{\partial u'_1}{\partial x_3}\right)^2}$  shown in Figure 5.7, it is reasonable to assume that the quantity  $\overline{\left(\frac{\partial u'_2}{\partial x_3}\right)^2}$  measured by the twin X-wire configuration is also reduced in magnitude at the same rate as the quantity  $\overline{\left(\frac{\partial u'_1}{\partial x_3}\right)^2}$ , if compared with a parallel probe measurement. With this assumption, we can obtain a correction coefficient from Figure 5.7, which is nothing but the ratio between  $\overline{\left(\frac{\partial u'_1}{\partial x_3}\right)^2}_{parallelprobe}$  and  $\overline{\left(\frac{\partial u'_1}{\partial x_3}\right)^2}_{twinX-wire}$  and then, apply this correction coefficient to  $\overline{\left(\frac{\partial u'_2}{\partial x_3}\right)^2}$  to improve the accuracy of the measurement, just like the treatment to  $\overline{\left(\frac{\partial u'_2}{\partial x_1}\right)^2}$  that we discussed in the above paragraph. The quantity  $\overline{\left(\frac{\partial u'_2}{\partial x_3}\right)^2}$  involved in the final dissipation estimate was corrected by this method.

Finally, after all four mean-square derivatives  $\overline{\left(\frac{\partial u'_1}{\partial x_1}\right)^2}$ ,  $\overline{\left(\frac{\partial u'_1}{\partial x_3}\right)^2}$ ,  $\overline{\left(\frac{\partial u'_2}{\partial x_1}\right)^2}$  and  $\overline{\left(\frac{\partial u'_2}{\partial x_3}\right)^2}$  are appropriately treated, we can use Equation (5.16) to estimate the dissipation term based on the locally axisymmetric homogeneous turbulence assumption, the result of which is shown in Figure 5.6.

#### 5.5.4.3 Dissipation Based on Semi-isotropic Turbulence Assumption

As described in Section 5.3, out of the nine fluctuating velocity derivatives appearing in the dissipation term in equation (5.4), the three streamwise mean-square derivatives  $\overline{\left(\frac{\partial u'_1}{\partial x_1}\right)^2}$ ,  $\overline{\left(\frac{\partial u'_2}{\partial x_1}\right)^2}$  and  $\overline{\left(\frac{\partial u'_3}{\partial x_1}\right)^2}$  are estimated on the basis of parallel and X-wire measurements by invoking the Taylor's hypothesis in Traverse I, II, III and IV. The lateral and spanwise mean-square derivatives,  $\overline{\left(\frac{\partial u'_1}{\partial x_2}\right)^2}$  and  $\overline{\left(\frac{\partial u'_1}{\partial x_3}\right)^2}$  are obtained by

a parallel hot-wire probe in Traverse III and IV. The two quantities  $\overline{\left(\frac{\partial u'_3}{\partial x_2}\right)^2}$  and  $\overline{\left(\frac{\partial u'_2}{\partial x_3}\right)^2}$  can be obtained by using the twin X-wire configuration in Traverse I and II. In summary, only two out the nine derivatives in the dissipation term as shown in Equation (5.4),  $\overline{\left(\frac{\partial u'_2}{\partial x_2}\right)^2}$  and  $\overline{\left(\frac{\partial u'_1}{\partial x_3}\right)^2}$ , have not been directly measured in this research project. The experimental results of these seven measured terms for the symmetric wake at zero pressure gradient at  $x/\theta_0 = 141$  are shown in Figure 5.8. All time mean derivatives shown in Figure 15 have been corrected for the resolution bias error using the method described in the previous section. It can be seen, as shown in Figure 5.8, the streamwise derivatives are much smaller than the two lateral and spanwise fluctuating velocity derivatives.

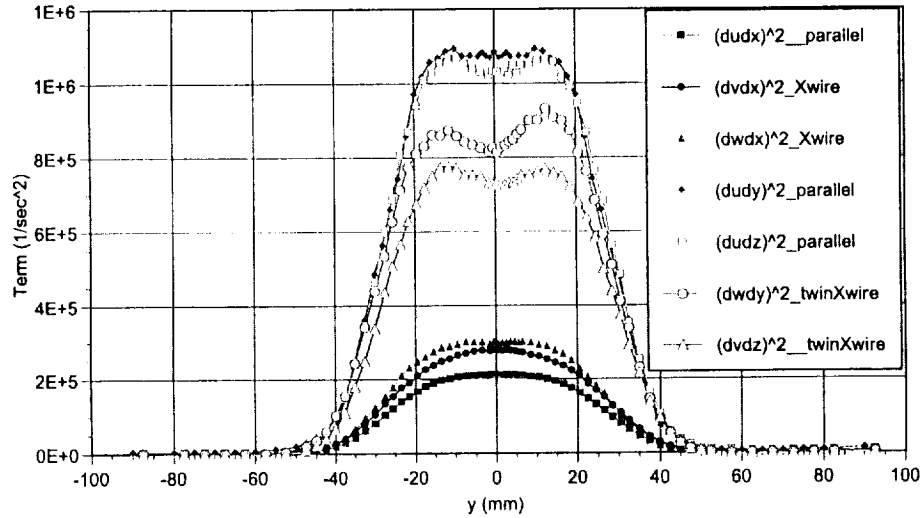


Figure 5.8. The Seven Measured Time Mean Square Derivatives in ZPG at  $x/\theta_0 = 141$ .

The two remaining derivatives  $\overline{\left(\frac{\partial u'_2}{\partial x_2}\right)^2}$  and  $\overline{\left(\frac{\partial u'_3}{\partial x_3}\right)^2}$  in the dissipation term are subsequently estimated by invoking a semi-isotropy assumption (Wyganski and Fiedler, 1969).

$$k_s \overline{\left(\frac{\partial u'_1}{\partial x_1}\right)^2} = \overline{\left(\frac{\partial u'_2}{\partial x_1}\right)^2} = \overline{\left(\frac{\partial u'_3}{\partial x_1}\right)^2}$$

$$\overline{\left(\frac{\partial u'_1}{\partial x_2}\right)^2} = k_s \overline{\left(\frac{\partial u'_2}{\partial x_2}\right)^2} = \overline{\left(\frac{\partial u'_3}{\partial x_2}\right)^2}$$

$$\overline{\left(\frac{\partial u'_1}{\partial x_3}\right)^2} = \overline{\left(\frac{\partial u'_2}{\partial x_3}\right)^2} = k_s \overline{\left(\frac{\partial u'_3}{\partial x_3}\right)^2}$$

where  $k_s$  is the semi-isotropy coefficient. To verify if the semi-isotropy assumption is valid for the wake flow investigated here, it can be seen from Figure 5.8, that  $\overline{\left(\frac{\partial u'_2}{\partial x_1}\right)^2} \approx \overline{\left(\frac{\partial u'_3}{\partial x_1}\right)^2}$  which means the last equality in the first row of the semi-isotropy assumption matrix is valid. From this figure, the semi-isotropy coefficient  $k_s$  can also be determined according to the assumption  $k_s \overline{\left(\frac{\partial u'_1}{\partial x_1}\right)^2} = \overline{\left(\frac{\partial u'_2}{\partial x_1}\right)^2}$ . With this experimentally determined semi-isotropy coefficient  $k_s$ , the remaining two derivatives  $\overline{\left(\frac{\partial u'_2}{\partial x_2}\right)^2}$  and  $\overline{\left(\frac{\partial u'_2}{\partial x_3}\right)^2}$  in the dissipation term can then be estimated. Finally, the total dissipation can be calculated from Equation (5.4). The result of the dissipation estimate obtained in this way is shown in Figure 5.6.

#### 5.5.4.4 Dissipation Based on Forced TKE Balance

As outlined in Section 5.3, the dissipation term may even be inferred by a forced balance of the TKE equation, if the pressure diffusion term can be neglected. Actually, the dissipation term obtained with this forced balance method contains the pressure diffusion term and the error term. Again, the dissipation term obtained by forcing a balance of the TKE equation is shown in Figure 5.6.

#### 5.5.4.5 Comparison of the Results of the Four Approaches

Compared to other approaches, the locally axisymmetric assumption leads to a result of lateral integration of pressure diffusion that is most close to zero

As shown in Figure 5.6, it can be seen that significant disparities occur for the estimates of the dissipation term through the four different approaches for the symmetric wake at ZPG. The dissipation term based on the isotropy assumption is much smaller in magnitude compared with the other three methods. In fact, the accuracy of the dissipation estimate can be examined by checking zero lateral integration character of the pressure diffusion term, which can be obtained from Equation (5.19) if convection, production, turbulent diffusion and the dissipation terms are all measured. It turns out that the dissipation estimate based on the locally axisymmetric assumption leads to a result of lateral integration of pressure diffusion that is most close to zero compared with other approaches, which means the locally axisymmetric assumption approach is most appropriate for the dissipation estimate for the wake flow studied in this research project. The estimate based on the semi-isotropy assumption over-estimated the dissipation while the estimate based on isotropy under-estimated the dissipation.

#### 5.5.4.6 Verification of the Prerequisites of the Locally Turbulence Assumption

Some of the conditions for the locally axisymmetric homogeneous turbulence assumption as outlined in Equations (5.9)-(5.15) can be verified from Figure 5.8, which shows that Equations (5.9) and (5.10) are almost perfectly valid, i.e.,  $\overline{\left(\frac{\partial u'_1}{\partial x_2}\right)^2} = \overline{\left(\frac{\partial u'_1}{\partial x_3}\right)^2}$  and  $\overline{\left(\frac{\partial u'_2}{\partial x_1}\right)^2} = \overline{\left(\frac{\partial u'_3}{\partial x_1}\right)^2}$ , while Equation (5.12) is approximately valid within the uncertainty of the measurement,  $\overline{\left(\frac{\partial u'_2}{\partial x_3}\right)^2} \approx \overline{\left(\frac{\partial u'_3}{\partial x_2}\right)^2}$ .

### 5.5.5 Turbulent Kinetic Energy Budget

Figure 5.9 presents all measured terms in Equation (5.19) of the turbulent kinetic energy budget for the symmetric wake at zero pressure gradient at  $x/\theta_0 = 141$ . In this plot, all terms except the pressure diffusion are obtained from direct measurement. Error bars associated with the measured terms based on an uncertainty analysis are also shown in this figure. The pressure diffusion profile shown in Figure 5.9 is obtained by forcing a balance of the TKE equation and it is actually a term that consists of both the true pressure diffusion and the total error of the whole measurement.

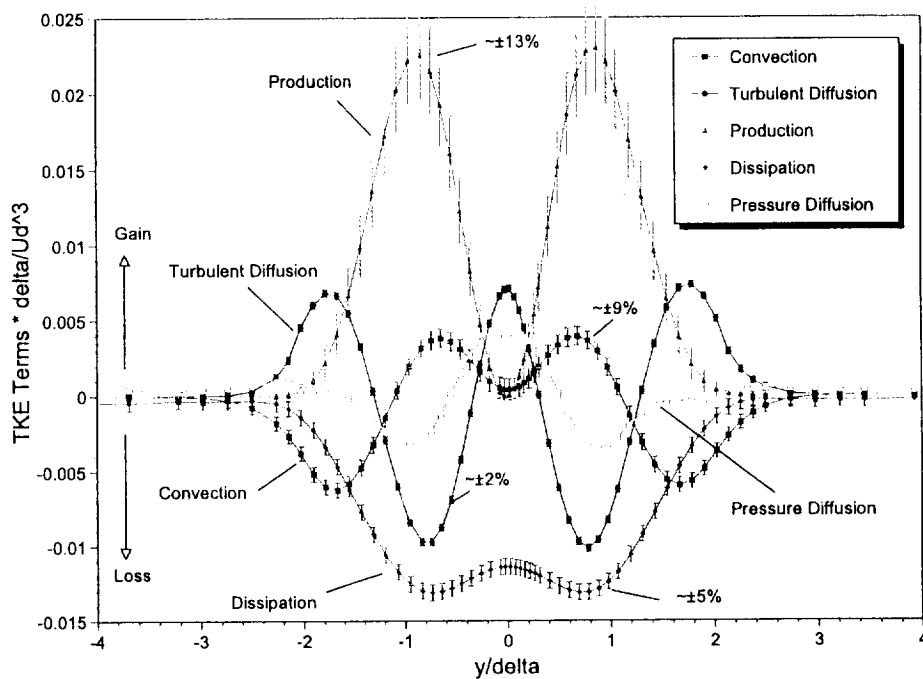


Figure 5.9. Turbulent Kinetic Energy Budget of Symmetric Wake in ZPG at  $x/\theta_0 = 141$ .

The double peaks of the production term approximately correspond to the locations of the maximum mean strain rate in the upper and lower shear layer of the

wake. At the center or near the edges of the wake, where the mean shear is zero or asymptotically approaches zero, the production term is also zero. The peak of the production term implies that a large amount of turbulence is newly generated in that region. This means there is a gradient associated with the newly generated turbulence kinetic energy in the flow field. This gradient associated with the newly generated turbulence kinetic energy is mainly aligned in the lateral direction. Wherever there is a gradient, the diffusion mechanism will take part in and play a role. From Figure 5.9, it can be seen it is the turbulent diffusion that transports the turbulence kinetic energy away from the region with higher density of newly generated turbulence to the regions with less density of newly generated turbulence, such as the center and the edges of the wake. The direction of the turbulent diffusion is governed by the production mechanism, mainly in the lateral direction. (This explains why the lateral diffusion dominates while the streamwise diffusion is negligible. The behavior of the turbulent diffusion depends on the behavior of the turbulence production.) More specifically, the turbulent diffusion will transport turbulence away from the location of the maximum mean shear and move the turbulence toward the center and the edges of the wake. As a consequence, we see there are two valleys of loss of the turbulent kinetic energy due to the turbulent diffusion near the locations of maximum mean shear while there are three peaks of gain due to turbulent diffusion at the center and near both edges of the wake. The turbulent diffusion is a conservative process and the role it plays is merely to re-distribute the turbulence kinetic energy and make the turbulence field more and more homogenized.

From Figure 5.9 it can also be seen that the pressure diffusion plays about the same role as that of the turbulent diffusion in the balance of the turbulent kinetic energy budget. The pressure diffusion also transports the turbulence away from the

region with higher density of newly generated turbulence kinetic energy. There is no evidence in Figure 5.9 that there is a so-called counter-gradient transport mechanism for the pressure diffusion term, as suggested by Demuren *et al.* (1996). Figure 5.9 also shows the magnitude of the pressure diffusion is quite considerable and is not a quantity that can be simply neglected.

As for the dissipation term, it can be seen from Figure 5.9 that most severe dissipation occurs at the central region of the wake, where the turbulence is also most intense. Approaching to the edge of the wake, the dissipation gradually decreases to zero. Actually, at the central region of the wake, the dissipation is so intense that after the aggregation of the gain/loss of the turbulence kinetic energy due to production, turbulent diffusion, pressure diffusion and dissipation there is a deficit of the turbulence kinetic energy which requires the contribution from convection to make up the balance. In other words, without a gain of turbulent kinetic energy from the convection process, the whole system is unable to reach a local balance at the central region of the wake. This explains why we see a gain due to convection at the central region of the wake. As a contrast, near the edge of the wake, the dissipation turns to be so weak that it can only roughly balance the similarly weak production process and in the meanwhile, leave a considerable amount of gain of turbulence kinetic energy due to the diffusion process to be balanced by the loss carried out by the convection process. From this analysis, we can see that the role of convection in the turbulence kinetic energy budget balance largely depends on the behavior of the dissipation process.

In fact, the convection term can also be viewed as an interface, and actually, the only interface for the exchange of turbulence kinetic energy of the local TKE balance system with the upstream and downstream TKE balance systems, as shown in Figure 5.10. Suppose there is a thin control volume, the thickness of which is  $dx$ ,

associated with the local TKE balance system. Obviously,  $k_{flux-in}$ , the turbulence kinetic energy flux from the upstream station is equal to the sum of the gain / loss of the turbulence kinetic energy of the local TKE balance system due to convection and  $k_{flux-out}$ , the turbulence kinetic energy flux to the downstream station. If there is a gain of the turbulence kinetic energy of the local TKE balance system due to convection, we should have,  $k_{flux-in} > k_{flux-out}$ , which implies that a decrease of the turbulence kinetic energy should be expected when the wake develops downstream. Similarly, if there is a loss of the turbulence kinetic energy of the local TKE balance system due to convection, we should have,  $k_{flux-in} < k_{flux-out}$ , which implies that an increase of the turbulence kinetic energy should be expected when the wake develops downstream.

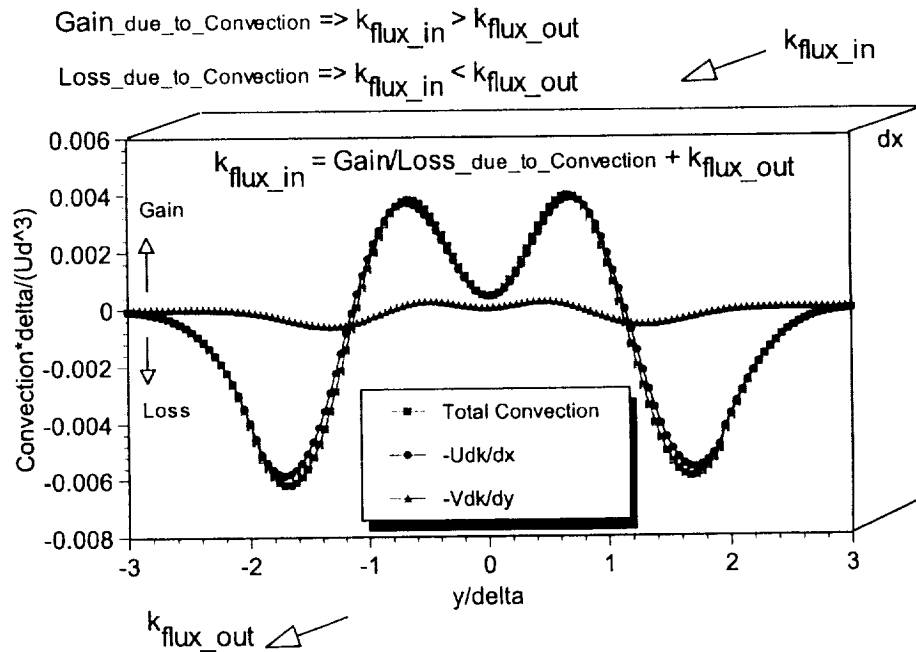


Figure 5.10. Relationship of Convection term and the Turbulent Kinetic Energy Flux.

In fact, the convection term is nothing but a material derivative of the turbulence kinetic energy, as expressed in Equation (5.2), predicting whether the turbulence field will decay or grow in the downstream direction. As pointed out earlier, in Figure 5.9, near the center of the wake, there is a gain of TKE for the local system due to convection, indicating that the turbulence is decreasing near the center of the wake as the wake develops downstream. Again in Figure 5.9, at the edge of the wake, there is a loss of TKE for the local system due to convection, implying that the turbulence kinetic energy will increase at the edge of the wake. This trend can be found in Figure 5.11, which shows the streamwise development of the turbulence kinetic energy for the zero pressure gradient. Indeed, from Figure 5.11, one can clearly see that the turbulence kinetic energy is decreasing at the center of the wake while it is growing at the edge of the wake.

## 5.6 Turbulent Kinetic Energy Budget in Adverse Pressure Gradient

### 5.6.1 Convection Term

Figure 5.12 shows the measured convection term for the symmetric wake in adverse pressure gradient at  $x/\theta_0 = 141$ . Again, near the center of the wake, the streamwise convection  $-\overline{U}_1 \frac{\partial}{\partial x_1} \left( \frac{q^2}{2} \right)$  dominates. However, unlike the ZPG case shown in Figure 8, the lateral convection  $-\overline{U}_2 \frac{\partial}{\partial x_2} \left( \frac{q^2}{2} \right)$  is quite significant in magnitude near the edge of the wake for the APG case. This behavior is determined by the V-mean profile, which is shown in Figure 5.13 along with V-mean profiles for the ZPG and FPG cases. Figure 5.13 shows that for the APG case, the V velocity component grows in magnitude toward the edge of the wake. The V velocity component acts to convect turbulence kinetic energy toward the edge of the wake. That is why we that a gain of turbulence kinetic energy in this region. Like the ZPG case, the U-component still provides a gain of turbulence kinetic energy near the center and a

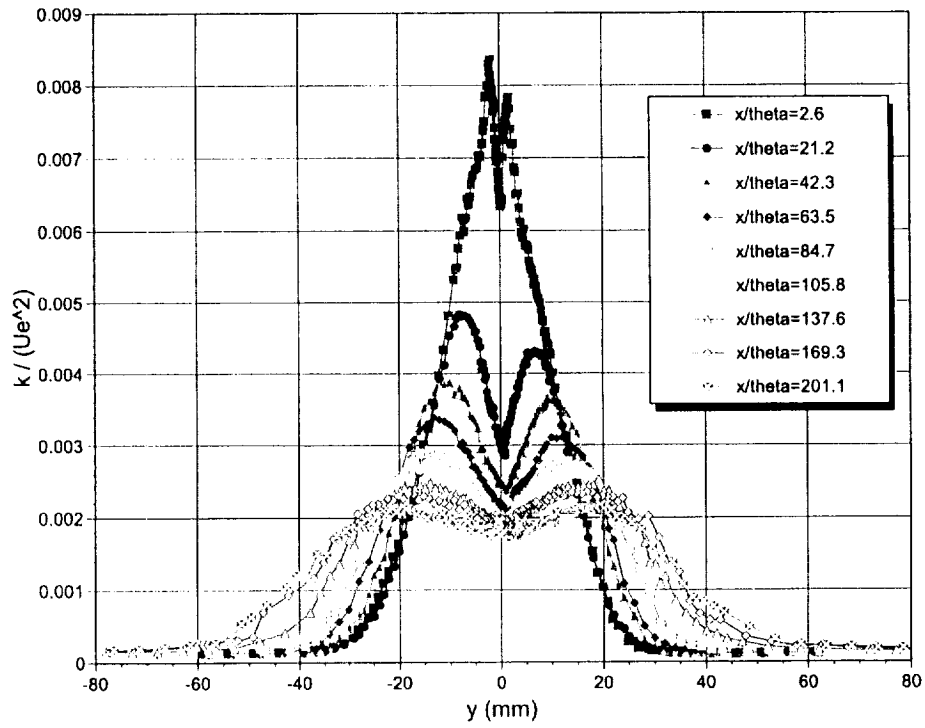


Figure 5.11. Streamwise Development of Turbulent Kinetic Energy of Symmetric Wake in ZPG.

loss at the edge of the wake. The competing gain and loss mechanism of the U and V component convection gives rise to a net loss of turbulence kinetic energy due to the total convection effect at the edge of the wake.

Figure 5.13 also shows that for the ZPG case, the magnitude of the V-mean profile is relatively much smaller across the wake than both APG and FPG cases. As a consequence, the lateral convection  $-\overline{U}_2 \frac{\partial}{\partial x_2} \left( \frac{q^2}{2} \right)$  for the ZPG case is not as significant as that of APG case near the edge of the wake. Since the sign of V-component at the FPG case is reversed from the APG case, it is expected that for the FPG case, the profile of the lateral convection  $-\overline{U}_2 \frac{\partial}{\partial x_2} \left( \frac{q^2}{2} \right)$  will be an inverted version of the APG case. This will be shown in Figure 5.19.

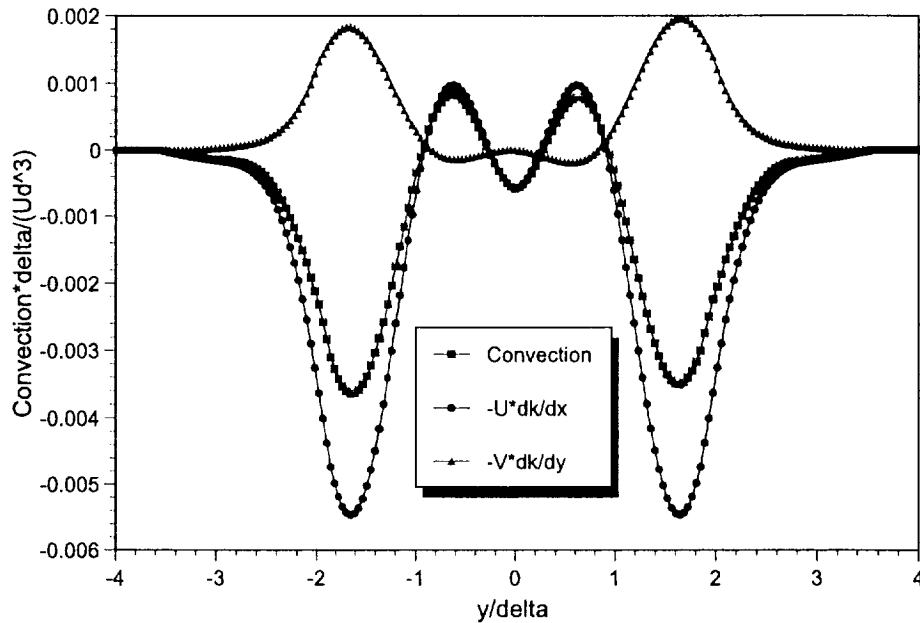


Figure 5.12. Convection Term of Symmetric Wake in APG at  $x/\theta_0 = 141$ .

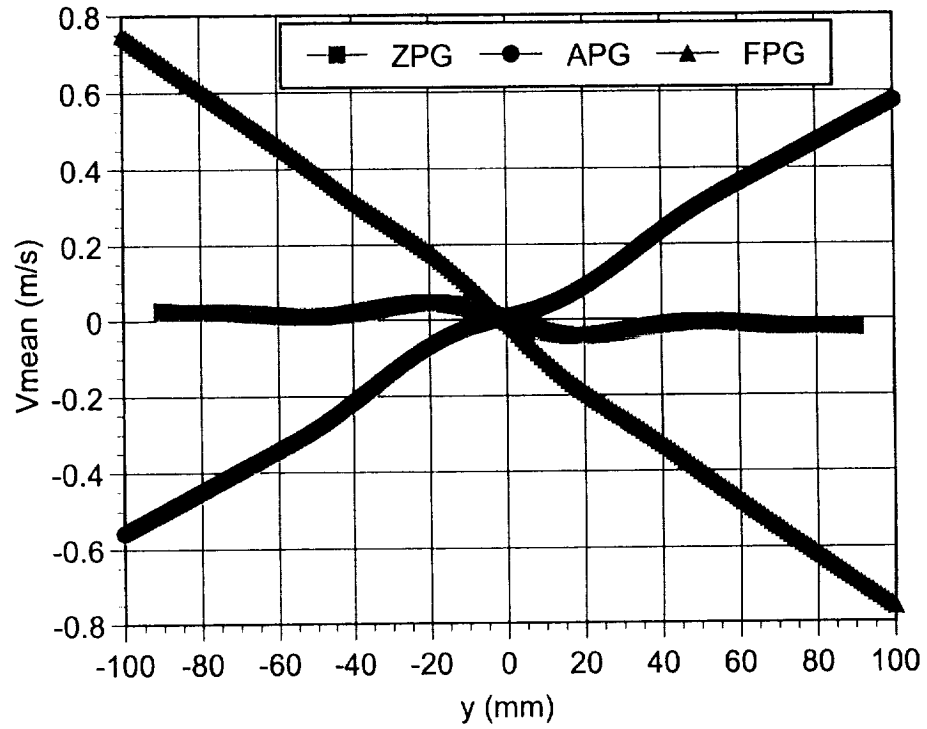


Figure 5.13. Comparison of V component Mean Profiles for the Symmetric Wake ZPG, APG and FPG Cases at  $x/\theta_0 = 141$ .

### 5.6.2 Production Term

Figure 5.14 shows the turbulence production of the symmetric wake at APG at  $x/\theta_0 = 141$ . In this figure, the dilatational production refers to the  $-\left(\overline{u_1'^2} - \overline{u_2'^2}\right) \frac{\partial \overline{U_1}}{\partial x_1}$  term. The shear production refers to the  $-\overline{u_1' u_2'} \left(\frac{\partial \overline{U_1}}{\partial x_2} + \frac{\partial \overline{U_2}}{\partial x_1}\right)$  term. The shear production part 1 refers to the  $-\overline{u_1' u_2'} \frac{\partial \overline{U_1}}{\partial x_2}$  term. The shear production part 2 refers to the  $-\overline{u_1' u_2'} \frac{\partial \overline{U_2}}{\partial x_1}$  term. This figure shows that like the ZPG case, the wake flow in APG case investigated remains shear dominated, although the dilatational production is not completely negligible near the locations of the maximum mean shear. In addition, from Figure 21 it is obvious that the role of the dilatational production term for the APG case is to augment the total production. For the shear production, the  $-\overline{u_1' u_2'} \frac{\partial \overline{U_2}}{\partial x_1}$  term is approximately zero across wake, due to the fact that  $\frac{\partial \overline{U_2}}{\partial x_1} \approx 0$ . Thus for the APG case investigated, the shear production is dominated by the first part, i.e.,  $-\overline{u_1' u_2'} \left(\frac{\partial \overline{U_1}}{\partial x_2} + \frac{\partial \overline{U_2}}{\partial x_1}\right) \approx -\overline{u_1' u_2'} \frac{\partial \overline{U_1}}{\partial x_2}$ .

### 5.6.3 Turbulence Diffusion Term

Figure 5.15 shows the profile of the turbulent diffusion for the symmetric wake in APG as obtained at  $x/\theta_0 = 141$ . It can be seen from this figure that like the ZPG case, the lateral turbulent diffusion term  $-\frac{\partial}{\partial x_2} \frac{1}{2} \overline{(u_1'^2 u_2' + u_2'^3 + u_2' u_3'^2)}$  is the dominant turbulent diffusion mechanism and the streamwise turbulent diffusion term  $-\frac{\partial}{\partial x_1} \frac{1}{2} \overline{(u_1'^3 + u_1' u_2'^2 + u_1' u_3'^2)}$  is negligible. To verify the accuracy of the measurement of the diffusion term, the profile of the total turbulent diffusion term was integrated across wake. The integration is essentially zero.

### 5.6.4 Dissipation Term

As described in Section 5.5.4, the estimate of the dissipation term for the APG case was conducted via four different approaches: (a), the isotropic turbulence assumption approach, (b), the locally axisymmetric turbulence assumption approach, (c),

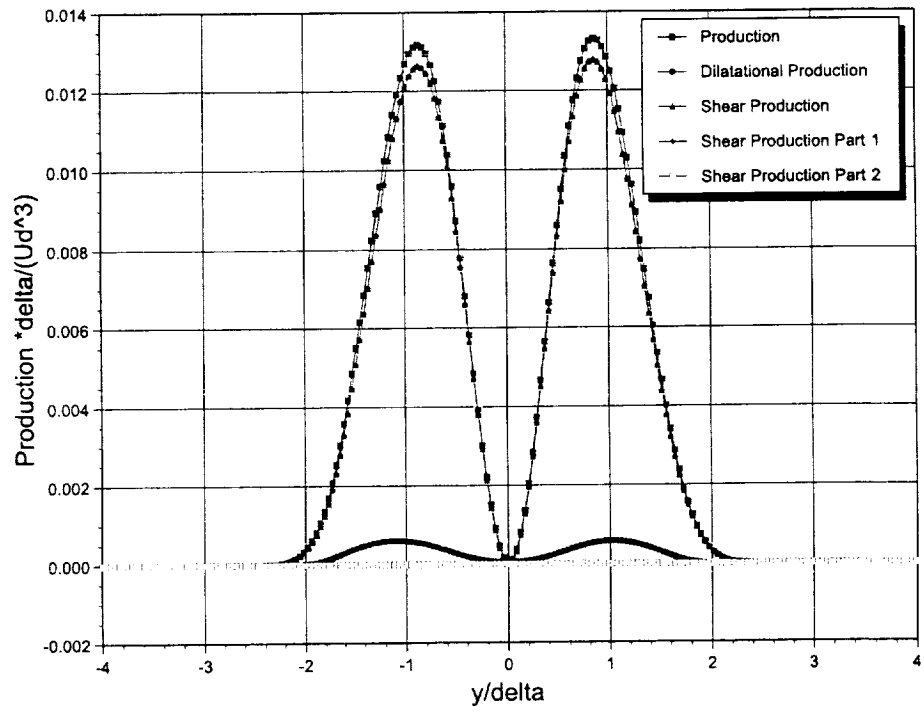


Figure 5.14. Production Term of Symmetric Wake in APG at  $x/\theta_0 = 141$ .

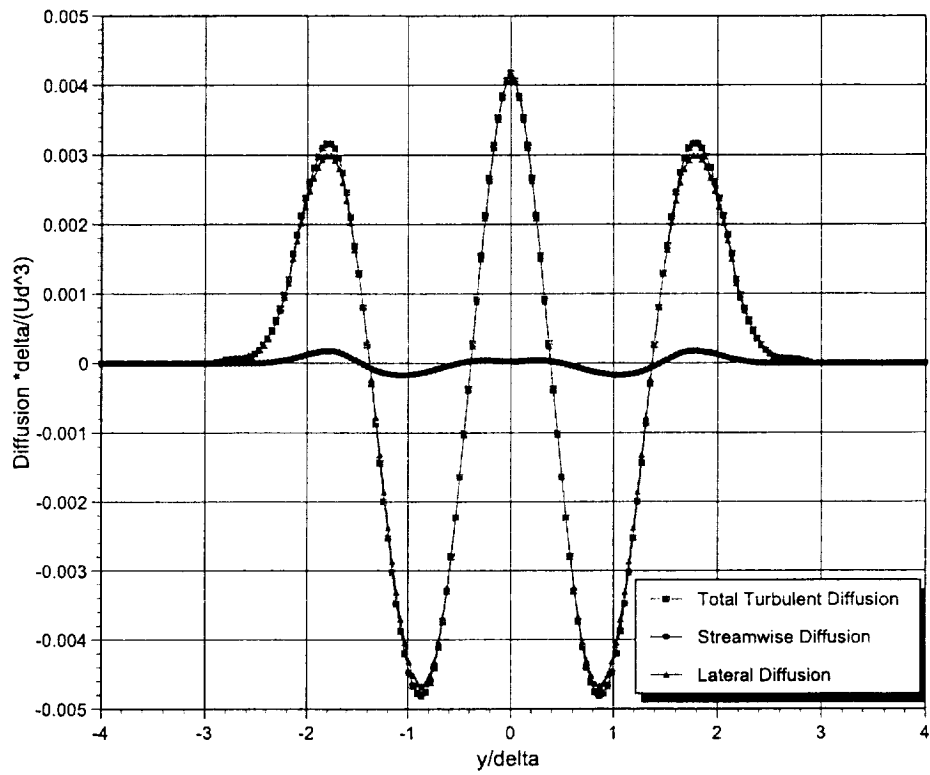


Figure 5.15. Diffusion Term of Symmetric Wake in APG at  $x/\theta_0 = 141$ .

the semi-isotropic assumption approach and (d) the forced TKE balance approach. Comparison of the dissipation estimate results with these four different approaches presented in Figure 5.16.

As in the ZPG case, there are significant disparities among the dissipation estimates based on the four approaches for the symmetric wake at APG. Again the isotropy assumption underestimates the dissipation term, while the semi-isotropy assumption over-estimates the dissipation. Once again, the dissipation estimate based on the locally axisymmetric assumption leads to a lateral integration of the pressure diffusion term which most approximates to zero compared with other approaches, suggesting that the locally axisymmetric assumption approach might be the most appropriate approach for the dissipation estimate for the wake flow in APG.

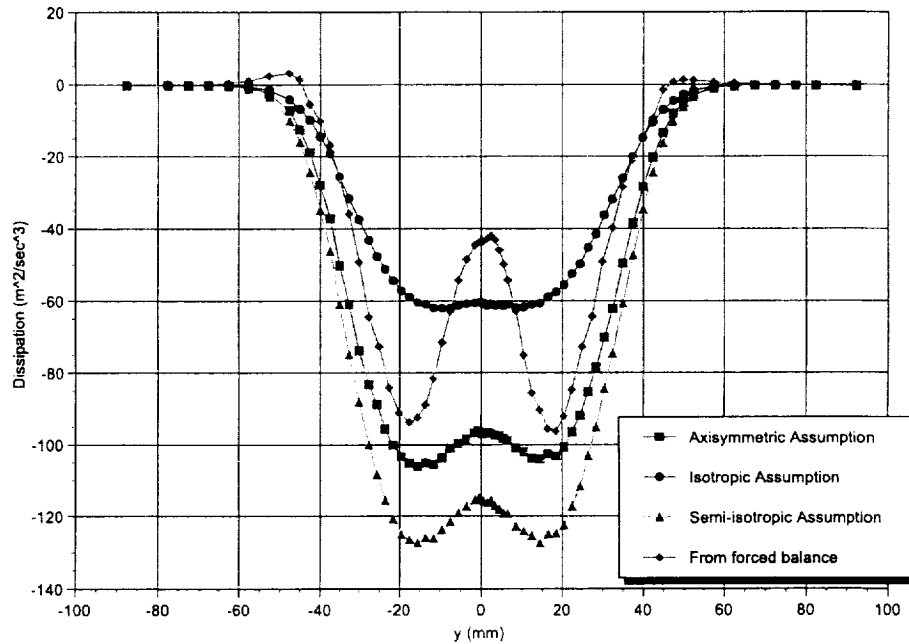


Figure 5.16. Comparison of Dissipation Estimate with Different Approaches for APG at  $x/\theta_0 = 141$ .

### 5.6.5 Turbulent Kinetic Energy Budget

The turbulent kinetic energy budget for the symmetric wake in adverse pressure gradient at  $x/\theta_0 = 141$  is presented in Figure 5.17. Error bars associated with the measured terms based on uncertainty analysis are also shown in this figure. Again, as in the ZPG case, the pressure diffusion profile shown in Figure 5.17 is obtained by forcing a balance of the TKE equation. Actually, this so-called pressure diffusion profile consists of both the true pressure diffusion and the total error of the whole measurement.

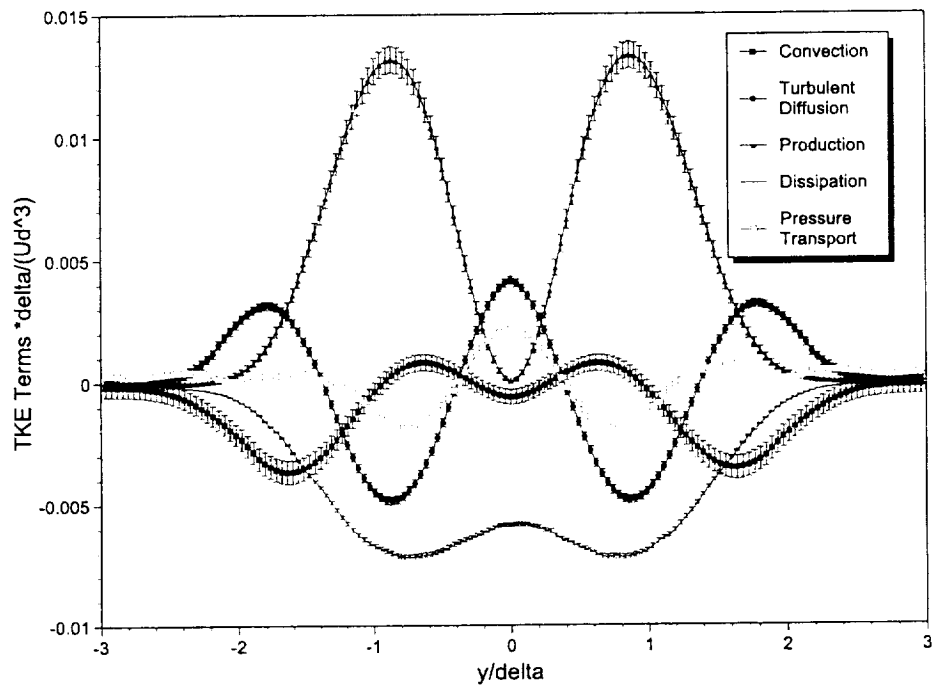


Figure 5.17. Turbulent Kinetic Energy Budget of Symmetric Wake in APG at  $x/\theta_0 = 141$ .

The interpretation of TKE budget of APG case shown in Figure 5.17 is similar to that for the ZPG case shown in Figure 5.9. However, there is one difference between the APG and ZPG turbulence kinetic energy budget that needs to be high-

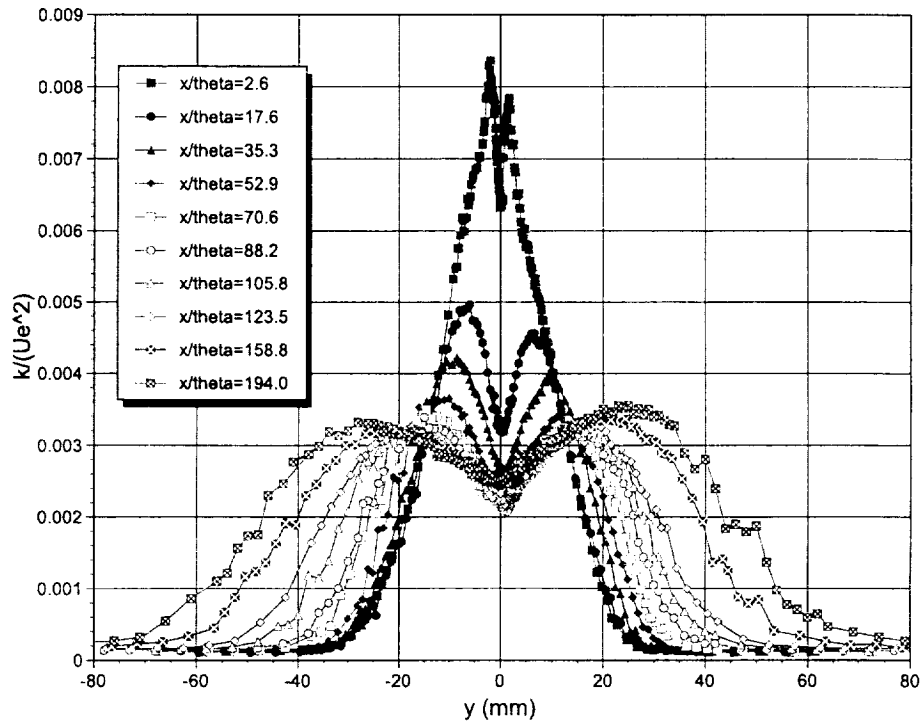


Figure 5.18. Streamwise Development of Turbulent Kinetic Energy of Symmetric Wake in APG.

lighted. For the APG case, near the center of the wake, the dissipation is not so intense as in the ZPG case. After the aggregation of the gain and loss due to production, diffusion and the dissipation near the center of the wake, there is still a surplus of the turbulence kinetic energy that is convected to the downstream stations. Correspondingly, we should observe an increase of turbulence kinetic energy in the adjacent downstream stations. This is supported by Figure 5.18 which shows the streamwise development of the turbulence kinetic energy for the APG case.

## 5.7 Turbulent Kinetic Energy Budget in Favorable Pressure Gradient

### 5.7.1 Convection Term

Figure 5.19 shows the convection term for the symmetric wake in favorable pressure gradient as obtained at  $x/\theta_0 = 141$ . Again, near the center of the wake, the streamwise convection  $-\overline{U}_1 \frac{\partial}{\partial x_1} \left( \frac{q^2}{2} \right)$  dominates. Like the APG case shown in Figure 19, the lateral convection  $-\overline{U}_2 \frac{\partial}{\partial x_2} \left( \frac{q^2}{2} \right)$  is quite significant in magnitude near the edge of the wake for the FPG case. But this time, the lateral convection at the edge of the wake results in a local loss of the turbulence kinetic energy since the inward V-component carries turbulence kinetic energy away to downstream stations. As a result, the total loss of the turbulence kinetic energy of the local system is augmented. This convection mechanism near the edge of the wake is different from that of the APG case, in which the streamwise convection contributes a loss while the lateral convection contributes a gain to the local TKE balance system.

### 5.7.2 Production Term

Figure 5.20 shows the turbulence production of the symmetric wake in FPG at  $x/\theta_0 = 141$ . The designations in this figure are the same as used previously in Section 5.6.2. Again like the ZPG and APG cases, the wake flow in FPG case

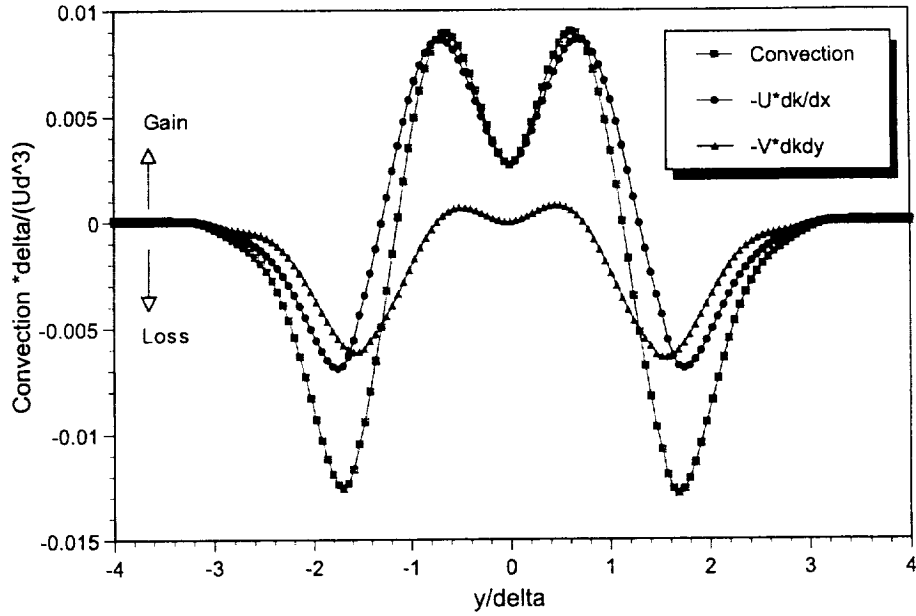


Figure 5.19. Convection Term of Symmetric Wake in FPG at  $x/\theta_0 = 141$ .

is shear dominated, although the dilatational production is not completely negligible near the locations of maximum mean shear. Unlike the APG case in which the dilatational production term augments the total production, for the FPG case, the dilatational production is actually a counter-production term and its effect is to reduce the total production. Again like the APG case, the  $-\overline{u'_1 u'_2} \frac{\partial \overline{U}_1}{\partial x_1}$  term is approximately zero across wake, due to the fact that  $\frac{\partial \overline{U}_2}{\partial x_1} \approx 0$ . Thus for the FPG case investigated, the shear production is dominated by the first part, i.e.,  $-\overline{u'_1 u'_2} \left( \frac{\partial \overline{U}_1}{\partial x_2} + \frac{\partial \overline{U}_2}{\partial x_1} \right) \approx -\overline{u'_1 u'_2} \frac{\partial \overline{U}_2}{\partial x_1}$ .

### 5.7.3 Turbulence Diffusion Term

Figure 5.21 shows the profile of the turbulent diffusion for the symmetric wake in FPG at  $x/\theta_0 = 141$ . Similar to the ZPG and the APG cases, the lateral turbulent diffusion  $-\frac{\partial}{\partial x_2} \frac{1}{2} \overline{(u_1'^2 u_2' + u_2'^3 + u_2' u_3'^2)}$  is the dominant turbulent diffusion mechanism

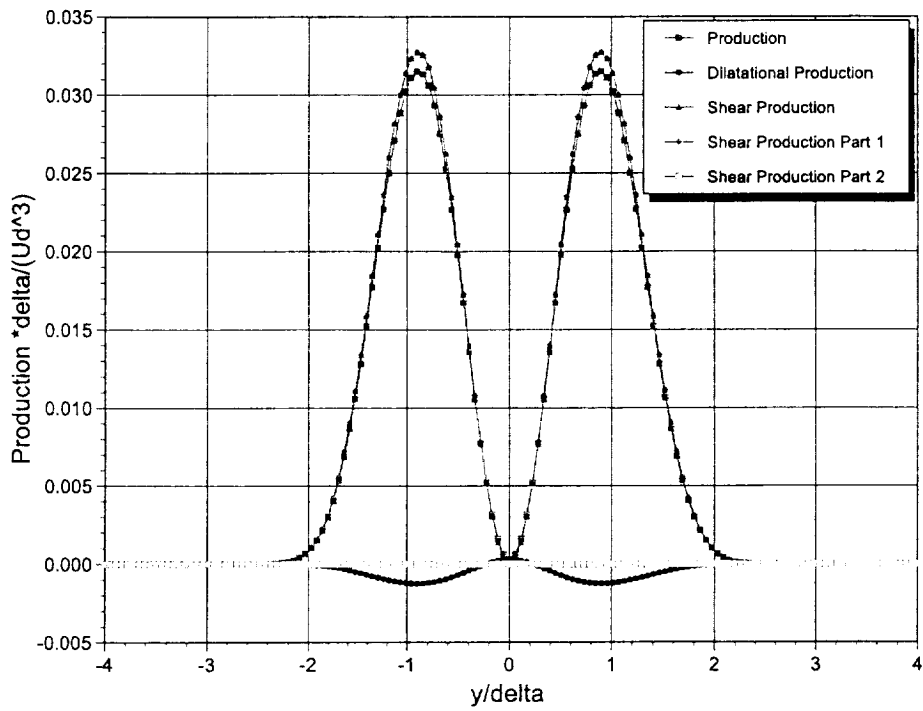


Figure 5.20. Production Term of Symmetric Wake in FPG at  $x/\theta_0 = 141$ .

and the streamwise turbulent diffusion  $-\frac{\partial}{\partial x_1} \frac{1}{2} (u_1'^3 + u_1' u_2'^2 + u_1' u_3'^2)$  is negligible for the FPG case. To verify the accuracy of the measurement of the diffusion term, the profile of the total turbulent diffusion term is integrated across wake. The integration result is essentially zero as one would expect.

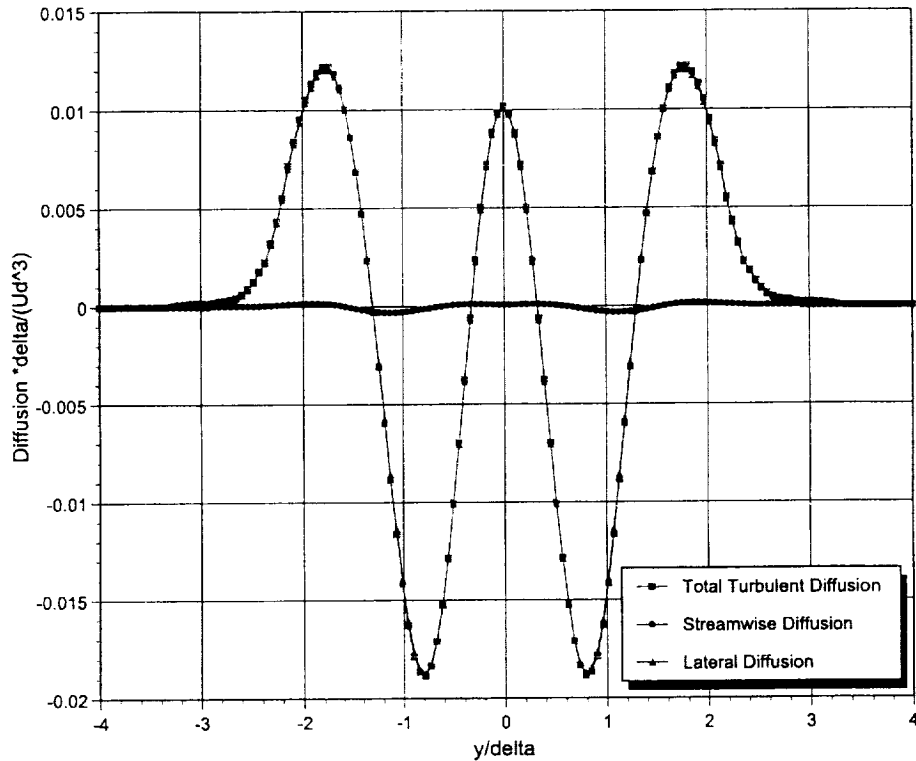


Figure 5.21. Diffusion Term of Symmetric Wake in FPG at  $x/\theta_0 = 141$ .

#### 5.7.4 Dissipation Terms

As described in ZPG and APG cases, the estimate of the dissipation term for the FPG case was again conducted via four different approaches: (a), the isotropic turbulence assumption approach, (b), the locally axisymmetric turbulence assumption approach, (c), the semi-isotropic assumption approach and (d) the forced TKE

balance approach. Comparison of the dissipation estimate results with these four different approaches presented in Figure 5.22.

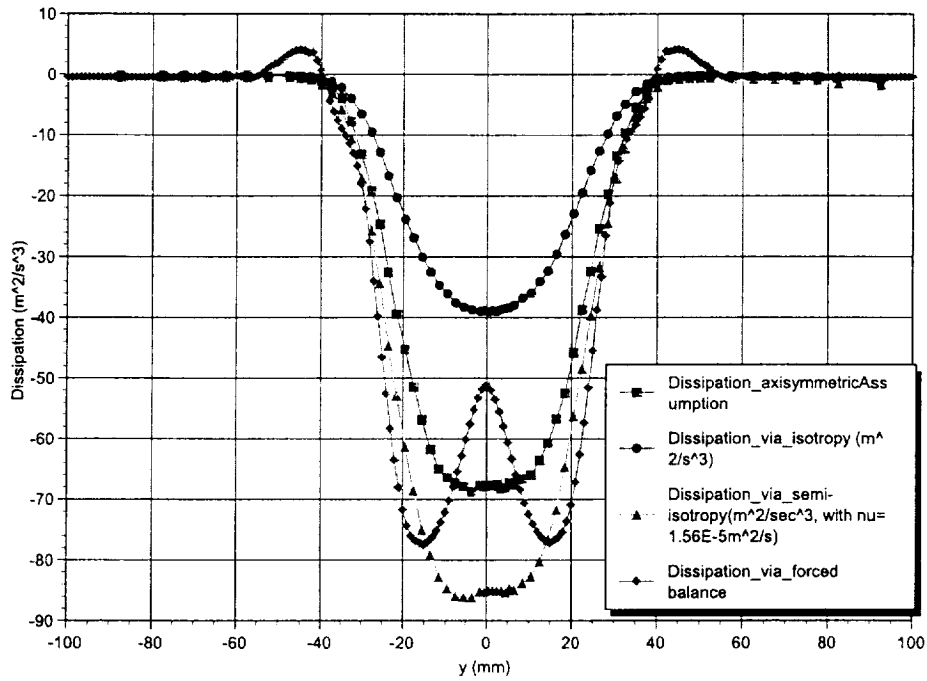


Figure 5.22. Comparison of Dissipation Estimate with Different Approaches for FPG at  $x/\theta_0 = 141$ .

As in the ZPG and APG cases, the isotropy assumption underestimates the dissipation term, while the semi-isotropy assumption over-estimates the dissipation. Once again, the dissipation estimate based on the locally axisymmetric assumption leads to an approximately zero lateral integration of the pressure diffusion term, suggesting that the locally axisymmetric assumption approach is also most appropriate for the dissipation estimate for the wake flow in FPG.

### 5.7.5 Turbulent Kinetic Energy Budget

The turbulent kinetic energy budget for the symmetric wake in favorable pressure gradient at  $x/\theta_0 = 141$  is presented in Figure 5.23. Again, as in the ZPG and APG cases, the pressure diffusion profile shown in Figure 5.23 is obtained by forcing a balance of the TKE equation.

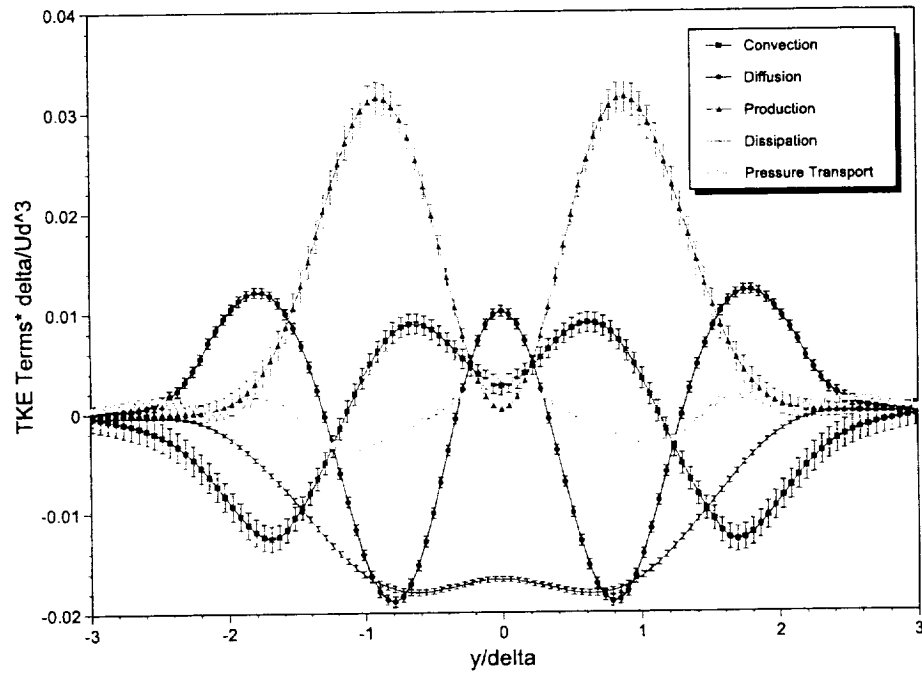


Figure 5.23. Turbulent Kinetic Energy Budget of Symmetric Wake in FPG at  $x/\theta_0 = 141$ .

The interpretation of TKE budget for the FPG case shown in Figure 5.23 is similar to that for the ZPG and APG cases. Unlike the APG case, through the central region of the wake, there is a considerable gain of turbulence kinetic energy due to convection. This is consistent with Figure 5.24, which shows the streamwise development of the turbulence kinetic energy for the FPG case.

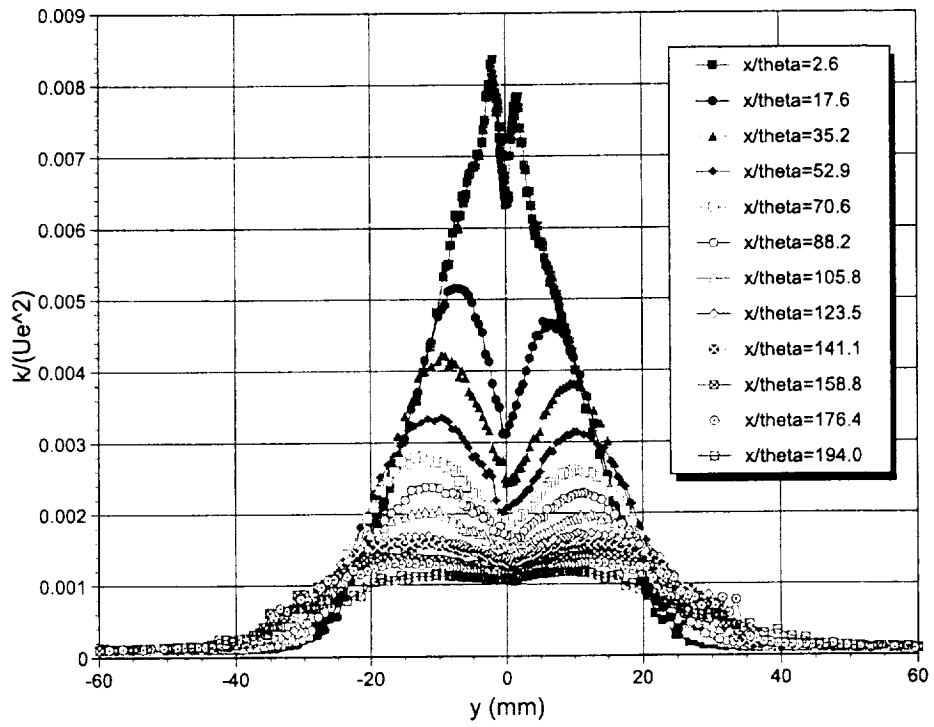


Figure 5.24. Streamwise Development of Turbulent Kinetic Energy of Symmetric Wake in FPG.

## 5.8 Comparison of the Turbulent Kinetic Energy Budget in ZPG with the DNS Result

Moser, Rogers and Ewing (1998) studied the turbulence kinetic energy budget of a temporally evolving plane wake based on direct numerical simulation (DNS) results. To facilitate their DNS simulation, they picked a section of spatially developed wake and let the wake develop in the temporal domain and then compute the turbulence quantities in the similarity region of the temporal-involving wake. They applied “forcing” to the initial wake and then investigated the influence of the “forcing” on the development of the wake. Their “unforced” wake corresponds to the ZPG conditions of our wake research, with two basic differences: (1) they obtained the TKE budget in the similarity region while ours is obtained in the near wake region and (2) their wake develops in the temporal domain while ours develops in the spatial domain. However, the spatially and temporally evolving wakes can be made equivalent by utilizing the initial wake velocity defect  $U_d$  as the convective velocity as specified by the DNS simulation, with the condition that the lateral convection term can be neglected for the ZPG case. Based on these assumptions, we were able to make direct comparison of the experimental TKE budget profiles with the DNS TKE budget profiles.

Figure 5.25, 5.26, 5.27, 5.28 and 5.29 shows the comparison of the convection, production, turbulent diffusion, dissipation and the pressure diffusion profiles between the experimental and the DNS results. Considering that the wake develops at different stages and at different Reynolds numbers for the experiment and the DNS simulation, one must admit that the agreement between the experimental and the DNS results is quite encouraging. In particular, the agreement on the turbulent diffusion term is quite good. The experimental and the DNS turbulent diffusion profiles almost overlap each other. Even the comparison of the pressure diffusion term

between the experimental and the DNS simulation shows a qualitative agreement. It must be remembered that the experimental pressure diffusion term contains not only the pressure diffusion itself, but also the total measurement error of the TKE budget. Thus the comparison of the pressure diffusion term can be regarded as a measure indicating the accuracy and reliability of the TKE budget measurement. The disparities between the convection, production and dissipation terms can be attributed to the Reynolds number and the different stages of development between the experimental and the DNS data. Moreover, the disparity between the convection term of the experimental and DNS data may also be attributed to the neglect of the lateral convection for the DNS simulation, which evolves in time as a parallel flow. Also it should be pointed out that the scatter of the DNS data points for the pressure diffusion term may be due to an insufficient period for the time averaging of the pressure diffusion term in DNS simulation.

### 5.9 Effect of the Pressure Gradient on Planar Wake TKE Budget

To investigate the influence of the pressure gradient on the wake TKE budget, the TKE budget terms for the ZPG, APG and FPG cases were normalized by using the local wake half-width,  $d$ , and the square root of the local maximum kinetic energy,  $k_{max}^{\frac{1}{2}}$ , as the reference length and velocity scales, respectively. The comparisons of the normalized TKE budget terms for different pressure gradient cases are presented in Figure 5.30.

Figure 5.30(d) shows that the scaled dissipation profile does not change very much when the wake is subjected to different pressure gradients. The effect of the imposed pressure gradient is most significant on the convection term, as shown in Figure 5.30(a). since this term is directly related to the mean motion of the flow field. Correspondingly, as an adjustment of the disparities due to the influence of the pressure gradient on the convection term, the turbulent diffusion and production

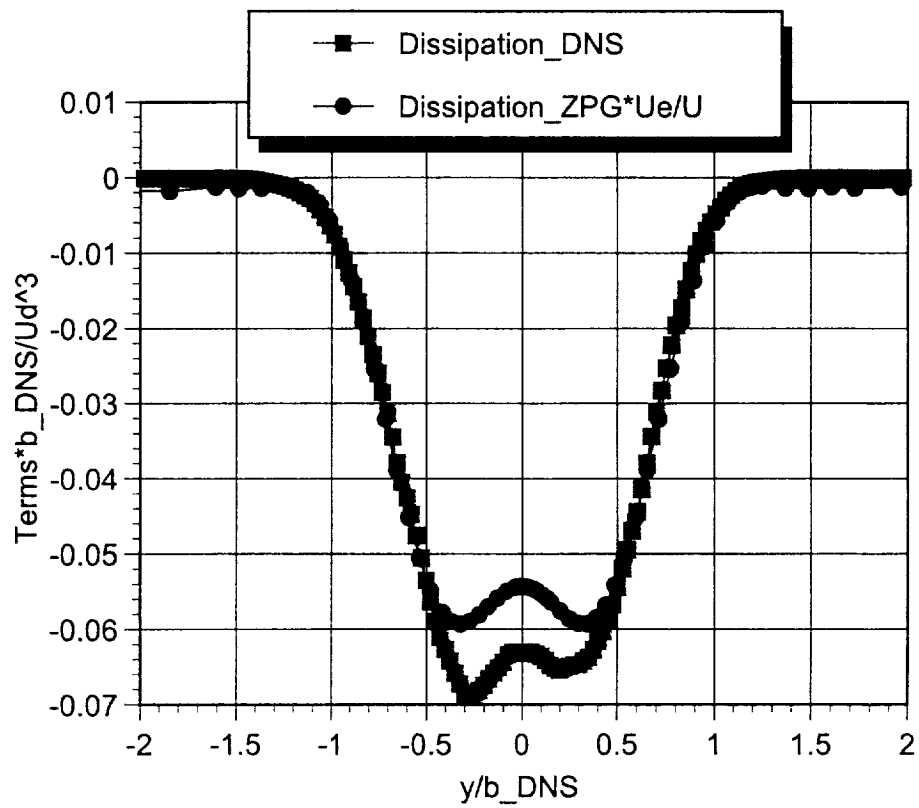


Figure 5.25. Comparison of Dissipation Profiles of Symmetric Wake in ZPG with DNS (Moser, Rogers & Ewing, 1998) Result.

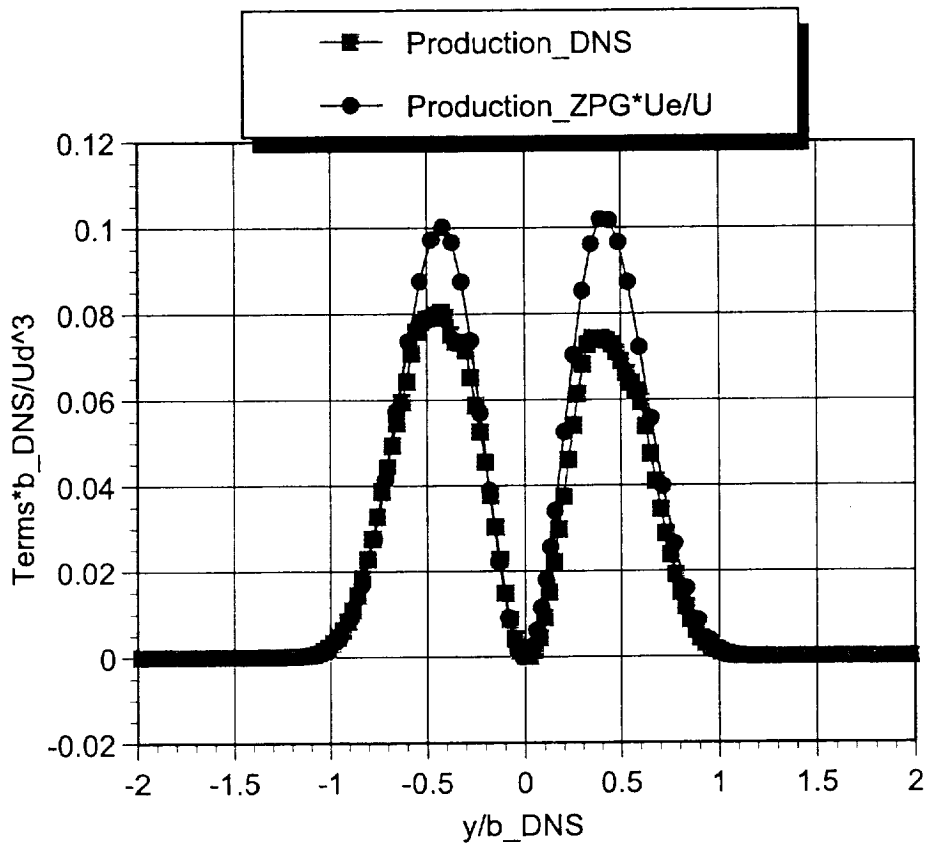


Figure 5.26. Comparison of Production Profiles of Symmetric Wake in ZPG with DNS (Moser, Rogers & Ewing, 1998) Result.

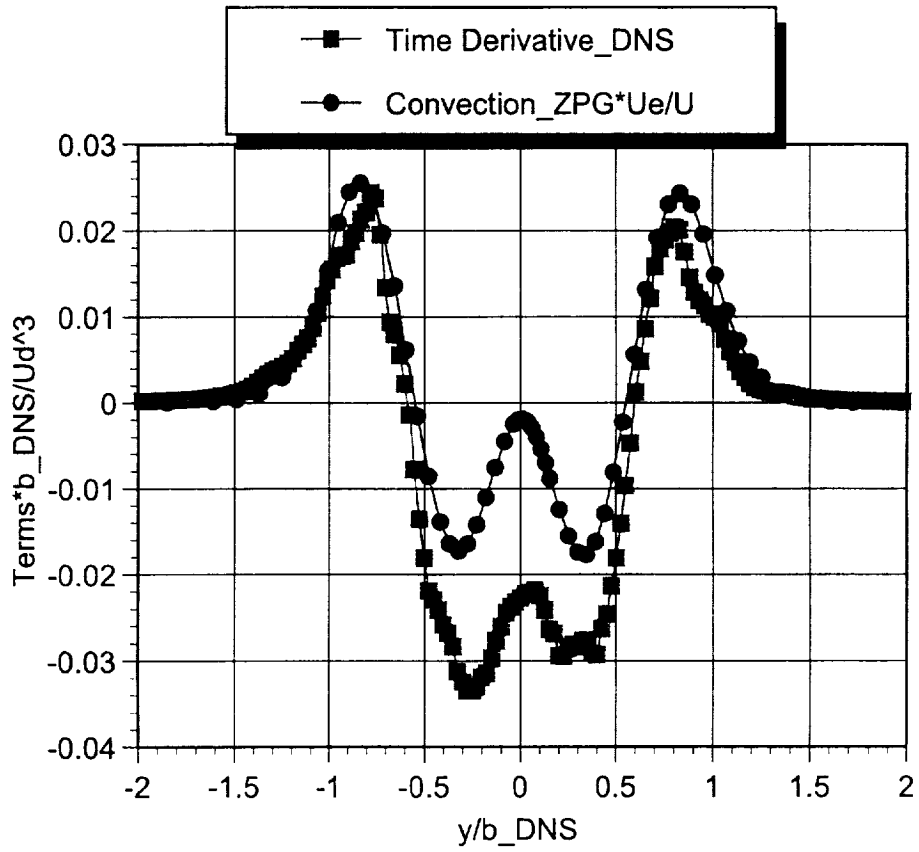


Figure 5.27. Comparison of Convection Profiles of Symmetric Wake in ZPG with DNS (Moser, Rogers & Ewing, 1998) Result.

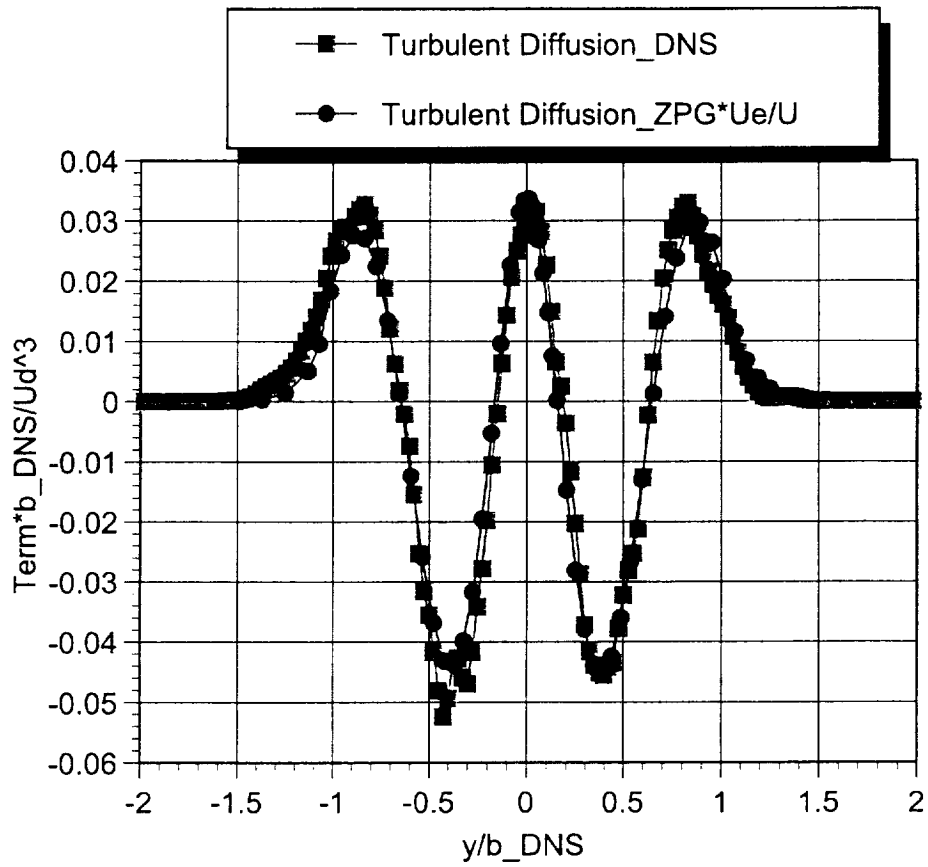


Figure 5.28. Comparison of Turbulence Diffusion Profiles of Symmetric Wake in ZPG with DNS (Moser, Rogers & Ewing, 1998) Result.

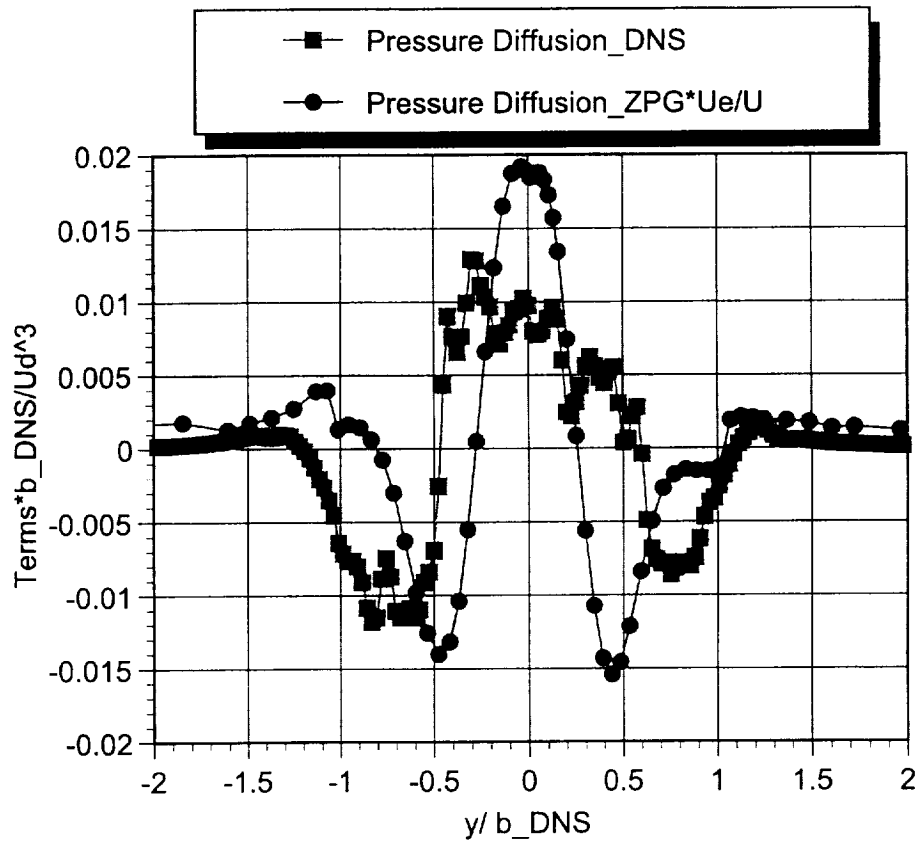


Figure 5.29. Comparison of Pressure Diffusion Profiles of Symmetric Wake in ZPG with DNS (Moser, Rogers & Ewing, 1998) Result.

terms will also change accordingly at different imposed pressure gradient, as shown in Figure 5.30(b) and (c). These comparisons indicate that the fundamental TKE transport mechanism is not altered by the imposed pressure gradient. It seems that the imposed pressure gradient exerts its influence on the turbulence field through the mean flow and largest motions rather than the small turbulence in the wake flow.

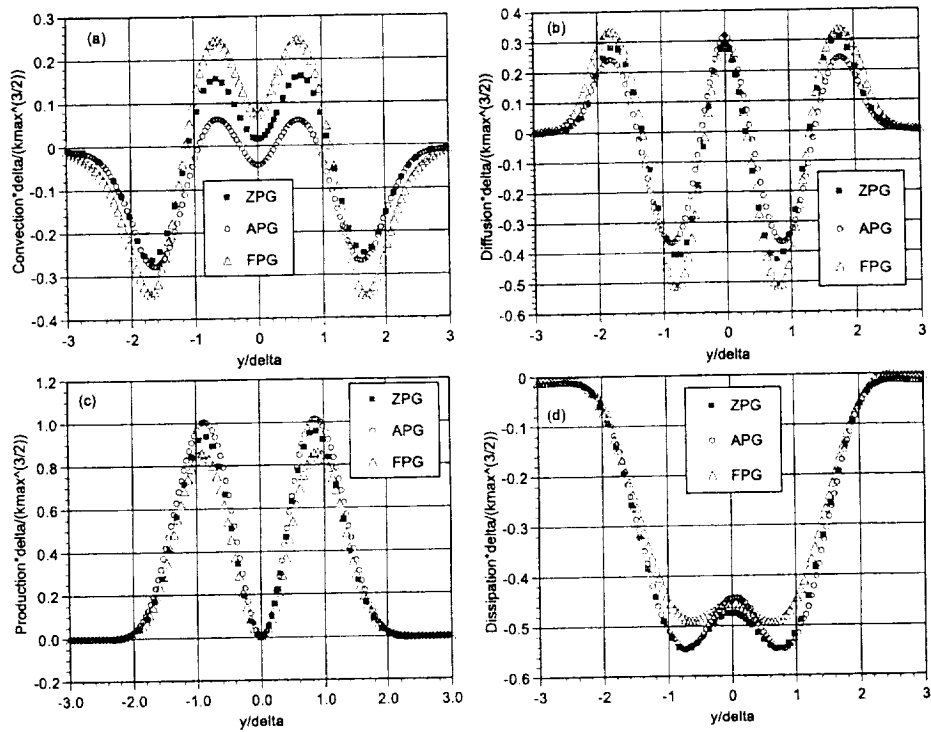


Figure 5.30. Comparison of TKE Budget Profiles of Symmetric Wake in ZPG, APG and FPG.

## 5.10 An Approach to Correct the Bias Error of the Dissipation Estimate

### 5.10.1 Sources of Bias Error Associated with the Dissipation Estimate

Among all measurable terms in the turbulence kinetic energy equation, the dissipation term is the one that is most likely to have a significant bias error. There are two types of error sources associated with the dissipation estimate. First, as described in Section 5.2, since we are unable to measure the cross derivative correlation terms in the inhomogeneous type of the dissipation expression (Equation (5.3)), we have to resort to the homogeneous turbulence assumption for the wake flow. This will give rise to *the bias error due to mathematical modelling*. Second, the limited spatial resolution of hot wire probes for the mean square derivative measurements will give rise to *the bias error due to instrument*.

Basically, for the mean square derivatives in the the dissipation term, there are two requirements for a reliable measurement. First, the spatial resolution of the probe should resolve the Kolmogorov length scale; Second, the temporal resolution of the data record should capture the fastest resolvable motion passing the probe. Currently, there is not too much difficulty for the data acquisition system to fulfill the temporal resolution requirement based on the available probe size. For example, the fastest frequency that can be resolved by the probes used in this study is roughly around  $20 \sim 30 \text{ kHz}$ . Correspondingly, the data is anti-bias filtered at  $20 \text{ kHz}$  and digitally sampled at  $40 \text{ kHz}$ . Thus the Nyquist frequency of the data record is  $20 \text{ kHz}$ , which roughly matches the temporal resolution requirement. However, for the spatial resolution requirement, unfortunately, none of the probes that we used in the mean square derivative measurement can match the Kolmogorov length scale. Kolmogorov length scale ( $L_k = (\nu^3/\epsilon)^{1/4}$ ) for the wake flow that we investigated is approximately  $0.1 \text{ mm}$ . But for the hot wire probes that we used, as described in Section 2.4.2, the spacing between the dual wires of the parallel probe is  $0.3 \text{ mm}$ ,

the wire length of parallel probe is 0.9 mm, the wire length for the X-wire is 1.2 mm, and the spacing between centers of the twin X-wire configuration is 1.3 mm. Obviously, the dimensions of these sensors are all well above the Kolmogorov length scale of the wake flow. However, as pointed out earlier in Section 5.5.4.1, the probe spacial resolution is crucial for a reliable mean square derivative estimate, according to Wallace and Foss (1995). Through an investigation of the effect of the finite difference spacing on the mean square derivative estimate based on DNS data, Wallace and Foss (1995) demonstrated that the estimate of the mean square derivative is attenuated dramatically as the increase of the finite difference spacing, which is equivalent to the issue of probe resolution in measurement. That is the reason why the parallel probe and the X-wire give rise to different magnitudes of measurement results for the same mean square derivative  $\overline{\left(\frac{\partial u_1'}{\partial x_1}\right)^2}$ , as shown in Figure 5.5.

Of course, as described in Section 5.5.4, the bias error due to the limited spatial resolution can be *partially* corrected by “aligning” all time mean square derivative results measured by the X-wire and the twin X-wire configuration to the “virtual” spatial resolution level of the parallel probe. The bias errors of dissipation estimate results shown in Figure 5.6, 5.16 and 5.22 have all been *partially* corrected in this way. However, this correction is only a partial correction of the bias error due to instrument. Moreover, the bias error due to mathematical modelling has not been corrected up to this point. To ensure the reliability of the final dissipation estimate, we ought to find a way to correct the *total* bias error, including *the bias error due to instrument* and *the bias error due to mathematical modelling*.

### 5.10.2 Self-similar Behavior of Time Mean Square Derivative Profiles

In order to correct the *total* bias error, we first check the property of the mean square derivatives. As shown in Figure 5.8, the seven measured time mean square derivatives in the dissipation term have different magnitude relative to each other.

However, if each individual time mean square derivative is scaled by its maximum value, then we can see all seven mean square derivatives collapse to a single uniform profile, indicating a self-similar behavior for the seven measured mean square derivatives, as shown in Figure 5.31. This reminds us that the unmeasured or immeasurable time mean square derivatives, including the cross derivative correlation terms in the inhomogeneous form of dissipation, might all have the same self-similar behavior and all collapse to the same curve. If we assume it is true, then the final dissipation profile must also collapse to the same curve. As a consequence, the final dissipation can be represented by any linear combinations of the measured mean square derivatives, and the difference is only a scaling factor. If we can find the appropriate scaling factor, then we will be able to correct the bias error. Now the question is how to find this scaling factor, namely, a constant  $\tau$ .

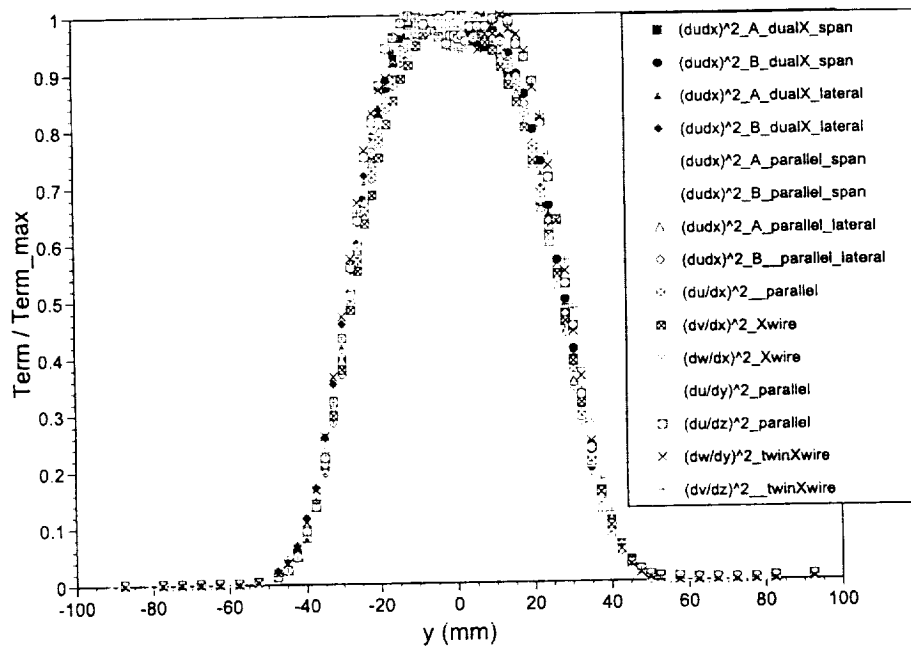


Figure 5.31. Self-similar Behavior of the Measured Mean Square Derivatives for ZPG at  $x/\theta_0 = 141$ .

### 5.10.3 Property of Pressure Diffusion Term

To find the appropriate scaling factor  $r$ , we need to examine the property of the pressure diffusion term of the TKE equation for the planar turbulent wake flow.

As pointed out earlier, the pressure diffusion terms in Figures 5.9, 5.17 and 5.23 are all obtained from the forced balance of the TKE equation. From the discussion in Section 5.5.5, we learn that for the local TKE balance system the only interface for the TKE exchange is the convection term. The diffusion, including the turbulent diffusion and the pressure diffusion, neither generates nor consumes the turbulence kinetic energy within the local TKE balance system. It does nothing but merely re-distribute the turbulence kinetic energy within the local system. In other word, the diffusion is conservative within the local TKE system. This is shown from the lateral integration result of the turbulent diffusion term, as indicated in Section 5.5.3. Similarly, we expect that the lateral integration of the pressure diffusion term should also be zero to ensure the conservation of the diffusion term. This behavior is verified by the examination of lateral integration of the pressure diffusion term of the DNS data of Moser *et al.* (1998).

### 5.10.4 The Shooting Method Approach to Correct the Bias Error of the Dissipation Estimate

The attribute of zero lateral integration of the pressure diffusion term can be utilized as a constraint to correct the bias error associated with the dissipation estimate. More specifically, with the pressure diffusion term obtained from the forced balance of the TKE equation, we can use a shooting method to iteratively adjust the scaling factor  $r$  of the dissipation term until we get a zero lateral integration of the pressure diffusion. In this way, the bias error associated with the dissipation estimate, including the error due to mathematical modelling, can be finally corrected.

This Shooting Method Approach is a novel approach to improve the accuracy of the dissipation estimate and has been applied to the dissipation curves in the TKE budgets for ZPG, APG and FPG as shown in Figures 5.9, 5.17 and 5.23. Through the comparison of the measured TKE budget in ZPG with the DNS results, the reliability of this approach is also validated. In addition to symmetric planar wake flow, this Shooting Method Approach can also be applied to other symmetric free shear flows such as symmetric planar jet and round wake flows.

## CHAPTER 6

### CONCLUSIONS AND RECOMMENDATIONS

#### 6.1 Conclusions

A systematic investigation into the symmetric/asymmetric wake development and structure in constant adverse, zero and favorable pressure gradients has been conducted at  $Re = 2.4 \times 10^6$  (based on the chord length of the splitter plate and a free stream velocity of  $30.0 \text{ m/s}$ ). As a prerequisite of this extensive research project, an environment of constant zero, favorable and adverse pressure gradients in the test section was successfully achieved. A unique feature of this wake study is that the streamwise pressure gradients imposed on the flow field are held *constant*.

To tackle the problem of the wake flow subjected to the imposed constant pressure gradients, this comprehensive wake study involves not only the conventional LDV and hot wire flow field survey, but also the similarity analysis, the numerical simulation and the sophisticated turbulent kinetic energy budget measurements.

As a result of the successful completion of this research project, an extensive experimental database documenting both mean flow and turbulence quantities of the symmetric and asymmetric wake flows subjected to constant adverse, zero and favorable pressure gradients has been established. This database enables us to seek a better understanding of the effects of pressure gradient and wake asymmetry on the wake flow behavior.

The major results of the wake study presented in this dissertation may be summarized in the following sections.

### 6.1.1 Flow Field Validation

To ensure the reliability of the experimental results, the two-dimensionality of the flow field of the test facility, including the boundary layer flow on the splitter plate and the wake flow in the diffuser test section, was carefully examined and found to be quite satisfactory. For example, the variation of the spanwise pressure is within the the range of  $\pm 4\%$  of the mean to the 95% confidence level.

The turbulent boundary layer mean velocity profile taken on the splitter plate conforms the classic log law-of-the-wall and the turbulence intensity and Reynolds stress profiles agree with the data obtained by Klebanoff (1954).

The well defined classic mean flow similarity scaling was observed for the symmetric wake starting at the location of  $x/\theta_0 \approx 40$  downstream of the splitter plate trailing edge. In particular, the wake half-width  $\delta(x)$  and the maximum velocity defect  $U_d(x)$  for the symmetric wake in zero pressure gradient vary as  $x^{1/2}$  and  $x^{-1/2}$ , respectively.

As expected, the similarity of the second moment such as the turbulence intensity and the Reynolds stress occurs further downstream than the mean flow for the symmetric wake in zero pressure gradient. More specifically, the second moment profiles do not exhibit similarity behavior until  $x/\theta_0 = 170$ .

### 6.1.2 Effects of Pressure Gradient on Wake Flow Development and Structure

Preliminary analysis of the experimental results reveals that the pressure gradient has tremendous influence on the wake widening and velocity defect decay rate. The effects are quite large despite the relatively modest gradients applied. When the adverse pressure gradient is imposed, the wake widening rate is enhanced, the velocity defect decay rate is reduced and the the turbulence intensity and the Reynolds stress are both amplified. In contrast, when the wake develops in a favorable pres-

sure gradient, the wake widening rate is reduced, the velocity defect decay rate is increased and the turbulence intensity and Reynolds stress are both decreased in relation to corresponding zero pressure gradient values. At the last measurement station ( $x/\theta_0 \approx 200$ ), the wake width for the adverse pressure gradient case is approximately 35% greater, and the maximum velocity defect is approximately 67% larger than those of the zero pressure gradient case. For the severe favorable pressure gradient case, the wake is nearly 40% thinner, and the maximum velocity defect is nearly 73% smaller than those of the zero pressure gradient case.

The aforementioned pressure gradient effect was observed not only for the symmetric wake cases, but also for the asymmetric wake cases, indicating that to some extent, the pressure gradient effect is independent of the wake asymmetry.

For the imposed pressure gradients investigated, the pressure gradient does not change the similarity behavior of the mean flow profile. Using the scaling of the local maximum velocity defect  $U_d$  and the wake half-width  $\delta$ , the wake mean velocity profiles for APG, ZPG and FPG cases investigated will all collapse to a universal wake shape. It should be pointed out that if larger adverse pressure gradient is applied, the similarity of the mean velocity profile might not be expected.

However, it seems that the imposed pressure gradients investigated does change the similarity behavior for the turbulence quantities such as the turbulence intensity and Reynolds stress for the symmetric wake. It seems that the adverse pressure gradient precipitates the turbulence development process and allows the similarity of the turbulence quantities to occur much earlier upstream than the zero pressure gradient case. As a contrast, the favorable pressure gradient delays the similarity of the turbulence quantities for the symmetric wake.

### 6.1.3 Results of the Similarity Analysis

Similarity analysis based on the work of Gartshore (1967) and Narasimha and Prabhu (1972) has been performed for the symmetric wake subjected to arbitrary pressure gradient. Explicit solutions for the wake half-width and maximum velocity defect for symmetric wake flow in arbitrary pressure gradients were derived.

The key assumption for the similarity analysis is the “shallow wake” assumption, that is, the maximum velocity defect is far less than the external velocity,  $U_d \ll U_e$ . Under this assumption, another key condition for the first order asymptotic solution is that the product  $U_e^2 U_d \delta$ , representing the wake mean flow kinetic energy deficit, is an invariant for different pressure gradients, which is backed up by the experimental evidence. According to the experimental data, it seems that the shallow wake assumption is roughly valid for  $U_d/U_e < 0.3$ . In other words, as long as the maximum velocity defect is less than 30% of the external velocity, the wake mean flow is likely to exhibit a similarity behavior, regardless of what pressure gradient is imposed to the flow field.

The similarity solution for symmetric wake flow in arbitrary pressure gradients might find a variety of engineering applications wherever the symmetric wake flow needs to be dealt with and wherever the shallow wake assumption is valid.

### 6.1.4 Effects of Wake Asymmetry on Wake Development and Structure

To investigate the influence of the wake asymmetry on wake development in pressure gradients, an initially asymmetric wake with a degree of asymmetry of 2.5 (the ratio between the momentum thicknesses of the upper and lower shear layers of the wake) was successfully obtained by means of both passive and active flow control on both sides of the splitter plate. The carefully designed experimental research scheme

ensures the effects of pressure gradient and wake asymmetry can be successfully isolated.

The effects of the wake asymmetry on the wake development can be summarized as follows.

- The asymmetric wake widens much faster than the symmetric wake;
- The velocity defect is enhanced compared with the symmetric wake;
- The asymmetry tends to further exaggerate the effect of the pressure gradient;
- The center of the wake drifts to the thicker side as the wake develops downstream. In addition, it seems that the whole wake is drifting to its thicker side when the asymmetric wake develops downstream.
- The degree of the asymmetry of the wake is reduced when the wake develops downstream, in other words, the wake becomes more symmetric in shape as it develops downstream.

#### 6.1.5 Numerical Simulation

Numerical simulation based on the code developed by Brooks (1999) was conducted for both the symmetric and asymmetric wake. The turbulence models utilized in the numerical simulation include the Cebeci-Smith algebraic model, the Spalart-Allmaras one-equation model and the Wilcox (1998)  $k - \omega$  two-equation model. The performance of the Spalart-Allmaras and the Wilcox (1998)  $k - \omega$  models were most extensively investigated. Both the Spalart-Allmaras and the Wilcox (1998)  $k - \omega$  models can capture the general trend of the effects of the pressure gradient and the wake asymmetry on the wake flow development. However, the fidelities of the two models in depicting the wake flow development under the influence of the pressure gradient and wake asymmetry are different. The Spalart-Allmaras model is

capable of faithfully handling the pressure gradient and asymmetry effects compared with the experimental results, except for the adverse pressure gradient. However, both the asymmetry and the adverse pressure gradient significantly degrade the performance of the Wilcox (1998)  $k-\omega$  model in predicting the near wake behavior.

#### 6.1.6 Turbulence Kinetic Energy Budget Measurement for Symmetric Wake

The TKE budget measurement has been conducted for the symmetric wake in constant zero, adverse and favorable pressure gradients in the near wake region at a Reynolds number of  $2.4 \times 10^6$  (based on the chord length of splitter plate and a free stream velocity of  $30.0 \text{ m/s}$ ).

The experimental procedure was designed on the basis of the uncertainty analysis to ensure the reliability of the experimental data. The maximum error associated with TKE budget measurement is less than 15% to the 95% confidence level.

Four different approaches, based on the isotropic turbulence assumption, the locally axisymmetric homogeneous turbulence assumption, the semi-isotropic turbulence assumption, and the forced balance of the TKE budget equation, were applied for the estimate of the dissipation term. Estimate of the dissipation term based on locally axisymmetric homogeneous turbulence assumption has the least bias error for all three pressure gradient cases compared to other methods.

Comparison of the TKE budget measurement results in ZPG case with DNS results (Moser, Rogers and Ewing, 1998) indicates good agreement between the experiments and the simulation and suggests that the TKE budget measurement procedure and results are reliable for the APG and FPG cases as well.

Comparison of the appropriately normalized TKE budget terms for APG, ZPG and FPG cases shows that the imposed pressure gradient does not change the fundamental flow physics for the turbulent kinetic energy transport. It seems that the

imposed pressure gradient exerts its influence through the mean flow and large scale structures with the smaller scales adjusting accordingly.

Among all measurable terms in the turbulence kinetic energy equation, the dissipation term is the one that is most likely to have a significant bias error. Two types of error sources due to the homogeneous turbulence assumption and the limited spatial resolution of hot wire probes, respectively, will both give rise to the bias error. A novel shooting method approach to correct the bias error associated the dissipation estimate is proposed on the basis of the identification of two facts, i.e., the self-similar behavior of mean square derivatives and the attribute of zero lateral integration of the pressure diffusion term in symmetric wake flows. This approach has been applied to the final TKE budget profiles in ZPG, APG and FPG. The reliability of this approach is validated through the comparison of the measured TKE budget profiles with the DNS results.

## 6.2 Recommendations

### 6.2.1 The Twin Airfoil Configuration Wake Experiment

The motivation of this wake research is the high-lift application. Although significant effects of pressure gradient have been observed in this wake study, the magnitude of the imposed pressure gradient is still far less than the actual pressure gradient encountered by a slat wake in an actual high-lift system. To overcome the limitation of the current wake study in terms of the magnitude of the imposed pressure gradient, a new experimental wake research project featuring higher magnitude of imposed pressure gradient might be necessary. A possible experimental implementation of this new research project might be the “twin-airfoil” configuration wake experiment, the schematic of which is shown in Figures 6.1. The basic idea of this experiment is to use the twin airfoil configuration instead of the flexible wall contour to impose the pressure gradient to the wake flow field. In this way, the

maximum adverse pressure gradient encountered by the wake could be at least as 20 times big as the one used in the current wake study. The successful conduction of the new project could serve the following purposes:

- To provide a new set of database for the validation of the existing high-lift numerical code;
- To check if the currently observed pressure gradient effect is still valid at higher pressure gradients;
- To examine if the similarity solution is applicable for wake development in higher pressure gradients;
- To examine if the TKE budget profiles are still invariant at higher pressure gradients.

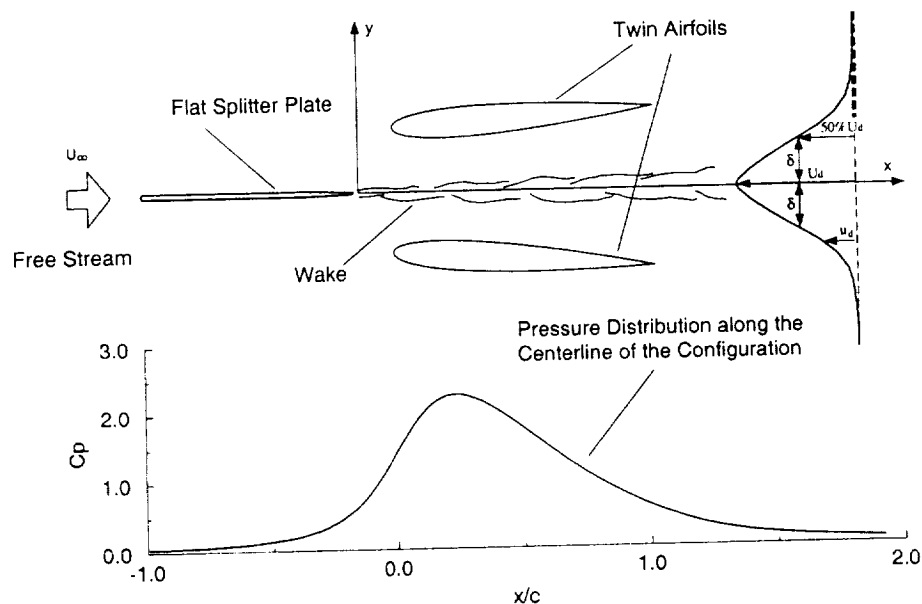


Figure 6.1. Schematic of the Twin Airfoil Configuration Wake Experiment.

### 6.2.2 Investigation of the Effects of Pressure Gradient and Wake Asymmetry on the Large Scale Structure of Wake Flow

Since the publication of the famous paper by Brown and Roshko (1974), the so-called large-scale coherent structure in turbulence flow has been received tremendous attention and exploration among the fluid dynamics community world wide. To incorporate the the large-scale structure in the analytical treatment of the turbulent flow, Hussein (1983, 1986) proposed a triple-decomposition of the flow into a mean flow, coherent structures and incoherent turbulence. The Proper Orthogonal Decomposition (POD) technique, proposed by Lumley (1967), provides another prospective approach to incorporate the coherent structure concept in a more definite and manageable sense into the analytical treatment of the turbulence flow. Recent applications of POD technique in plane mixing layer by Delville, Ukeiley, Cordier, Bonnet and Glauser (1999), planar jet flow by Gordeyev and Thomas (2000, 2001) and the cylinder wake in low Reynolds number by Ma, Karamanos and Karniadakis (2000) demonstrated the capability of characterizing and even modelling the large scale structures in free turbulence flow. In addition to the POD technique, the linear stochastic estimate (LSE) technique proposed by Adrian (1975) and successfully implemented by several groups of researchers (Adrian (1979), Tung *et al* (1980), Adrian *et al* (1989), Guezennec (1989), Cole *et al* (1992), Adrian (1994), Bonnet *et al* (1994) and Bonnet *et al* (1998)), is also a powerful tool for the investigation of large scale structures in turbulence.

So far, all analyses of the current wake study presented in this dissertation are investigated within the conventional framework of Reynolds Averaged Navier-Stokes (RANS) equation. However, one shortcoming of the RANS approach is that the RANS approach simply filters out the large scale structure through the averaging process and it does not incorporate any appropriate treatment to reflect the actual

flow physics for which the existence of coherent structure or any large scale structure in turbulent free shear flows should never be neglected. The investigation into the large scale structures in the symmetric/asymmetric wake flow subjected to pressure gradients using both LSE and POD techniques could open a new fruitful dimension of the current wake research and the exploration of the pressure gradient and wake asymmetry effects on the large scale structure should also be a unique research topic.

## BIBLIOGRAPHY

- Alber, I.E., Turbulent wake of a Thin, Flat Plate. *AIAA Journal*, vol. 18, No.9, pp. 1044-1051, 1980.
- Adrian, R.J., On the Role of Conditional Averages in Turbulence Theory, *Turbulence in Liquids: Proceedings of the 4th Biennial Symposium on Turbulence in Liquids*, September, 1975. Science Press, Princeton, NJ, pp323-332.
- Adrian, R.J., Conditional Eddies in Isotropic Turbulence, *Phys. Fluids*, Vol. 22, No. 11, 1979.
- Adrian, R.J., Jones, B.G., Chung, M.K., Hassan, Y., Nithianandan, C.K. and Tung, A.T.-C., Approximation of Turbulent Conditional Averages by Stochastic Estimation, *Phys. Fluids A*, Vol. 1, No. 6, 1989.
- Andereopoulos, J., and Bradshaw, P., Measurements of Interacting Turbulent Shear layers in the near Wake of a Flat Plate, *Journal of Fluid Mechanics*, vol. 100, part 3, pp.639-668, 1980.
- Antonia, R., Browne, W. and Bisset, D., A Description of Organized Motion in the Turbulent Far Wake of a Cylinder at Low Reynolds Number, *Journal of Fluid Mechanics*, vol. 184, pp.423, 1987.
- Azad, R.S. and Kassab, S.Z., New Method of Obtaining Dissipation, *Experiments in Fluids*, Vol. 7, pp. 81-87, 1989.
- Bendat, J.S., Piersol, A.G., *Random Data Analysis and Measurement Procedures*, John Wiley Sons, Inc., Third Edition, 2000.
- Bonnet, J.P., Cole, D.R., Delville, J., Glauser, M.N. and Ukeiley, L.S., Stochastic Estimation and Proper Orthogonal Decomposition: Complementary Techniques for Identifying Structure, *Experiments in Fluids*, 17, pp. 307-314, 1994.
- Bonnet, J.P., Delville, J., Glauser, M.N., Antonia, R.A., Bisset, D.K., Cole, D.R., Fiedler, H.E., Garem, J.H., Hilberg, D., Jeong, J., Kevlahan, N.K.R., Ukeiley, L.S. and Vincendeau, E., Collaborative testing of Eddy Structure Identification Methods in Free Turbulent Shear Flows, *Experiments in Fluids*, 25, pp. 197-225, 1998
- Brooks, G., *Numerical Simulation of a Planar Turbulent Wake in Arbitrary Pressure Gradient*, M.S. Thesis, University of Notre Dame, 1999.

- Brown, G.L. and Roshko, G., On Density Effects and Large Structure in Turbulent Mixing Layers, *J. Fluid Mech.*, 64, pp. 775-816, 1974.
- Browne, L.W., Antonia, R.A. and Shah, D.A., , Turbulent Energy Dissipation in a Wake, *J. Fluid. Mech.*, vol. 179, pp. 307-326, 1987.
- Carlson, J.R., Duquesne, N., Runsey, C.L. and Gatski, T.B., Computation of Turbulent Wake Flows in Variable Pressure Gradient, *Computers Fluids* , vol. 30, pp. 161-187, 2001.
- Cebeci, T. and Smith, A.M.O., Analysis of Turbulent Boundary Layers, *Ser. in Appl. Math. Mech.*, Vol. XV, Academic Press, Orlando, FL., 1974.
- Cebeci, T., Thiele, F., Williams, P.G. and Stewartson, K., On the Calculation of Symmetric wake I. Two-dimensional Flows, *Numerical Heat Transfer*, vol. 2, pp. 35-60, 1979.
- Chevray, R. and Kovaszny, L.S.G., Turbulence Measurements in the Wake of a Thin Flat Plate, *AIAA Journal*, vol. 7, pp. 1641-1643, 1969.
- Chin, V.D., Peters, D.W., Spaid, F.W. and McGhee, R.J., Flowfield Measurements About a Multi-Element Airfoil at High Reynolds Numbers, *AIAA paper 93-3137*, 1993.
- Cimbala, J.M. and Park, W.J., An experimental Investigation of the Turbulent Structure in a Two-dimensional momentumless Wake, *Journal of Fluid Mechanics*, vol. 213, pp.479-509, 1990.
- Cole, D.R., Glauser, M.N. and Guezennec, Y.G., An Application of the Stochastic Estimation to the Jet Mixing Layer, *Phys. Fluids A*, Vol.4, No.1, pp.192-194, 1992.
- Compton, D.A. and Eaton, J.K., Near-wall Measurements in a Three-Dimensional Turbulent Boundary Layer, *J. Fluid. Mech.*, Vol. 350, pp. 189-208, 1997.
- Corke, T.C., Krull, J.D. and Ghassemi, M., Three-Dimensional-Mode Resonance in Far Wakes, *Journal of Fluid Mechanics*, vol. 239, pp.99-132, 1992.
- Demuren, A.O., Rogers, M.M., Durbin, P. and Lele, S.K., On Modeling Pressure Diffusion in Non-homogeneous Shear Flows, *Proceedings of the Summer Program 1996*, Center of Turbulent Research, Stanford University, 1996.
- Delville, J., Ukeiley, L., Cordier, L., Bonnet, J.P. and Glauser, M., Examination of Large Scale Structures in a Turbulent Plane Mixing Layer. Part 1. Proper Orthogonal Decomposition, *J. of Fluid Mech.*, Vol. 391, pp.91-122,1999.
- Driver, D.M. and Mateer, 2000, Wake Flow in an Adverse Pressure Gradient, *AIAA Paper 2000-5511*.
- Duquesne, N., Carlson, J.R., Runsey, C.L. and Gatski, T.B., Computation of Turbulent Wake Flows in Variable Pressure Gradient, *AIAA paper 99-3781*,

1999.

Fabris, G., High-Order Statistics of Turbulent Fluctuations in the Plane Wake, *Physics of Fluids*, vol. 26, pp.1437-1445, 1983.

Faure, T. and Robert G., Turbulent Kinetic Energy Balance in the Wake of a Self-propelled Body, *Experiments in Fluids*, Vol. 21, pp268-274, 1996.

Garner, P.L., Meredith, P.T., and Stoner, R.C., Areas for CFD Development as Illustrated by Transport Aircraft Applications, *AIAA paper 91-1527*, 1991.

Gartshore, I.S., Two-dimensional Turbulent Wakes, *Journal of Fluid Mechanics*, vol.30, part 3, pp.547-560, 1967.

George, W.K. and Hussein, H.J., Locally Axisymmetric Turbulence, *J. Fluid. Mech.*, vol. 233, pp. 1-23, 1991.

Gerrard, J.H., The Three-dimensional Structure of a Wake of a Circular Cylinder, *Journal of Fluid Mechanics*, vol.25, pp.143. 1966.

Gharib, M. and Williams-Stuber, K., Experiments on the Forced Wake of an Airfoil, *Journal of Fluid Mechanics*, vol.208, pp.225-255, 1989.

Gordeyev, S.V. and Thomas, F.O., Coherent Structure in the Turbulent Planar Jet. Part 1. Extraction of Proper Orthogonal Decomposition Eigenmodes and Their Self-Similarity", *J. of Fluid Mech.*, vol. 414, pp. 145-194, 2000

Gordeyev, S.V. and Thomas, F.O., Coherent Structure in the Turbulent Planar Jet. Part 2. Structural Topology via POD Eigenmode Projection, submitted to *J. of Fluid Mech.*, 2001.

Guezennec, Y.G. Stochastic Estimation of Coherent Structures in Turbulent Boundary Layers, *Phys. Fluids A*, Vol. 1, No. 6, 1989.

Gutmark, E and Wygnanski, I., The Planar turbulent Jet, *J. Fluid. Mech.*, vol. 73, part 3, pp. 465-495, 1976.

Hah, C. and Lakshminarayana, B., Measurement and Prediction of Mean Velocity and Turbulence Structure in the Near Wake of an Airfoil, *Journal of Fluid Mechanics*, vol.115, pp.251-282, 1982.

Hayakawa, M. and Iida, S., Behavior of Turbulence in the Near-Wake of a Thin Flat plate at Low Reynolds Numbers, *Physics of Fluids A*, vol.4, No. 10, pp.2282-2291, 1992.

Heskestad, G., Hot-Wire Measurements in a Plane Turbulent Jet, Transactions of ASME, *Journal of Applied Mechanics*, December, 1965, pp. 721-734, 1965.

Hill, P.G., Schaub, U.W., and Senoo, Y., Turbulent wakes in Pressure Gradients, *Journal of Applied Mechanics*. Vol. 30, No. 12, pp 518-524, 1963.

Hinze, J. O., *Turbulence*, McGraw-Hill Book Company, New York, 1975.

- Hoffenberg, R., Sullivan, J.P., and Schneider, S.P., Wake Measurements in a Strong Adverse Pressure Gradient, *AIAA Paper 95-1912*, 1995.
- Hoffenberg, R. and Sullivan, J.P., Measurement and Simulation of a Decelerated Wake, *AIAA Paper 98-0522*, 1998.
- Hussein, A.K.M.F., Coherent Structures - Reality and Myth, *Phys. Fluids*, 26, pp. 2816-2850, 1983.
- Hussein, A.K.M.F., Coherent Structures and Turbulence, *J. Fluid Mech.*, 173, pp. 303-356, 1986.
- Hussein, H.J., Capp, S.P. and George, W.K., Velocity Measurements in a High-Reynolds-number, Momentum-conserving, Axisymmetric, Turbulent Jet, *J. Fluid. Mech.*, vol. 258, pp. 31-75, 1994.
- John, J. and Schobeiri, M.T., Development of a Two-dimensional Turbulent Wake in a Curved Channel with a Positive Streamwise Pressure Gradient, *Journal of Fluids Engineering, Transactions of the ASME*, Vol. 118, pp.292-299.
- Keffer, J.F., The Uniform Distortion of a Turbulent Wake, *Journal of Fluid Mechanics*, vol.22, part 122, pp.135-159, 1965.
- Kopp, G.A., Kawall, J.G. and Keffer, J.F., The evolution of the Coherent Structures in a Uniformly Distorted Plane Turbulent Wake, *Journal of Fluid Mechanics*, vol. 291, pp.299-322, 1995.
- Lasheras, J.C., Cho, J.S. and Maxworthy, T., On the Origin and Evolution of Streamwise Vortical Structures in a Plane, Free Shear Layer, *Journal of Fluid Mechanics*, vol. 172, pp.231-258,1986.
- Lasheras, J.C., Choi, H., Three-dimensional Instability of a Plane Free Shear Layer: An Experimental Study of the Formation and Evolution of Streamwise Vortices, *Journal of Fluid Mechanics*, vol. 189, pp.53-86, 1988.
- Laufer, J., The Structure of Turbulence in Fully Developed Pipe Flow, *NACA report 1174*, 1954.
- Lemay, J., Delville, J. and Bonnet, J.P., Turbulent Kinetic Energy Balance in a LEBU Modified Turbulent Boundary Layer, *Experiments in Fluids*, vol. 9, pp. 301-308.
- Lin, J.C., Robinson, S.K., and McGhee, R.J., Separation Control on High Reynolds number Multi-Element Airfoils, *AIAA paper 92-2636*, 1992.
- Liu, X., Thomas, F.O. and Nelson, R.C., Measurement of the Turbulence Kinetic Energy Budget of Symmetric Planar Wake Flows in Pressure Gradient, *Bulletin of the American Physical Society*, Vol. 45, No.9, pp. 164, 2000.

- Liu, X., Thomas, F.O. and Nelson, R.C., An Experimental Investigation of Wake Development in Arbitrary Pressure Gradients, *AIAA paper 99-0677*, 1999a.
- Liu, X., Thomas, F.O., and Nelson, R.C., Experimental and Numerical Investigation of Pressure Gradient Effects on Asymmetric Wake Development, *Bulletin of the American Physical Society*, Vol. 44, No. 8, pp133-134, 1999b.
- Liu, X., Thomas, F.O. and Nelson, R.C., Asymmetric Wake Development and Structure in Arbitrary Pressure Gradients, *Bulletin of the American Physical Society*, Vol. 43, No.9, pp. 2006, 1998.
- Lumley, J., The Structure of Inhomogeneous Turbulent Flows, *Proceedings of the International Colloquium on the Fine Scale Structure of the Atmosphere and Its Influence on Radio Wave Propagation* (ed., A.M. Yaglom and V.I. Tatarski), Moscow, Nauka, pp. 166-178, 1967.
- Ma, X., Karamanos, G.-S., Karniadakis, G. E., Dynamics and low-dimensionality of a turbulent near wake, *J. of Fluid Mech.*, Vol. 410, pp. 29-65, 2000.
- MacLennan, A.S.M. and Vincent, J.H., Transport in the Near Aerodynamic wakes of Flat Plates, *Journal of Fluid Mechanics*, vol. 120, pp.185-197, 1982.
- Mack, M.D., and McMasters, J. H., High Reynolds Number Testing in Support of Transport Airplane Development, *AIAA paper 92-3982*, 1992.
- Marasli, B., Champagne, F.H. and Wygnanski, I.J., Modal Decomposition of Velocity Signals in a Plane, Turbulent Wake, *J. Fluid Mech.*, vol. 198, pp255-273, 1989.
- Marasli, B., Champagne, F.H. and Wygnanski, I.J., On Linear Evolution of Unstable Disturbances in a Plane Turbulent Wake, *Phys. Fluids A*, vol. 3, No. 4, pp665-674, 1991.
- Marasli, B., Champagne, F.H. and Wygnanski, I.J., Effect of Travelling Waves on the Growth of a Plane Turbulent Wake, *J. Fluid Mech.*, vol. 235, pp511-528, 1992.
- Mattingly, G.E. and Criminale, W.O., The Stability of an Incompressible Two-dimensional Wake, *Journal of Fluid Mechanics*, vol. 51, pp.233-272, 1972.
- Maekawa, H., Mansour, N.N. and Buell, J.C., Instability Mode Interactions in a Spatially Developing Plane Wake, *Journal of Fluid Mechanics*, vol. 235, pp.223-254, 1992.
- Meiburg, E. and Lasheras, J.C., Experimental and Numerical Investigation of the Three-dimensional Transition in Plane Wakes, *Journal of Fluid Mechanics*, vol. 190, pp.1-37, 1988.
- Meyers, J.F., The Elusive Third Component, *FED Vol.33*, International Symposium on Laser Anemometry, the Winter Annual Meeting of the ASME, Miami Beach, Florida, November 17-22, 1985, 1985.

- Moser, R.D., Rogers, M.M., and Ewing, D.W., Self-similarity of Time-evolving Plane Wakes, *J. Fluid. Mech.*, vol. 367, pp. 255-289, 1998.
- Nakayama, A., Curvature and Pressure-gradient Effects on a Small-defect Wake, *Journal of Fluid Mechanics*, vol.175, pp.215-246, 1987.
- Narasimha, R., and Prabhu, A., Equilibrium and Relaxation in Turbulent Wakes, *Journal of Fluid Mechanics*, vol.54, part1, pp.1-17, 1972.
- Panchapakesan, N.R. and Lumley, J.L., Turbulence Measurements in Axisymmetric Jets of Air and Helium Part 1. Air Jet, *J. Fluid. Mech.*, vol. 246, pp. 197-223, 1993.
- Patel, R. P. and Newman, B. G., Self-preserving, Two-dimensional Turbulent Jets and Wall Jets in a Moving Stream, McGill University, *MERL Report Ae5*, 1961.
- Patel, V.C. and Chen, H.C., Turbulent Wake of a Flat Plate, *AIAA Journal*, Vol. 25, No. 8, pp. 1078-1085, 1987.
- Patel, V.C. and Sarda, O.P., Mean-flow and Turbulence Measurements in the Boundary Layer and Wake of a Ship Double Model, *Experiments in Fluids*, vol. 8, pp. 319-335, 1990.
- Petrov, A.V., Certain Types of Separated Flow over Slotted Wings, *Fluid Mechanics-Soviet Research*, Vol. 7, No.5, pp 80-89, 1978.
- Prabhu, A., and Narasimha, R., Turbulent Non-equilibrium Wakes, *Journal of Fluid Mechanics*, vol.54, part1, pp.19-38, 1972.
- Raffoul, C.N., Nejad, A.S. and Gould, R.D., Investigation of Three-dimensional Turbulent Transport behind a Bluff Body, *FED-vol.217*, Separated and Complex Flows, ASME, pp. 121-128, 1995.
- Ramaprian, B.R., and Patel, V.C., The symmetric Turbulent Wake of a Flat Plate, *AIAA journal*, Vol. 20, No.9, pp1228-1235, 1982.
- Ranjee, V. and Neelakandan, D., Development of Wake of a Rectangular Cylinder in a Curved Stream, *Experiments in Fluids*, Vol.7, pp. 395-399, 1989.
- Reynolds, A.J., Observation on Distorted turbulent Wakes, *Journal of Fluid Mechanics*, vol.13, pp.333-356, 1962.
- Rogers, M.M., The Evolution of Strained Turbulent Plane Wakes, *J. Fluid. Mech.*, in press, 2001.
- Roos F.W., Experimental Studies of Wake Retardation in a Simulated High-Lift system Flow Field, *AIAA Paper 97-1813*, 1997.

- Rumsey, C.L., Gatski, T.B., Ying, S.X., and Bertelrud, A., Prediction of High-lift Flows using Turbulent Closure models, *AIAA paper 97-2260*, June, 1997.
- Savill, A.M., The turbulent Structure of a Highly Curved Two-Dimensional Wake, *Structure of Complex Turbulent Shear Flow*, IUTAM Symposium 1982, R. Dumas and L. Fulachier, eds., Springer, New York, pp185-197, 1983.
- Schlichting, H., *Boundary Layer Theory*, McGraw-Hill Book Company, Seventh Edition, 1979
- Smith, A.M.O., High-Lift Aerodynamics, *AIAA Journal of Aircraft*, 12, 6, pp. 501-530, 1975.
- Spalart, P.R. and Allmaras, S.R., A One-Equation Turbulence Model for Aerodynamic Flows, *AIAA Paper 92-0439*, 1992.
- Thennekes, H. and Lumley, J.L., *A First Course in Turbulence*, The MIT Press, 1972.
- Thomas, F.O., Liu, X. and Nelson, R.C., Experimental Investigation of the Confluent Boundary Layer of a High-Lift System, *AIAA paper 97-1934*, 1997.
- Thomas, F.O., Nelson, R.C. and Liu, X., An Experimental Investigation of Unsteady Effects in a High-Lift System, *AIAA paper 98-0704*, 1998.
- Thomas, F.O., Nelson, R.C. and Liu, X., Experimental Investigation of the Confluent Boundary Layer of a High-Lift System, *AIAA Journal*, Vol. 38, No. 6, pp978-988, 2000.
- Townsend, A.A., *The Structure of Turbulent Shear Flow*, Cambridge University Press, 1956.
- Tummers, M.J., Passchier, D.M. and Henkes, R.A.W.M., Experimental Investigation of an Adverse Pressure Gradient Wake and Comparison with Calculations, *Experimental Thermal and Fluid Science*, Vol. 14, pp17-24, 1997.
- Tung, T.C. and Adrian, R.J., Higher-order Estimates of Conditional Eddies in Isotropic Turbulence, *Phys. Fluids*, vol. 23, No. 7, pp. 1469-1470, 1980.
- Wallace, J.M. and Foss, J.F., The Measurement of Vorticity in Turbulent Flows, *Annual Review of Fluid Mechanics*, vol. 27, pp. 469-514, 1995.
- Wilcox, D. C., *Turbulence Modeling for CFD*, 2nd Edition, DCW Industries, Inc., La Canada, California, 1998.
- Wu, H., Patterson, G.K. and Van Doorn, M., Distribution of Turbulence Energy Dissipation Rates in a Rushton Turbine Stirred Mixer, *Experiments in Fluids*, vol. 8, pp. 153-160, 1989.
- Wygnański, I., Champagne, F. and Marasli, B., On the Large-scale Struc-

ture in Two-dimensional, Small-Deficit, Turbulent Wakes, *Journal of Fluid Mechanics*, vol.168, pp.31-71, 1986.

Wyganski, I. and Fiedler, H., Some Measurements in the Self-preserving Jet, *J. Fluid. Mech.*, vol. 38, part 3, pp. 577-612, 1969.

Wyganski, I. and Fiedler, H.E., The Two-dimensional Mixing Region, *J. Fluid. Mech.*, vol. 41, part2, pp. 327-361, 1970.

Zhou, Y. and Antonia, R.A., Memory Effects in a Turbulent Plane Wake, *Experiments in Fluids*, Vol. 19, pp112-120. 1995.

Zhou, M.D., Heine, C. and Wygnanski, I., The effects of excitation on the coherent and random motion in a plane wall jet, *J. Fluid. Mech.*, vol. 310, pp. 1-37, 1996.

Zhou, M. D. and Squire, L. C., The Interaction of a Wake with a Turbulent Boundary Layer, *Aeronautical Journal*, pp. 72-81, 1985.

## APPENDIX A

### DETERMINATION OF THE OPTIMAL SPACING BETWEEN MEASUREMENT STATIONS FOR THE TKE BUDGET MEASUREMENTS

#### A.1 Lagrangian Interpolation and Central Difference Scheme

The streamwise derivatives in the TKE budget were estimated from the data taken at three consecutive streamwise measurement stations. A natural approach for taking the spatial derivative of function  $f(x)$  based on the experimental data might be first taking the Lagrangian interpolation, denoted by  $p(x)$ , as expressed in Equation (A.1), through the three arbitrary spatially separated nodal points and then taking the derivative of the Lagrangian interpolation, as shown in Figure A.1.

$$f(x) \approx p(x) = \frac{(x - x_i)(x - x_{i+1})}{(x_{i-1} - x_i)(x_{i-1} - x_{i+1})}y_{i-1} + \frac{(x - x_{i-1})(x - x_{i+1})}{(x_i - x_{i-1})(x_i - x_{i+1})}y_i + \frac{(x - x_{i-1})(x - x_i)}{(x_{i+1} - x_{i-1})(x_{i+1} - x_i)}y_{i+1} \quad (\text{A.1})$$

However, for  $x_i = x$ ,  $x_i - x_{i-1} = h$  and  $x_{i+1} - x_i = h$ , we have

$$\frac{df}{dx} \approx \frac{dp}{dx} = \frac{y_{i+1} - y_{i-1}}{2h} \quad (\text{A.2})$$

which is the central difference scheme. This demonstrates that the numerical differentiation based on the even-spaced quadratic Lagrangian polynomial interpolation

is identical to the central difference scheme. In other words, the central difference scheme is based on the implicit assumption that the curve passing through the three nodal points is a quadratic Lagrangian polynomial. From Gerald and Wheatly (1994), when  $x_i = x$ ,  $x_i - x_{i-1} = h$  and  $x_{i+1} - x_i = h$ , the error term of the derivative based on Lagrangian interpolation is

$$\frac{df}{dx} - \frac{dp}{dx} = -\frac{h^2}{3!} f'''(\xi) \quad (\text{A.3})$$

which is again identical to the truncation error term of the central difference scheme. Thus, the true value of  $\frac{df}{dx}$  can be written as

$$\frac{df}{dx} = \frac{dp}{dx} + \text{error} = \frac{y_{i+1} - y_{i-1}}{2h} - \frac{h^2}{3!} f'''(\xi) \quad (\text{A.4})$$

## A.2 Uncertainty of the Streamwise Derivative

Denote

$$D = \frac{y_{i+1} - y_{i-1}}{2h},$$

$$\delta_t = -\frac{h^2}{3!} f'''(\xi),$$

then

$$\frac{df}{dx} = D + \delta_t \quad (\text{A.5})$$

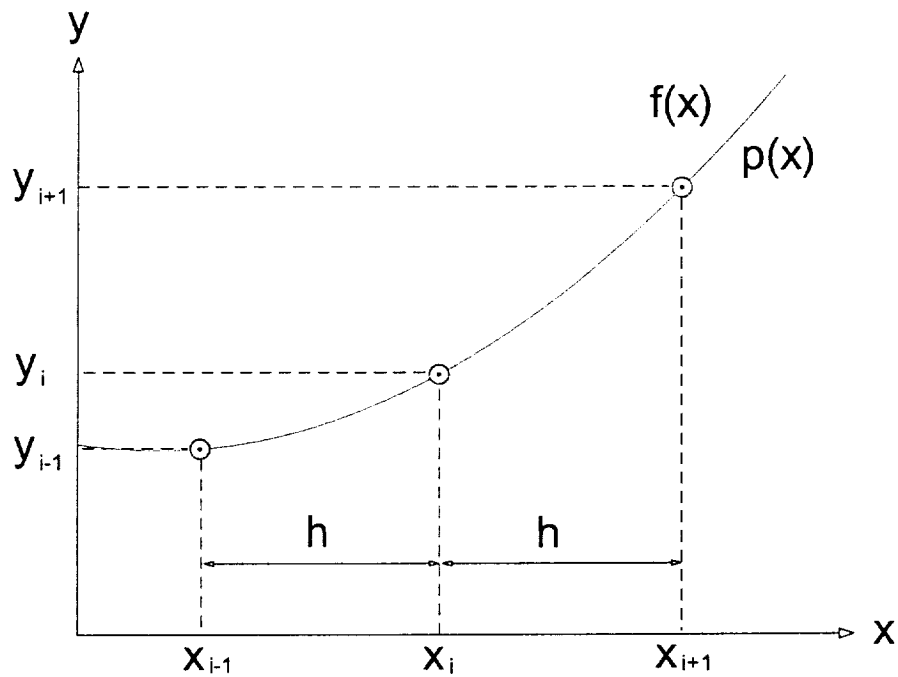


Figure A.1. Lagrangian Interpolation

Ideally, if there is no positioning error associated with the movement of the measuring probes, the error of the estimate of  $\frac{df}{dx}$  is solely determined by  $\delta_t$ , which is in nature a bias error due to the use of the central difference scheme. This error will increase if  $h$  increases. So ideally, we want the spacing between the two measurement stations as close as possible. However, in reality, there are positioning errors associated with the streamwise and lateral locations of the probe, i.e.,  $x$  and  $y$  laboratory positions of the probe. With the consideration of this positioning error, the behavior of the total uncertainty of  $\frac{df}{dx}$  will be totally different. Let  $\delta h$  and  $\delta y$  be the positioning errors associated with  $x$  and  $y$  coordinates, respectively. Then the propagation of these errors to the quantity  $\delta D$  can be estimated as

$$\begin{aligned}\delta D &= \sqrt{\left(\frac{\partial D}{\partial h}\delta h\right)^2 + \left(\frac{\partial D}{\partial y_{i+1}}\delta y_{i+1}\right)^2 + \left(\frac{\partial D}{\partial y_{i-1}}\delta y_{i-1}\right)^2} \\ &= \sqrt{\frac{(y_{i+1} - y_{i-1})^2}{4h^4}(\delta h)^2 + \frac{1}{2h^2}(\delta y)^2}\end{aligned}\quad (\text{A.6})$$

The uncertainty of  $\delta_t$  due to the positioning error is

$$\delta(\delta_t) = \sqrt{\left(\frac{\partial \delta_t}{\partial h}\right)^2 (\delta h)^2} = \frac{h\delta h}{3} f'''(\xi) \quad (\text{A.7})$$

Finally, the total uncertainty of the streamwise derivative  $\frac{df}{dx}$  is given by

$$\delta\left(\frac{df}{dx}\right) = \sqrt{(\text{Random Error})^2 + (\text{Bias Error})^2} \quad (\text{A.8})$$

where

$$\begin{aligned}\text{Random Error} &= \sqrt{(\delta D)^2 + (\delta(\delta_t))^2} \\ &= \sqrt{\frac{(y_{i+1} - y_{i-1})^2}{4h^4}(\delta h)^2 + \frac{1}{2h^2}(\delta y)^2 + \left(\frac{h}{3}f'''(\xi)\right)^2 (\delta h)^2}\end{aligned}\quad (\text{A.9})$$

$$\text{Bias Error} = \delta_t = \frac{h^2}{3!} f'''(\xi) \quad (\text{A.10})$$

i.e.,

$$\begin{aligned} \delta \left( \frac{df}{dx} \right) &= \sqrt{(\delta D)^2 + (\delta(\delta_t))^2 + (\delta_t)^2} \\ &= \sqrt{\frac{(y_{i+1} - y_{i-1})^2}{4h^4} (\delta h)^2 + \frac{1}{2h^2} (\delta y)^2 + \left( \frac{h}{3} f'''(\xi) \right)^2 (\delta h)^2 + \left( \frac{h^2}{3!} f'''(\xi) \right)^2} \quad (\text{A.11}) \end{aligned}$$

### A.3 The Optimal Spacing between Measurement Stations

As indicated in Equation (A8), the final total uncertainty of  $\frac{df}{dx}$  comprises two parts, the random error part and the bias error part. The variations of these two parts with  $h$  are different, as shown in Figures A.2 and A.3 in which the comparisons of the total uncertainty of  $dk/dx$  and  $dU/dx$  and the corresponding random and bias error parts are shown. Obviously, the first two terms in the random error part dominate the random error behavior, decreasing as  $h$  increases. However, the bias error increases as  $h$  increases. The two competing parts give rise to the optimal separation  $h$ . Based on these two plots, one can choose approximately the optimal separation of the measurement station as around 12.7 cm (5 in).

### A.4 Location of Measurement Stations

The previous analysis shows the optimal spacing between the streamwise measurement stations is roughly 12.7 cm (5 in). For our TKE budget measurement, we choose  $x = 88.9$  cm, 101.6 cm and 114.3 cm as the locations for the streamwise measurement stations. The TKE budget is then estimated at  $x = 101.6$  cm for ZPG, APG and FPG cases. This region of measurement is located roughly in the middle of the imposed pressure gradient zone in the diffuser test section and any possible ambiguity due to the end effect of the diffuser test section can be avoided with this arrangement of the measurement stations.

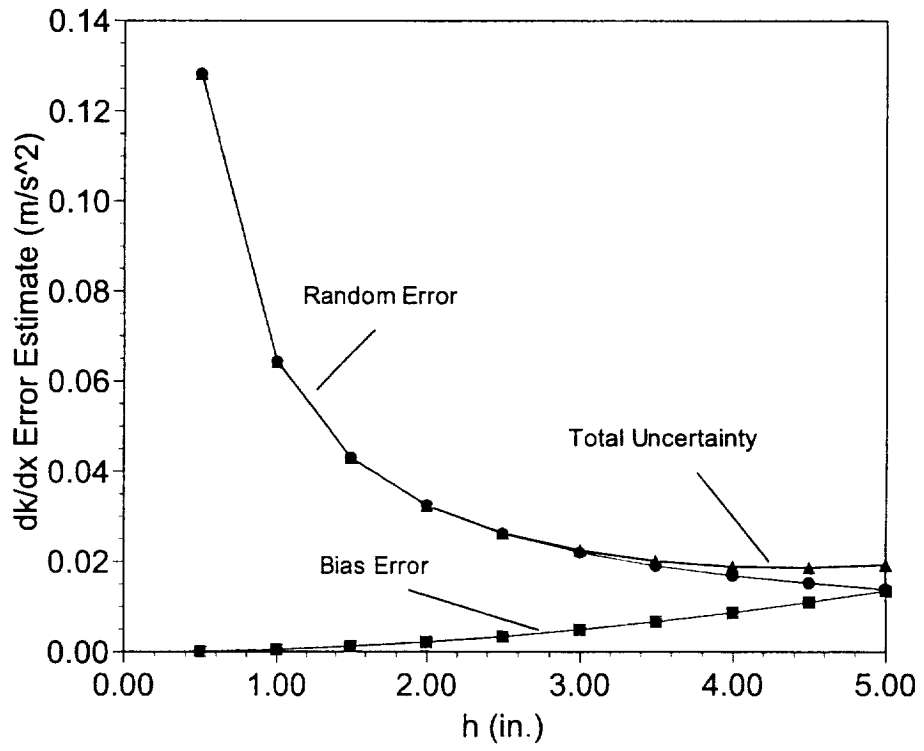


Figure A.2. Uncertainty Analysis of  $dk/dx$  for ZPG at  $x = 101.6 \text{ cm}$ ,  $y = 0.0 \text{ cm}$ .

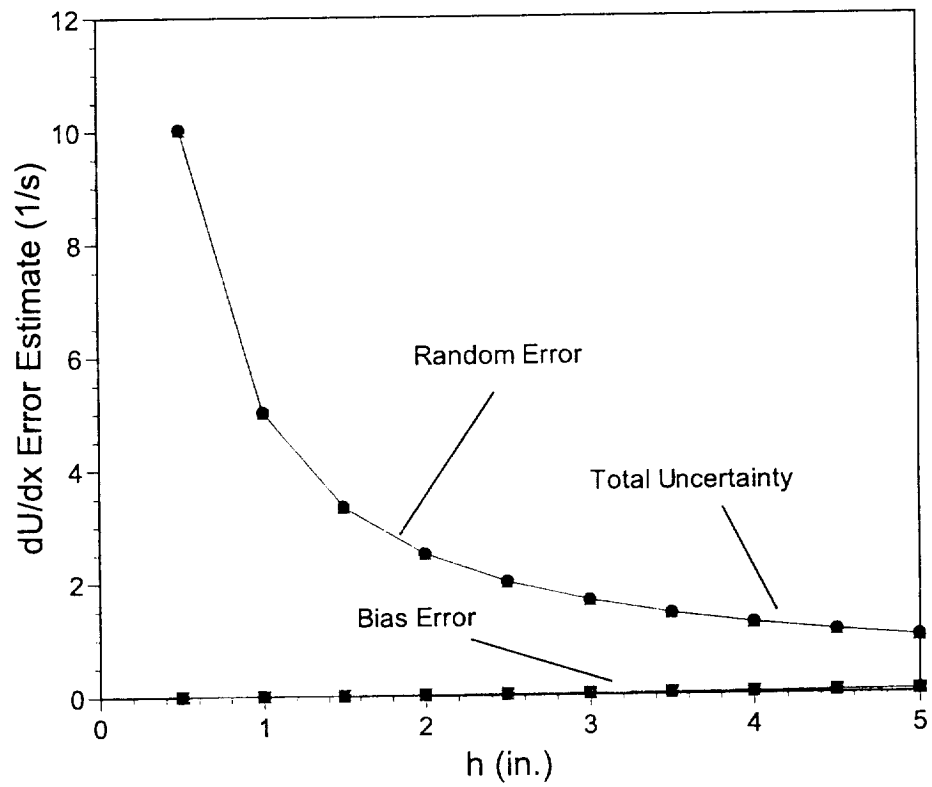


Figure A.3. Uncertainty Analysis of  $dU/dx$  for ZPG at  $x = 101.6 \text{ cm}$ ,  $y = 0.0 \text{ cm}$ .

